Shape Statistics via Skeletal Structures

by

Mohsen Taheri Shalmani

Thesis submitted in fulfilment of
the requirements for the degree of
PHILOSOPHIAE DOCTOR
(PhD)

Faculty of Science and Technology
Department of Mathematics and Physics
2024

In memory of Prof. James Damon

iv

Acknowledgments

Mohsen Taheri Shalmani

Stavanger, April 2024

Abstract

Statistical shape analysis has emerged as a crucial tool for medical researchers and clinicians to study medical objects such as brain subcortical structures. The insights gained from such analyses hold immense potential for diagnoses and enhancing our understanding of various diseases, particularly neurological disorders.

This thesis explores three important areas of statistical shape analysis, which are detailed in three separate papers: "Statistical Analysis of Locally Parameterized Shapes," "Fitting Discrete Swept Skeletal Structures to Slabular Objects," and "The Mean Shape under the Relative Curvature Condition." The innovative approaches discussed in these papers offer a fresh perspective for representing complex shapes, enabling more nuanced analysis and interpretation. Central to this work is the discussion surrounding the introduction of robust skeletal representations for establishing correspondences for a class of swept regions called slabular objects and providing proper mathematical methodologies supporting the statistical objectives such as hypothesis testing and classification. The proposed skeletal models are alignment-independent and invariant to the act of Euclidean similarity transformations of translation, rotations, and scaling.

Damon's criterion of the relative curvature condition (RCC) is an essential factor for valid swept skeletal structures. This work extensively discusses fitting skeletal models, defining shape space, and calculating the mean shape for such models following the RCC.

The efficacy of the proposed methodology is underscored through rigorous examinations, both visually and statistically. These methodologies are specifically applied to medical contexts, focusing on analyzing subcortical structures. Synthetic and actual datasets serve for validation, facilitating a comprehensive comparison with existing skeletal representations. This work highlights the resilience and adaptability of innovative approaches, paving the way for further medical research and diagnostic endeavors.

List of papers

Paper I

Taheri, Mohsen, and Jörn Schulz (2022). "Statistical Analysis of Locally Parameterized Shapes." *Journal of Computational and Graphical Statistics* **32.2 (2023): 658-670.**

Paper II

Taheri, Mohsen, Stephen M. Pizer, and Jörn Schulz (2023). "Fitting the Discrete Swept Skeletal Representation to Slabular Object." *Submitted for publication in Journal of Mathematical Imaging and Vision.*

Paper III

Taheri, Mohsen, Stephen M. Pizer, and Jörn Schulz (2024). "The Mean Shape under the Relative Curvature Condition." *Submitted for publication in Journal of Computational and Graphical Statistics*

The three papers mentioned above utilize data from The Norwegian ParkWest Study (Alves et al., 2009), a prospective population-based, longitudinal cohort study of patients with incident Parkinson's disease in Western and Southern Norway in collaboration with The Stavanger University Hospital.

Abbreviations

Abbreviation	Meaning
CMS	Central Medial Skeleton
DSRep	Discrete Skeletal Representation
DSSRep	Discrete Swept Skeletal Representation
EDM	Euclidean Distance Matrix
ETRep	Elliptical Tube Representation
ETube	Elliptical Tube
FDR	False Discovery Rate
GC	Generalized Cylinder
GOP	Geometric Object Property
IDSREP	Intermediate Discrete Skeletal Representation
LPDSRep	Locally Parameterized Discrete Skeletal Representation
LPDSSRep	Locally Parameterized Discrete Swept Skeletal Representation
MRep	Medial Representation
MRI	Magnetic Resonance Imaging
PD	Parkinson's Disease
PDM	Point Distribution Model
PCA	Principal Component Analysis
PGA	Principal Geodesic Analysis
PNS	Principal Nested Sphere
RCC	Relative Curvature Condition
SlO	Slabular Object
SPHARM-PDM	Spherical Harmonic Point Distribution Model
SRep	Skeletal Representation

Table of Contents

Papers

1 Introduction

1.1 Background and motivation

Over the years, scientists have endeavored to investigate the *shapes* and formations of biological organisms. Among the early pioneers in this field were the renowned Italian scholars Leonardo da Vinci (1452 - 1519) and Galileo Galilei (1564 - 1642). Leonardo documented the anatomy of the human body and recorded his observations of diseases, with a particular focus on conditions such as cardiovascular and musculoskeletal diseases. He also tried to articulate the ideal proportions of the human body reflected in his well-known artwork, the "Vitruvian Man" (Oksanish, 2019). Additionally, Galileo made a significant discovery regarding the animals' skeletons. He realized the skeletons of large animals not only exhibit size variations compared to smaller ones but also distinct shape differences. Bones in larger animals become proportionally thicker to support their heavier weight, while bones in smaller animals remain thinner (Dryden and Mardia, 1998).

Despite the efforts of Leonardo and Galileo, we can attribute the foundation of shape analysis to the Scottish biologist and mathematician D'Arcy Wentworth Thompson (1860 - 1948). Thompson's expertise in biology led him to focus on morphogenesis, which refers to the development of tissues and the comparative analysis of shapes across various cells, organs, plants, and animals. His objective was to identify similarities and differences in the appearance of living organisms via mathematical approaches. In 1917, Thompson published the book "On Growth and Form" (Thompson, 1992), an influential work that gained significant attention for its mathematical analysis of biological structures. For instance, the book explored a potential similarity between two distinct fish species, Argyropelecus Olfersi versus Sternoptyx Diaphana. This suggests that Sternoptyx Diaphana can be regarded as a moderately altered version of Argyropelecus Olfersi (or vice versa) through a linear transformation.

Coinciding with the emergence of shape analysis, mathematicians such as Francis Galton (1822 - 1911) and Karl Pearson (1857 - 1936) pioneered modern statistics and statistical methodologies. These methodologies were developed to rigorously study the information of a set of entities. The primary goals of statistical analysis include collecting, organizing, and summarizing data, which refers to a set of values of qualitative or quantitative variables about one or more objects (OECD, 2008). Within this framework, *statistical shape analysis* refers to employing statistical methods to study the shapes of a group of *objects*[1], where the shape of an object encompasses all geometric information that remains unchanged under the act of Euclidean similarity transformations of scaling, translation, and rotation (Kendall, 1977; Dryden and Mardia, 1998; Lele and Richtsmeier, 2001).

The emergence of computer science has revolutionized statistical shape analysis, making it an essential tool for medical researchers and clinicians. By leveraging advanced image analysis techniques, they can gain valuable insights into patient data and improve medical outcomes (Pennec et al., 2019; Marron and Dryden, 2021). In fact, statistical shape analysis offers valuable insights by facilitating the detection of differences between samples of human organs. For instance, it enables the comparison of the subcortical structures (like the hippocampi) of patients with neurodegenerative disorders with those of a healthy control group (Apostolova et al., 2012; Schulz et al., 2016).

A variety of human body parts like the kidney, mandible, and most brain subcortical structures such as the caudate nucleus and hippocampus are slab-shaped elliptical objects, namely *slabular objects* (SlOs) (Pizer et al., 2022). Given the significant value of SlO analysis, particularly in the diagnosis and prognosis of neurological disorders, shape statistics of SlOs have remained a focal point of research for decades. Such analysis, alongside clinical assessments and genetic testing, is vital in diagnosing disorders at early stages. Early diagnosis and prediction

---

[1]This work considers a set in $\mathbb{R}^{2,3}$ as an object if it is homeomorphic to a closed ball (Siddiqi and Pizer, 2008).

of the disorders' behaviors leads to initiation of treatment at the outset, reducing healthcare costs and improving patient quality of life.
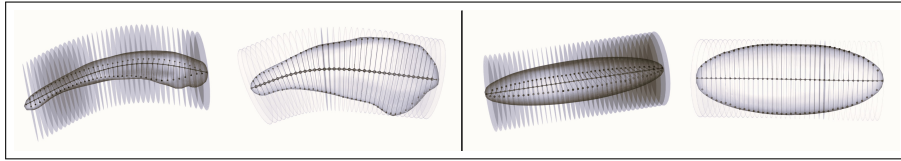

Figure 1.1: Similarity between a caudate nucleus as an SlO (left) and an eccentric ellipsoid (right). Grey disks represent the sweep of slicing planes along the objects' center curves.

An SlO can be seen as a swept region with a center curve and a sweep of slicing planes along the center curve such that the slicing planes do not intersect within the object (Pizer et al., 2022; Taheri and Schulz, 2022). An SlO is analogous to an eccentric ellipsoid in the sense that it has a crest corresponding to the crest of the ellipsoid (i.e., the intersection of the ellipsoid's first principal plane with its boundary) and two vertices corresponding to the ellipsoid's vertices (i.e., the endpoints of the ellipsoid's major axis) (Pizer et al., 2022; Taheri et al., 2023). Figure 1.1 illustrates the mentioned similarities between a caudate nucleus as an SlO and an eccentric ellipsoid.

Numerous techniques and approaches are available for SlO analysis. For example, landmark-based analysis (Dryden and Mardia, 2016), the analysis of *point distribution models* (PDMs) based on *spherical harmonic PDM* (SPHARM-PDM) (Styner et al., 2006) or *elastic registration* (Jermyn et al., 2017), *persistent homology* methods (Gamble and Heo, 2010; Turner et al., 2014), volumetric analysis of 3D objects (Malykhin et al., 2007), *radial distance analysis* (Apostolova et al., 2012), etc. However, these techniques are basically alignment-dependent as they aim to represent objects within a global coordinate system. Thus, alignment (or superimposing) serves as a prerequisite for them. They often follow the idea of Kendall (1984) to translate, rotate, and scale the models to minimize their global differences prior to the analysis.

For instance, in PDM analysis, we present an SlO as a set of points

distributed on the object's boundary. Thus, an SlO can be seen as a vector with $3n$ elements as $\boldsymbol{v} = \mathbf{vec}(\boldsymbol{p}_1, ..., \boldsymbol{p}_n)$, where $\boldsymbol{p}_1, ..., \boldsymbol{p}_n \in \mathbb{R}^3$ are the distributed points on the boundary and $\mathbf{vec}$ is the vectorization operator. To remove rigid transformations, we can translate and scale the object's representation so that the centroid of the points is located at the origin of the coordinate system, and the size of the representation becomes equal to 1.0. Thus, by considering $\frac{1}{n}\sum_{i=1}^{n}\boldsymbol{p}_i = \mathbf{0}$ the normalized vector $\boldsymbol{u} = \frac{\boldsymbol{v}}{\|\boldsymbol{v}\|}$ represents the object as a point on the unit hypersphere $\mathbb{S}^{3n-1}$ (known as *Kendall's pre-shape space*). Thus, having a population of PDMs (associated with a population of SlOs), we have a distribution of points on the hypersphere, where the distance between the spherical points is the geodesic distance $d_g(\boldsymbol{x}, \boldsymbol{y}) = \cos^{-1}(\boldsymbol{y}^T\boldsymbol{x})$ (Jung et al., 2012). To remove the effects of rotation, we can rotate the PDMs around their centroids. This process can be carried out by Procrustes analysis in a way that optimizes the sum of squared geodesic distances between the corresponding points on the hypersphere, as comprehensively discussed by Dryden and Mardia (2016). Hence, we align the PDMs using the Procrustes analysis and assume that alignment removes the effect of Euclidean similarity transformations from the PDMs.

Let $\boldsymbol{u}_1, ..., \boldsymbol{u}_N \in \mathbb{S}^{3n-1}$ representing a set of aligned PDMs. The shape statistics, including the mean shape and shape variation, can be computed based on the distribution of $\boldsymbol{u}_1, ..., \boldsymbol{u}_N$. In particular, the mean shape can be considered as the Fréchet mean of the distribution (Fréchet, 1948; Pennec et al., 2019) as

$$\bar{\boldsymbol{u}} = \operatorname*{argmin}_{\boldsymbol{u} \in \mathbb{S}^{n-1}} \sum_{j=1}^{N} d_g^2(\boldsymbol{u}, \boldsymbol{u}_j). \tag{1.1}$$

Nevertheless, such alignment-dependent analyses are misleading and biased, as explored by Lele and Richtsmeier (2001). Paper I of this thesis (Taheri and Schulz, 2022) offers examples to illustrate that alignment-dependent methods usually struggle to detect differences, even between very simple objects. In some sense, alignment is like the elephant

in the room in the realm of shape analysis. It is a significant issue that researchers frequently prefer to overlook. This tendency for implementing alignment-dependent approaches may stem from the perceived simplicity of their implementation. Further, SlOs as swept regions possess unique properties that are often ignored by many of the mentioned approaches. For example, it can be shown that the mean shape of a set of swept regions calculated via Procrustes analysis may not necessarily represent a swept region or even an object homeomorphic to a closed ball (see Supplementary Materials of Paper III). This topic is thoroughly discussed in Paper III of this work (Taheri et al., 2024).

This work follows the *principle of invariance* of Berger (1985) to provide SlO analysis in accordance with the definition of shape considering the shape or structure of an organism is *invariant* to rigid transformations. Such shape analysis methods can be established based on the *skeletal structure* of objects (Blum, 1973; Pizer et al., 1999; Damon, 2003; Fletcher et al., 2004; Siddiqi and Pizer, 2008).

Skeletal structures provide an appropriate foundation to define robust invariant shape models, which are highly effective in identifying local dissimilarities based on diverse deformations such as protrusions, bending, shrinkage, elongation, twisting, and more (Pizer et al., 2022; Taheri and Schulz, 2022). Therefore, the objective of this work is to define and employ robust SlO analysis based on skeletal structures. The following section offers a simple and casual overview of the skeletal structures of SlO and statistical concepts pertinent to the three papers of this thesis.

1.2 Skeletal structures

This section presents an overview of skeletal models and definitions studied in the three papers.

We realize the skeletal structure of an object Ω as a radial vector field U defined on the object's skeleton M denoted by (M, U), where

M in the generic case[2] is a Whitney stratified set as a union of disjoint smooth strata (Damon, 2003). Intuitively, M can be seen as a disjoint union of a set of locally centered smooth manifolds obtained by the process of continuous contraction of the boundary components (Siddiqi and Pizer, 2008; Bærentzen and Rotenberg, 2021). The radial vector field defines a flow from the skeleton to the boundary, which is similar to the inverse of *Blum's grassfire flow* (Blum et al., 1967). Thus, given the skeletal structure (M, U) the boundary of Ω can be defined as $\partial\Omega = \{\boldsymbol{p} + U(\boldsymbol{p}) | \boldsymbol{p} \in M\}$.

Therefore, Blum's skeletal structure can be defined as $(M_{\odot}, U_{\odot})$, where $M_{\odot}$ is the medial skeleton (or medial axis), and $U_{\odot}$ is the Blum radial vector field such that at each point of $M_{\odot}$ there exist at least two radial vectors with equal lengths tangent to the boundary. Since each radial vector defines a straight path from the skeleton to the boundary, the medial skeleton $M_{\odot}$ can be seen as the locus of centers of inscribed spheres bi-tangent or multi-tangent to the boundary as

$$M_{\odot} = \{\boldsymbol{p} \in \Omega_{in} \mid \left|\{\boldsymbol{q} \in \partial\Omega \mid \|\boldsymbol{p} - \boldsymbol{q}\| = d_{min}(\boldsymbol{p}, \partial\Omega)\}\right|_c \geq 2\}, \quad (1.2)$$

where Ω_{in} denotes the interior of Ω, $d_{min}(\boldsymbol{p}, \partial\Omega)$ is the minimum Euclidean distance between point $\boldsymbol{p}$ and the object boundary $\partial\Omega$, $\|.\|$ is the Euclidean norm, and $|.|_c$ represents the cardinality of a set.

The primary key for statistical shape analysis is establishing a meaningful correspondence (Van Kaick et al., 2011) across a population of objects based on similar geometrical properties (Laga et al., 2019). The medial skeleton is usually bushy and highly sensitive to boundary noise. That is, even a small protrusion or intrusion can significantly alter the medial skeleton. As a result, it is difficult to establish a meaningful correspondence using Blum's skeletal structure. Additionally, skeletal models based on the medial skeleton can be vastly different even for very similar objects, which may lead to a large number of false positives and make the analysis less informative.

---

[2]In simple terms, a property of a geometric object is considered generic, if it persists under "almost all" small changes of the entity (Siddiqi and Pizer, 2008)

As discussed by (Giblin and Kimia, 2003, 2004) and (Damon, 2003), based on Blum radial vector field, at each smooth point of the medial skeleton $p \in M_\odot$, there exist two radial vectors originating from p as $U_\odot^1(p)$ and $U_\odot^2(p)$, where $\|U_\odot^1(p)\| = \|U_\odot^2(p)\|$ and the vector $U_\odot^1(p) - U_\odot^2(p)$ is orthogonal to the tangent plane $T_p(M_\odot)$. Thus, $U_\odot^1(p)$ and $U_\odot^2(p)$ are perfectly symmetric relative to $T_p(M_\odot)$.

Pizer et al. (1999) showed by slightly relaxing the medial skeleton, it is possible to define a relaxed skeletal structure with a fixed branching topology suitable for correspondence establishment. He called such quasi-medial skeletal models as *medial representations* (MRep) (Siddiqi and Pizer, 2008). An MRep is a field of non-crossing vectors called *medial spokes* such that spokes with common tail positions have equal lengths and the envelope of all spokes' tips called the *implied boundary* approximates the object boundary (Joshi et al., 2001, 2002). The robustness of MRep in statistical shape analysis of subcortical structures is explored in various studies such as the *principal geodesic analysis* (PGA) of Fletcher et al. (2003, 2004).

Pizer's efforts inspired mathematician James Damon (1945-2022) to propose an explicit mathematical approach for relaxing Blum's criteria. Eventually, Damon (2003) achieved success in relaxing Blum's criteria by defining his three conditions: 1. Radial curvature condition ($r < \min\{\frac{1}{\kappa_{ri}}\}$ for all positive principal radial curvatures κ_{ri}, where r is the magnitude of the radial vector), 2. Edge condition ($r < \min\{\frac{1}{\kappa_{Ei}}\}$ for all positive principal edge curvatures κ_{Ei}), and 3. Compatibility condition (1-form $\eta_U \equiv 0$ for all singular points of M including its edge points). The first two conditions control the local behavior of the radial flow, ensuring the singularities do not develop from smooth points. Thus, the level sets of the flow project diffeomorphically from the skeleton to the boundary (and vice versa). The third condition ensures that only when the flow reaches the boundary, all singularities simultaneously disappear. Intuitively, the flow preserves the singularities until it reaches the boundary.

Based on Damon's three conditions, the radial vectors originating

from the same point do not need to be symmetric with equal lengths. Later Damon (2008) combined his three conditions and defined the *relative curvature condition* (RCC) for swept regions (as $r < \frac{1}{\kappa_{rel}}$ where κ_{rel} is the principal relative curvature) (Ma et al., 2018). The RCC regulates the behavior of the slicing planes established along the center curve of a swept region, preventing them from intersecting with each other within the object. Damon (2008) also defined the *swept skeletal structures* of swept regions based on the RCC.

Assume Γ as the center curve of a swept region Ω. Let $\Gamma_{(t)}$ be the curve length parameterization of Γ such that $t \in [0, 1]$, where $\Gamma_{(0,1)}$ denotes the curves' endpoints. Further, let $\Pi_{(t)}$ be the slicing plane crossing $\Gamma_{(t)}$, and let $\Omega_{(t)} = \Pi_{(t)} \cap \Omega$ be the cross-section at $\Gamma_{(t)}$. The skeletal structure (M, U) is a swept skeletal structure if it satisfies the RCC and for each $\boldsymbol{p} \in \Omega_{(t)} \cap M$, the $U_{(\boldsymbol{p})} \in \Omega_{(t)}$. In this sense, a 3D swept region (like a generalized cylinder or an SlO) is an object with a swept skeletal structure defined based on a smooth sequence of affine slicing planes along its center curve such that cross-sections do not intersect within the object, and each cross-section is a two-dimensional object with a skeletal structure. The union of the cross-sections' skeletal structures forms the swept skeletal structure of the object (Taheri and Schulz, 2022; Taheri et al., 2023).

Damon's contributions facilitated the development of shape models suitable for establishing correspondence. Pizer et al. (2013) defined a skeletal structure called the *skeletal representation* (SRep) for an SlO. Analogous to an MRep, an SRep defines the skeletal structure for an SlO such that the SlO's skeleton is a smooth two-dimensional topological disc called *skeletal sheet* and the radial vector field is represented by a field on non-intersecting vectors called *skeletal spokes* emanating from the skeletal sheet. In discrete form, we call an SRep a *discrete SRep* (DSRep) (Tu et al., 2016). The SRep can be seen as a penalized version of an MRep because the skeletal spokes with common tail positions may have non-identical lengths. The DSRep is an appropriate representation of SlO for establishing correspondence and conducting statistical shape

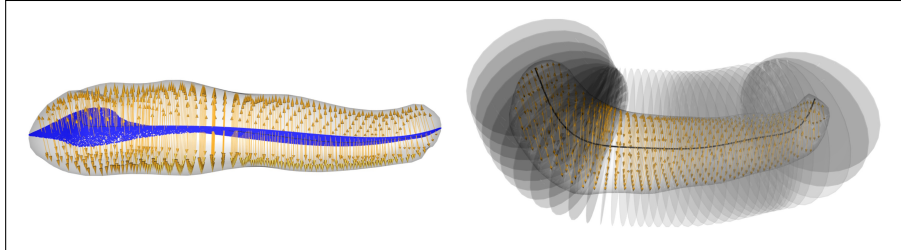analysis due to its non-branching structure (Pennec et al., 2019).

Figure 1.2: Illustration of a DSSRep of a hippocampus (left). The vectors are skeletal spokes representing the radial vectors U, while the blue surface denotes the skeletal sheet representing the object's skeleton M. In the right figure, slicing planes have been incorporated into the model to demonstrate the coplanarity of the skeletal spokes associated with each slicing plane.

An SlO can be conceptualized as a swept region where each cross-section resembles a 2D generalized cylinder (GC), defined as a two-dimensional swept region with a smooth center curve. In this sense, an SlO is a swept region with a swept skeletal structure formed by the swept skeletal structures of the cross-sections. Paper II of this work discusses the *discrete swept skeletal representation* (DSSRep) for SlOs. The DSSRep is defined similarly to a DSRep, with the difference that skeletal spokes associated with each slicing plane are coplanar, as defined by Damon (2008). Also, the edge of the skeletal sheet coincides with the SlO's crest by considering the center curve of each cross-section as a smooth curve that connects the cross-section's two vertices (analogous to the chordal locus of Brady and Asada (1984) for 2D GCs). Figure 1.2 illustrates a DSSRep of a hippocampus where orange vectors are skeletal spokes representing the radial vectors and the blue surface is the skeletal sheet representing the object's skeleton. The slicing planes sweep the object's boundary and skeleton. Notice that the skeletal spokes associated with each slicing plane are coplanar.

Within a certain category of SlOs, the cross-sections can be approximated by elliptical disks. Consequently, it becomes feasible to streamline the shape representation and portray the object as a 3D generalized cylinder with elliptical cross-sections. Thus, the coplanar radial
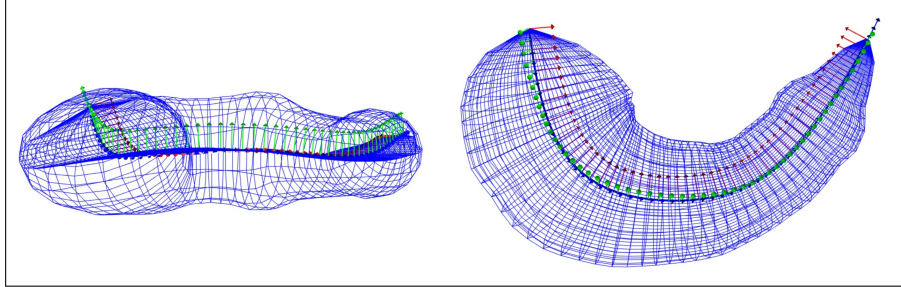
Figure 1.3: An ETRep of a hippocampus where the cross-sections are elliptical disks.

vectors can be seen as the chordal structure of an ellipse, as defined by Brady and Asada (1984). This simplification aids in reducing the dimensionality of the shape representation, thereby addressing the issue of the curse of dimensionality. Additionally, it assists in mitigating the problem of self-intersection when calculating the mean shape and defining the shape space. In this regard, Paper III of this work introduces *elliptical tube representation* (ETRep) as a simplified version of the DSSRep for a class of SlOs. Figure 1.3 illustrates an ETRep of a hippocampus.

2 Shape statistics of skeletal structures

Once a skeletal model is established, defining shape and shape space concepts is essential for calculating the mean shape and shape distributions, which are crucial for hypothesis testing and classifications. The following sections Section 2.1 and Section 2.2 discuss the shape, shape space, and shape statistics of the introduced skeletal models.

2.1 Shape and shape space

This section first explains the shape and shape space of DSReps and then discusses the shape and shape space of ETReps. All discussions regarding DSReps are also valid for DSSReps.

As discussed in Section 1.2, a DSRep is a finite subset of an SRep, where the SRep is a field of skeletal spokes emanating from the skeletal sheet defined by the local geometry of the skeletal structure. Therefore, in a simple format, a DSrep can be seen as an n-tuple of spokes like $s = (s_i)_{i=1}^n$ where $s_i = (\boldsymbol{p}_i, \boldsymbol{u}_i, \boldsymbol{r}_i)$ is the ith spoke, and $\boldsymbol{p}_i$, $\boldsymbol{u}_i$ and r_i are the tail position, unit direction and the length of the s_i, respectively. Thus, a DSRep is living on a Cartesian product space of $(\mathbb{R}^3)^n \times (\mathbb{S}^2)^n \times (\mathbb{R}^+)^n$, where $(\mathbb{R}^3)^n$ is the space of spokes' tail positions, the $(\mathbb{S}^2)^n$ is the space of spokes' directions based on the unit sphere $\mathbb{S}^2$, and $(\mathbb{R}^+)^n$ is the space of spokes' lengths (Pizer et al., 2020).

However, such shape representation is alignment-dependent because the positional components and directional components of the spokes are in the global coordinate system. Therefore, such a parameterization is not ideal for statistical analysis. As proposed in Paper I and Paper II of this study, we can reparameterize the conventional representation of the DSRep and define the *locally parameterized DSRep* (LPDSRep). As depicted in Figure 2.1, an LPDSRep defines a tree-like structure for the skeletal sheet equipped with a set of local frames. The tree-like structure establishes a hierarchical connection among the frames through a collection of vectors called *connection vectors*. In
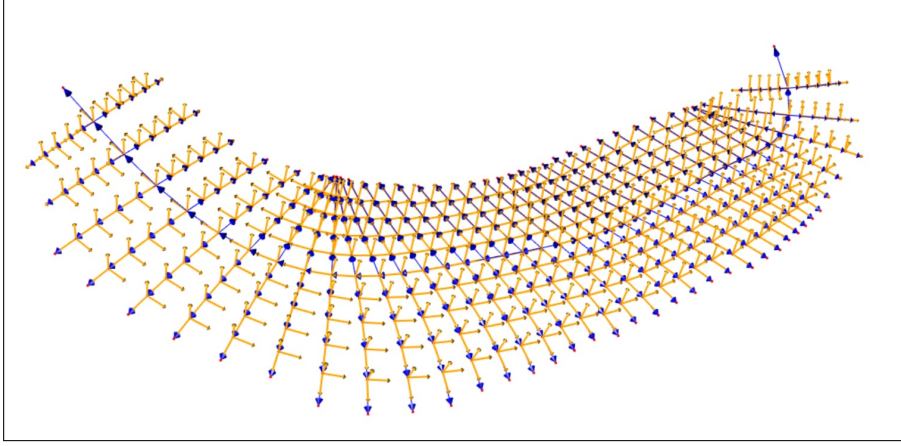
Figure 2.1: Hierarchical structure of a skeletal sheet equipped with the local frames. The blue vectors are connection vectors and the yellow vectors are the elements of local frames.

this arrangement, each frame resides at the endpoint of a connection vector, with a parent frame situated at the origin of the same vector. Also, at each frame, we have two skeletal spokes, namely an *up spoke* and a *down spoke* with opposite directions. Let n_f and n_c be the number of local frames and connection vectors, respectively, and assume $i = 1, ..., n_f$ and $j = 1, ..., n_c$. An LPDSRep can be expressed as

$$s = (F_1^*, ..., F_{n_f}^*, v_1^*, ..., v_{n_c}^*, u_1^{\pm *}, ..., u_{n_f}^{\pm *}, v_1, ..., v_{n_c}, r_1^{\pm}, ..., r_{n_f}^{\pm}), \quad (2.1)$$

where $F_i^* \in SO(3)$ is the ith frame orientation based on its parent coordinate system, $SO(3)$ is the orthogonal rotation group, $v_j^* \in \mathbb{S}^2$ is the direction of jth connection vector based on its local frame (i.e., the frame that tail of the connection vector is located on), $v_j \in \mathbb{R}^+$ is the length of the jth connection vector, $u_i^{\pm *} \in \mathbb{S}^2$ are the directions of the ith up and down spokes based on their local frames, $r_i^{\pm} \in \mathbb{R}^+$ are the lengths of the up and down spokes at the ith frame. Thus, an LPDSRep lives in the product space of

$$\mathbf{S} = (SO(3))^{n_f} \times (\mathbb{S}^2)^{n_c + 2n_f} \times (\mathbb{R}^+)^{n_c + 2n_f}. \quad (2.2)$$

The LPDSRep constitutes an invariant shape representation as its components are defined relative to the coordinate system of the local frames.

In essence, rigid transformations do not alter the representation. The generalization of this approach is proposed by Pizer et al. (2022) based on the level set of the radial flow. That is, the fitted frames are located on the level sets of the flow corresponding to the configuration of the skeletal sheet.

Let's consider representing an SlO using an ETRep based on a series of elliptical disks, as depicted in Figure 1.3. The combination of the centroids of these disks delineates the object's central curve, while the union of their major axes constructs a developable skeletal sheet. By considering a moving frame on the skeletal sheet along the center curve, an ETRep can be defined as an invariant shape representation based on $i = 1, ..., n$ elliptical cross-sections as

$$s_e = (F_1^*, ..., F_n^*, x_1, ..., x_n, a_1, ..., a_n, b_1, ..., b_n), \qquad (2.3)$$

where F_i^* is the orientation of the ith frame based on its previous frame (i.e., $(i-1)$th frame), x_i is the distance between the ith frame and its previous frame, and a_i and b_i are the lengths of the semi-major and semi-minor axes of the ith cross-section. Therefore, the ETRep space is the product space $(SO(3))^n \times (\mathbb{R}_+^3)^{3n}$. The details of ETReps are discussed in paper II.

2.2 Shape analysis

Section 2.1 discussed possible invariant shape representations for SlOs. This section explains the statistical shape analysis based on the introduced shape representations.

Assume two SlOs are represented by two LPDSReps as s_1 and s_2 with the same number of corresponding elements. We can define the distance between s_1 and s_2 as defined by Equation 2 of Paper I. Consequently, the mean shape can be considered as (the Fréchet mean, i.e.,) a shape with minimum squared distance to s_1 and s_2 as $\operatorname{argmin}_{s \in \mathbf{S}} \sum_{m=1}^{2} d_s^2(s, s_m)$. Similarly, having a sample of LPDSReps as

13

$s_1, ..., s_N$, the sample mean shape can be defined as

$$\bar{s} = \operatorname*{argmin}_{s \in \mathbf{S}} \sum_{m=1}^{N} d_s^2(s, s_m). \tag{2.4}$$

Note that we do not need to align the objects to calculate the mean shape as the LPDSReps are alignment-independent.

Each element of an LPDSRep can be seen as a *geometrical object property* (GOP) of the associated SlO (e.g., a spoke's length represents the object's local width). Calculating the mean shape enables us to compare two (or more) groups of LPDSReps to detect local dissimilarities by comparing their corresponding GOPs. This can be done by designing partial hypothesis tests.

Let $A = \{s_{Am}\}_{m=1}^{N_1}$ and $B = \{s_{Bm}\}_{m=1}^{N_2}$ be two groups of Euclideanized LPDSReps of sizes N_1 and N_2 such that all the LPDSReps have the same number of GOPs. To compare corresponding GOPs, we can design partial tests as $H_{0i} : \bar{s}_A(i) = \bar{s}_B(i)$ versus $H_{1i} : \bar{s}_A(i) \neq \bar{s}_B(i)$, where $\bar{s}_A(i)$ and $\bar{s}_B(i)$ are the ith GOP of the observed sample mean of A and B, respectively.

Further, since local frames can be seen as unit quaternion vectors belonging to $\mathbb{S}^3$, we can Euclideanize and vectorize LPDSReps such that each LPDSRep can be seen as a vector in a feature space, which is a high-dimensional Euclidean space. The Euclideanization process can be executed using *principal nested spheres analysis* (PNS) of Jung et al. (2012). Consequently, besides hypothesis testing, diverse classification techniques can be employed to classify LPDSReps within the high dimensional feature space, as discussed in Paper I & II.

However, determining the mean shape and shape space by considering Damon's criteria presents a fundamental challenge. In fact, without considering the RCC for the underlying shape space, the obtained mean shape by Equation (2.4) is not necessarily an SlO, as it may have self-intersections. Paper III of this work devotes exclusive attention to discussing the mean shape and shape space of SlOs, taking into account the RCC.

3 Summary of the papers

3.1 Paper I

Taheri, Mohsen, and Jörn Schulz (2022). "Statistical Analysis of Locally Parameterized Shapes." Journal of Computational and Graphical Statistics 32.2 (2023): 658-670.

The focus of the paper is to introduce an invariant skeletal shape representation for SlO analysis capable of explicitly explaining types of dissimilarities. The paper is divided into five sections. In the first section, the authors comprehensively discuss critical issues related to alignment-dependent methods such as point distribution analysis like SPHARM-PDM (Styner et al., 2006) and explain why available invariant methods, such as the Euclidean distance matrix (EDM) analysis (Lele and Richtsmeier, 2001), cannot reflect the type of dissimilarities. The core section of the paper is the second section. The section reviews the basic terms regarding DSReps and discusses the conventional noninvariant parameterization of DSReps. It also introduces the LPDSRep as a novel parameterization of a DSRep. The LPDSRep represents an SlO based on a hierarchical tree-like structure of the skeletal sheet equipped with the local frames, as defined at the beginning of Section 2.1. The section also explains the Euclideanization of spherical data, shape distance, mean shape, object deformation, and boundary reconstruction utilizing the LPDSRep. In the third section, the authors discuss hypothesis testing and controlling false positives regarding LPDSRep analysis. The hypothesis pipeline is demonstrated in the paper's supplementary materials. The fourth section evaluates the LPDSRep and proposed methodologies based on simulation and the analysis of real data. For the real data analysis, the section studies hippocampal differences between a group of patients with Parkinson's disease (PD) versus a control group (CG). Finally, the fifth section summarizes and concludes the paper.

15

3.2 Paper II

Taheri, Mohsen, Stephen M. Pizer, and Jörn Schulz (2023). "Fitting the Discrete Swept Skeletal Representation to Slabular Object." Submitted for publication in Journal of Mathematical Imaging and Vision.

The objective of the paper is to introduce a model fitting procedure for DSSReps based on the swept skeletal structure of SlOs. The paper consists of nine sections. The first section discusses the paper's objective and explains the relationship between the swept skeletal structures of an eccentric ellipsoid and SlOs. It also highlights the importance of the RCC in the model fitting and serious issues in applying the *curve skeleton* (Dey and Sun, 2006) to define the center curve of a swept region. Section two provides explicit definitions of swept regions, SlO, skeletal structures, and swept skeletal structures and reviews basic terms. In section three, the central medial skeleton (CMS) is introduced. The CMS can be seen as a unique subset of the medial skeleton that has no holes, discontinuity, or branches. The CMS of an SlO can be calculated by dividing the Voronoi diagram (Attali and Montanvert, 1997) of the SlO based on the crest of the object. Section four proposes a DSSRep model fitting based on the flattened CMS. The section discusses CMS flattening based on dimensionality reduction methods, such as principal component analysis and t-distributed stochastic neighbor embedding (t-SNE) (Van Der Maaten, 2014). Sections five and six parameterize the DSSRep to introduce the LPDSSRep as an invariant shape representation. They also discuss the goodness of fit based on skeletal symmetry, tidiness, and the volume of the implied boundary of a fitted model. In section seven, LPDSSRep hypothesis testing and classification are demonstrated. Section eight compares the proposed LPDSSRep and LPDSRep models, where the LPDSRep models are based on the DSRep model fitting of Liu et al. (2021). The section discusses that Liu's method has critical issues in defining correspondence, as it suffers from skeletal perturbation and asymmetricity. The final section summarizes and concludes the paper.

3.3 Paper III

Taheri, Mohsen, Stephen M. Pizer, and Jörn Schulz (2024). "The Mean Shape under the Relative Curvature Condition." Submitted for publication in Journal of Computational and Graphical Statistics.

The paper focuses on calculating the mean shape of SlO under the relative curvature condition (RCC) across six sections. The first section highlights the importance of RCC in defining the shape space of swept regions and how it ensures that adjacent slicing planes do not intersect within the object. The second section defines basic terms and definitions regarding the swept skeletal structures of SlOs. The third section explains the discrete material frames and Frenet frames along the center curve of an SlO, which are crucial for defining the RCC. The fourth section is the main core of the paper. It introduces the ETRep and demonstrates the ETRep model fitting. An ETRep represents an SlO as a combination of elliptical cross-sections (see Figure 1.3). The section then discusses the intrinsic and semi-intrinsic approaches to define the ETRep space by considering the RCC for ETReps. The intrinsic approach defines the ETRep space as a high-dimensional space with a hyperbolic boundary and a swept skeletal coordinate system. The fifth section discusses statistical inferences derived from ETRep hypothesis testing. Finally, the sixth section summarizes and concludes the work.

In addition, the paper's supplementary materials offer an algorithm to address non-local self-intersection of swept regions. This is important for future research since the RCC only addresses local self-intersection.

4 Discussion

The following sections investigate the strengths and weaknesses of the methods suggested in this work's three papers and explore the potential directions for future research.

4.1 Validity of the deformation-based DSRep fitting

The initial paper in this study introduced LPDSRep, which is founded upon the DSRep model as proposed by Liu et al. (2021). Damon (2021) elucidated that a generic medial skeletal structure exhibits a level of rigidity conducive to maintaining correspondence through minor boundary deformations. Consequently, if we can achieve an SIO by slightly deforming an eccentric ellipsoid, the skeletal structure of the deformed ellipsoid can be considered as the skeletal structure of the SlO. While the subsequent paper highlighted critical issues with Liu's approach, it can be shown that the theoretical discussions of Liu's approach hold validity. Thus, the theoretical frameworks delineated in the first paper, along with their extension posited by Pizer et al. (2022), remain theoretically valid. In fact, the primary drawback of Liu's method stems from overlooking the crest and vertices of an SIO. Consequently, after the deformation, we lose the correspondence between the crest and vertices of the deformed ellipsoid and those of the original ellipsoid. Therefore, addressing this concern could lead to the acquisition of a DSRep characterized by elevated symmetricity and tidiness, which could be the subject of future research.

4.2 Intermediate DSRep

The establishment of skeletal structures between two or more SlOs presents an intriguing prospect, particularly because the intermediate area between subcortical objects mirrors the geometric properties of the brain's white matter. As defined by Damon and Gasparovic (2017), such intermediate skeletal structure can be defined based on the extension

of the objects' radial flows. That is, the intersection of the radial flows outside the objects defines an intermediate skeleton. Liu et al. (2023) proposed a model fitting of such intermediate skeletal structure based on the extension of the skeletal spokes for well-posed SlOs, namely *intermediate DSREP* (IDSRep). Well-posed SlOs are objects where their skeletal sheets can be regarded as approximately parallel sheets. The critical issue with Liu's approach is that the intermediate area between objects is not well-defined, as it is not bounded, leading to an unbounded IDSRep where the skeleton extends infinitely. Additionally, the approach fails to explicitly address the self-linking issue. The self-linking arises when an object's radial flow intersects with itself before reaching other objects' flows. Furthermore, well-posed SlOs are rare occurrences.
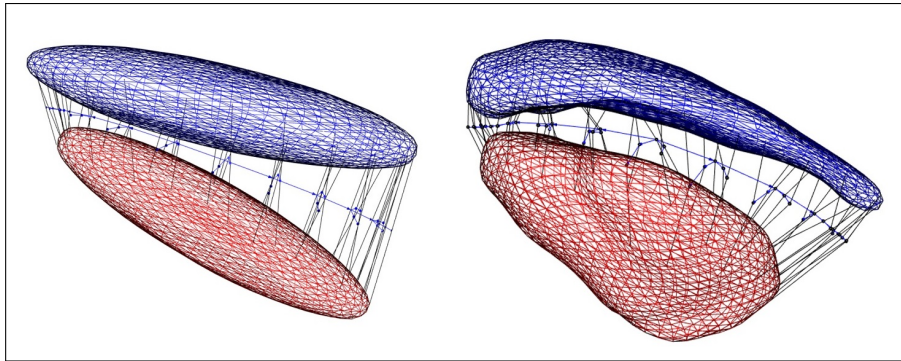
Figure 4.1: Left: The IDSRep of two ellipsoids. Right: The IDSRep of a caudate and putamen obtained by deforming the IDSRep of their corresponding ellipsoids.

Nonetheless, defining a well-defined bounded intermediate area between any two ellipsoids is usually possible based on their convex hull region as suggested by Damon and Gasparovic (2017). Using this well-defined bounded region, we can define bounded IDSRep for any arbitrary ellipsoids. Leveraging the rigidity of skeletal structures discussed by Damon (2021), it appears feasible to define IDSReps for ellipsoids and then slightly deform the space using a diffeomorphic mapping (such as thin-plate splines) to fit the IDSRep between the SlOs. Figure 4.1 illustrates a prototype IDSRep between a caudate and

putamen (which are not well-posed objects) obtained by deforming the intermediate space of their corresponding ellipsoids. This approach avoids the self-linking issue as it is based on a diffeomorphic mapping. Further, it is possible to parameterize the IDSRep locally (analogous to the LPDSRep) so that it becomes alignment-independent.

4.3   CMS of a surface

Paper II used the DSSRep model to fit the skeletal sheet by flattening it and defining its center curve (Taheri et al., 2023). The center curve was then projected onto the skeletal sheet and considered as the center curve of the SlO called *spine*. This method works well for regular SlOs where the flattened sheet is similar to the original sheet. However, for irregular SlOs, flattening the skeletal sheet is significantly different from its flattened version. Thus, the spine obtained via surface flattening might be an inappropriate representative of the center curve of the irregular SlO. One alternative is to calculate the spine directly on the skeletal sheet without flattening it.

Similar to the definition of the medial skeleton, a point can be considered as a medial point on a surface if there are two shortest straight geodesic paths that connect the point to the surface edge. This concept is discussed by Chambers et al. (2013). We know the skeletal sheet of an SIO is a surface that can be represented as a triangle surface. Since straight paths on a triangle surface can be calculated (Polthier and Schmies, 1998), it seems possible to calculate the medial skeleton of the skeletal sheet and consider such a skeleton as the spine of the object. This section proposes a possible method that can be used to define the spine without flattening the skeletal sheet based on the generalization of the pruning methods of Foskey et al. (2003); Chazal and Lieutier (2005). To achieve this, the section introduces the *urchin*.

As illustrated in Figure 4.2, an urchin with the *core* $p \in \Omega_{in}$ is a set of all spokes emanating from p as $\mathcal{S}(p) = \{s_{(p,u)} \mid u \in \mathbb{S}^{d-1}\}$. We consider a discrete urchin as $\hat{\mathcal{S}}(p) = \{s_{(p,u)} \mid u \in \hat{\mathbb{S}}^{d-1}\}$, where

$\hat{\mathbb{S}}^{d-1}$ represents the vertices of a discrete unit sphere as a symmetric geodesic polyhedron (for example, an icosahedron sphere) in 3D or a regular polygon in 2D.
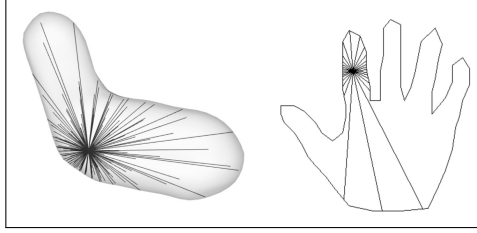

Figure 4.2: Visualization of an urchin in a 3D object (left) and a 2D object (right).

Based on the Tomson (1904) problem, we can assume identical angles between all adjacent spokes of an urchin. Let $n_{\hat{S}} = \left| \hat{S}(\boldsymbol{p}) \right|_c$ be the urchin's number of spokes, and $\Delta\theta \in (0, \pi]$ be the angle between two adjacent spokes of $\hat{S}(\boldsymbol{p})$. Obviously, if $\Delta\theta \to 0$ then $n_{\hat{S}} \to \infty$ and $\hat{S}(\boldsymbol{p}) \to S(\boldsymbol{p})$, i.e., $\hat{S}(\boldsymbol{p})$ includes all the possible straight paths (i.e., spokes) from $\boldsymbol{p}$ to $\partial\Omega$.

Theoretically, $\boldsymbol{p} \in \Omega_{in}$ is a medial point if the shortest straight path from $\boldsymbol{p}$ to $\partial\Omega$ is not unique. That is, at least two shortest straight paths have equal lengths but different directions, i.e., $\exists \boldsymbol{u}_1 \neq \boldsymbol{u}_2$ such that $\|\boldsymbol{s}_{(\boldsymbol{p}, \boldsymbol{u}_1)}\| = \|\boldsymbol{s}_{(\boldsymbol{p}, \boldsymbol{u}_2)}\| = d_{min}(\boldsymbol{p}, \partial\Omega)$. Thus, to check whether $\boldsymbol{p}$ is a medial point or not, it is sufficient to check whether the two shortest spokes of $\hat{S}(\boldsymbol{p})$ have an equal length or not, given a sufficiently small $\Delta\theta$. However, in practice, even if a point is indeed medial, almost always all the urchin's spokes have different lengths because of noise, computation errors, and the limitation of choosing $\Delta\theta$ small enough. Further, the probability of picking a medial point by chance from Ω is very low because the space that the medial skeleton occupies relative to the object volume is close to zero. However, following the idea of Foskey et al. (2003), it is possible to approximate the medial skeleton based on the *object angle* (i.e., the angle between spokes with a common tail position) Attali and Montanvert (1997).

Let the *minimal angle* $\delta_{\hat{S}(\boldsymbol{p})} \in [0, \pi]$ be the angle between the

22

two shortest spokes of $\hat{\mathcal{S}}(\boldsymbol{p})$. Assume $\boldsymbol{p}$ as a *semi-medial point* if $\delta_{\hat{\mathcal{S}}(\boldsymbol{p})} > \Delta\theta$, and otherwise, as is a *nonsemi-medial point* (i.e., $\delta_{\hat{\mathcal{S}}(\boldsymbol{p})} = \Delta\theta$). Note that when $\delta_{\hat{\mathcal{S}}(\boldsymbol{p})}$ is close to π, the point is located at the middle of two approximately parallel surfaces as discussed by Giblin and Kimia (2003). The semi-medial skeleton can be considered as the union of all semi-medial points as $M_{\odot}^{\Delta\theta} = \{\boldsymbol{p} \in \Omega_{in} \mid \delta_{\hat{\mathcal{S}}(\boldsymbol{p})} > \Delta\theta\}$. Analogous to Theorem 4 of (Foskey et al., 2003), it can be shown that the difference between the semi-medial axis and the medial axis vanishes when $\Delta\theta \rightarrow 0$.

Theorem 1 *For an object $\Omega \subset \mathbb{R}^{d=2,3}$ with smooth boundary, the semi-medial skeleton $M_{\odot}^{\Delta\theta}$ converges to the medial skeleton $M_{\odot}$ when $\Delta\theta \rightarrow 0$.*

Proof: Recall the semi-medial skeleton of the object Ω is the collection of all semi-medial points as $M_{\odot}^{\Delta\theta} = \{\boldsymbol{p} \in \Omega_{in} \mid \delta_{\hat{\mathcal{S}}(\boldsymbol{p})} > \Delta\theta\}$, where $\delta_{\hat{\mathcal{S}}(\boldsymbol{p})} \in [0, \pi]$ is the angle between the two shortest spokes of the discrete urchin $\hat{\mathcal{S}}(\boldsymbol{p})$. For any $\boldsymbol{p} \in M_{\odot}^{\Delta\theta}$, $\exists \boldsymbol{u}_1, \boldsymbol{u}_2 \in \mathbb{S}^{d-1}$ such that $d_g(\boldsymbol{u}_1, \boldsymbol{u}_2) > \Delta\theta$, and $\boldsymbol{s}_{(\boldsymbol{p},\boldsymbol{u}_1)}$ and $\boldsymbol{s}_{(\boldsymbol{p},\boldsymbol{u}_2)}$ are the two shortest spokes. If $\Delta\theta \rightarrow 0$, without loss of generality, we can assume $\|\boldsymbol{s}_{(\boldsymbol{p},\boldsymbol{u}_1)}\| = d_{min}(\boldsymbol{p}, \partial\Omega)$ as $\hat{\mathcal{S}}(\boldsymbol{p})$ consists of all possible spokes with tail at $\boldsymbol{p}$. Thus, $\boldsymbol{s}_{(\boldsymbol{p},\boldsymbol{u}_1)}$ is normal to $\partial\Omega$ because $\boldsymbol{p}$ is the center of an inscribed sphere tangent to $\partial\Omega$. Let $\boldsymbol{q}$ be the tip of $\boldsymbol{s}_{(\boldsymbol{p},\boldsymbol{u}_1)}$. The $\partial\Omega$ has positive, negative, or zero curvature at $\boldsymbol{q}$. Also, the positive curvature at $\boldsymbol{q}$ cannot be greater than $\frac{1}{\|\boldsymbol{s}_{(\boldsymbol{p},\boldsymbol{u}_1)}\|}$, because the osculating sphere tangent to $\partial\Omega$ at $\boldsymbol{q}$ with positive curvature includes the maximal inscribed sphere with tangency point $\boldsymbol{q}$ (see Appendix of (Attali et al., 2007) and (Siddiqi and Pizer, 2008, Page. 41)). Thus, if we (infinitesimally) move away from $\boldsymbol{q}$ to $\boldsymbol{q}' \in \partial\Omega$, the length of the spoke with tail at $\boldsymbol{p}$ and tip at $\boldsymbol{q}'$ become greater or equal than $\|\boldsymbol{s}_{(\boldsymbol{p},\boldsymbol{u}_1)}\|$. Therefore, $\forall \boldsymbol{u} \in \hat{\mathbb{S}}^{d-1}$: $\|\boldsymbol{s}_{(\boldsymbol{p},\boldsymbol{u}_1)}\| \leq \|\boldsymbol{s}_{(\boldsymbol{p},\boldsymbol{u}_2)}\| \leq \|\boldsymbol{s}_{(\boldsymbol{p},\boldsymbol{u})}\|$. Let $\boldsymbol{s}_{(\boldsymbol{p},\boldsymbol{u})}$ be an adjacent spoke to $\boldsymbol{s}_{(\boldsymbol{p},\boldsymbol{u}_1)}$ (e.g., $\boldsymbol{u} = (0, \sin(\Delta\theta), \cos(\Delta\theta))^T$ when $\boldsymbol{u}_1 = (0, 0, 1)^T$ is the north pole of the unit sphere). Thus, $\|\boldsymbol{s}_{(\boldsymbol{p},\boldsymbol{u})}\| \rightarrow \|\boldsymbol{s}_{(\boldsymbol{p},\boldsymbol{u}_1)}\|$ when $\Delta\theta \rightarrow 0$ and consequently based on the squeeze theorem $\|\boldsymbol{s}_{(\boldsymbol{p},\boldsymbol{u}_1)}\| \rightarrow \|\boldsymbol{s}_{(\boldsymbol{p},\boldsymbol{u}_2)}\|$. So the two shortest spokes would have equal lengths with different directions as $d_g(\boldsymbol{u}_1, \boldsymbol{u}_2) > 0$. Therefore, $\boldsymbol{p} \in M_{\odot}$. On the

23

other hand, if $p \notin M_{\odot}^{\Delta\theta}$, then $d_g(u_1, u_2) = \Delta\theta$, i.e., the two shortest spokes are adjacent. So when $\Delta\theta \to 0$, the two shortest spokes literally coincide. Thus, the shortest path to the boundary is unique and $p \notin M_{\odot}$. □

Based on Theorem 1, by choosing a small enough $\Delta\theta$ the semi-medial skeleton approximates the medial skeleton. The resolution of the semi-medial skeleton depends on two factors the number of urchins and the value of $\Delta\theta$, i.e., more urchins and smaller $\Delta\theta$ result in a semi-medial skeleton closer to the actual medial skeleton. Recall $\forall p \in \Omega_{in} : \delta_{\hat{S}(p)} \in [\Delta\theta, \pi]$. Let $s_{(p,u_1)}$ and $s_{(p,u_2)}$ be the two shortest spokes of $\hat{S}(p)$, and consider $\Delta\theta = \frac{\pi}{n+1}$ such that $n \in \mathbb{N}$. Therefore, we can categorize all the internal points into *n semi-medial levels* $L_i = \{p \in \Omega_{in} \mid \delta_{\hat{S}(p)} \geq (i+1)\Delta\theta\}$, where $i = 0, ..., n-1$. Therefore, L_1 represents the semi-medial skeleton (i.e., the union of all interior points that the angle between their two shortest spokes is greater than $\Delta\theta$). Figure 4.3 depicts highest to lowest semi-medial levels of a 2D object by $\Delta\theta = \frac{\pi}{8}$.
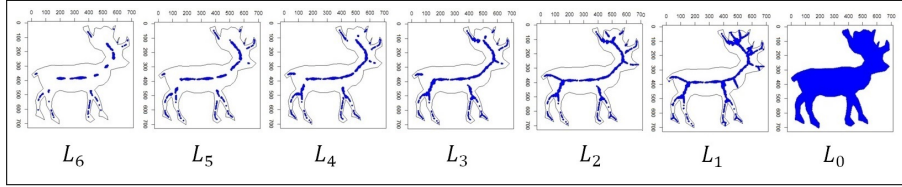
Figure 4.3: Semi-medial skeleton levels of a 2D object.

Analogously, we can determine a *non-linear urchin* on a surface by assuming its non-linear spokes as straight geodesic paths with starting directions on the surface. Further, as Chambers et al. (2013) discussed, for a medial point on a surface, there exist two shortest straight geodesic paths connecting the point to the edge of the surface with different starting directions. Thus, as depicted in Figure 4.4, we can define the semi-medial skeleton for surfaces based on the non-linear urchins. In this sense, the core of a non-linear urchin is a medial point if the angle between the two shortest non-linear spokes of the urchin is greater than

24

$\Delta\theta$, where $\Delta\theta \in (0, \pi]$ is the angle between the starting directions of two adjacent non-linear spokes based on the tangent space of the core. The detailed discussion of this approach is out of the scope of this work and could be the subject of future research. For example, the surface must be well-behaved in the sense that all the spokes of any non-linear urchin must have finite lengths and not cross each other.
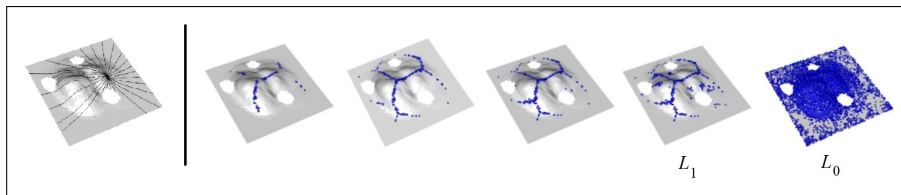
Figure 4.4: A non-linear urchin on a surface (Left) with semi-medial levels (Right).

Let p be a semi-medial point, and let $s_{(p,u_1)}$ and $s_{(p,u_2)}$ be its two shortest non-linear spokes. Analogous to the boundary of a 2D object, the edge of a connected surface can be divided into two components as two non-overlapping curves such that the union of the curves forms the edge. We say p belongs to the CMS if the tip of the two shortest non-linear spokes is at different edge components. Thus, the CMS is a subset of the semi-medial skeleton based on the two edge components (i.e., the tips of the two shortest non-linear spokes are not at the same edge component). Figure 4.5 depicts the semi-medial skeleton of a surface (middle) and the CMS based on two edge components (right).

Figure 4.5: Left: A nonlinear urchin on the surface. Middle: The semi-medial skeleton of a surface. Right: The CMS of the surface based on two edge components that are depicted as blue and red curves separated by two bold dots.

25

4.4 DSRep of objects with branching structures

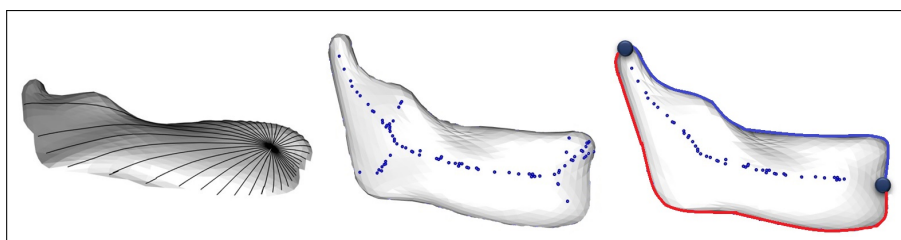Fitting skeletal structures to complex slab-shaped objects such as hemi-mandibles with the coronoid process that are not necessarily SlOs is particularly relevant given the frequent focus on such objects in research studies (AlHadidi et al., 2012). Although such slab-shaped objects are not necessarily SlOs, they can be divided into several sub-objects such that each sub-object can be seen as an SlO. In this sense, the skeletal structure of the object can be seen as the union of the skeletal structures of its sub-objects.
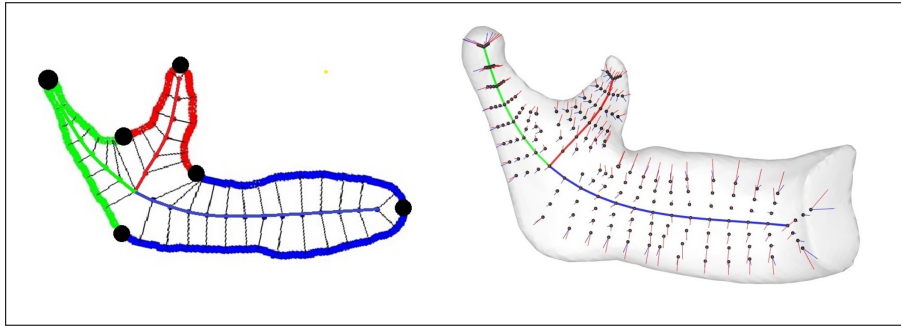
Figure 4.6: Left: The skeletal structure of the flattened skeletal sheet of a hemimandible. The six vertices with the highest local curvatures are depicted as bold dots. The skeletal structure of each sub-object is depicted by the color of its associated boundary components. Right: The DSRep of the hemimandible.

There are available approaches for obtaining 3D sub-objects such as local separators of Bærentzen and Rotenberg (2021); Bærentzen et al. (2023). However, such approaches usually ignore important boundary properties such as the crest, leading to inappropriate boundary division (see Supplementary Materials of Paper II). Paper II determined the skeletal structure of an SlO using the skeletal structure of its flattened skeletal sheet, where the skeletal sheet is the relaxed CMS delineated by the object's crest. It appears that for a class of slab-shaped objects, such as a hemimandible, the flattened skeletal sheet has multiple distinct vertices with the highest local curvature that can be used to divide it into several 2D sub-objects. The combination of the skeletal structures

of these sub-objects can be considered as the skeletal structure of the flattened sheet. As a result, the projection of this skeletal structure onto the skeletal sheet creates a tree-like structure that can be utilized to determine the skeletal structure of the object. This approach has shown promising results in initial implementations and can be a subject of future research. Figure 4.6 (left) shows the skeletal structure of the flattened skeletal sheet of a hemimandible as a union of three skeletal structures of three 2D sub-objects depicted in different colors. Figure 4.6 (right) illustrates the DSRep of the hemimandible obtained by projecting the skeletal structure of the flattened sheet to the relaxed CMS of the object. Note that it is also conceivable that we apply the methodology discussed in Section 4.3 to calculate the skeletal structure of the relaxed CMS without flattening it.

4.5   ETRep space as $(\mathbb{S}^5)^{n+1}$

Paper III introduces $\mathcal{A}^{\dagger n+1} = (\mathbb{S}^3 \times (\mathbb{R}^+)^3)^{n+1}$ as a convex space of ETReps based on the ETRep representation as a sequence of elliptical cross-sections as $s^\dagger = (\omega_i)_{i=0}^n$, where $\omega_i = (f_i, x_i, \tau_i, \rho_i)_i$ represents the ith cross-section, the unit quaternion $f_i \in \mathbb{S}^3$ is the orientation of ω_i, x_i is the distance between the centroid of ω_i and ω_{i-1}, and $\tau_i, \rho_i \in [0, 1]$ reflect the scaled size of ω_i. Considering the robust performance demonstrated by the principal nested sphere analysis (PNS) in classification and hypothesis testing across different studies, e.g., (Schulz et al., 2016; Liu et al., 2023), analyzing ETReps based on PNS could be advantageous. This can be done by mapping the cross-sectional data to a hypersphere. Thus, the ETRep space becomes the product space of $n + 1$ hyperspheres.

Given a finite set of scalars $\phi_1, ..., \phi_{m-1} \in [0, \pi]$, we can represent these scalars as a vector $\boldsymbol{x} = (x_1, ..., x_m)' \in \mathbb{S}^{m-1}$ using the generaliza-

tion of the spherical coordinate system ([Blumenson](), [1960]())

$$
\begin{aligned}
x_1 &= \cos \phi_1 \\
x_2 &= \sin \phi_1 \cos \phi_2 \\
x_3 &= \sin \phi_1 \sin \phi_2 \cos \phi_3 \\
&\vdots \\
x_{m-1} &= \sin \phi_1 ... \sin \phi_{m-2} \cos \phi_{m-1} \\
x_m &= \sin \phi_1 ... \sin \phi_{m-2} \sin \phi_{m-1}.
\end{aligned}
\tag{4.1}
$$

Therefore, to apply PNS analysis, it is sufficient to map the elements of ω_i to $[0, \pi]$. Since $f_i \in \mathbb{S}^3$ is the unit quaternion representation of an orthogonal frame, it can be represented as three Tait-Bryan angles (as Euler angles) such as $\phi_{1i}, \phi_{2i}, \phi_{3i} \in [0, \pi]$ ([Hoffman et al.](), [1972](); [Murray et al.](), [2017]()). Assume $\phi_{4i} = 2 \tan^{-1}(x_i)$, and $\phi_{5i} = \pi \tau_i$ and $\phi_{6i} = \pi \rho_i$. Thus, we have $\phi_{1i}, ..., \phi_{6i} \in [0, \pi]$. By considering [Equation (4.1)](), the ω_i can be represented as a vector in $\mathbb{S}^5$. Therefore, the ETRep space can be seen as a poly-hypersphere $(\mathbb{S}^5)^{n+1}$. Consequently, with a population of ETReps, the PNS can be applied $n + 1$ times on $\mathbb{S}^5$.

Moreover, Section 5 of Paper III explained how to map an ETRep to $\mathbb{R}^{6(n+1)}$ based on ETRep vectorization. Let s be a vectorized ETRep. Since $s \in \mathbb{R}^{6(n+1)}$, we have the normalized ETRep as $\frac{s}{\|s\|} \in \mathbb{S}^{6n+5}$. In this sense, (analogous to Kendall's pre-shape space) $\mathbb{S}^{6n+5}$ can be seen as the shape space of normalized ETReps such that a normalized ETRep is a point on the hypersphere. Thus, by having a population of ETReps, one can directly use the PNS for statistical analysis on the hypersphere. Although this method may result in strong statistical analysis, the main challenge lies in defining an inverse mapping from $\mathbb{S}^{6n+5}$ to the ETRep space $\mathcal{A}^{\dagger n+1}$, which can be explored in future studies.

References

AlHadidi, A., L. H. Cevidanes, B. Paniagua, R. Cook, F. Festy, and D. Tyndall (2012). 3d quantification of mandibular asymmetry using the spharm-pdm tool box. *International journal of computer assisted radiology and surgery 7*, 265–271.

Alves, G., B. Müller, K. Herlofson, I. HogenEsch, W. Telstad, D. Aarsland, O.-B. Tysnes, and J. P. Larsen (2009). Incidence of parkinson's disease in norway: the norwegian parkwest study. *Journal of Neurology, Neurosurgery & Psychiatry 80*(8), 851–857.

Apostolova, L., G. Alves, K. S. Hwang, S. Babakchanian, K. S. Bronnick, J. P. Larsen, P. M. Thompson, Y.-Y. Chou, O. B. Tysnes, H. K. Vefring, et al. (2012). Hippocampal and ventricular changes in parkinson's disease mild cognitive impairment. *Neurobiology of aging 33*(9), 2113–2124.

Attali, D., H. Edelsbrunner, and Y. Mileyko (2007). Weak witnesses for delaunay triangulations of submanifolds. In *Proceedings of the 2007 ACM symposium on Solid and physical modeling*, pp. 143–150.

Attali, D. and A. Montanvert (1997). Computing and simplifying 2d and 3d continuous skeletons. *Computer vision and image understanding 67*(3), 261–273.

Bærentzen, A. and E. Rotenberg (2021). Skeletonization via local separators. *ACM Transactions on Graphics (TOG) 40*(5), 1–18.

Bærentzen, J. A., R. E. Christensen, E. T. Gæde, and E. Rotenberg (2023). Multilevel skeletonization using local separators. *arXiv preprint arXiv:2303.07210 1*, 1–32.

Berger, J. (1985). *Statistical Decision Theory and Bayesian Analysis*. Springer Series in Statistics. Springer.

Blum, H. (1973). Biological shape and visual science (part i). *Journal of theoretical Biology 38*(2), 205–287.

Blum, H. et al. (1967). A transformation for extracting new descriptors of shape. *Models for the perception of speech and visual form 19*(5), 362–380.

Blumenson, L. (1960). A derivation of n-dimensional spherical coordinates. *The American Mathematical Monthly 67*(1), 63–66.

Brady, M. and H. Asada (1984). Smoothed local symmetries and their implementation. *The International Journal of Robotics Research 3*(3), 36–61.

Chambers, E. W., T. Ju, and D. Letscher (2013). Medial residues of piecewise linear manifolds. In *CCCG*, pp. 1–14.

Chazal, F. and A. Lieutier (2005). The "λ-medial axis". *Graphical models 67*(4), 304–331.

Damon, J. (2003). Smoothness and geometry of boundaries associated to skeletal structures i: Sufficient conditions for smoothness. In *Annales de l'institut Fourier*, Volume 53, pp. 1941–1985.

Damon, J. (2008). Swept regions and surfaces: Modeling and volumetric properties. *Theoretical Computer Science 392*(1-3), 66–91.

Damon, J. (2021). Rigidity properties of the blum medial axis. *Journal of Mathematical Imaging and Vision 63*(1), 120–129.

Damon, J. and E. Gasparovic (2017). Modeling multi-object configurations via medial/skeletal linking structures. *International Journal of Computer Vision 124*, 255–272.

Dey, T. K. and J. Sun (2006). Defining and computing curve-skeletons with medial geodesic function. In *Symposium on geometry processing*, Volume 6, pp. 143–152.

Dryden, I. and K. Mardia (1998). *Statistical Shape Analysis*. Wiley Series in Probability & Statistics. Wiley.

Dryden, I. and K. Mardia (2016). *Statistical Shape Analysis: With Applications in R*. Wiley Series in Probability and Statistics. Wiley.

Fletcher, P. T., C. Lu, and S. Joshi (2003). Statistics of shape via principal geodesic analysis on lie groups. In *2003 IEEE Computer Society Conference on Computer Vision and Pattern Recognition, 2003. Proceedings.*, Volume 1, pp. I–I. IEEE.

Fletcher, P. T., C. Lu, S. M. Pizer, and S. Joshi (2004). Principal geodesic analysis for the study of nonlinear statistics of shape. *IEEE transactions on medical imaging 23*(8), 995–1005.

Foskey, M., M. C. Lin, and D. Manocha (2003). Efficient computation of a simplified medial axis. In *Proceedings of the eighth ACM symposium on Solid modeling and applications*, pp. 96–107.

Fréchet, M. R. (1948). Les éléments aléatoires de nature quelconque dans un espace distancié. *Annales de l'institut Henri Poincaré 10*(4), 215–310.

Gamble, J. and G. Heo (2010). Exploring uses of persistent homology for statistical analysis of landmark-based shape data. *Journal of Multivariate Analysis 101*(9), 2184–2199.

Giblin, P. and B. B. Kimia (2004). A formal classification of 3d medial axis points and their local geometry. *IEEE Transactions on Pattern Analysis and Machine Intelligence 26*(2), 238–251.

Giblin, P. J. and B. B. Kimia (2003). On the intrinsic reconstruction of shape from its symmetries. *IEEE Transactions on Pattern Analysis and Machine Intelligence 25*(7), 895–911.

Hoffman, D. K., R. C. Raffenetti, and K. Ruedenberg (1972). Generalization of euler angles to n-dimensional orthogonal matrices. *Journal of Mathematical Physics 13*(4), 528–533.

Jermyn, I., S. Kurtek, H. Laga, A. Srivastava, G. Medioni, and S. Dickinson (2017). *Elastic Shape Analysis of Three-Dimensional Objects*. Synthesis Lectures on Computer Vision. Morgan & Claypool Publishers.

31

Joshi, S., S. Pizer, P. T. Fletcher, A. Thall, and G. Tracton (2001). Multi-scale 3-d deformable model segmentation based on medial description. In *Biennial International Conference on Information Processing in Medical Imaging*, pp. 64–77. Springer.

Joshi, S., S. Pizer, P. T. Fletcher, P. Yushkevich, A. Thall, and J. Marron (2002). Multiscale deformable model segmentation and statistical shape analysis using medial descriptions. *IEEE transactions on medical imaging 21*(5), 538–550.

Jung, S., I. L. Dryden, and J. Marron (2012). Analysis of principal nested spheres. *Biometrika 99*(3), 551–568.

Kendall, D. G. (1977). The diffusion of shape. *Advances in applied probability 9*(3), 428–430.

Kendall, D. G. (1984). Shape manifolds, procrustean metrics, and complex projective spaces. *Bulletin of the London Mathematical Society 16*(2), 81–121.

Laga, H., Y. Guo, H. Tabia, R. Fisher, and M. Bennamoun (2019). *3D Shape Analysis: Fundamentals, Theory, and Applications*. Wiley.

Lele, S. R. and J. T. Richtsmeier (2001). *An invariant approach to statistical analysis of shapes*. Chapman and Hall/CRC.

Liu, Z., J. Damon, J. Marron, and S. Pizer (2023). Geometric and statistical models for analysis of two-object complexes. *International Journal of Computer Vision 131*(8), 1877–1891.

Liu, Z., J. Hong, J. Vicory, J. N. Damon, and S. M. Pizer (2021). Fitting unbranching skeletal structures to objects. *Medical Image Analysis 70*, 102020.

Liu, Z., J. Schulz, M. Taheri, M. Styner, J. Damon, S. Pizer, and J. Marron (2023). Analysis of joint shape variation from multi-object complexes. *Journal of Mathematical Imaging and Vision 65*(3), 542–562.

Ma, R., Q. Zhao, R. Wang, J. N. Damon, J. G. Rosenman, and S. M. Pizer (2018). Skeleton-based generalized cylinder deformation under the relative curvature condition. In *PG (Short Papers and Posters)*, pp. 37–40.

Malykhin, N. V., T. P. Bouchard, C. J. Ogilvie, N. J. Coupland, P. Seres, and R. Camicioli (2007). Three-dimensional volumetric analysis and reconstruction of amygdala and hippocampal head, body and tail. *Psychiatry Research: Neuroimaging 155*(2), 155–165.

Marron, J. and I. Dryden (2021). *Object Oriented Data Analysis*. Chapman & Hall/CRC Monographs on Statistics and Applied Probability. CRC Press.

Murray, R. M., Z. Li, and S. S. Sastry (2017). *A mathematical introduction to robotic manipulation*. CRC press.

OECD (2008). *OECD Glossary of Statistical Terms*. OECD glossaries OECD glossary of statistical terms. OECD Publishing.

Oksanish, J. (2019). *Vitruvian Man*. Oxford University Press, USA.

Pennec, X., S. Sommer, and T. Fletcher (2019). *Riemannian Geometric Statistics in Medical Image Analysis*. Elsevier Science.

Pizer, S. M., D. S. Fritsch, P. A. Yushkevich, V. E. Johnson, and E. L. Chaney (1999). Segmentation, registration, and measurement of shape variation via image object shape. *IEEE transactions on medical imaging 18*(10), 851–865.

Pizer, S. M., J. Hong, J. Vicory, Z. Liu, J. Marron, H.-y. Choi, J. Damon, S. Jung, B. Paniagua, J. Schulz, et al. (2020). Object shape representation via skeletal models (s-reps) and statistical analysis. In *Riemannian Geometric Statistics in Medical Image Analysis*, pp. 233–271. Elsevier.

Pizer, S. M., S. Jung, D. Goswami, J. Vicory, X. Zhao, R. Chaudhuri, J. N. Damon, S. Huckemann, and J. Marron (2013). Nested sphere statistics of skeletal models. In *Innovations for Shape Analysis*, pp. 93–115. Springer.

Pizer, S. M., J. Marron, J. N. Damon, J. Vicory, A. Krishna, Z. Liu, and M. Taheri (2022). Skeletons, object shape, statistics. *Frontiers in Computer Science 4*, 842637.

Polthier, K. and M. Schmies (1998). *Straightest Geodesics on Polyhedral Surfaces*, pp. 135–150. Berlin, Heidelberg: Springer Berlin Heidelberg.

Schulz, J., S. M. Pizer, J. Marron, and F. Godtliebsen (2016). Non-linear hypothesis testing of geometric object properties of shapes applied to hippocampi. *Journal of Mathematical Imaging and Vision 54*(1), 15–34.

Siddiqi, K. and S. Pizer (2008). *Medial Representations: Mathematics, Algorithms and Applications*. Computational Imaging and Vision. Springer Netherlands.

Styner, M., I. Oguz, S. Xu, C. Brechbühler, D. Pantazis, J. J. Levitt, M. E. Shenton, and G. Gerig (2006). Framework for the statistical shape analysis of brain structures using spharm-pdm. *The insight journal 1*(1071), 242.

Taheri, M., S. M. Pizer, and J. Schulz (2023). Fitting the discrete swept skeletal representation to slabular objects. submitted.

Taheri, M., S. M. Pizer, and J. Schulz (2024). The mean shape under the relative curvature condition. submitted.

Taheri, M. and J. Schulz (2022). Statistical analysis of locally parameterized shapes. *Journal of Computational and Graphical Statistics 0*(ja), 1–28.

Thompson, D. (1992). *On Growth and Form*. Number v. 1 in Dover Books on Biology Series. Dover Publications.

Tomson, J. (1904). On the structure of the atom: an investigation of the stability and periods of osciletion of a number of corpuscles arranged at equal intervals around the circumference of a circle; with application of the results to the theory atomic structure. *Philos. Mag. Series 6 7*(39), 237.

Tu, L., J. Vicory, S. Elhabian, B. Paniagua, J. C. Prieto, J. N. Damon, R. Whitaker, M. Styner, and S. M. Pizer (2016). Entropy-based correspondence improvement of interpolated skeletal models. *Computer Vision and Image Understanding 151*, 72–79.

Turner, K., S. Mukherjee, and D. M. Boyer (2014). Persistent homology transform for modeling shapes and surfaces. *Information and Inference: A Journal of the IMA 3*(4), 310–344.

Van Der Maaten, L. (2014). Accelerating t-sne using tree-based algorithms. *The Journal of Machine Learning Research 15*(1), 3221–3245.

Van Kaick, O., H. Zhang, G. Hamarneh, and D. Cohen-Or (2011). A survey on shape correspondence. In *Computer graphics forum*, Volume 30, pp. 1681–1707. Wiley Online Library.

Paper I

Statistical Analysis of Locally Parameterized Shapes

Statistical Analysis of Locally Parameterized Shapes

Mohsen Taheri & Jörn Schulz

View supplementary material

Published online: 14 Oct 2022.

Submit your article to this journal

Article views: 660

View related articles

View Crossmark data

Citing articles: 2 View citing articles

37

Paper I

Taylor & Francis
Taylor & Francis Group

🔓 OPEN ACCESS | Check for updates

Statistical Analysis of Locally Parameterized Shapes

Mohsen Taheri[a] 🔟 and Jörn Schulz[b] 🔟

Department of Mathematics & Physics, University of Stavanger, Stavanger, Norway

ABSTRACT

In statistical shape analysis, the establishment of correspondence and defining shape representation are crucial steps for hypothesis testing to detect and explain local dissimilarities between two groups of objects. Most commonly used shape representations are based on object properties that are either extrinsic or noninvariant to rigid transformation. Shape analysis based on noninvariant properties is biased because the act of alignment is necessary, and shape analysis based on extrinsic properties could be misleading. Besides, a mathematical explanation of the type of dissimilarity, for example, bending, twisting, stretching, etc., is desirable. This work proposes a novel hierarchical shape representation based on invariant and intrinsic properties to detect and explain locational dissimilarities by using local coordinate systems. The proposed shape representation is also superior for shape deformation and simulation. The power of the method is demonstrated on the hypothesis testing of simulated data as well as the left hippocampi of patients with Parkinson's disease and controls. Supplementary materials for this article are available online.

1. Introduction

In statistical shape analysis, detecting and characterizing locational differences between two groups of *objects* is a matter of special interest. For instance, in medical applications, analysis of shape dissimilarities has the power to shed light on organ deformations, supporting diagnosis and treatment.

Detecting locational differences is a challenging task. For decades, medical researchers have been trying to answer four common questions when comparing a specific organ of a group of patients versus a *control group* (CG). 1. Existence: Is there any local dissimilarity? 2. Location: What is the location of the dissimilarity? 3. Intensity: What is the size of the dissimilarity? 4. Type: What is the type or interpretation of the dissimilarity (e.g., bending, twisting, or elongation)? Since a dissimilarity can be seen as a distance between two entities, each shape analysis method introduces distances between objects' corresponding parts (i.e., local dissimilarities) based on a specific shape representation to answer these questions. The shape representation could be *invariant* or *noninvariant* to object rigid transformation (i.e., translation and rotation). Therefore, as Lele and Richtsmeier (2001) discussed, roughly we can categorize shape analysis methods into alignment-independent and alignment-dependent approaches that we call invariant and noninvariant methods, respectively. Invariant methods use invariant shape representations to follow the *principle of invariance* (Berger 1985) based on the fact that the true form of an organism does not change if it translates or rotates. In contrast, noninvariant methods follow the idea of Kendall (1977) to factor out translation, rotation, and (occasionally) scaling from noninvariant shape representations by alignment. Usually, noninvariant methods are more straightforward, faster, and provide a better

intuition than invariant methods, which explains their popularity. In comparison, invariant methods are more reliable because they are independent of choosing the alignment method or the coordinate system.

In this work, we propose an invariant method equipped with an invariant shape representation that benefits from the advantages of both types of methods. Further, it answers all the four above questions in a single framework. For this, we locally reparameterize a noninvariant *skeletal representation* (s-rep) (Pizer et al. 2013) to an entirely invariant shape representation. To better understand and highlight the advantages of our approach, first we need to review other methods in more detail.

Given two groups of objects, in the most common approaches, whether invariant or noninvariant, researchers try to answer the above questions by hypothesis testing based on the following steps. Step 1: Introduce shape representation as a tuple of corresponding *geometric object properties* (GOPs) among objects. Step 2: Defining a distance between the corresponding GOPs of the two groups known as a *test statistic* representing the local dissimilarity. Step 3: Measuring and analyzing the test statistics to find significant GOPs. Step 4: Applying multiple testing methods to control false positives.

A GOP can be a geometric or spatial feature (e.g., point's position, surface normal direction, Gaussian curvature, etc.), a combination of features and their correlations (Tabia and Laga 2015), or more general a local descriptor as discussed in (Laga et al. 2018, Ch.5). A GOP may or may not be invariant to object translation and rotation. We call a shape representation invariant if all of its GOPs are invariant, otherwise noninvariant.

Examples of noninvariant shape representations are the *point distribution model* (PDM) and the *discrete s-rep* (ds-rep). A PDM consists of an *n*-tuple of points $(x_1, \ldots, x_n)$, $x_i \in \mathbb{R}^d$ distributed on or inside a *d*-dimensional object where $d = 2, 3$ as comprehensively discussed in Srivastava and Klassen (2016), Jermyn et al. (2017), Laga et al. (2018), and Dryden and Mardia (2016). Thus, the GOPs in a PDM are the points' Cartesian coordinates. A ds-rep (Pizer et al. 2013) consists of a tuple of directions, tail positions and lengths of a set of internal vectors and will be discussed in further detail in Section 2.1. A ds-rep is partly invariant as the vectors' lengths are invariant. An example for an invariant shape representation is to convert a PDM to *Euclidean distance matrix* (EDM) representation as a tuple of pairwise Euclidean distances of points (Lele and Richtsmeier 2001).

Having two groups of shape representations, we can define hypothesis tests based on the corresponding GOPs. In other words, we simply test two groups of tuples element-wise. Note that it is necessary to factor out translation and rotation from noninvariant GOPs by alignment before the analysis. We say the analysis is invariant if the shape representation is invariant, otherwise it is noninvariant. For example, Styner et al. (2006) and Schulz (2013) methods are noninvariant as Styner et al. (2006) compared PDMs of brain objects of patients with schizophrenia v.s. CG, and Schulz (2013) compared the objects' ds-reps. In contrast, Lele and Richtsmeier (1991) approach is invariant as they used EDM representations to study skull abnormality of patients with Crouzon and Apert syndromes. We briefly discuss both invariant and noninvariant methods by an example.

Figure 1(a) illustrates two *ellipsoidal* objects as defined in Section 2.1.2, where the left one is an ellipse, and the right one is a bent ellipse. The objects can be seen as an open arm (left one) and a closed arm (right one), where each arm consists of three parts, namely the upper arm, elbow, and forearm. Since the closed arm is a locally deformed version of the open arm, we consider the main difference at the elbow, which is compatible with our visual inspection. Both shapes are manually registered with 20 corresponding boundary points depicted by circles and crosses. By adding independent random noise to each point, we simulated 15 PDMs for each object, as depicted in Figure 1(b). Since a PDM is noninvariant, alignment is necessary.

From several available alignment methods, we choose *generalized Procrustes analysis* (GPA), *weighted GPA* (WGPA) (Dryden and Mardia 2016), and *square root velocity framework* (SRVF) (Srivastava and Klassen 2016). Figure 1(c)–(e) illustrate alignments based on GPA, WGPA, and SRVF, respectively. Apparently, there are two main issues. First, the outcomes of different alignment methods are remarkably different as each method tries to minimize a specific type of distance. Thus, choosing the superior alignment method is challenging. Second, detecting locational dissimilarities could be extremely biased because alignment affects the distributions of noninvariant GOPs of points' positions. As a result, PDM analysis introduces false positives and false negatives. In Figure 1(c), WGPA (based on a manually defined covariance matrix) reduces the variation of forearm GOPs and increases the variation of upper arm GOPs. Similarly, the right point at the elbow in Figure 1(e) has a remarkably smaller GOP variation in comparison with other points. Based on these types of observations, Lele and Richtsmeier (2001) explained why noninvariant methods are biased and why invariant methods are more reliable. However, also for invariant methods a local dissimilarity can lead to false positives and false negatives. For instance, if we convert each PDM of our example to an invariant shape representation, where GOPs are invariant Euclidean distances between points and the centroid of the PDM (i.e., center of gravity $\bar{x} = \frac{1}{n} \sum_{i=1}^{n} x_i$ depicted by bold points in Figure 1(a)), then almost all the GOPs in our example become significantly different. Note, in this example, the GOPs are defined as *extrinsic* distances between the points and the extrinsic centroid. If the centroid as well as the distances to the centroid are defined *intrinsic* (e.g., by barycentroid (Rustamov, Lipman, and Funkhouser 2009)), no differences would be detected. To some extent, the same discussion is valid for *EDM analysis* (EDMA) as discussed in supplementary material (SUP). Besides, when we consider only invariant GOPs, it is not always easy to map various analysis results from the feature space to the object space (Jermyn et al. 2017, 6). Consequently, some fundamental aspects of shape analysis, such as mean shape, are unattainable. For instance, it is easy to calculate the EDM of a point-based model like a PDM, but it is difficult or sometimes impossible to reconstruct the model based on its EDM. We have the same situation in *persistent homology* methods (Gamble and Heo 2010; Turner, Mukherjee, and Boyer 2014) where the informa-

(a) ellipsoidals   (b) Simulated PDMs   (c) GPA alignment   (d) WGPA alignment   (e) SRVF alignment
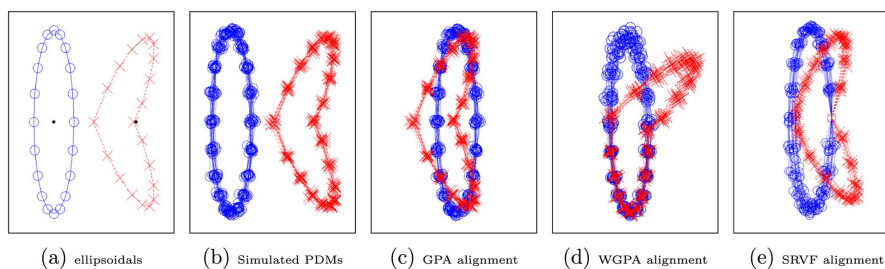
Figure 1. Problem of false positives due to alignment. (a) Two ellipsoidals are depicted by line and dashed line. Circles and crosses show corresponding boundary points. Bold points are shapes' centroids. (b) Two populations of simulated PDMs. (c), (d), (e) Separation of corresponding local distributions.
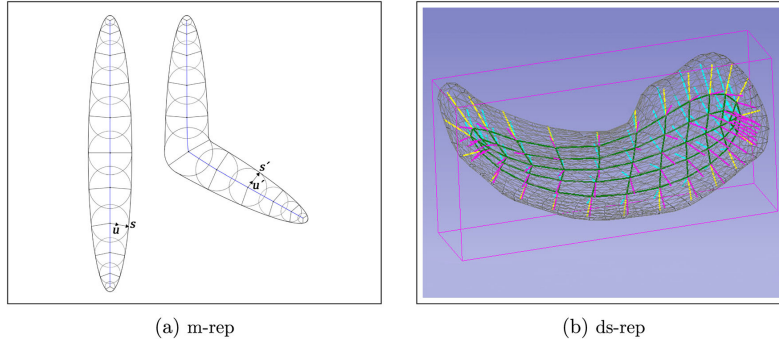
39

(a) m-rep
(b) ds-rep

Figure 2. Skeletal structure of ellipsoidal objects. (a) 2D m-reps. *s* and *s′* are corresponding spokes with unit directions *u* and *u′*. (b) A fitted ds-rep to a left hippocampus's mesh including up, down, crest spokes, and the skeletal sheet.

tion of the persistent diagram is not convertible to the object space.

In summary, on the one hand, noninvariant methods are biased due to alignment, and on the other hand, invariant methods based on extrinsic properties could be misleading. Thus, from our point of view, a suitable method should be invariant, based on intrinsic object properties, ensure good correspondence between the GOPs, and be able to answer the fourth question, that is, to provide a mathematical (and medical) interpretation of the type of dissimilarity such as bending, twisting, stretching, protrusion, etc. For example, boundary PDMs cannot explain the local bending in closed arms. In contrast, a skeletal model (see Figure 2(a)) can explain the bending mathematically, as we will discuss in Section 2.4. However, the main obstacle in the skeletal analysis is the definition of correspondence.

For a specific class of ellipsoidal objects, Pizer et al. (2013) introduced s-rep and defined correspondence based on its discrete version ds-rep (see Figure 2(b)). As pointed out above, ds-reps are noninvariant and thus might bias the analysis. Further, ds-rep analysis is able to identify only a few types of dissimilarities, for example, protrusion or bending. The identification of other types remains challenging. To overcome these limitations, we propose a novel hierarchical ds-rep parameterization based on local coordinate systems known as *local frames*. The proposed hierarchical local parameterization of ds-rep, called LP-ds-rep, is an invariant shape representation which supports sensitive hypothesis testing, that is, not biased by alignment. Note that the hierarchical structure equipped with local frames can be modified and fit to any kind of objects (not only ellipsoidals) as long as a robust tree structure can be established for the shape model. This is the subject of further studies.

The article is structured as follows. In Section 2, we first review basic notations and amenities of s-reps and discuss the conventional noninvariant definition of ds-rep with the discussed challenges. Then, in Sections 2.1.3 and 2.1.4, we propose the novel LP-ds-rep parameterization. Further, we explain the euclideanization of spherical data, mean shape, the transformation between two parameterizations, skeletal deformation, and

simulation. Section 3 introduces a hypothesis test method and discusses controlling false positives. In Section 4 we study hippocampal differences between a group of patients with *Parkinson's disease* and CG. Besides, we compare the results of both parameterizations plus EDMA and show the advantages of our method on simulated data. Finally, we summarize and conclude the work in Section 5. A flowchart depicting the framework of the presented methods can be found in the SUP.

2. Skeletal Representation

To understand skeletal representation, we need to review some fundamental definitions.

In this work, the set $\Omega \subset \mathbb{R}^d$ is a d-dimensional (or dD) object if it is homeomorphic to the d-dimensional closed ball, where $d = 2, 3$. We denote the boundary and the interior of Ω, by $\partial\Omega$ and Ω_{in}, respectively. Thus, $\Omega = \partial\Omega \cup \Omega_{in}$. Also, we consider only objects with smooth boundaries. Therefore, $\partial\Omega$ is a closed connected genus-zero smooth surface if $d = 3$, and it is a smooth closed curve if $d = 2$ (Jermyn et al. 2017, Ch.2). The *medial locus* of Ω is a collection of entirely connected curves or sheets in Ω_{in} forming the centers of all maximal inscribed spheres bi-tangent or multi-tangent to $\partial\Omega$. We denote the medial locus of Ω by M_Ω. The *skeleton* of Ω is any curve or sheet from which non-crossing *spokes* to $\partial\Omega$ emanate at each point of it. Note that a spoke is a vector whose tail is on the object's skeleton, and its tip is on $\partial\Omega$. We consider a *skeletal* of an object as a set of all non-crossing spokes emanating from its skeleton. Thus, the skeletal can be seen as a field of spokes on the skeleton. The medial locus is a form of skeleton where *medial spokes* connecting the center of maximal inscribed spheres to their tangency points. The union of the medial spokes forms the *medial skeletal* (Siddiqi and Pizer 2008).

Medial representation (m-rep) and its properties have been extensively studied in the literature (Pizer et al. 1999; Fletcher et al. 2004; Siddiqi and Pizer 2008). Figure 2(a) illustrates m-reps of two ellipsoidal objects. Briefly, an m-rep is a discrete medial skeletal (i.e., finite set of medial spokes). Thus, an m-rep reflects the interior object properties such as local widths and directions.

However, as pointed out in (Pizer et al. 2013), the m-rep is sensitive to boundary noise because every protruding boundary kink results in additional medial branches. This sensitivity affects m-rep correspondence among a population as two versions of the same objects can result in significantly different m-reps. Thus, Pizer et al. (2013) relaxed the medial conditions and defined s-rep for a class of ellipsoidal objects like hippocampus (discussed in detail in Section 2.1.2) as a penalized version of m-rep. As Liu et al. (2021) described, the s-rep of 3D ellipsoidal object Ω has the form (M, S), where skeleton $M \subset \Omega_{in}$ known as *skeletal sheet* is a smooth 2-disk (i.e., an embedded, oriented two-dimensional manifold of genus-zero with a single boundary component), and skeletal S is the field of noncrossing spokes on M. The field S consists of three distinct fields of spokes: S_0 along M_0 where M_0 is the boundary of M, S_+ (respectively, S_-) defined on the relative interior of M, agreeing (respectively, disagreeing) with the orientation of M. Thus, S_+ and S_- map $M \setminus M_0$ to two sides of $\partial\Omega$ considered as northern and southern part, and S_0 maps M_0 to the crest of $\partial\Omega$. We call a spoke s an *up spoke, down spoke,* or *crest spoke* if it belongs to S_+, S_-, or S_0, respectively. The same definition is applicable for 2D objects where M is a smooth open curve. The relaxed conditions assure stability in the branching structure and thus good case-to-case correspondence across a population of s-reps. The ds-rep is a discrete form of s-rep (i.e., a finite set of spokes). The conventional ds-rep parameterization is noninvariant as explained in more detail in Section 2.1.1. Afterward, the proposed invariant parameterization based on a hierarchical structure of the local frames is introduced. Also, we name the conventional parameterization as *globally parameterized ds-rep* (GP-ds-rep), and the new parameterization as *locally parameterized ds-rep* (LP-ds-rep). Further, s^{GP} and s^{LP} denote GP-ds-rep and LP-ds-rep, respectively.

2.1. Parameterizations

2.1.1. GP-ds-rep
There are different ways to fit and parameterize a GP-ds-rep. Depending on the method of model fitting, for example, (Liu et al. 2021), some spokes may share a common tail position (see Figure 2(b)). Let n_s be the number of spokes, and n_p be the number of tail positions s.t. $n_p \leq n_s$. A GP-ds-rep can be seen as a tuple $s^{GP} = (\boldsymbol{p}_j, \boldsymbol{u}_i, r_i)_{i,j} = (\boldsymbol{p}_1, \ldots, \boldsymbol{p}_{n_p}, \boldsymbol{u}_1, \ldots, \boldsymbol{u}_{n_s}, r_1, \ldots, r_{n_s})$ where $\forall j \in \{1, \ldots, n_p\}$: $\boldsymbol{p}_j \in \mathbb{R}^3$ is jth spoke's tail position, $\forall i \in \{1, \ldots, n_s\}$: $\boldsymbol{u}_i \in \mathbb{S}^2$, and $r_i \in \mathbb{R}^+$ are ith spoke's direction, and length, respectively. Note $\mathbb{S}^d = \{\boldsymbol{x} \in \mathbb{R}^{d+1} | \|\boldsymbol{x}\| = 1\}$ is the unit d-sphere where $d \in \mathbb{N}$. From now on we assume $i = 1, \ldots, n_s$ and $j = 1, \ldots, n_p$.

The set $\{\boldsymbol{p}_j\}_{j=1}^{n_p}$ forms an $n_p \times 3$ configuration matrix P representing the skeletal PDM. Let I_{n_p} be the $n_p \times n_p$ identity matrix and $\mathbf{1}_{n_p}$ be the $n_p \times 1$ vector of ones. Location and scale can be removed by centering and normalizing P to obtain the pre-shape $\tilde{P} = \frac{C_{n_p} P}{\|C_{n_p} P\|}$, where $C_{n_p} = I_{n_p} - \frac{1}{n_p} \mathbf{1}_{n_p} \mathbf{1}_{n_p}^T$ is the centering matrix, and $\|X\| = \sqrt{\text{trace}(X^T X)}$ is the Euclidean norm. Since $\|\tilde{P}\| = 1$, the pre-shape $\tilde{P}$ lives on the hypersphere $\mathbb{S}^{3n_p-1}$ (Pizer et al. 2013). Therefore, a GP-ds-rep lives on a manifold as a direct product of Riemannian symmetric spaces $\mathbb{S}^{3n_p-1} \times (\mathbb{S}^2)^{n_s} \times \mathbb{R}_+^{n_s+1}$ where $\mathbb{S}^{3n_p-1}$ indicates the pre-shape

space of the skeletal positions, $(\mathbb{S}^2)^{n_s}$ is the space of n_s spokes' directions, and $\mathbb{R}_+^{n_s+1}$ is the space of spokes' lengths and the scaling factor. As we mentioned before, spoke positions and directions are noninvariant as they are in a *global coordinate system* (GCS). Thus, ds-rep analysis based on this representation is biased.

For m-rep, a semi-local parameterization was proposed by Fletcher, Lu, and Joshi (2003) based on local frames $(\boldsymbol{n}, \boldsymbol{b}, \boldsymbol{b}^\perp) \in SO(3)$, where $\boldsymbol{n}$ is normal to the medial locus M_Ω at $\boldsymbol{p} \in M_\Omega$, $\boldsymbol{b} = \frac{\boldsymbol{u}_1+\boldsymbol{u}_2}{\|\boldsymbol{u}_1+\boldsymbol{u}_2\|}$ is the bisector direction of two equal-length spokes with common position, $\boldsymbol{b}^\perp = \boldsymbol{n} \times \boldsymbol{b}$, and $SO(3)$ is the 3D rotation group. Spokes' directions are defined relative to the local frames by the angle $\theta \in [0, \pi)$ between $\boldsymbol{b}$ and the spokes (see Figure 5(a)). Because the direction of $\boldsymbol{b}$ and $\boldsymbol{b}^\perp$ depends on the spokes' directions, if $\theta = \frac{\pi}{2}$ then $\boldsymbol{b}$ takes an arbitrary direction that violates the uniqueness and consistency of the fitted frame. Besides, the spokes' tail positions and frame directions are noninvariant as they are in GCS.

Inspired by Cartan's moving frames on space curves (Cartan 1937) and Fletcher's semi-local parameterization, we propose a fully local ds-rep parameterization. By uisng the inherent hierarchical structure of ds-reps, we provide a consistent definition of local frames independent of GCS that avoids arbitrary frame rotation. This can be done by introducing a leaf-shaped skeletal structure for ellipsoidal objects, that is, reflected in (Liu et al. 2021) (see Figure 6 on page 664). For this, we need to discuss ellipsoidal objects.

2.1.2. Ellipsoidal Objects
Intuitively, an object is ellipsoidal if its skeletal structure corresponds to the skeletal of an eccentric ellipsoid (i.e., ellipsoid with unequal principal radii).

Let $\mathcal{E}_3 \subset \mathbb{R}^3$ be a 3D eccentric ellipsoid. The medial locus of $\mathcal{E}_3$ is a 2D ellipsoid (i.e., an ellipse) $\mathcal{E}_2 \subset \mathbb{R}^2$ that we call *medial ellipse*. The medial locus of $\mathcal{E}_2$ is a 1D ellipsoid (i.e., a line segment) $\mathcal{E}_1 \subset \mathbb{R}^1$ that we call *medial line*. The medial locus of $\mathcal{E}_1$ is a 0D ellipsoid (i.e., a point) $\mathcal{E}_0 \subset \mathbb{R}^0$ that we call *medial centroid*. Thus, $M_{\mathcal{E}_n} = \mathcal{E}_{n-1}$ is the medial locus of $\mathcal{E}_n$ where $n = 1, 2, 3$. Analogous to backward *principal component analysis* (PCA) (Damon and Marron 2014), we consider $\mathcal{E}_3$, $\mathcal{E}_2$, $\mathcal{E}_1$, and $\mathcal{E}_0$ as four principal ellipsoids (see Figure 4(Left)).

We call a 2D object a *perfect 2D-ellipsoidal* if its medial locus is a smooth open curve that we call *medial curve* (see Figures 2a and 3a). Let Ω_2 be a perfect 2D-ellipsoidal with medial locus M_{Ω_2}. Since $M_{\mathcal{E}_2}$ (i.e., medial line $\mathcal{E}_1$) is also a smooth open curve, we can define correspondence between $M_{\mathcal{E}_2}$ and M_{Ω_2} based on (Srivastava and Klassen 2016). We consider a point on M_{Ω_2} corresponding to $\mathcal{E}_0$ as the medial centroid of Ω_2. Let γ represent the medial locus M_{Ω_2} (or $M_{\mathcal{E}_2}$) based on curve length parameterization l. We know that for each medial point $\gamma(l)$, there are two medial spokes, one for each side of the medial locus, with tail on $\gamma(l)$ and tip $\gamma^\pm$ on the object boundary at

$$\gamma^\pm = \gamma(l) - \mathcal{R}(l)|\frac{d}{dl}\mathcal{R}(l)|\boldsymbol{t} \pm \mathcal{R}(l)\sqrt{1 - |\frac{d}{dl}\mathcal{R}(l)|^2}\boldsymbol{n}, \quad (1)$$

where $\boldsymbol{n}$ and $\boldsymbol{t}$ are normal and tangent vectors of the medial locus at $\gamma(l)$, and $\mathcal{R}$ is the radius function such that $\mathcal{R}(l)$ is the radius of the maximal inscribe sphere centered at $\gamma(l)$ (Siddiqi
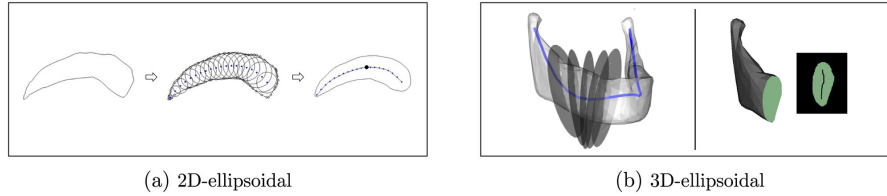
(a) 2D-ellipsoidal

(b) 3D-ellipsoidal

Figure 3. (a) Illustration of a 2D-ellipsoidal (left) approximated by a perfect 2D-ellipsoidal (right). The solid curve and the bold dot (right) depict the medial curve and medial centroid, respectively. (b) Left: A mandible (without coronoid processes) as an example of a 3D-ellipsoidal with slicing planes. The solid curve is the center curve. Right: A cross-section as a 2D-ellipsoidal including its medial curve.

and Pizer 2008, Ch.2). Note that the two spokes at the edge (i.e., endpoints) of the medial locus coincide. Thus, in addition to the medial locus, the medial skeletal of Ω_2 corresponds to the medial skeletal of $\mathcal{E}_2$.

We say a 2D object $\hat{\Omega}_2$ is 2D-ellipsoidal if its boundary can be precisely approximated[1] by the boundary of a perfect 2D-ellipsoidal Ω_2. Following m-rep idea of Pizer et al. (1999), it is reasonable to consider the skeletal of $\hat{\Omega}_2$ as the skeletal of Ω_2 to have a better correspondence among a population. Thus, we assume M_{Ω_2} as the skeleton of $\hat{\Omega}_2$ as depicted in Figure 3(a). In 3D, we define *3D-ellipsoidal* analogous to *generalized offset surface*.

Damon (2008) defined generalized offset surfaces as 3D objects similar to *generalized tubes*[2] based on sequences of affine slicing planes (not necessarily parallel) such that the cross-sections of a generalized offset surface (i.e., the intersection of the slicing planes with the object) do not intersect within object, and the boundary of the cross-sections forms the object's boundary. The skeleton of a generalized tube is a smooth curve, and the skeleton of a generalized offset surface is a smooth two-disk. In practice, we can represent a generalized tube or an offset surface by a finite but large number of disjoint cross-sections. Similarly, we say an object is 3D-ellipsoidal if it can be represented by a large number of disjoint cross-sections such that all the cross-sections are 2D-ellipsoidals, and the length of a curve called the *center curve* connecting the medial centroids of the successive cross-sections is remarkably larger than the length of the medial curve of each cross-section. Since the union of the medial curves can be seen as a discrete skeletal sheet, Pizer et al. (2013) realized such 3D-ellipsoidals as *slabular*[3] and introduced (slabular) ds-reps such that for a slabular, the implied boundary of its ds-rep (i.e., envelope of the spokes' tips) approximates the slabular's boundary. Examples of 3D-ellipsoidals are mandible (without considering the coronoid processes), caudate nucleus, kidney, and hippocampus. Figure 3(b) illustrates the center curve and the slicing planes of a mandible as a 3D-ellipsoidal (left) and a cross-section as a 2D-ellipsoidal (right).

Any eccentric ellipsoid $\mathcal{E}_3$ can be seen as a 3D-ellipsoidal such that parallel cross-sections are perpendicular to the center

curve (i.e., the major axis of $\mathcal{E}_2$). In this sense, a meaningful correspondence[4] between the skeletal of a 3D-ellipsoidal and skeletal of $\mathcal{E}_3$ is assumable as the skeleton of both of them consists of a center curve, a set of medial curves emanating from the center curves, and two spokes at each point of the medial curves pointing toward two sides of the skeletal sheet based on Equation (1). However, obtaining such correspondence is difficult as it is challenging to define corresponding cross-sections for a population of c-shape objects, for example, a set of hippocampi.

A possible approach for defining a skeletal sheet of a 3D-ellipsoidal is to understand the object via a diffeomorphism from a reference 3D-ellipsoidal such as $\mathcal{E}_3$. Assume Ω_3 be a 3D-ellipsoidal. Since $\mathcal{E}_3$ as a reference object is a 3D-ellipsoidal and a meaningful correspondence between Ω_3 and $\mathcal{E}_3$ is assumable, Liu et al. (2021) defined a (more or less) diffeomorphic transformation $\mathscr{F} : \Omega_3 \rightarrow \mathcal{E}_3$ based on stratified *mean curvature flow* (MCF). The transformation provides a boundary registration between $\mathcal{E}_3$ and Ω_3. Then, they applied inverse transformation $\mathscr{F}^{-1}$ (based on the obtained registration and inverse MCF) to deform $\mathcal{E}_3$ and its interior (i.e., skeletal) to Ω_3. After deformation (i.e., $\mathscr{F}^{-1} : \mathcal{E}_3 \rightarrow \Omega_3$), $\mathcal{E}_2$ transforms to a nonlinear surface M that can be seen as a 2-disk. Consequently, straight lines on $\mathcal{E}_2$ (e.g., medial line and medial spokes) become curves. Since we assumed a diffeomorphic transformation, the generated curves do not cross each other. We call the deformed medial line $\mathscr{F}^{-1}(\mathcal{E}_1)$ the *spine*, and deformed medial spokes *veins*. Thus, veins are a set of noncrossing curves emanating from the spine. Also, we assume the displaced medial centroid $\mathscr{F}^{-1}(\mathcal{E}_0)$ as an intrinsic centroid, and call it *skeletal centroid* or *s-centroid*. Thus, M has curvilinear skeletal corresponding to the medial skeletal of $\mathcal{E}_2$. Figure 4 provides an intuition about the ellipsoid's medial locus deformation. Finally, Liu et al. (2021) generated non-crossing spokes on the skeletal sheet such that the implied boundary approximates $\partial\Omega_3$. The generated spokes represent a s-rep as a field of noncrossing spokes on the skeletal sheet.

Although we apply the method of Liu et al. (2021), we believe it is possible to improve the model fitting in many aspects such as a better boundary registration based on Jermyn et al. (2017) that we leave for future studies.

---

[1] The required energy to deform one object to the other one is negligible, for example, see Sorkine (2006).

[2] Tube refers to a 3D object made by a sweeping disk such that its medial locus is a smooth curve.

[3] Slab refers to a 3D object such that its medial locus is a sheet.

[4] See Van Kaick et al. (2011) for a comprehensive discussion about meaningful correspondence.
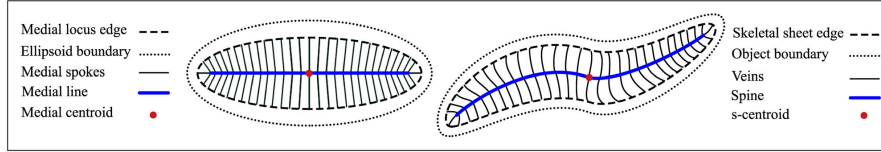
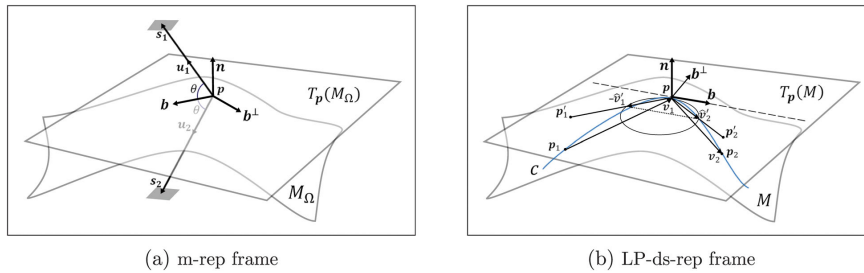**Figure 4.** Skeletal sheet. Left: Ellipsoid's medial locus. Right: s-rep skeletal sheet of a 3D-ellipsoidal.

(a) m-rep frame   (b) LP-ds-rep frame

Figure 5. Illustration of a local frame. n is normal to tangent planes $T_p(M)$ and $T_p(M_\Omega)$. (a) s_1 and s_2 are equal-length spokes with unit directions u_1 and u_2, and $b = \frac{u_1+u_2}{\|u_1+u_2\|}$ (b) c is a smooth curve on M. $-p_1'$ and p_2' are the projection of p_1 and p_2 on $T_p(M)$. $\hat{v}_1' = \frac{p-p_1'}{\|p-p_1'\|}$, $\hat{v}_2' = \frac{p_2'-p}{\|p_2'-p\|}$, and $b = \frac{\hat{v}_2'+\hat{v}_1'}{\|\hat{v}_2'+\hat{v}_1'\|}$.

2.1.3. Local Frames

Based on the defined curves on the s-rep skeletal sheet of ellipsoidals, we can fit local frames. Let $c \subset M$ be a smooth curve in $\mathbb{R}^3$. We consider $b \in T_p(M)$ as the unit velocity vector tangent to c where $T_p(M)$ is the local tangent plane of M at $p \in c$ with normal n. The local frame can be defined as $(n, b, b^\perp) \in SO(3)$ where $b^\perp = n \times b$ (see Figure 5(b)). The unit vector b chooses two opposite directions depending on the definition of the curve starting and ending points. Besides, the frame directions are noninvariant. To have a consistent invariant frame definition, we design a hierarchical structure. Then on the basis of the structure, we define consistent fitted frames in a population of GP-ds-reps.

Consider the principal ellipsoids. Similar to Blum's grassfire flow (Blum 1967), we can say each point on $\partial\mathcal{E}_2$ moves to reach the medial line $\mathcal{E}_1$, and then moves to reach the medial centroid $\mathcal{E}_0$. Thus, for each boundary point there is a path from the point to the medial centroid. In discrete format, each path can be represented by a finite set of consequent points sorted based on the distance they travel to reach the medial centroid. Imagine two consequent points on the same path. We consider the point that takes the shorter route as the *parent*, and the other one as the *child*. Therefore, like a spanning tree, each point (except medial centroid) has a parent but may have multiple children (see Figure 6(Top)). Similarly, based on the correspondence between the $\mathcal{E}_2$ and the skeletal sheet M, each point on the boundary (i.e., edge) of M moves on a vein to reach the spine and then moves to reach the s-centroid. Therefore, in discrete format, we define parent and child relationship on M as we defined on $\mathcal{E}_2$. In addition, given a frame at each skeletal point, we consider the same hierarchical structure for the frames.

A vector that connects a frame to its parent frame is called *connection*. The tip of a connection is at the frame's origin, and its tail is at the parent's origin. Further, we assume that the s-centroid frame is its own parent without any connection to itself. We approximate the direction of b at point $p \in M$ based on three consecutive frames. Frames on the spine are parent of multiple children. To have a consistent frame definition first we fit frames on the spine. Except for the s-centroid frame and two critical endpoints of the spine that we will explain later, each spinal frame has a spinal parent frame and a spinal child frame. Let p_1 and p_2 be the position of the parent and the child frame of p. As illustrated in Figure 5, assume $v_1 = p - p_1$ and $v_2 = p_2 - p$ as connections. Let p_1' and p_2' be the projection of p_1 and p_2 on $T_p(M)$, respectively. We consider $b = \frac{\hat{v}_2'+\hat{v}_1'}{\|\hat{v}_2'+\hat{v}_1'\|}$ where $\hat{v}_1' = \frac{p-p_1'}{\|p-p_1'\|}$, and $\hat{v}_2' = \frac{p_2'-p}{\|p_2'-p\|}$. In this sense, b is a unit vector tangent to a circle (or a line) crossing $p - \hat{v}_1'$, p, and $p + \hat{v}_2'$.

The endpoints of the spine are critical because their frames have no children on the spine. By construction, the medial line is part of the major axis of the medial ellipse. Thus, there is a curve on the skeletal sheet correspond to the major axis that we call *major curve*. The major curve contains the spine and two veins. We consider the closest skeletal point (in geodesic sense) on these veins to the spine as the spine's extension and treat the critical points as any other spinal point. The s-centroid frame has two spinal children. Let p_1 and p_2 be the position of the children. We define $b = \frac{\hat{v}_2'-\hat{v}_1'}{\|\hat{v}_2'-\hat{v}_1'\|}$, where $\hat{v}_1' = \frac{p-p_1'}{\|p-p_1'\|}$, and $\hat{v}_2' = \frac{p_2'-p}{\|p_2'-p\|}$. Since a vein frame has a parent and a child on the same vein, we consider the same definition for them as discussed for spinal frames. Note that we treat a vein frame at the intersection of a vein and the spine as a spinal frame. For the
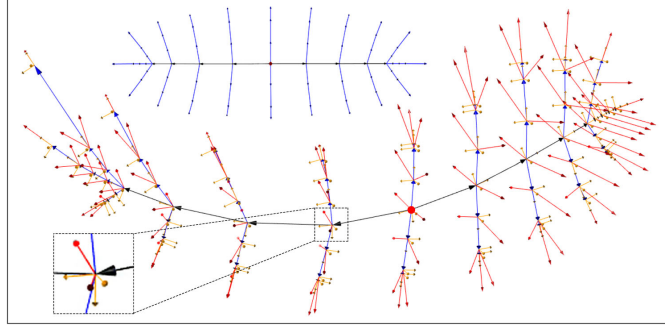
43

Figure 6. LP-ds-rep. Top: Hierarchical structure of the ellipsoid's medial locus. Arrows are connections. The dot is the medial centroid. Bottom: A fitted LP-ds-rep to a hippocampus. Arrows indicate spokes, connections, and frames. The magnified image depicts a spinal frame. The dot is the s-centroid.

frames on the edge of the skeletal, we assume the tip of the crest spokes from Liu et al. (2021) as the position of the child frames. The same procedure is applicable for the ellipsoid's GP-ds-rep.

Figure 6 illustrates the hierarchical structure and a fitted LP-ds-rep to a left hippocampus as we discuss in the next section.

2.1.4. LP-ds-rep

Given the fitted hierarchical frame structure introduced in the previous section, we are now in the position to define LP-ds-rep. In an LP-ds-rep, spokes and connections are measured based on their local frames, that is, their tails are located at the origin of a frame. Assume n_s, n_p, and n_c as the number of spokes, frames, and connections, respectively. Note that $n_c = n_p - 1$. Let $\boldsymbol{u}_i$ and $\boldsymbol{v}_k$ be the ith spoke direction and kth connection direction in GCS, respectively, where $i = 1, \ldots, n_s$, $j = 1, \ldots, n_p$, and $k = 1, \ldots, n_c$. Consequently, we denote $\boldsymbol{u}_i^*$ and $\boldsymbol{v}_k^*$ as spoke and connection directions based on their local frame, that is, we reparameterize $\boldsymbol{u}_i$ and $\boldsymbol{v}_k$ to $\boldsymbol{u}_i^*$ and $\boldsymbol{v}_k^*$, respectively. Similarly, if $F_j = (\boldsymbol{n}_j, \boldsymbol{b}_j, \boldsymbol{b}_j^\perp)$ be the frame F_j in GCS then $F_j^* = (\boldsymbol{n}_j^*, \boldsymbol{b}_j^*, \boldsymbol{b}_j^{*\perp})$ denotes F_j based on its parent frame.

To calculate a vector direction according to a local frame, we use the spherical rotation matrix $R(\boldsymbol{x}, \boldsymbol{y}) = I_d + (\sin \alpha)(\boldsymbol{y}\boldsymbol{w}^T - \boldsymbol{w}\boldsymbol{y}^T) + (\cos \alpha - 1)(\boldsymbol{y}\boldsymbol{y}^T + \boldsymbol{w}\boldsymbol{w}^T)$, where $\boldsymbol{x}, \boldsymbol{y} \in \mathbb{S}^{d-1}$, $\boldsymbol{w} = \frac{\boldsymbol{x} - \boldsymbol{y}(\boldsymbol{y}^T\boldsymbol{x})}{\|\boldsymbol{x} - \boldsymbol{y}(\boldsymbol{y}^T\boldsymbol{x})\|}$, and $\alpha = \cos^{-1}(\boldsymbol{y}^T\boldsymbol{x})$. Therefore, $R(\boldsymbol{x}, \boldsymbol{y})$ transfers $\boldsymbol{x}$ to $\boldsymbol{y}$ along the shortest geodesic and we have $R(\boldsymbol{x}, \boldsymbol{y})\boldsymbol{x} = \boldsymbol{y}$ (Amaral, Dryden, and Wood 2007).

For example, let frame $F^\dagger = (\boldsymbol{n}, \boldsymbol{b}, \boldsymbol{b}^\perp)$ be the parent of $\tilde{F}$, both in GCS. Let $\boldsymbol{e}_1 = (1, 0, 0)^T$, $\boldsymbol{e}_2 = (0, 1, 0)^T$, and $\boldsymbol{e}_3 = (0, 0, 1)^T$ be the axes unit vectors of GCS. We align $F^\dagger$ to $\tilde{I} = (\boldsymbol{e}_3, \boldsymbol{e}_1, \boldsymbol{e}_2)$ such that $R_2R_1F^\dagger = \tilde{I}$, where $R_1 = R(\boldsymbol{n}, \boldsymbol{e}_3)$, and $R_2 = R(R_1\boldsymbol{b}, \boldsymbol{e}_1)$. Thus, $\tilde{F}^* = R_2R_1\tilde{F}$ represents $\tilde{F}$ in its parent coordinate system. In case we obtain $R_2R_1F^\dagger = (\boldsymbol{e}_3, \boldsymbol{e}_1, -\boldsymbol{e}_2)$, we adjust the result by $R_2R_1\tilde{F}(\boldsymbol{1}_3, \boldsymbol{1}_3, -\boldsymbol{1}_3)$ because $R_2R_1F^\dagger(\boldsymbol{1}_3, \boldsymbol{1}_3, -\boldsymbol{1}_3) = \tilde{I}$ where $\boldsymbol{1}_3 = (1, 1, 1)^T$. Note that frame vectors are orthogonal, so after rotating $\boldsymbol{n}$ to the north pole by R_1, the shortest geodesic between $\boldsymbol{b}$ and $\boldsymbol{e}_1$ would be on the equator. This preserves the direction of $R_1\boldsymbol{n}$ while R_2 rotates $R_1\tilde{F}$.

We follow the same procedure to calculate the spokes' and connections' directions based on their local frames F_j^*. As a

result, we consider a LP-ds-rep as a tuple $s^{\text{LP}} = (\boldsymbol{u}_i^*, r_i, F_j^*, \boldsymbol{v}_k^*, v_k)_{i,j,k} = (\boldsymbol{u}_1^*, \ldots, \boldsymbol{u}_{n_s}^*, r_1, \ldots, r_{n_s}, F_1^*, \ldots, F_{n_p}^*, \boldsymbol{v}_1^*, \ldots, \boldsymbol{v}_{n_c}^*, v_1, \ldots, v_{n_c})$, such that $\boldsymbol{u}_i^* \in \mathbb{S}^2$ and $\boldsymbol{v}_k^* \in \mathbb{S}^2$ are ith and kth spoke direction and connection direction relative to their local frame with lengths $r_i \in \mathbb{R}^+$ and $v_k \in \mathbb{R}^+$ respectively, and $F_j^* \in SO(3)$ is the jth frame in its parent coordinate system.

Thus, by construction, the LP-ds-rep is invariant under the act of rigid transformation. To remove the scale, we define *LP-size* as the geometric mean of the vectors' lengths $\ell = \exp\left(\frac{1}{n_s + n_c}\left(\sum_{i=1}^{n_s} \ln(r_i) + \sum_{k=1}^{n_c} \ln(v_k)\right)\right)$. Assume $\rho_i = \frac{r_i}{\ell}$, and $\tau_k = \frac{v_k}{\ell}$. A scaled LP-ds-rep can be expressed by $s^{\text{LP}} = (\boldsymbol{u}_i^*, \rho_i, F_j^*, \boldsymbol{v}_k^*, \tau_k)_{i,j,k}$.

Result 1. The LP-size of a scaled LP-ds-rep is equal to one (see the proof in SUP).

Recall, for a GP-ds-rep, the *GP-size* is defined as the centroid size of the skeletal PDM. As we discussed in the introduction, the centroid is an extrinsic property. Thus, the centroid size might be a poor measure for the size of an object. The same discussion is also true for *EDM-size* where EDM-size is the geometric mean of all pairwise distances (Lele and Richtsmeier 2001, Ch.4.7.3). Intuitively, by opening or closing an arm, the arm's volume remains the same despite its centroid size or EDM-size, that is, the closed arm has smaller centroid size and EDM-size in comparison with the open arm (see Figure 1(a)).

As Section 2.1.1 discussed, the GP-ds-rep space is $\mathbf{S}^{\text{GP}} = \mathbb{S}^{3n_p - 1} \times (\mathbb{S}^2)^{n_s} \times \mathbb{R}_+^{n_s + 1}$. In LP-ds-rep, we do not have any pre-shape space. The GOPs of an LP-ds-rep are directions and lengths of spokes, directions and lengths of connections, LP-size, and frames. Thus, the space is $\mathbf{S}^{\text{LP}} = (\mathbb{S}^2)^{n_s + n_c} \times (SO(3))^{n_p} \times \mathbb{R}_+^{n_s + n_c + 1}$, where $(\mathbb{S}^2)^{n_s + n_c}$ is the space of vectors' directions, $(SO(3))^{n_p}$ is the space of the frames, and $\mathbb{R}_+^{n_s + n_c + 1}$ is the space of vectors' lengths plus LP-size. Further, we can represent an LP-ds-rep as $s^{\text{LP}} = (\boldsymbol{u}_i^*, \rho_i, \boldsymbol{q}_j^*, \boldsymbol{v}_k^*, \tau_k)_{i,j,k}$, where $\boldsymbol{q}_j^* \in \mathbb{S}^3$ is the unit quaternion representation of the frame F_j^* (Huynh 2009). Thus, we have $\mathbf{S}^{\text{LP}} = (\mathbb{S}^2)^{n_s + n_c} \times (\mathbb{S}^3)^{n_p} \times \mathbb{R}_+^{n_s + n_c + 1}$, where $(\mathbb{S}^3)^{n_p}$ is the space of the frames based on their unit quaternion representations.

2.2. Euclideanization and Mean Shape

Having a population of ds-reps, suitable methods to calculate means are required in order to perform hypothesis tests on mean differences. The corresponding method should incorporate all geometrical components of the model. Both shape spaces, the GP-ds-rep space, and the LP-ds-rep space are composed of several spheres and a real space. This section will first discuss an approach to analyze the spherical parts by *principal nested spheres* (PNS). Afterward, approaches to produce GP-ds-rep means and LP-ds-rep means are discussed.

2.2.1. PNS

PNS (Jung, Dryden, and Marron 2012) estimates the joint probability distribution of data on d-sphere $\mathbb{S}^d$ by a backward view, that is, in decreasing dimension. Starting with $\mathbb{S}^d$, PNS fits the best lower-dimensional subsphere in each dimension. A subsphere is called *great subsphere* if its radius is equal to one; otherwise, it is called *small subsphere*. To choose between the great or small subsphere, we use the Kurtosis test from (Kim, Schulz, and Jung 2020).

PNS is designed for spherical data (particularly for small sphere distributions) to capture the curviness of circular distributions as discussed by Kim et al. (2019). PNS is similar to PCA because PCA provides observations' coordinates called *residuals* as their distances from fitted (hyper)planes, while PNS residuals are the observations' geodesic distances from the fitted subspheres. For example, the PNS residuals on $\mathbb{S}^2$ consist of the geodesic distances between the observations and the fitted circle and the minimal arc length between projected data on the fitted circle to the PNS mean. Basically, PNS euclideanize the data by defining a mapping from $\mathbb{S}^d$ to $\mathbb{R}^d$. In many cases, the distribution of the PNS residuals is similar to the multivariate normal distribution (see an example in SUP).

Alternatively, a simpler but faster euclideanization is to map the data on the tangent space. We transform observations to the north pole $\boldsymbol{e} = (0, \ldots, 0, 1)^T \in \mathbb{S}^d$ by $R(\boldsymbol{\mu}_F, \boldsymbol{e})$, where $\boldsymbol{\mu}_F$ is the Fréchet mean. Then, we map the transformed data to the tangent space $T_{\boldsymbol{e}}(\mathbb{S}^d)$ by the Log map $\text{Log}_{\boldsymbol{e}}(\boldsymbol{v}) = \frac{\theta}{\sin\theta}(v_1, \ldots, v_d)^T \in \mathbb{R}^d$, where $\boldsymbol{v} = (v_1, \ldots, v_{d+1})^T \in \mathbb{S}^d$, and $\theta = \cos^{-1}(v_{d+1})$ (Jung, Dryden, and Marron 2012; Kim, Schulz, and Jung 2020). For concentrated von Mises-Fisher distribution, the distribution of projected data to the tangent space is close to the distribution of PNS residuals (see SUP).

2.2.2. Mean GP-ds-rep

A method to produce means and shape distributions of a population of GP-ds-reps is *composite PNS* (CPNS) introduced by Pizer et al. (2013). The method consists of two steps. First, the two spherical parts of the GP-ds-rep shape space $\mathbb{S}^{3n_p-1} \times (\mathbb{S}^2)^{n_s} \times \mathbb{R}_+^{n_s+1}$ are analyzed by PNS. Spokes' lengths and scaling factor can be mapped to $\mathbb{R}^{n_s+1}$ with the *log*. Afterward, all Euclideanized variables are concatenated in addition to some scaling factors that make all variables commensurate. The covariance structure of the resulting matrix is investigated by PCA. Consequently, the mean GP-ds-rep is defined as the origin of the CPNS space. This method depends on a proper pre-alignment and is computationally expensive because PNS has to fit sequential high dimensional sub-spheres to $\mathbb{S}^{3n_p-1}$.

2.2.3. Mean LP-ds-rep

To formalize the estimation of LP-ds-rep mean, first we define a metric for the product space $\mathbf{S}^{\text{LP}}$. Assume metric spaces $(\mathbb{R}^+, d_l)$, $(\mathbb{S}^2, d_g)$ and $(SO(3), d_R)$, where $d_l(x, y) = |\ln x - \ln y|$ is the Euclidean distance of log-scaled values, $d_g(\boldsymbol{x}, \boldsymbol{y}) = \cos^{-1}(\boldsymbol{y}^T\boldsymbol{x})$ is the geodesic distance on the unit sphere (Jung, Dryden, and Marron 2012), and $d_R(F_1, F_2) = \frac{1}{\sqrt{2}}\|\log(F_1^T F_2)\|_F$ is the Riemannian distance on $SO(3)$ where $\|.\|_F$ is the Frobenius norm (Moakher 2002). The distance between two scaled LP-ds-reps $s_1^{\text{LP}} = (\boldsymbol{u}_{1i}^*, \rho_{1i}, F_{1j}^*, \boldsymbol{v}_{1k}^*, \tau_{1k})_{i,j,k}$ and $s_2^{\text{LP}} = (\boldsymbol{u}_{2i}^*, \rho_{2i}, F_{2j}^*, \boldsymbol{v}_{2k}^*, \tau_{2k})_{i,j,k}$ is given by

$$d_s(s_1^{\text{LP}}, s_2^{\text{LP}}) = \left(\sum_{i=1}^{n_s} d_g^2(\boldsymbol{u}_{1i}^*, \boldsymbol{u}_{2i}^*) + \sum_{i=1}^{n_s} d_l^2(\rho_{1i}, \rho_{2i}) \right.$$
$$+ \sum_{j=1}^{n_p} d_R^2(F_{1j}^*, F_{2j}^*) + \sum_{k=1}^{n_c} d_g^2(\boldsymbol{v}_{1k}^*, \boldsymbol{v}_{2k}^*)$$
$$\left. + \sum_{k=1}^{n_c} d_l^2(\tau_{1k}, \tau_{2k}) \right)^{\frac{1}{2}}. \quad (2)$$

Remark 1. LP-ds-rep space $\mathbf{S}^{\text{LP}}$ is a metric space equipped by $d_s(.)$ (see the proof in SUP).

If $s_1^{\text{LP}}, \ldots, s_N^{\text{LP}}$ be a population of scaled LP-ds-reps then mean LP-ds-rep is

$$\bar{s}^{\text{LP}} = \text{argmin}_{s^{\text{LP}} \in \mathbf{S}^{\text{LP}}} \sum_{m=1}^{N} d_s^2(s^{\text{LP}}, s_m^{\text{LP}}). \quad (3)$$

Assume $\bar{s}^{\text{LP}} = (\bar{\boldsymbol{u}}_i^*, \bar{\rho}_i, \bar{F}_j^*, \bar{\boldsymbol{v}}_k^*, \bar{\tau}_k)_{i,j,k}$ and $\forall i, j, k$ let

$$\bar{\boldsymbol{u}}_i^* = \text{argmin}_{\boldsymbol{u} \in \mathbb{S}^2} \sum_{m=1}^{N} d_g^2(\boldsymbol{u}, \boldsymbol{u}_{im}),$$

$$\bar{\rho}_i = \text{argmin}_{\rho \in \mathbb{R}^+} \sum_{m=1}^{N} d_l^2(\rho, \rho_{im}),$$

$$\bar{F}_j^* = \text{argmin}_{F \in SO(3)} \sum_{m=1}^{N} d_R^2(F, F_{jm}^*),$$

$$\bar{\boldsymbol{v}}_k^* = \text{argmin}_{\boldsymbol{v} \in \mathbb{S}^2} \sum_{m=1}^{N} d_g^2(\boldsymbol{v}, \boldsymbol{v}_{km}^*),$$

$$\bar{\tau}_k = \text{argmin}_{\tau \in \mathbb{R}^+} \sum_{m=1}^{N} d_l^2(\tau, \tau_{km}). \quad (4)$$

By assuming the existence of unique solutions for optimization problems (4), $\bar{\boldsymbol{u}}_i^*$ and $\bar{\boldsymbol{v}}_k^*$ can be estimated as the Fréchet or PNS mean of $\{\boldsymbol{u}_{im}^*\}_{m=1}^N$ and $\{\boldsymbol{v}_{km}^*\}_{m=1}^N$, respectively. Obviously, $\bar{\rho}_i$ and $\bar{\tau}_k$ represent the geometric means of $\{\rho_{im}\}_{m=1}^N$ and $\{\tau_{km}\}_{m=1}^N$, respectively. Further, we can calculate the mean frame $\bar{F}_j^*$ of $\{F_{jm}^*\}_{m=1}^N$ as discussed by Moakher (2002).

Result 2. If $\bar{s}^{\text{LP}}$ be the mean of a population of scaled LP-ds-reps, then LP-size of $\bar{s}^{\text{LP}}$ is equal to one (see the proof in SUP).

2.3. Converting LP-ds-rep to GP-ds-rep

Sections 2.1.3 and 2.1.4 discuss how to obtain an LP-ds-rep from a GP-ds-rep. For several reasons, for example, for visualization, we may need to reverse the procedure. For GP-ds-rep visualization, it is sufficient to draw spokes individually. To visualize an LP-ds-rep, we convert it to a GP-ds-rep. We start from $\bar{I}$ as the s-centroid frame. Then, we reconstruct frames by finding the position and orientation of the frame's children based on $\bar{I}$. Afterward, we find the information of grandchildren frames based on their parents and so on.

Let frame F^* be in the coordinate system of its parent $F^{\dagger}$. To find F^* based on GCS, we rotate $F^{\dagger}$ by $R_2 R_1$ such that $R_2 R_1 F^{\dagger} = \bar{I}$. Then $[R_2 R_1]^{-1} F^*$ is the representation of F^* in GCS. Similarly, we find the direction of connections and spokes in GCS.

Finding the mean shape of a set of objects' boundaries without an alignment is almost impossible. But we can use LP-ds-reps to estimate the mean boundary without alignment. First, we calculate the mean LP-ds-rep. Then, we convert the mean LP-ds-rep to a GP-ds-rep. Finally, we generate the implied boundary from the GP-ds-rep as demonstrated in (Liu et al. 2021). Therefore, it is possible to approximate the mean boundary without alignment, which shows the power of LP-ds-reps.

2.4. Deformation

In statistical shape analysis generating random shapes is a matter of interest. Designing simulations based on GP-ds-reps is challenging as we usually need to identify a local frame to bend or twist the object locally. It turned out that LP-ds-reps support naturally skeletal deformations. We can stretch, shrink, bend, and twist the skeletal by manipulating the frames' orientations and vectors' lengths. Then, we convert the LP-ds-rep to a GP-ds-rep to generate the boundary. Consequently, we can add variation to a set of deformed LP-ds-reps' GOPs to simulate random ds-reps. Figure 7 shows a deformed hippocampus including bending and twisting. The deformation is based on the rotation of spinal frames.

3. Hypothesis Testing

For LP-ds-rep hypothesis testing, we consider frames as unit quaternions (i.e., $s^{\mathrm{LP}} = (\boldsymbol{u}_i^*, \rho_i, \boldsymbol{q}_j^*, \boldsymbol{v}_k^*, \tau_k)_{i,j,k}$). In this sense, euclideanization of the frames based on their unit quaternion representation is the same as other spherical data as we discussed in Section 2.2.

Let $A = \{s_{Am}\}_{m=1}^{N_1}$ and $B = \{s_{Bm}\}_{m=1}^{N_2}$ be two groups of either GP-ds-reps or LP-ds-reps of sizes N_1 and N_2. Let n_{GOP} be the total number of GOPs. To test GOPs' mean difference, we design n_{GOP} partial tests. Let $\bar{s}_A(n)$ and $\bar{s}_B(n)$ be the observed sample mean of the nth GOP from A and B respectively. The partial test is $H_{0n} : \bar{s}_A(n) = \bar{s}_B(n)$ versus $H_{1n} : \bar{s}_A(n) \neq \bar{s}_B(n)$. Note that for GP-ds-rep, LP-ds-rep, and EDM of the skeletal PDM, n_{GOP} is $(n_p + 2n_s + 1)$, $(2n_s + n_p + 2n_c + 1)$, and $(\frac{(n_p - 1)n_p}{2} + 1)$, respectively.

To test mean differences, we adapted a nonparametric permutation test with minimal assumptions similar to Styner's approach (Styner et al. 2006). For the univariate data, that is, vectors' lengths and shapes' sizes, the test statistic is t-statistic $T = \frac{\bar{x} - \bar{y}}{S_p \sqrt{\frac{1}{N_1} + \frac{1}{N_2}}}$ where S_p is the pooled standard deviation. For the multivariate data, that is, euclideanized directions and GP-ds-rep skeletal positions, the test statistic is Hotelling's T^2 metric $T^2 = (\bar{\boldsymbol{x}} - \bar{\boldsymbol{y}})^T \hat{\Sigma}^{-1} (\bar{\boldsymbol{x}} - \bar{\boldsymbol{y}})$, where $\hat{\Sigma}$ is an unbiased estimate of common covariance matrix (Martin and Maes 1979, ch.3). Given the pooled group $\{A, B\}$, the permutation method randomly partitions B times the pooled group into two paired groups of sizes N_1 and N_2 without replacement, where usually we consider $B \geq 10^4$. Afterward, it measures the test statistic between the paired groups. The empirical p-value for the nth GOP is $\eta_n = \frac{1 + \sum_{h=1}^{B} \chi_E(|T_{nh}| \geq T_{no})}{B+1}$, where T_{no} is the nth observed test statistics, T_{nh} is the hth permutation test statistic, and χ_E is the indicator function, that is, $\chi_E(\varphi) = 1$ if φ is true, otherwise $\chi_E(\varphi) = 0$. Note that if we have normally distributed data, it is reasonable to apply Hotelling's T^2 test (with normality assumption) instead of the permutation test as it is much faster.

In order to account for the problem of multiple hypothesis testing, one could use the method of Bonferroni (1936). Bonferroni's method tests each hypothesis at level $\alpha / n_{\mathrm{GOP}}$ and guarantees the probability of at least one Type I error $P(\nu \geq 1)$ be less than the significance level α. Since the method is highly conservative we prefer to use Benjamini and Hochberg (1995) (BH) method as a more moderate approach.

4. Evaluation

4.1. Data

To test our method, we study the hippocampal difference between early Parkinson's disease (PD) and CG at baseline. Data
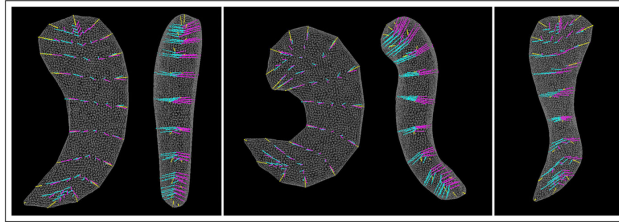

Figure 7. Skeletal deformation by LP-ds-rep. Left: A ds-rep with its implied boundary in two angles. Middle: Shape bending by spinal frame rotation about $\boldsymbol{n}$ and $\boldsymbol{b}^{\perp}$ axes. Right: Shape twisting by spinal frames rotation about $\boldsymbol{b}$ axis.

are provided by ParkWest (*http://parkvest.no*), in cooperation with Stavanger University Hospital (*https://helse-stavanger.no*). At the baseline, we have 182 magnetic resonance images for PD and 108 for CG with corresponding segmentation of hippocampi. As described in Section 2, GP-ds-reps are fitted to left hippocampi by SlicerSALT toolkit (*http://salt.slicer.org*) and reparameterize into LP-ds-reps. For the model fitting, we used GP-ds-reps with 122 spokes consisting of 51 up, 51 down, and 20 crest spokes. As up and down spokes share the same tail positions, we have in total 71 tail positions. The generated LP-ds-reps have 122 spokes, 71 local frames, and 70 connections. Before analyzing the ParkWest data, we first study our method based on simulations.

4.2. Simulation

For the simulation study, we select a LP-ds-rep close to the mean LP-ds-rep of CG as a template. Based on the template, we generate two groups of LP-ds-reps each of size 150 with different amount of tail bending, that is, bending in a local region. Such bending was observed, for example, in (Pizer et al. 2003) between schizophrenics and controls. Let $\mathcal{M}_d(\boldsymbol{\mu}, \kappa)$ denotes von Mises-Fisher distribution with mean $\boldsymbol{\mu}$ and concentration parameter κ on $\mathbb{S}^{d-1}$ (Dhillon and Sra 2003). For the special case $d = 2$ we assume the distribution in radian, that is, $\theta, \mu \in [0, 2\pi)$ if $\theta \sim \mathcal{M}_2(\mu, \kappa)$. Given a random rotation angle of bending $\theta \sim \mathcal{M}_2(\mu = 0, \kappa = 100)$ for the first group and $\theta \sim \mathcal{M}_2(\mu = \frac{-\pi}{15}, \kappa = 100)$ for the second group, we simulate the orientation of three spinal frames by successively rotating them about their $\boldsymbol{b}^\perp$-axis with $[R_2 R_1]^{-1} R(\boldsymbol{e}_3, (\cos\theta, 0, \sin\theta)^T) I$. This means the tails in the second group are successively bent on average 12° downward for three consecutive spinal frames. Chosen frames are the closest ones on the hippocampus tail to the s-centroid. Thus, in total, we have a slight downward bending about 36° at the hippocampus tail. Finally, by preserving

frame orthogonality, we add noise to all directions by $\mathcal{M}_3(\boldsymbol{\mu}, \kappa)$, where κ for frames' vectors, spokes, and connections is equal to 600, 250, and 5000, respectively. Further additional noise is added to vectors' lengths by the truncated normal distribution $\psi(\mu, \sigma, a > 0, b < \infty)$ where μ is the vector length of the template, and parameters σ, a, and b are heuristically chosen. As a result, we have two groups of random LP-ds-reps, which are approximately similar in most of their GOPs but only different in the orientation of three frames. Figure 8 illustrates twenty samples of each group. Note that LP-ds-reps are not aligned, but since we reconstruct them from the s-centroid frame, shapes have Bookstein's alignment (Dryden and Mardia 2016, Ch.2) because the s-centroid frames are perfectly aligned.

As depicted in Figure 8(Right), hypothesis test on LP-ds-rep from Section 3 correctly detects significant frame directions and label almost all other GOPs as statistically nonsignificant given a significance level $\alpha = 0.05$. On the contrary, as depicted in Figure 9, the test on GP-ds-reps indicates a large number of false positives, that is, almost all of the positions and directions are statistically significant. Also, from EDMA on the skeletal PDM we can see that about half of the distances are significant. This example confirms our observation from Figure 1 in Section 1, and highlights the fact that noninvariant GP-ds-rep analysis is biased and invariant EDMA could be misleading. The power of LP-ds-rep is further highlighted by additional simulation examples provided in SUP.

4.3. Real Data Analysis

The Parkinson dataset described in Section 4.1 was studied earlier by (Apostolova et al. 2012) based on radial distance analysis and parallel slicing and showed some regional atrophy. Since shape correspondence in noninvariant parallel slicing method is controversial, we attempt to reanalyze data by utilizing LP-ds-reps.
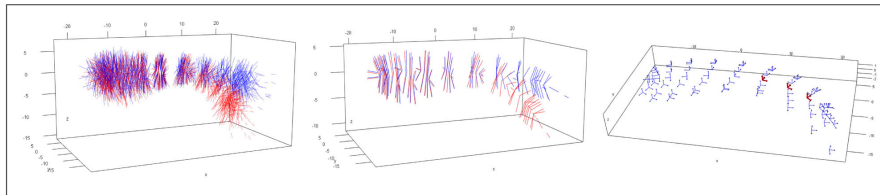

Figure 8. Simulation. Left: Two groups of simulated ds-reps. Middle: Overlaid mean LP-ds-reps. Right: Illustration of local frames. Bold frames are statistically significant.
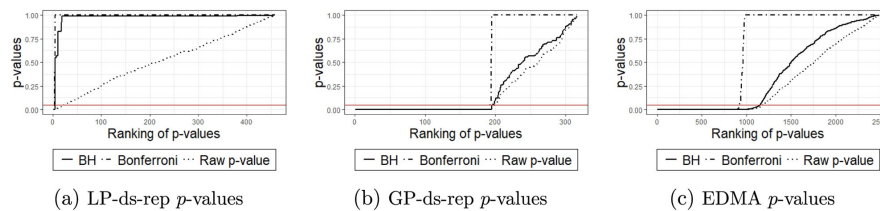

(a) LP-ds-rep *p*-values   (b) GP-ds-rep *p*-values   (c) EDMA *p*-values

Figure 9. Sorted raw and adjusted *p*-values. The horizontal line indicates significance level $\alpha = 0.05$.

668   M. TAHERI AND J. SCHULZ

Table 1. *T*-test on shape size.

	MeanCG	MeanPD	SDCG	SDPD	*p*-value
Object volume (mm^3)	3352.23	3271.44	563.39	616.68	0.26
LP-size	2.37	2.33	0.17	0.18	0.04
GP-size of spokes' tips	161.05	162.51	8.97	8.62	0.17
EDM-size of skeletal PDM	12.66	12.76	0.83	0.84	0.36

First let us compare the shape sizes from Table 1. The volume measurement confirms the LP-size is more compatible with the object volume because both, the mean object volume and the LP-size of CG, are greater than PD. In opposite the mean GP-size and EDM-size of CG are smaller than PD. Also, tests on shape size indicate significant difference in LP-size.

Figure 10 illustrates significant LP-ds-rep and GP-ds-rep GOPs before and after BH adjustment. In LP-ds-rep, all the spokes directions are insignificant. In contrast, about 40% of GP-ds-rep spokes' directions are significant. Also, in LP-ds-rep, there are a few significant connection and frame directions after the adjustment. Based on the LP-ds-rep analysis, it seems the main difference comes from connections' lengths on the spine. Figure 11 shows sorted *p*-values before and after adjustment of

the applied methods. Based on Bonferroni adjustment, PD and CG are similar because almost all adjusted *p*-values are greater than 0.05. Based on BH adjustment, all GOPs in EDMA are not significant but about 30% of them are significant before BH adjustment. The reason is the sensitivity of BH to the number of tests, that is, by increasing the number of tests, BH becomes conservative. In GP-ds-rep half of the GOPs are significant even after the BH adjustment. In contrast, LP-ds-rep shows a small portion of significant GOPs before and after the adjustment. In addition, we analyzed the shapes without scaling to show the sensitivity of GP-ds-rep to the scaling and the superiority of LP-ds-rep compared to GP-ds-rep and EDMA. Detailed results are available in SUP.

5. Conclusion

Generally, it is common to detect locational dissimilarity between two groups of objects based on the alignment. As discussed, noninvariant (i.e., alignment-dependent) methods such as GP-ds-rep analysis could be highly biased, and invariant methods based on extrinsic object properties like EDMA could be misleading. Thus, we propose an invariant shape representa-
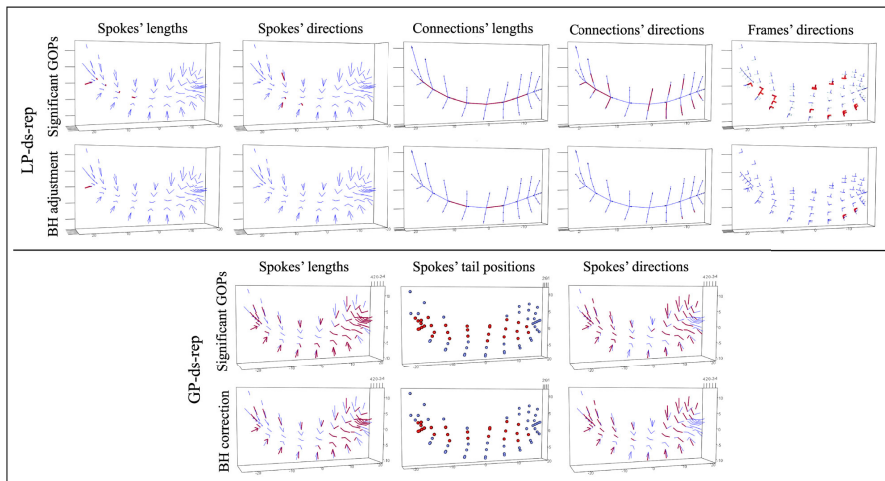
Figure 10. ds-rep significant GOPs. Bold indicate significant GOPs. FDR=0.05 for BH adjustment.

(a) LP-ds-rep *p*-values   (b) GP-ds-rep *p*-values   (c) EDM *p*-values
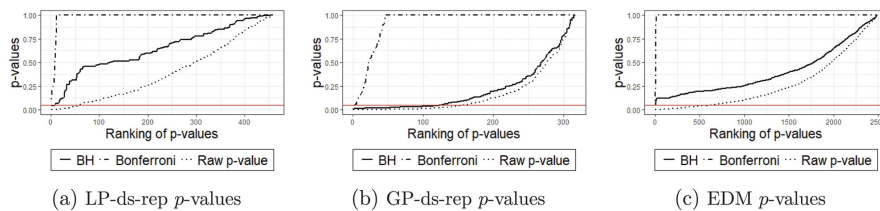
Figure 11. Test on real data. Sorted raw and adjusted *p*-values. The horizontal line indicates significance level 0.05.

tion called LP-ds-rep by putting a partial order on the skeletal positions of a GP-ds-rep and constructing local frames at each skeletal position. Such partial order exists on any tree structure, by considering the flow away from a chosen basepoint. Therefore, the proposed idea is not limited to ellipsoidal objects, neither to skeletal models, as long as a tree structure can be established for a shape model that ensures good correspondence between objects. Further, we compared LP-ds-rep analysis with GP-ds-rep analysis and EDMA to show the power and the advantages of LP-ds-reps. For comparison, we applied simulation and real data analysis. The simulation confirmed that even if two populations of ds-reps differ only in a small local region, the hypothesis tests based on GP-ds-reps and EDMs result in a large number of significant GOPs while the tests based on LP-ds-reps indeed detect the true underlying differences. We studied left hippocampi of PD versus CG for real data analysis. Although hypothesis tests on GP-ds-reps and EDMs indicated many significant GOPs, tests on LP-ds-reps showed only a few, which seems medically more reasonable. We concluded that PD and CG groups are very similar, but the main difference comes from the spine length.

Acknowledgments

Funding

Supplementary Materials

Supplementary: SUP materials referenced in this work are available as a pdf. (pdf)
R-code: In Supplementary.zip, simulation codes and files are placed. (zip)

ORCID

Mohsen Taheri ⬥ http://orcid.org/0000-0003-4044-8507
Jörn Schulz ⬥ http://orcid.org/0000-0002-6240-4794

References

Amaral, G. A., Dryden, I., and Wood, A. T. A. (2007), "Pivotal Bootstrap Methods for k-Sample Problems in Directional Statistics and Shape Analysis," *Journal of the American Statistical Association*, 102, 695–707. [664]

Apostolova, L., Alves, G., Hwang, K. S., Babakchanian, S., Bronnick, K. S., Larsen, J. P., Thompson, P. M., Chou, Y. Y., Tysnes, O. B., and Vefring, H. K. (2012), "Hippocampal and Ventricular Changes in Parkinson's Disease Mild Cognitive Impairment," *Neurobiology of Aging*, 33, 2113–2124. [667]

Benjamini, Y., and Hochberg, Y. (1995), "Controlling the False Discovery Rate: A Practical and Powerful Approach to Multiple Testing," *Journal of the Royal Statistical Society*, Series B, 57, 289–300. [666]

Berger, J. (1985), *Statistical Decision Theory and Bayesian Analysis.* Springer Series in Statistics, Berlin: Springer. *https://books.google.no/books?id=oY_x7dE15_AC.* [658]

Blum, H. (1967), "A Transformation for Extracting New Descriptors of Shape," Symp. on *Models for the Perception of Speech and Visual Form.* Cambridge, MA: MIT Press. [663]

Bonferroni, C. (1936), "Teoria Statistica delle Classi e Calcolo delle Probabilita," *Pubblicazioni del R Istituto Superiore di Scienze Economiche e Commericiali di Firenze*, 8, 3–62. [666]

Cartan, E. (1937), *La théorie des groupes finis et continus et la géométrie différentielle : traitées par la méthode du repère mobile / leçons professées la Sorbonne par Elie Cartan,…; rédigées par Jean Leray,…Cahiers scientifiques*, Paris: Gauthier-Villars. [661]

Damon, J. (2008), "Swept Regions and Surfaces: Modeling and Volumetric Properties," *Theoretical Computer Science*, 392, 66–91. [662]

Damon, J., and Marron, J. (2014), "Backwards Principal Component Analysis and Principal Nested Relations," *Journal of Mathematical Imaging and Vision*, 50, 107–114. [661]

Dhillon, I. S., and Sra, S. (2003), "Modeling Data Using Directional Distributions," Technical Report, Citeseer. [667]

Dryden, I., and Mardia, K. (2016), *Statistical Shape Analysis: With Applications in R.* (Vol. 995). Chichester: John Wiley & Sons. [659,667]

Fletcher, P. T., Lu, C., and Joshi, S. (2003), "Statistics of Shape via Principal Geodesic Analysis on Lie Groups," In Proceedings, 2003 IEEE Computer Society Conference on Computer Vision and Pattern Recognition, 2003. IEEE, vol 1, pp. I–I. [661]

Fletcher, P. T., Lu, C., Pizer, S. M., and Joshi, S. (2004), "Principal Geodesic Analysis for the Study of Nonlinear Statistics of Shape," *IEEE Transactions on Medical Imaging*, 23, 995–1005. [660]

Gamble, J., and Heo, G. (2010), "Exploring Uses of Persistent Homology for Statistical Analysis of Landmark-Based Shape Data," *Journal of Multivariate Analysis*, 101, 2184–2199. [659]

Huynh, D. Q. (2009), "Metrics for 3D Rotations: Comparison and Analysis," *Journal of Mathematical Imaging and Vision*, 35, 155–164. [664]

Jermyn, I. H., Kurtek, S., Laga, H., Srivastava, A. (2017), "Elastic Shape Analysis of Three-Dimensional Objects," *Synthesis Lectures on Computer Vision*, 12, 1–185. [659,660,662]

Jung, S., Dryden, I. L., and Marron, J. (2012), "Analysis of Principal Nested Spheres," *Biometrika*, 99, 551–568. [665]

Kendall, D. G. (1977), "The Diffusion of Shape," *Advances in Applied Probability*, 9, 428–430. [658]

Kim, B., Huckemann, S., Schulz, J., and Jung, S. (2019), "Small-Sphere Distributions for Directional Data with Application to Medical Imaging," *Scandinavian Journal of Statistics*, 46, 1047–1071. [665]

Kim, B., Schulz, J., and Jung, S. (2020), "Kurtosis Test of Modality for Rotationally Symmetric Distributions on Hyperspheres," *Journal of Multivariate Analysis*, 178, 104603. [665]

Laga, H., Guo, Y., Tabia, H., Fisher, R., and Bennamoun, M. (2018), *3D Shape Analysis: Fundamentals, Theory, and Applications.* Hoboken, NJ: Wiley. *https://books.google.no/books?id=ds16DwAAQBAJ.* [658,659]

Lele, S. R., and Richtsmeier, J. T. (1991), "Euclidean Distance Matrix Analysis: A Coordinate-Free Approach for Comparing Biological Shapes Using Landmark Data," *American Journal of Physical Anthropology*, 86, 415–427. [659]

——— (2001), *An Invariant Approach to Statistical Analysis of Shapes.* Boca Raton, FL: Chapman and Hall/CRC. [658,659,664]

Liu, Z., Hong, J., Vicory, J., Damon, J. N., and Pizer, S. M. (2021), "Fitting Unbranching Skeletal Structures to Objects," *Medical Image Analysis*, 70, 102020. [661,662,664,666]

Martin, N., and H. Maes. (1979). *Multivariate analysis.* London, UK: Academic Press. [666]

Moakher, M. (2002), "Means and Averaging in the Group of Rotations," *SIAM Journal on Matrix Analysis and Applications*, 24, 1–16. [665]

Pizer, S. M., Fritsch, D. S., Yushkevich, P. A., Johnson, V. E., and Chaney, E. L. (1999), "Segmentation, Registration, and Measurement of Shape Variation via Image Object Shape," *IEEE Transactions on Medical Imaging*, 18, 851–865. [660,662]

Pizer, S. M., Fletcher, P. T., Thall, A., Styner, M., Gerig, G., and Joshi, S. (2003), "Object Models in Multiscale Intrinsic Coordinates via m-Reps," *Image and Vision Computing*, 21, 5–15. [667]

Pizer, S. M., Jung, S., Goswami, D., Vicory, J., Zhao, X., Chaudhuri, R., Damon, J. N., Huckemann, S., and Marron, J. (2013), "Nested Sphere Statistics of Skeletal Models," in *Innovations for Shape Analysis*, Berlin, Heidelberg: Springer, pp. 93–115. [658,659,660,661,662,665]

Rustamov, R. M., Lipman, Y., and Funkhouser, T. (2009), "Interior Distance Using Barycentric Coordinates," in *Computer Graphics Forum*, Oxford, UK: Blackwell Publishing Ltd, Vol. 28, pp. 1279–1288. [659]

Schulz, J. (2013), "Statistical Analysis of Medical Shapes and Directional Data," PhD thesis, UiT Norges arktiske universitet. [659]

Siddiqi, K., and Pizer, S. (2008), *Medial Representations: Mathematics, Algorithms and Applications. Computational Imaging and Vision*, Dordrecht, Netherlands: Springer Netherlands [660,662]

Sorkine, O. (2006), "Differential Representations for Mesh Processing," in *Computer Graphics Forum*, Oxford, UK: Blackwell Publishing Ltd, vol. 25, pp. 789–807. [662]

Srivastava, A. and Klassen, E. (2016), *Functional and Shape Data Analysis*. Springer. Series in Statistics, New York: Springer, *https://books.google.no/books?id=0cMwDQAAQBAJ*. [659,661]

Styner, M., Oguz, I., Xu, S., Brechbühler, C., Pantazis, D., Levitt, J. J., Shenton, M. E., and Gerig, G. (2006), "Framework for the Statistical Shape Analysis of Brain Structures Using spharm-pdm." The Insight Journal, 242–250. [659,666]

Tabia, H., and Laga, H. (2015), "Covariance-Based Descriptors for Efficient 3D Shape Matching, Retrieval, and Classification," *IEEE Transactions on Multimedia*, 17, 1591–1603. [658]

Turner, K., Mukherjee, S., and Boyer, D. M. (2014), "Persistent Homology Transform for Modeling Shapes and Surfaces," *Information and Inference: A Journal of the IMA*, 3, 310–344. [659]

Van Kaick, O., Zhang, H., Hamarneh, G., and Cohen-Or, D. (2011), "A Survey on Shape Correspondence," in *Computer Graphics Forum*, Oxford, UK: Blackwell Publishing Ltd, vol. 30, pp. 1681–1707. [662]

Supplementary materials of "Statistical analysis of locally parameterized shapes"

Mohsen Taheri   and   Jörn Schulz

Department of Mathematics & Physics, University of Stavanger

July 29, 2022

1   Proofs

Recall: The geometric mean of $x_1, ..., x_n \in \mathbb{R}^+$ is $\exp(\frac{1}{n}\sum_{i=1}^n \ln x_i) = (\prod_{i=1}^n x_i)^{\frac{1}{n}}$.

Proof of Result 1. Let ℓ be the LP-size of an LP-ds-rep. Thus the LP-size of the LP-ds-rep after scaling is given by,

$$\left(\prod_{i=1}^{n_s} \frac{r_i}{\ell} \cdot \prod_{k=1}^{n_c} \frac{v_k}{\ell}\right)^{\frac{1}{n_s+n_c}} = \left(\frac{\prod_{i=1}^{n_s} r_i \cdot \prod_{k=1}^{n_c} v_k}{\ell^{(n_s+n_c)}}\right)^{\frac{1}{n_s+n_c}} = \frac{(\prod_{i=1}^{n_s} r_i \cdot \prod_{k=1}^{n_c} v_k)^{\frac{1}{n_s+n_c}}}{\ell} = \frac{\ell}{\ell} = 1$$

$\square$

Proof of Remark 1. We know that if $(O_1, d_1), (O_2, d_2), ..., (O_n, d_n)$ are finite number of metric spaces then $(\sum_{i=1}^n d_i^2(x_i, y_i))^{\frac{1}{2}}$ is a metric for the product space $O_1 \times O_2 \times ... \times O_n$ where $x_i, y_i \in O_i$, and $i = 1, ..., n$ (O'Searcoid, 2006, Section 1.6.1; Deza and Deza, 2016, Section 4.2). Since the LP-ds-rep space $\mathbf{S}^{\mathrm{LP}} = (\mathbb{S}^2)^{n_s+n_c} \times (SO(3))^{n_p} \times \mathbb{R}_+^{n_s+n_c+1}$ is a product of metric spaces (i.e., $(\mathbb{S}^2, d_g)$, $(\mathbb{R}_+, d_l)$ and $(SO(3), d_R)$), the introduced distance function $d_s : \mathbf{S}^{\mathrm{LP}} \times \mathbf{S}^{\mathrm{LP}} \to \mathbb{R}^+$ is a metric for $\mathbf{S}^{\mathrm{LP}}$. $\square$

Proof of Result 2. Let $s_1^{\mathrm{LP}}, ..., s_N^{\mathrm{LP}}$ be a population of scaled LP-ds-reps. Then assume $\rho_{m1}, ..., \rho_{mn_s}$ and $\tau_{m1}, ..., \tau_{mn_c}$ be the spokes' lengths and connections' lengths of the mth scaled LP-ds-rep s_m^{LP}, respectively. Also, let $\bar{\rho}_1, ..., \bar{\rho}_{n_s}$ and $\bar{\tau}_1, ..., \bar{\tau}_{n_c}$ be the spokes' lengths

1

and connections' lengths of the mean LP-ds-rep $\bar{s}^{LP}$, respectively. Based on Result 1, the LP-size of s_m^{LP} is equal to one. Thus the LP-size of $\bar{s}^{LP}$ is given by,

$$
\left(\prod_{i=1}^{n_s} \bar{\rho}_i \cdot \prod_{k=1}^{n_c} \bar{\tau}_k \right)^{\frac{1}{n_s+n_c}} =
$$

$$
\left(\left(\left(\prod_{m=1}^{N} \rho_{m1} \right)^{\frac{1}{N}} \cdot \ldots \cdot \left(\prod_{m=1}^{N} \rho_{mn_s} \right)^{\frac{1}{N}} \cdot \left(\prod_{m=1}^{N} \tau_{m1} \right)^{\frac{1}{N}} \cdot \ldots \cdot \left(\prod_{m=1}^{N} \tau_{mn_c} \right)^{\frac{1}{N}} \right)^{\frac{1}{n_s+n_c}} =
$$

$$
\left(\left(\prod_{m=1}^{N} \rho_{m1} \cdot \ldots \cdot \prod_{m=1}^{N} \rho_{mn_s} \cdot \prod_{m=1}^{N} \tau_{m1} \cdot \ldots \cdot \prod_{m=1}^{N} \tau_{mn_c} \right)^{\frac{1}{n_s+n_c}} \right)^{\frac{1}{N}} =
$$

$$
\left(\underbrace{\left(\prod_{i=1}^{n_s} \rho_{1i} \cdot \prod_{k=1}^{n_c} \tau_{1k} \right)^{\frac{1}{n_s+n_c}}}_{=1} \cdot \ldots \cdot \underbrace{\left(\prod_{i=1}^{n_s} \rho_{Ni} \cdot \prod_{k=1}^{n_c} \tau_{Nk} \right)^{\frac{1}{n_s+n_c}}}_{=1} \right)^{\frac{1}{N}} = 1
$$

$\square$

2 Examples

2.1 EDMA example

Figure 1a illustrates the pairwise distances of EDMA for the open and closed arm example (see section 1 in the main manuscript). According to Figure 1b, EDMA for the open and closed arm example shows that about half of the pairwise distances of the two groups are significant. Based on landmark deletion approach (Lele and Richtsmeier, 2001, Ch.4.10), the EDMs of both groups become similar by removing the upper arm (or forearm) points. Therefore, we can interpret that the upper arm (or forearm) points are significantly different. Although this interpretation makes sense, on the one hand, we cannot state which part (i.e., upper arm or the forearm) is non-significant, and on the other hand, it is not possible to explain the type of dissimilarity.

2

(a) PDMs' distances

(b) EDM *p*-values
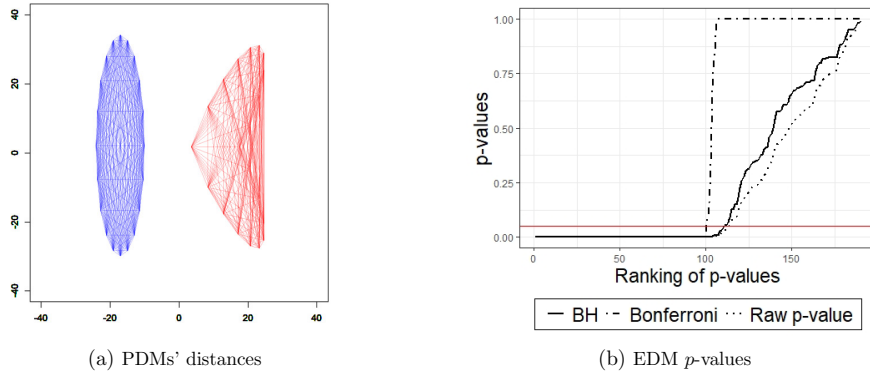
Figure 1: EDMA. (a) Visualization of pairwise distances between boundary points. (b) Raw and adjusted
p-values of the distances by BH and Bonferroni.

2.2 PNS example

Figure 2 illustrates a fitted circle to a cluster of 1000 observations on $\mathbb{S}^2$, and the PNS resid-
uals. Random points are generated from small sphere distribution $X \sim f_{S2}(\mu_0, \mu_1, \kappa_0, \kappa_1)$
(Kim et al., 2019) where $\mu_0 = (0, 0, 1)^T$, $\mu_1 = (\cos\frac{\pi}{3}, 0, \sin\frac{\pi}{3})^T$, $\kappa_0 = 500$, and $\kappa_1 = 2$.
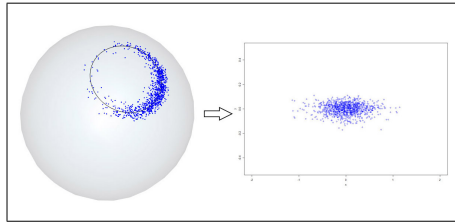
Figure 2: PNS euclideanization. Left: Small circle distribution and the fitted circle on $\mathbb{S}^2$. Right:
Euclideanizated data.

3

3 LP-ds-rep

3.1 Outline

Figure 3 shows LP-ds-rep hypothesis testing of two groups of 3D-ellipsoidal objects as the outline of the main manuscript.
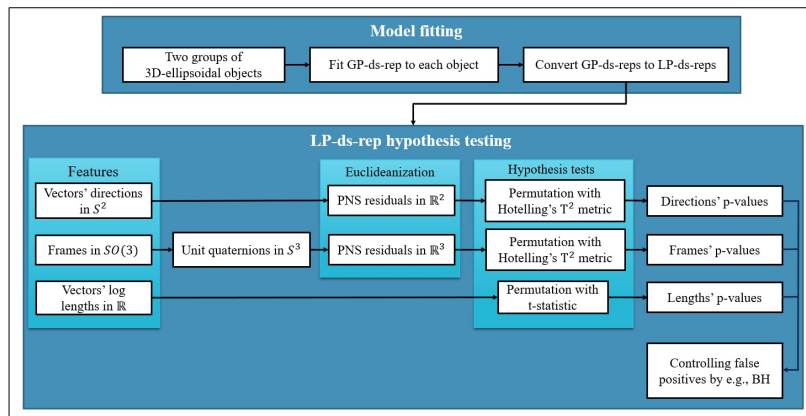
Figure 3: Outline of LP-ds-rep hypothesis testing for two groups of 3D-ellipsoidal objects.

3.2 Simulation

In the main manuscript, we explained how to simulate data with LP-ds-rep. This section simulates ds-reps in various ways to show the superiority of LP-ds-rep analysis over GP-ds-rep analysis. In Section 3.2.1 analogous to the main article, we discuss simulation and results based on spinal frames' orientations but with different parameters. In Section 3.2.2 we explain the obtained results from a simulation on vectors' lengths.

3.2.1 Simulation based on frame orientation

In this section, we change the orientation of the same three spinal frames as selected in the main paper. But we choose various bending rotation angles and different noise parameters. Note that the orientation of only three spinal frames are significantly different. We simulate

4

	# significant GOPs						# significant GOPs after BH					
	LP-ds-rep		GP-ds-rep		EDMA		LP-ds-rep		GP-ds-rep		EDMA	
	Mean	SD	Mean	SD	Mean	SD	Mean	SD	Mean	SD	Mean	SD
$\theta = \frac{-\pi}{12}$, $\kappa_1 = 100$, $\kappa_2 = 600$, $\kappa_3 = 250$	25.9	3.6	238.1	11.69	1606.4	153.2	3.3	0.67	232.6	12.8	1494.7	180.3
$\theta = \frac{-\pi}{12}$, $\kappa_1 = 10$, $\kappa_2 = 60$, $\kappa_3 = 25$	24.9	5.3	240.2	9.4	1609.2	100.7	3.3	0.4	234.6	10.1	1500.1	122.1
$\theta = \frac{-\pi}{24}$, $\kappa_1 = 100$, $\kappa_2 = 600$, $\kappa_3 = 250$	25.9	6.4	176.5	11.1	736.2	187.4	2.1	1.1	163.8	13.3	473.4	219.68
$\theta = \frac{-\pi}{24}$, $\kappa_1 = 10$, $\kappa_2 = 60$, $\kappa_3 = 25$	23.2	5.2	35.4	22.8	150.1	142.3	0.1	0.3	0.7	1.8	8.3	37.1
$\theta = \frac{-\pi}{48}$, $\kappa_1 = 100$, $\kappa_2 = 600$, $\kappa_3 = 250$	24.0	5.5	94.6	34.6	293.5	177.6	0.1	0.3	43.2	41.9	22.8	88.6
$\theta = \frac{-\pi}{48}$, $\kappa_1 = 10$, $\kappa_2 = 60$, $\kappa_3 = 25$	23.2	3.0	21.9	20.2	161.5	211.3	0.1	0.2	0.9	4.0	24.6	110.2

Table 1: Number of significant GOPs obtained from 50 simulations. Parameter θ is the rotation angle of the three spinal frames, while κ_1, κ_2, and κ_3 are the concentration factor of noise for θ, frames' vectors, and spokes, respectively.

two groups of LP-ds-rep of sizes 100 for 50 times. Then we estimate the average and standard deviation of the number of significant GOPs of three methods (i.e., LP-ds-rep, GP-ds-rep, and spokes' tails EDMA) before and after p-value adjustment. For the simulation we choose rotation angle θ as 12°, 6°, and 3° downward about $\boldsymbol{b}^{\perp}$-axis. Further, we add noise to directional data by von Mises-Fisher distribution $\mathcal{M}_3(\boldsymbol{\mu}, \kappa)$. Table 1 summarizes the results where κ_1, κ_2, and κ_3 are the concentration factor of noise for the rotation angle, frames' vectors, and spokes, respectively. Obviously, by reducing the bending angle or increasing the noise variations, we obtain less significant GOPs in all three methods. Overall, LP-ds-rep analysis is more robust against noise and thus superior because of the lower number of false positives. Theoretically, by considering significance level $\alpha = 0.05$, we expect to see n_{GOP}/α false positives by chance where n_{GOP} is the number of GOPs. This fact is observable in the number of LP-ds-rep significant GOPs before the adjustment. Note that in this study, n_{GOP} is 456, 316, and 2485 for LP-ds-rep, GP-d-rep, and EDMA, respectively.

3.2.2 Simulation based on vector length

In this section, we consider elongation simulation. To show the power of LP-ds-rep, we slightly increased the length of only one connection. The chosen connection is between the s-centroid frame and the children towards the hippocampus tail. We simulated 100

5

ds-reps for two groups as discussed in Section 4.2 of the main manuscript. In one of the groups, the length of the mentioned connection is approximately in average one unit larger than the other group. Again as we can see in Figure 5b almost half of the GP-ds-rep GOPs are statistically significant while LP-ds-rep according to Figure 5a, truly detects the only difference as depicted by the bold solid line in Figure 4. Interestingly, as depicted in Figure 5c, this slight change makes most of the pairwise distances significant in EDMA, showing how EDMA is misleading when dealing with elongation.
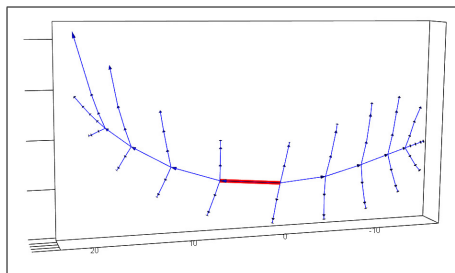
Figure 4: Significant connection length based on LP-ds-rep analysis.

(a) LP-ds-rep p-values

(b) GP-ds-rep p-values

(c) EDMA p-values

Figure 5: Simulations' p-values.

3.3   Real data analysis

In this section, we analyze the left hippocampi of PD vs. CG. First, we compare LP-ds-rep analysis based on PNS vs. LP-ds-rep analysis based on tangent PCA. Then we analyze PD vs. CG by LP-ds-rep, GP-ds-rep, and EDMA without scaling. As described in the main article, the data are provided by ParkWest 2021 in cooperation with Helse Stavanger

6

2021. Model fitting is implemented in SlicerSalt platform (Vicory et al., 2018) based on (Liu et al., 2021).

3.3.1 LP-ds-rep analysis by PNS & Tangent PCA

We compared LP-ds-rep analysis based on PNS and tangent PCA. As depicted in Figure 6, the result of both approaches is very similar. The reason is that we have concentrated von Mises-Fisher distributions for the spherical data (i.e., spokes' directions, connections' directions, and frames based on their unit quaternion representations). Hence, as we mentioned in the main manuscript, the distributions of the projected data to the tangent space is close to the distributions as PNS residuals.

(a) LP-ds-rep *p*-values based on PNS. (b) LP-ds-rep *p*-values based on tangent PCA.
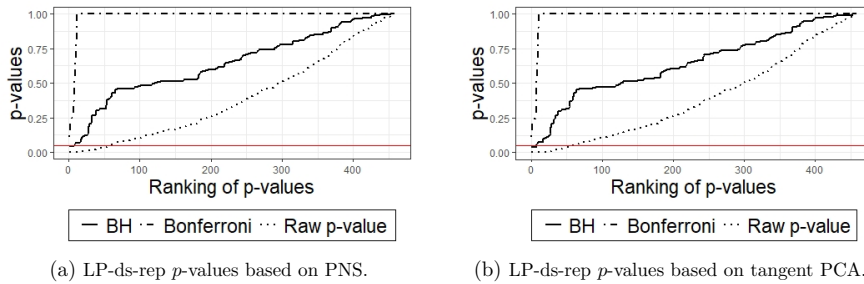
Figure 6: Sorted *p*-values of PNS vs. Tangent PCA.

3.3.2 Analysis without scaling
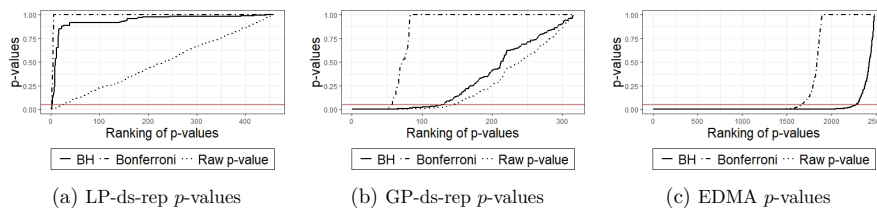
In this section we analyze left hippocampi of PD vs. CG without scaling.

Figure 7 depicts the distribution of spokes' tips and tails of PD GP-ds-reps and CG GP-ds-reps after GPA alignment. Figure 8a and Figure 8b show the overlaid mean LP-ds-reps and mean GP-ds-reps of PD and CG. Figure 10 and Figure 11 show the result of hypothesis testing on LP-ds-rep and GP-ds-rep of left hippocampi of PD vs. CG without scaling.

The general belief is scaling makes shapes more similar. But Figure 9 expresses the percentage of significant GP-ds-rep GOPs increases dramatically after the scaling (from

7
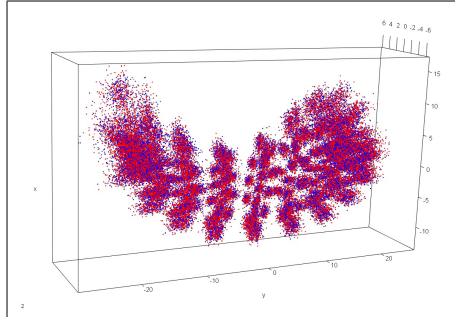
Figure 7: Distribution of spokes' tips and tails of GP-ds-reps after GPA alignment.

(a) Mean LP-ds-rep
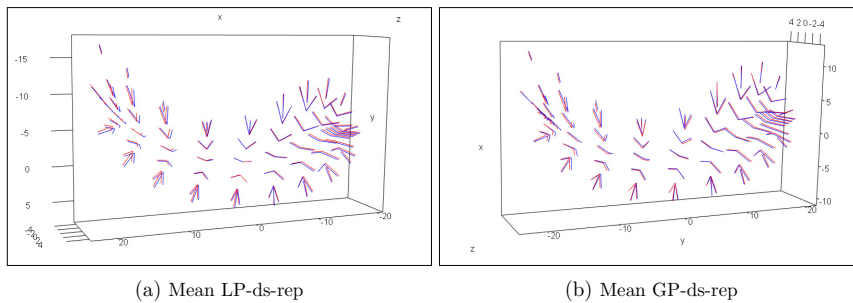
(b) Mean GP-ds-rep

Figure 8: Mean shape. (a) Mean LP-ds-reps are overlaid by reconstruction based on s-centroid frame. (b) Mean GP-ds-reps are overlaid by GPA alignment.

38% to 50%). In other words, scaling increases the number of raw p-values less than the level of significance $\alpha = 0.05$ and consequently increases the number of BH adjusted p-values less than FDR=0.05. A possible explanation is that GPA tries to make shapes as close as possible by reducing GOPs' variation. By removing the scale, GPA reduces the variation even more. Hotelling's T^2 metric is proportional to the inverse common covariance matrix. So by reducing the variation, the test statistic increases, and consequently, the p-value decreases. On the contrary, the LP-ds-rep and EDMA are not sensitive to scaling as they are invariant. Again, we conclude the GP-ds-rep analysis is biased

Since the mean shapes in both parameterizations are very similar, we conclude that LP-ds-rep is superior because we see less significant GOPs based on raw p-values in comparison with GP-ds-rep and EDMA.

8
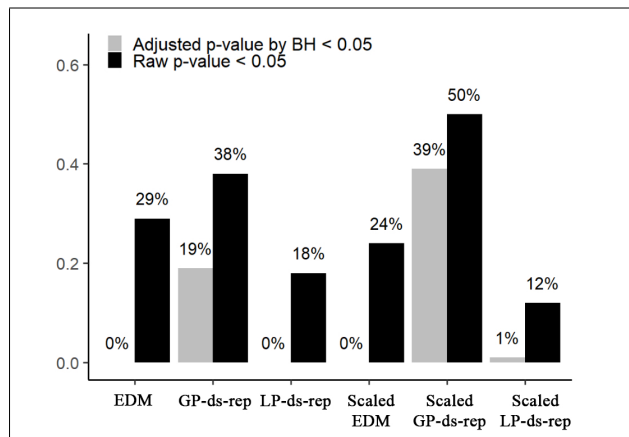
Figure 9: Scaling effect.

4 Conclusion

Simulation on bending and elongation confirms that noninvariant method like GP-ds-rep analysis could be highly biased and invariant methods based on extrinsic GOPs like EDMA can be missleading. Additional LP-ds-rep analysis on real data without scaling shows that CG and early PD's left hippocampi are similar. Since the mean shapes are very similar, we consider most of the obtained significant p-values from GP-ds-rep as false positives. Also, we see more significant p-values in EDMA by pairwise construction, making it more difficult to detect location and the type of deformation.

References

Deza M, Deza E (2016) Encyclopedia of Distances. Springer Berlin Heidelberg, URL https://books.google.no/books?id=KQHdDAAAQBAJ

Helse Stavanger (2021) Stavanger university hospital. https://helse-stavanger.no/

Kim B, Huckemann S, Schulz J, Jung S (2019) Small-sphere distributions for directional

9

data with application to medical imaging. Scandinavian Journal of Statistics 46(4):1047–1071

Lele SR, Richtsmeier JT (2001) An invariant approach to statistical analysis of shapes. Chapman and Hall/CRC

Liu Z, Hong J, Vicory J, Damon JN, Pizer SM (2021) Fitting unbranching skeletal structures to objects. Medical Image Analysis p 102020

O'Searcoid M (2006) Metric Spaces. Springer Undergraduate Mathematics Series, Springer London, URL https://books.google.no/books?id=aP37I4QWFRcC

ParkWest (2021) Parkwest study. http://www.parkvest.no/

Vicory J, Pascal L, Hernandez P, Fishbaugh J, Prieto J, Mostapha M, Huang C, Shah H, Hong J, Liu Z, et al. (2018) Slicersalt: Shape analysis toolbox. In: International Workshop on Shape in Medical Imaging, Springer, pp 65–72, URL http://salt.slicer.org/

10
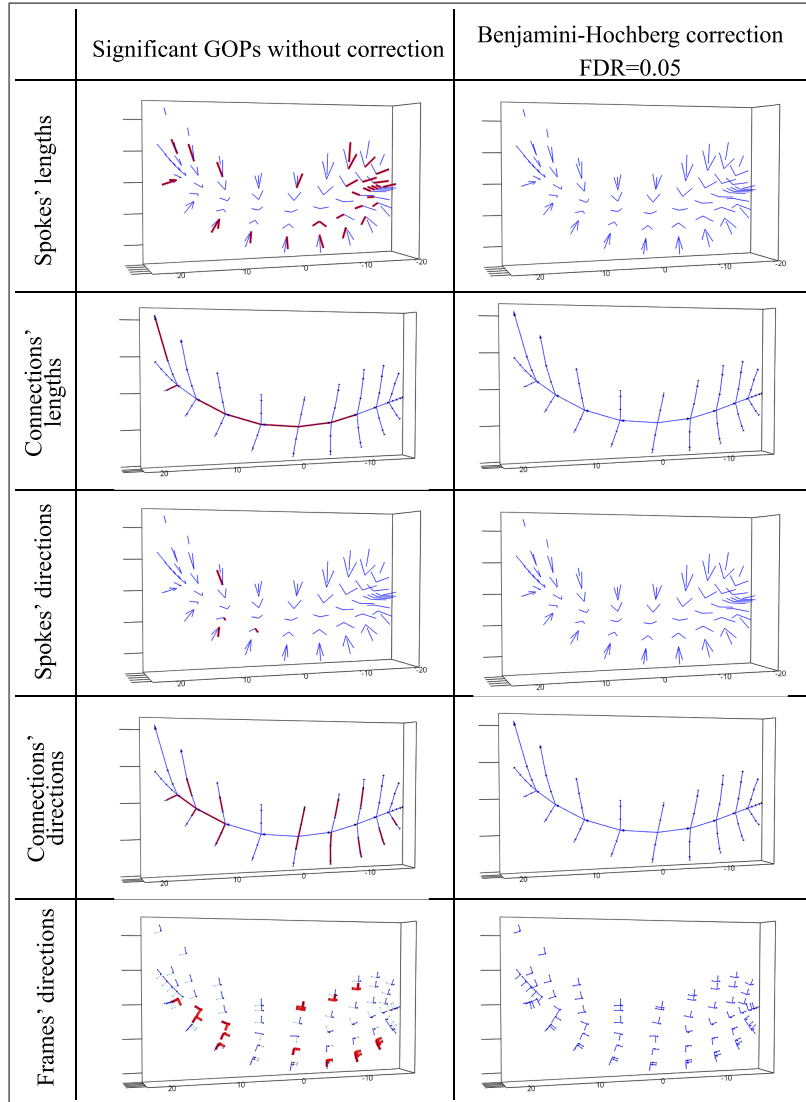
Figure 10: Test on LP-ds-rep. Bold indicate significant GOPs. The left and right columns illustrate significant GOPs before and after BH adjustment with FDR=0.05, respectively.

11
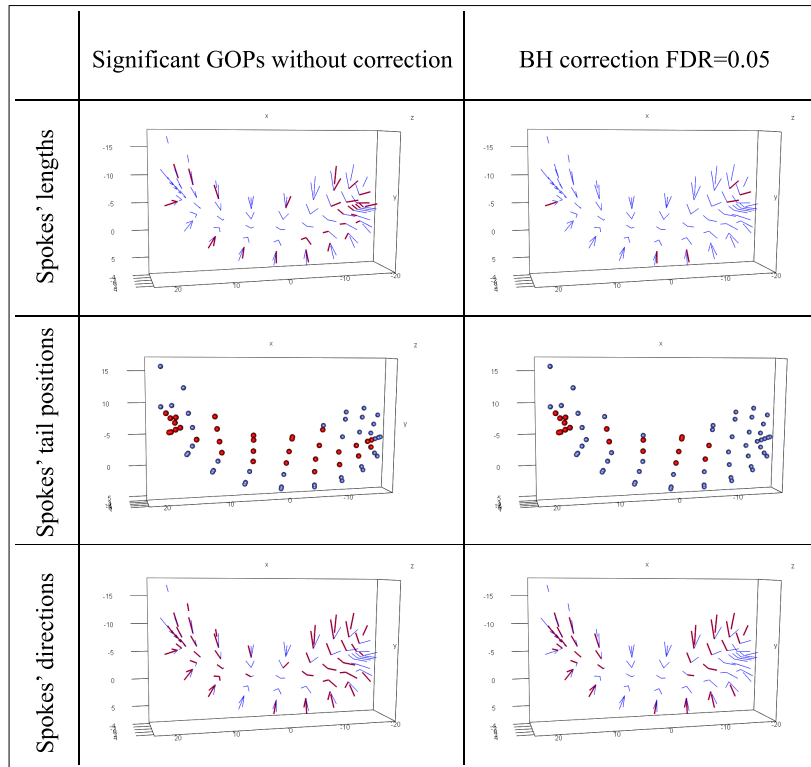
Figure 11: Test on GP-ds-rep. Red indicates significant GOPs. The left and right columns illustrate significant GOPs before and after BH adjustment with FDR=0.05, respectively.

12

Paper II

Fitting the Discrete Swept Skeletal Representation to Slabular Objects

Fitting the Discrete Swept Skeletal Representation to Slabular Objects

Mohsen Taheri[1*], Stephen M. Pizer[2] and Jörn Schulz[1]

[1*]Department of Mathematics and Physics, University of Stavanger, Norway.
[2]Department of Computer Science, University of North Carolina at Chapel Hill, USA.

*Corresponding author(s). E-mail(s):
mohsen.taherishalmani@uis.no;
Contributing authors: pizer@cs.unc.edu; jorn.schulz@uis.no;

Abstract

Statistical shape analysis of slabular objects like groups of hippocampi is highly useful for medical researchers as it can be useful for diagnoses and understanding diseases. This work proposes a novel object representation based on locally parameterized discrete swept skeletal structures. Further, model fitting and analysis of such representations are discussed. The model fitting procedure is based on boundary division and surface flattening. The quality of the model fitting is evaluated based on the symmetry and tidiness of the skeletal structure as well as the volume of the implied boundary. The power of the method is demonstrated by visual inspection and statistical analysis of a synthetic and an actual data set in comparison with an available skeletal representation.

Keywords: Discrete skeletal representation, Medial axis, Medical image analysis, Statistical shape analysis, Swept skeletal structure

1 Introduction

Statistical shape analysis of *slabular objects* (SlOs) (Pizer et al., 2022), such as the hippocampus and caudate nucleus, is highly useful for medical researchers

2   *Fitting the Discrete Swept Skeletal Representation to Slabular Objects*

and clinicians. Such analysis offers valuable insights into detecting dissimilarities between two sets of brain objects, for instance, by comparing the hippocampi of patients with neurodegenerative disorders versus a healthy group (Styner et al., 2006; Apostolova et al., 2012; Schulz, 2013). The main goal is to help physicians diagnose, predict, or understand disorders more accurately and to start treatment at early stages.

The primary need for statistical shape analysis is to establish correspondences among the objects in a population based on their geometric properties (Laga et al., 2019). Thus, the target objective of this work is a shape representation that supports statistical analysis, such as hypothesis testing and classification. Our representation is designed to achieve correspondence for SlOs by focusing on dividing the object through a sweep of slicing planes that correspond accordingly.

Analogous to a *generalized cylinder* (GC)[1], an SlO is a swept region with a center curve called a *spine* and a smooth sequence of affine slicing planes along the spine that do not cross within the object. The *skeleton*[2] of an SlO called the *skeletal sheet* is a smooth 2-dimensional topological disk (Damon, 2008; Pizer et al., 2022; Taheri and Schulz, 2022). The slicing planes sweep the SlO's boundary and skeletal sheet, as illustrated in Figure 1.
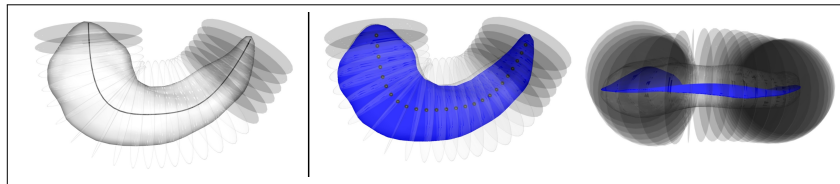
Fig. 1 A hippocampus as an SlO. Grey disks are slicing planes along the spine. Left: The black curve is the spine. Right: Two views of the SlO. The blue surface is the skeletal sheet.

Motivated by Damon (2003, 2008), we understand the *skeletal structure* of an SlO as a field of non-crossing internal vectors called *skeletal spokes* with tips on the boundary and tails on the SlO's skeletal sheet (see Figure 2). Skeletal spokes provide geometric information such as locational width and direction. One powerful SlO representation is the *discrete skeletal representation* (ds-rep) as a finite subset of the SlO's skeletal structure (Pizer et al., 2013; Liu et al., 2021; Taheri and Schulz, 2022). Assuming a sample of SlOs, their ds-reps define a meaningful correspondence (Van Kaick et al., 2011) across the sample based on the assumption that there is a correspondence between the SlOs

---

[1]A generalized cylinder is a swept region with a center curve and cross-sections that are star-convex sets, as discussed by Ballard and Brown (1982); Damon (2008); Ma et al. (2018).

[2]The skeleton of an object is a curve or a sheet that can be understood as a locally centered shape abstraction obtainable from a given shape by the process of continuous contraction (Bærentzen and Rotenberg, 2021; Siddiqi and Pizer, 2008).

and an eccentric ellipsoid. That is, each SlO has a crest[3] corresponding to the ellipsoid's crest, two vertices corresponding to the ellipsoid's vertices (i.e., the endpoints of the ellipse's major axis with maximum Gaussian curvature), and the spine corresponding to the ellipsoid's major axis (Pizer et al., 2013, 2020, 2022) (see Figures 1 and 2). In this sense, a ds-rep is a tuple of skeletal spokes, and a set of ds-reps is a set of tuples such that the tuples correspond to each other element-wise. Therefore, we can compare and analyze the corresponding ds-reps element-wise (Schulz et al., 2016; Pizer et al., 2020).

As Taheri and Schulz (2022) discussed, the advantage of the ds-rep over most shape representations like the *landmark-based model* (Dryden and Mardia, 1998), *point distribution model* (PDM) (Laga et al., 2019; Styner et al., 2006), *Euclidean distance matrix* (Lele and Richtsmeier, 2001) and *persistent homology* (Gamble and Heo, 2010; Turner et al., 2014) is that a ds-rep captures the interior curvature and width along the object. Moreover, we can parameterize ds-rep so that it becomes invariant to rigid transformations (i.e., alignment-independent), which enables us to detect local dissimilarities between objects accurately. Further, such a skeletal model is able to explain the types of dissimilarities like shrinkage, bending, and protrusion explicitly. Although a ds-rep ensures good correspondence by construction, fitting a ds-rep to an SlO remains challenging. Thus, the objective of this work is to define a ds-rep such that fitting it to an object boundary defines a good correspondence across a sample of SlOs (i.e., the geometric properties of the model provide a meaningful relationship across a population, resulting in strong statistical performance). To define a suitable ds-rep, we need to have an explicit definition of the skeletal structure.

A well-known skeletal structure is Blum's medial skeletal structure. The medial skeletal structure is a field of *medial spokes* on the *medial skeleton* (or medial axis as defined in Section 2), where the skeleton is the locus of centers of all bitangent inscribed spheres. The medial spokes are tangent to the boundary, and medial spokes with common tail positions have equal lengths. The medial skeletal structure is unique and defines a radial flow (i.e., the inverse grassfire flow of Blum et al. (1967)) based on the portion of the spokes' lengths from the skeleton to the boundary. Therefore, the object's boundary can be reconstructed by having the medial skeleton and the radial flow. However, Damon (2003) believed that Blum's conditions were too strict for defining the radial flow that leads to boundary formation. For example, spokes with common tail positions do not need (to be either symmetric relative to the skeleton or) have equal lengths. Thus, he relaxed Blum's conditions by defining three conditions: 1. Radial curvature condition, 2. Edge condition, and 3. Compatibility condition. Based on the three conditions, the radial vector field does not necessarily need to be Blum's radial vector field. In other words, by having the medial skeleton, we may define different radial vector fields satisfying the

---

[3]The crest of an SlO is a closed curve on the boundary such that at each crest point, the curvature across the crest is convex, and the magnitude of the principal curvature has a relative maximum. The crest of an ellipsoid is the intersection of its first principal plane with its boundary (Siddiqi and Pizer, 2008).

4   *Fitting the Discrete Swept Skeletal Representation to Slabular Objects*

three conditions and still construct the boundary. Moreover, as pointed out by Damon (2003), as far as we preserve the three conditions, we may define different skeletal structures with different skeletons such that they produce the same boundary (e.g., based on the chordal axis of Brady and Asada (1984)). Thus, the skeletal structure of an object is not necessarily unique. Later Damon (2008) used the three conditions and defined the swept skeletal structure for swept regions by introducing the *relative curvature condition* (RCC).

The medial skeleton typically has a bushy structure. Thus, establishing correspondence based on the medial skeleton is challenging. Pizer et al. (2013) embraced Damon's idea and introduced the *skeletal representation* (s-rep) for SlOs. The s-rep is a quasi-medial representation designed to produce the correspondences needed for statistical shape analysis. From Pizer's point of view based on the Jordan-Schoenflies Theorem (Mendelson, 2012), the crest of an SlO is a closed curve on the SlO's boundary that divides the boundary into two boundary components. Therefore, an SlO has a *central medial skeleton* (CMS) as a unique connected manifold with no holes or branches corresponding to the two boundary components (see Figure 6). The CMS can be seen as the locus of all centers of inscribed spheres that are bitangent to both boundary components, as we discuss in Section 3. Although the CMS is usually non-smooth and bumpy, a relaxed version of the CMS can be considered as the object's skeleton. In this sense, an s-rep represents the SlO's skeletal structure, where the skeleton (i.e., the skeletal sheet) is a smooth sheet, and the envelope of the non-crossing skeletal spokes represents the boundary (see Figures 1 and 2). We call the envelope of the spokes the *implied boundary* (Pizer et al., 1999). The ds-rep is a finite subset of the s-rep. Thus, to fit a ds-rep, we need to fit the skeletal sheet with non-crossing skeletal spokes on it such that the implied boundary represents the actual boundary. Further, a SlO is a swept region. Therefore, the skeletal structure of the fitted model should also reflect the swept plane properties defining the SlO.

In the state-of-the-art model fitting, Liu et al. (2021) used boundary registration to deform the ds-rep of an ellipsoid as the reference object to fit the model into a target SlO like a hippocampus. However, there are some concerns with Liu's method. Basically, it applies to any object homeomorphic to an ellipsoid. Since almost all objects with no holes or handles are homeomorphic to an ellipsoid (Jermyn et al., 2017), it is difficult to show that the obtained ds-rep represents the skeletal structure of an SlO. Also, it is a boundary deformation method. Thus, model fitting heavily relies on boundary registration for deriving skeletal correspondence. Still, proper boundary registration is challenging and has been controversial for decades. Based on our observations, various registration methods, including the *spherical harmonic PDM* (SPHARM-PDM) (Styner et al., 2006), elastic registration (Srivastava and Klassen, 2016; Jermyn et al., 2017), or *mean curvature flow* registration (Liu et al., 2021), fail to define an excellent correspondence between an SlO and an ellipsoid, as discussed in the Supplementary Material (SUP). Besides, such models are usually asymmetric and perturbed with an untidy structure.

The reason is that any boundary noise, protrusion, and intrusion significantly affect the model. Analysis based on such models could be misleading because they introduce false positives, as we discuss in Section 8.

As defined in Section 2, an SlO is a swept region such that each *cross-section* (i.e., the intersection of a slicing plane with the object) is a symmetric 2D object with two vertices and a center curve. Thus, for each cross-section there is a smooth sequence of line segments (i.e., 1D cross-sections) on its center curve (see Figure 3). The line segments are coplanar, and each line segment can be seen as two skeletal spokes with a common tail position in opposite directions. Thus, an SlO has a *swept skeletal structure* (Damon, 2008). The union of the cross-sections' center curves forms the skeletal sheet, and the union of the skeletal spokes forms the radial vector field on the skeletal sheet that defines the flow from the skeletal sheet to the boundary (Pizer et al., 2022). The spine is a curve on the skeletal sheet that (approximately) transverses the middle of cross-sections and connects two vertices of the SlO as depicted in Figure 1. Therefore, we can define a meaningful correspondence across a sample of SlOs by defining the correspondence between their spines based on curve registration (Srivastava and Klassen, 2016). Consequently, we have corresponding spinal cross-sections associated with the corresponding spinal points. In the same way that we define corresponding cross-sections on the spine, we can define corresponding line segments on the center curves of the spinal cross-sections (based on the curve registration in 2D). This approach is thus designed to yield a finite set of corresponding skeletal spokes. We call such a ds-rep a *discrete swept skeletal representation* (dss-rep). The dss-rep represents the SlO's swept skeletal structure, as depicted in Figure 2.
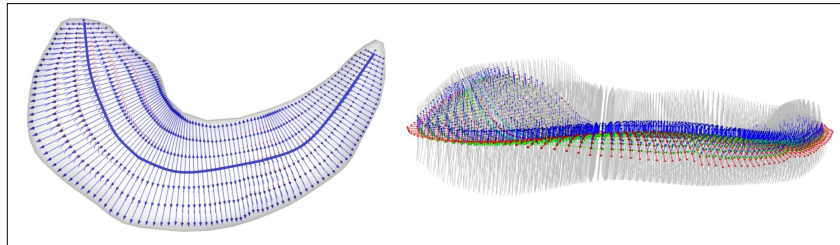
Fig. 2 A dss-rep of a hippocampus. Left: Discrete skeletal sheet. Right: Skeletal spokes in grey with tails on the skeletal sheet.

The swept skeletal structure is also a form of skeletal structure that is not unique. Therefore, the center curve of a swept region with a swept skeletal structure is also not unique. In fact, as long as the center curve of a swept region satisfies Damon's criterion of the RCC, it can be bent such that the cross-sections do not intersect within the object. The RCC defines a curvature tolerance for the center curve to ensure the cross-sections do not intersect within the object (Damon, 2008; Ma et al., 2018) (see Figure 24 in SUP). For example, for a 2D GC, the RCC can simply be determined at each point along

6   *Fitting the Discrete Swept Skeletal Representation to Slabular Objects*

the center curve based on its normal as $r < \frac{1}{\kappa}$, where r is the object's width in the direction of the normal, and κ is the curve's curvature. Let us consider an example in 2D to illustrate our approach.
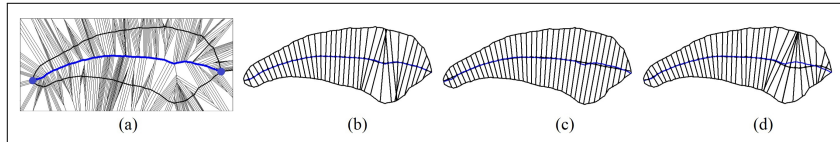
Fig. 3 The skeletal structure of a 2D GC. (a) The approximation of the medial axis based on the Voronoi diagram. The CMS is the blue curve connecting the two vertices (blue dots). (b) A model based on a smooth curve very close to the CMS is invalid as it violates the RCC. (c) A valid model based on a slightly relaxed CMS, which is tidy but not highly symmetric. (d) A valid model with high symmetricity. The model is close to violating the RCC.

Assume a 2D GC as depicted in Figure 3 (a). The medial skeleton of the object is calculated as shown in Figure 3 (a) based on the Voronoi diagram (Attali et al., 2009; Dey and Zhao, 2004). The object can be divided in two parts, as discussed in Section 3, resulting in two vertices depicted by blue dots. The CMS of the object is a unique curve (depicted in blue) with no branch or discontinuity connecting the two vertices of the 2D GC. The CMS is a pruned version of the medial skeleton and is unique. Thus, it seems reasonable to construct the swept skeletal structure based on it. However, the CMS is not smooth and has a bumpy structure (specifically at the intersection of the branches). In this example, we cannot consider the CMS or a smooth differentiable curve very close to the CMS as the center curve because they violate the RCC (i.e., the cross-sections intersect within the object because of its high local curvature), as shown in Figure 3 (b). Therefore, the dss-rep cannot be established. However, following Pizer et al. (2013), by relaxing the CMS, the center curve satisfies the RCC, as depicted in Figure 3 (c) and Figure 3 (d). In Figure 3 (c), we slightly relaxed the CMS in the sense that the relaxed version is very close to the CMS. Based on Damon's discussions, Figure 3 (c) is a valid model even though it is not perfectly symmetric (as the spokes with a common tail position do not need to have equal length). In Figure 3 (d), we increased the flexibility of the model so that it becomes more symmetric, i.e., the center curve is closer to the middle of the cross-sections. However, we observe that the center curve is very close to violating the RCC. Note that defining a perfectly symmetric model with cross-sections normal to the center curve usually is not feasible even if the object has a smooth non-branching medial skeleton (Shani and Ballard, 1984) (see Figure 23 in SUP). Obviously, the structure of Figure 3 (c) is tidier than Figure 3 (d) as the center curve has lower local curvature. In other words, the orientations of adjacent cross-sections in Figure 3 (c) are not significantly different. There is a trade-off between skeletal-symmetry and skeletal-tidiness, and both are crucial factors in defining a model in addition to the volume-coverage. Thus, in Section 6, we

introduce an overall score based on these three criteria to measure the goodness of fit within a set of model candidates for the swept skeletal structure.

One conceivable method for fitting a dss-rep into an SlO is to calculate the spine as a *curve skeleton* (Dey and Sun, 2006) in the first place and define the cross-sections along the spine. However, there are concerns with the curve skeleton. For example, even a smooth curve skeleton may still have branches because there is no criterion that a curve skeleton must be a simple curve. There are approaches for simplifying the curve skeleton to defining a simple curve, for instance, the Laplacian contraction of Au et al. (2008), Mean curvature skeleton of Tagliasacchi et al. (2012), L1-medial skeleton of Huang et al. (2013), and skeletonization via local separators of Bærentzen and Rotenberg (2021). However, according to our observations, they fail to offer a suitable spine. In fact, the majority of these methods blindly search for the SlO's skeleton without considering its important geometric properties, such as the crest and vertices. Moreover, these methods commonly overlook the RCC entirely, as it is not a prerequisite for defining the curve skeleton. Therefore, the spine exhibits unpredictable behavior. For example, it may bend and swing freely inside the object, as discussed in SUP.

By assuming a unique crest for an SlO, the CMS is unique. In this work, we use the CMS to propose a novel dss-rep model fitting. We start by defining the skeletal sheet by relaxing the SlO's CMS. Then, we use the relaxed CMS to define the spine as a curve located on the skeletal sheet connecting the SlO's two vertices, as we discuss in Section 4.2. The method we describe ensures that it achieves good correspondence across the population samples based on the uniqueness of the CMS. The method is independent of boundary registration and complies with the definition of SlO. Further, the model fitting procedure is flexible and can be tuned to obtain a tidy and symmetric model. We discuss the tuning based on the essential properties of skeletal-symmetry, tidiness, and the volume of the implied boundary.

To make the analysis alignment independent and to capture the type of local dissimilarities (e.g., protrusion, elongation, etc.), we adapt the idea of *locally parameterized ds-rep* (LP-ds-rep) suggested by Taheri and Schulz (2022) to introduce *locally parameterized dss-rep* (LP-dss-rep) by parameterizing the dss-rep based on a tree-like structure of its skeletal sheets equipped with local frames as discussed in Section 5. The structure of this work is as follows.

Section 2 reviews basic terms and provides explicit definitions of a swept region, SlO, skeletal structure, and swept skeletal structure. Section 3 introduces the CMS. Section 4 uses the CMS to propose a dss-rep model fitting procedure based on *skeleton flattening* using dimensionality reduction methods. Section 5 and Section 6 introduce the LP-dss-rep and discuss the goodness of fit for a proper model based on essential skeletal symmetry and tidiness as well as the volume of the implied boundary. Section 7 demonstrates LP-dss-rep hypothesis testing and classification based on LP-dss-rep Euclideanization. Section 8 compares the LP-ds-rep with the LP-dss-rep based on a set of toy

8   *Fitting the Discrete Swept Skeletal Representation to Slabular Objects*

examples and a real data set to discuss the pros and cons of our method. Finally, Section 9 summarizes and concludes the work.

2 Basic terms and definitions

In this section, we review basic terms and definitions regarding skeletal structures.

We consider the set $\Omega \subset \mathbb{R}^d$ as a d-dimensional object if Ω is homeomorphic to the d-dimensional closed ball, where $d \in \mathbb{N}$. We denote the boundary of Ω by $\partial\Omega$ and its interior by Ω_{in}, so $\Omega = \Omega_{in} \cup \partial\Omega$. Assume point $\boldsymbol{p} \in \Omega_{in}$ and a unit direction $\boldsymbol{u} \in \mathbb{S}^{d-1}$, where $\mathbb{S}^{d-1} = \{\boldsymbol{x} \in \mathbb{R}^d \mid \|\boldsymbol{x}\| = 1\}$ is the unit $(d-1)$-sphere. Assume Ω as a 2 or 3-dimensional object. If we start at $\boldsymbol{p}$ and move straight forward based on $\boldsymbol{u}$, we ultimately reach a boundary point. We call such a straight interior path with starting point $\boldsymbol{p}$ and direction $\boldsymbol{u}$ a *spoke*. We denote a spoke based on its positional and directional components by $\boldsymbol{s}_{(\boldsymbol{p},\boldsymbol{u})}$.

We consider the skeletal spokes of Ω as a set of all non-crossing spokes emanating from its skeleton M. The skeletal structure of Ω is a field of skeletal spokes U on M denoted by (M, U) (see Figures 3 and 4). The medial skeletal structure is one form of skeletal structure where the object's skeleton is the medial skeleton. The medial skeleton of object Ω is the set

$$M_{\odot} = \{\boldsymbol{p} \in \Omega_{in} \mid \; |\{\boldsymbol{q} \in \partial\Omega \mid \; \|\boldsymbol{p} - \boldsymbol{q}\| = d_{min}(\boldsymbol{p}, \partial\Omega)\}|_c \geq 2\}, \qquad (1)$$

where $d_{min}(\boldsymbol{p}, \partial\Omega)$ is the minimum Euclidean distance between $\boldsymbol{p}$ and $\partial\Omega$, and $\|.\|$ and $|.|_c$ represent the Euclidean norm and cardinality, respectively. In other words, $M_{\odot}$ is the center of all maximal (inscribed) spheres bi-tangent (or multi-tangent) to $\partial\Omega$. A medial spoke is a spoke connecting the center of a maximal sphere to its tangency point. The collection of all medial spokes $U_{\odot} = \{\boldsymbol{s}_{(\boldsymbol{p},\boldsymbol{u})} \mid \boldsymbol{p} \in M_{\Omega} \text{ and } \|\boldsymbol{s}_{(\boldsymbol{p},\boldsymbol{u})}\| = d_{min}(\boldsymbol{p}, \partial\Omega)\}$ on the medial skeleton $M_{\odot}$ forms the medial skeletal structure $(M_{\odot}, U_{\odot})$ (Siddiqi and Pizer, 2008). Figure 4 illustrates the medial skeleton and a few medial spokes of a 2D object.
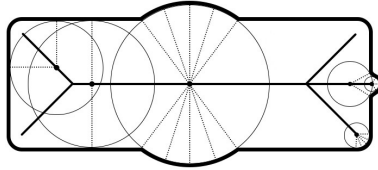

Fig. 4 Illustration of a medial skeleton and maximal spheres. The bold curve is the medial skeleton. The dotted lines are medial spokes.

A swept region is a d-dimensional object with a smooth sequence of affine slicing planes along a center curve (not necessarily normal to the center curve)

such that cross-sections do not intersect within the object, and each cross-section is a $(d-1)$-dimensional object (Damon, 2008). In other words, the slicing planes sweep the object's interior and boundary (see Figures 1 and 3).

Let Γ be the center curve of the swept region Ω, and let M be the skeleton of Ω. Assume $\Gamma_{(t)}$ as the curve length parameterization of Ω such that $t \in [0,1]$, where $\Gamma_{(0,1)}$ denotes the curves' endpoints (Srivastava and Klassen, 2016). Let $\Pi_{(t)}$ be the slicing plane crossing $\Gamma_{(t)}$, and let $\Omega_{(t)} = \Pi_{(t)} \cap \Omega$ be the cross-section at $\Gamma_{(t)}$. Let $U_{(\boldsymbol{p})}$ denote the set of skeletal spokes with tails on $\boldsymbol{p} \in M$. The skeletal structure of Ω is a swept skeletal structure if, for each $\boldsymbol{p} \in \Omega_{(t)} \cap M$, the $U_{(\boldsymbol{p})} \in \Omega_{(t)}$, i.e., all the skeletal spokes with tails on a cross-section are coplanar. Thus, the slicing planes also sweep the object's skeletal structure (Damon, 2008). We consider an object as a GC if its skeletal structure is a swept skeletal structure and its skeleton M is a smooth open curve. For example, a cylinder is a 3D GC, and an ellipse is a 2D GC, where the skeleton is the major axis and the slicing planes are perpendicular to the center curve (Brady and Asada, 1984; Giblin and Brassett, 1985; Ma et al., 2018).

Following Pizer et al. (2022) and Taheri and Schulz (2022), in this work, we consider an SlO as a swept region with a swept skeletal structure such that each cross-section is a 2D GC, the length of the spine (i.e., the SlO's center curve) is notably larger than the length of the skeleton of each cross-section. The intersection of the spine with each 2D GC is a point on and approximately at the middle of the 2D GC's skeleton. The union of the 2D GCs' boundaries forms the SlO's boundary, and the union of the 2D GCs' skeletons forms the SlO's skeleton, called the skeletal sheet. For instance, any eccentric ellipsoid (i.e., an ellipsoid with unequal principal radii) is an SlO by considering the ellipsoid's major axis (i.e., the intersection of the first principal axis with the ellipsoid) as the spine and (parallel) slicing planes perpendicular to the spine with cross-sections as ellipses which are 2D GCs. Thus, the skeletal sheet of the ellipsoid is the union of the ellipses' skeletons, i.e., the intersection of the first principal plane of the ellipsoid with itself.

3 Central medial skeleton

In this section, we discuss the CMS of 2D GCs and SlOs as a subset of their medial skeleton. In Section 4, we use the CMS to fit the SlO's dss-rep.
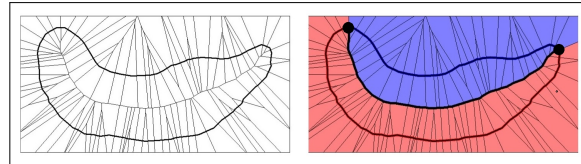

Fig. 5 Left: The Voronoi diagram of a 2D GC. Right: The top and bottom parts are depicted as blue and red curves. The two sub-regions are two union polygons associated with the top and bottom parts with the same color. The CMS is the black curve as part of the shared boundary of the union polygons connecting the object vertices.

10   *Fitting the Discrete Swept Skeletal Representation to Slabular Objects*

We know the medial skeleton can be approximated by the Voronoi diagram (Attali et al., 2009). A Voronoi diagram is a geometric structure that partitions a space into regions based on the proximity to a specified set of points called sites. In a Voronoi diagram, each region is a polygon consisting of all the points in the space that are closer to a particular site than to any other site. By assuming the sites as a large number of points uniformly distributed on the object's boundary, the polygons' borders located inside the object approximate the medial skeleton (Dey and Zhao, 2004), as depicted in Figure 5 (Left).

Assume Ω as a 2D GC object with two vertices. The two vertices divide the boundary $\partial\Omega$ into two non-overlapping components, namely *top part* and *bottom part*. Each part is a simply connected manifold with no holes or discontinuity. These two parts cover the entire boundary without any gaps. In a discrete sense, $\partial\Omega$ and its two parts can be represented by a set of adjacent points. Thus, each boundary point belongs to only one part, and each part is a set of adjacent points (De Berg, 2000). Let $\partial\hat{\Omega}$ be the discrete form of $\partial\Omega$, and $\partial\hat{\Omega}^+$ and $\partial\hat{\Omega}^-$ be the top and bottom parts, respectively. Thus, $\partial\hat{\Omega} = \cup\partial\hat{\Omega}^\pm$. Assume a box that contains $\partial\hat{\Omega}$. The Voronoi diagram of each part consists of a set of adjacent polygons such that adjacent polygons share a common edge. The union of these adjacent polygons is a union polygon as a connected subset of the box. Therefore, the box (or the embedding space) is partitioned into two sub-regions. Let Ω^+ and Ω^- be the intersection of the two sub-regions with Ω associated with $\partial\hat{\Omega}^+$ and $\partial\hat{\Omega}^-$. Thus, Ω^+ and Ω^- can be seen as two sub-objects, such that $\Omega = \cup\Omega^\pm$. The intersection of these sub-objects $\Omega^+ \cap \Omega^-$ defines their shared boundary that we consider as the central medial skeleton (CMS) of Ω.

The CMS can be seen as the locus of the centers of all inscribed spheres bitangent to both parts. In other words, the CMS is a subset of the medial skeleton that is central relative to the $\partial\hat{\Omega}^+$ and $\partial\hat{\Omega}^-$. This occurs because the distances from any point on the CMS to both the top and bottom parts are equal. Therefore, the CMS is a unique subset of the medial skeleton. Further, the CMS has no branches because it is part of $\partial\Omega^+$ (i.e., the boundary of the object Ω^+). Also, the CMS has no discontinuity because if it has a discontinuity, it means Ω^+ and Ω^- are adjacent, but there is a gap between them. Thus, there is a polygon inside Ω that its interior does not belong to Ω^+ or Ω^-, which contradicts the definition of the Voronoi diagram. Figure 5 illustrates the Voronoi diagram and the CMS of a 2D GC.

Similarly, by assuming a unique crest of an SlO as a closed curve (corresponding to the crest of an eccentric ellipsoid), the crest divides the SlO's boundary into two parts- the top and bottom parts. The Voronoi diagrams of the two parts define two union polyhedrons (i.e., two 3D polygons) as two sub-objects. The CMS of a SlO is the shared boundary of these two sub-objects. Thus, the CMS is a unique subset of the medial skeleton. Analogous to the CMS of a 2D GC, the CMS of an SlO is manifold with no holes or branches. Figure 6 (a) illustrates the top part, the bottom part, and the crest of a caudate nucleus as an SlO. Figure 6 (b) shows the Voronoi diagram of the SlO
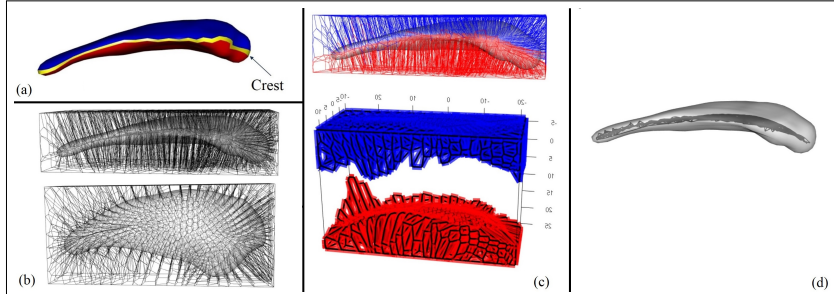
Fig. 6 (a) The top part, the bottom part, and the crest of a caudate are depicted in blue, red, and yellow, respectively. (b) Voronoi diagram of the caudate in two views. (c) Top: Illustration of the two sub-regions in blue and red. Bottom: The sub-regions are separated to provide a better intuition. (d) The CMS is depicted as a black triangle surface.

located in a box. Figure 6 (c) depicts the two sub-regions associated with the top and bottom parts. The sub-regions are also separated to provide a clear intuition about the sub-regions. Figure 6 (d) illustrates the CMS.

4 Fitting swept skeletal structure

In this section, we discuss fitting swept skeletal structures for 2D GCs, and then we generalize the method for SlOs.

We assume the skeleton or the center curve of a 2D GC is a smooth open curve. If we move on the boundary of a 2D GC, the directions of the normals do not change intensively except near the vertices associated with the endpoint of the center curve Siddiqi and Pizer (2008, Ch.8.8). The same discussion is valid for an SlO near the crest (Giblin and Kimia, 2003, 2004; Siddiqi and Pizer, 2008; Fletcher et al., 2004).

Thus, for an SlO, the normal directions of any two close points on each boundary part are not significantly different unless at the area near the crest. Abulnaga et al. (2021) used this property to calculate the crest and the two boundary parts. They considered the discrete boundary and measured the geodesic distance between any two boundary points (to find how far apart they are) and their normal difference. Then, they applied spectral clustering of Ng et al. (2001) (as a binary classification method) to classify the boundary points into the top and bottom parts.

The main idea of our model fitting is to apply Abulnaga's method to divide the SlO's boundary, obtain the CMS based on the two boundary parts, fit a smooth manifold representing the skeletal sheet close to the CMS, and finally find the spokes from the skeleton to the boundary such that the obtained skeletal structure is a swept skeletal structure. For better intuition, we start our discussion using a 2D GC, as depicted in Figure 7.

12   *Fitting the Discrete Swept Skeletal Representation to Slabular Objects*

4.1   Fitting a swept skeletal structure to a 2D GC

Assume a 2D GC with two vertices. The objective is to calculate the center curve as an open curve connecting the two vertices and a sequence of slicing planes along the center curve so that the slicing planes do not intersect within the object. To do so, first, we find the top and bottom parts of the object. Then, we calculate the CMS. The CMS is a curve connecting the two vertices. Finally, we relax CMS to define the center curve and slicing planes.

Let Ω_2 be a 2D GC with the center curve Γ_{Ω_2}. Assume $\Gamma_{\Omega_2}^0$ and $\Gamma_{\Omega_2}^1$ as the curve's endpoints corresponding to the two vertices. Also, let $\partial\Omega_2^+$ and $\partial\Omega_2^-$ be the top and bottom parts of $\partial\Omega_2$, respectively. Thus, $\Gamma_{\Omega_2}^{0,1}$ are at the edge of the top and bottom parts. Therefore, to find the $\Gamma_{\Omega_2}^{0,1}$ and the CMS of the object, it is sufficient to find the top and bottom parts.

For this purpose, we cluster boundary points into two groups as explained by Abulnaga et al. (2021) with the assumption that the directions of the boundary normals only change significantly around $\Gamma_{\Omega_2}^{\pm}$, the same way they behave at the vertices of an ellipse. Abulnaga et al. (2021) defined the affinity matrix $[W]_{i,j} = \exp\{\delta\langle\boldsymbol{n}_i,\boldsymbol{n}_j\rangle d_g(\boldsymbol{x}_i,\boldsymbol{x}_j)\}$, where $\boldsymbol{n}_i$ is the normal vector at the ith boundary vertex $\boldsymbol{x}_i$, d_g indicate the geodesics distance and δ is a penalization parameter to control the local effect of normals' variation. Therefore, the elements of the affinity matrix reflect the distance between two boundary points and how much their normals are different. Thus, based on spectral clustering of Ng et al. (2001), the sign of the second smallest eigenvectors of the normalized Laplacian $\mathcal{L} = I - D^{\frac{-1}{2}}WD^{\frac{-1}{2}}$ classifies the boundary points into two classes as top and bottom parts that are consistent with the orientation of the normals, where I is the identity matrix, and $[D]_{i,j} = \Sigma_j[W]_{i,j}$. The same discussion is valid for SlOs (see Figure 8). In this work, we choose $\delta = 0.5$ as it usually results in a reasonable crest. In SUP, the boundary division of a caudate is visualized based on different values of δ.
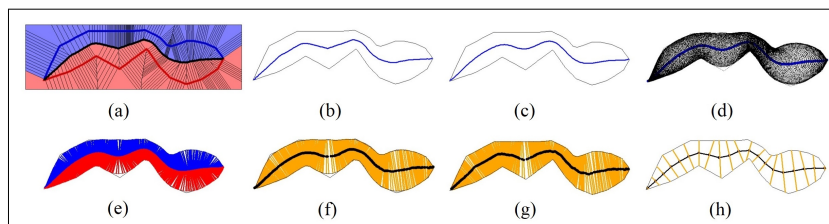
Fig. 7 Obtaining the center curve of a 2D GC. (a) Blue and red show the sub-regions associated with the boundary's top and bottom parts. (b) The CMS. (c) The relaxed CMS. (d) The maximal inscribed circles are centered at the relaxed CMS. The implied boundary is the envelope of the inscribed circles. (e) Up and down skeletal spokes of a large number of points on the relaxed CMS in blue and red. (f) Chordal structure of the implied boundary. (g) Semi-chordal structure of the object. Black dots show the semi-chordal skeleton. (h) The dss-rep of the 2D GC based on the curve length registration.

As discussed in Section 3, by having the top and bottom parts, we can calculate the CMS based on the Voronoi diagram, as shown in Figure 7 (a). The two sub-regions are in blue and red. Figure 7 (b) depicts the CMS, which is not smooth. We relax the CMS by fitting a smooth curve close to it (e.g., by implicit polynomial (Unsalan and Erçil, 1999), principal curve (Hastie and Stuetzle, 1989), nonlinear regression (Ritz and Streibig, 2008), etc.), as depicted in Figure 7 (c). Let $\hat{\Gamma}_{\Omega_2}$ be the relaxed CMS. We generate a large number of maximal inscribed circles inside Ω_2 with a center on $\hat{\Gamma}_{\Omega_2}$ as illustrated in Figure 7 (d). Since $\hat{\Gamma}_{\Omega_2}$ is continuous, we can consider the envelope of the maximal inscribed spheres as the boundary of an object $\hat{\Omega}_2$ such that $\hat{\Gamma}_{\Omega_2}$ is the medial skeleton of $\hat{\Omega}_2$. We know when the medial skeleton is a smooth open curve, for each medial point $\boldsymbol{p}$; there are two spokes at two sides of the medial skeleton with the tail at $\boldsymbol{p}$ and tip at the object boundary as

$$\boldsymbol{b} = \boldsymbol{p} - \mathscr{R}(l)|\frac{d}{dl}\mathscr{R}(l)|\boldsymbol{t} \pm \mathscr{R}(l)\sqrt{1 - |\frac{d}{dl}\mathscr{R}(l)|^2}\boldsymbol{n}, \tag{2}$$

where $\boldsymbol{n}$ and $\boldsymbol{t}$ are normal and tangent vectors of the medial skeleton at $\boldsymbol{p}$, and $\mathscr{R}$ is the radius function based on curve length parameterization l such that $\mathscr{R}(l)$ is the radius of the maximal inscribe sphere centered at $\boldsymbol{p}$ (Giblin and Kimia, 2003). Therefore, for a large number of medial points, we generate two spokes pointing toward the top and bottom parts as depicted in Figure 7 (e). Note that we can also make the relaxed CMS curvier as long as it produces non-intersecting spokes (similar to Figure 3 (d)).

We consider two top and bottom parts for $\partial\hat{\Omega}_2^{\pm}$ based on the endpoints of $\hat{\Gamma}_{\Omega_2}$. We call spokes connecting medial points to the $\partial\hat{\Omega}_2^+$ and $\partial\hat{\Omega}_2^-$ as *up* and *down* spokes, respectively. The relaxed CMS equipped with the spokes as shown in Figure 7 (e) can be seen as the *medial representation* (m-rep) of the 2D GC if the implied boundary of the spokes approximates the object boundary (Pizer et al., 1999; Fletcher et al., 2004). In other words, $\hat{\Omega}_2$ represents Ω_2 if the Jaccard index $J(\Omega_2, \hat{\Omega}_2) \approx 1$, where $J(\Omega_2, \hat{\Omega}_2) = \frac{\|\Omega_2 \cap \hat{\Omega}_2\|_A}{\|\Omega_2 \cup \hat{\Omega}_2\|_A}$ and $\|.\|_A$ measures the area. In Section 6.1, we discuss the Jaccard index based on the volume coverage for our 3D models.

If we connect the tips of the up and down spokes, we obtain the *chordal structure* as a set of non-crossing line segments connecting $\partial\hat{\Omega}_2^+$ and $\partial\hat{\Omega}_2^-$ as discussed by Giblin and Brassett (1985). Thus, $\hat{\Omega}_2$ is a 2D GC with cross-sections defined as the chordal structure of $\hat{\Omega}_2$. Note that the chordal skeleton depicted in black in Figure 7 (g) (i.e., the union of the middle of the chords) is slightly different from the medial skeleton of Figure 7 (f) (see (Giblin and Brassett, 1985)). In the next step, we stretch the chords until they reach the actual boundary $\partial\Omega$, as shown in Figure 7 (g). We consider the stretched chords as *semi-chords*. The semi-chords represent the cross-sections of the 2D GC Ω_2, and the curve connecting the middle of the semi-chords, called the *semi-chordal skeleton*, represents the center curve of Ω_2. The semi-chords may intersect somewhere between the implied boundary $\partial\hat{\Omega}_2$ and the actual boundary $\partial\Omega_2$.

14   *Fitting the Discrete Swept Skeletal Representation to Slabular Objects*

In this case, we trim the semi-chords based on the point of intersection. However, the trimming stage can be skipped if the relaxed CMS has low curvature everywhere (because based on the RCC, $r \to \infty$ when $\kappa \to 0$). Thus, the *semi-chordal structure* (i.e., semi-chords plus the semi-chordal skeleton) satisfies the RCC. The implied boundary of the semi-chordal structure (i.e., the envelope of the cross-sections) represents the actual boundary even though they are not exactly the same. Similar to m-rep, a good semi-chordal structure should approximate the actual boundary with the Jaccard index as ≈ 1.0. The semi-chordal structure can also be used for straightening the 2D GC, as discussed in SUP. Finally, based on the discussion of Srivastava and Klassen (2016) on curve registration, we can choose corresponding semi-chords (e.g., based on curve length registration) across a sample of 2D GCs. In this sense, we have the dss-rep of the 2D GC as shown in Figure 7 (h).

4.2 Fitting a swept skeletal structure to an SlO

For fitting a dss-rep to an SlO, similar to fitting a dss-rep to a 2D GC, we divide $\partial\Omega_3$ into the top and bottom parts $\partial\Omega_3^{\pm}$. Figure 8 shows the top and bottom parts of a mandible (without coronoid processes), a caudate nucleus, and a hippocampus. We consider the border between $\partial\Omega_3^{+}$ and $\partial\Omega_3^{-}$ as the
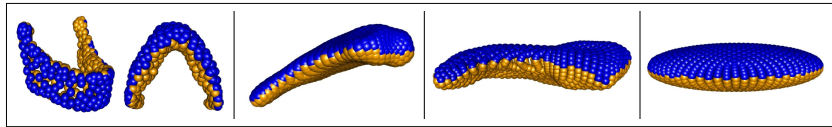
Fig. 8 Visualization of SlOs. Blue and yellow indicate the top and bottom parts of a mandible (in two angles), a caudate, a hippocampus, and an ellipsoid from left to right.

crest denoted by $\partial\Omega_3^0$ as shown in Figure 6 (a). Thus, $\partial\Omega_3^0$ corresponds to the crest of an eccentric ellipsoid, which is an ellipse, i.e., the intersection of the ellipsoid's first principal plane with its boundary. Based on $\partial\Omega_3^{\pm}$ we obtain the CMS, as depicted in Figure 6 (d) and Figure 9 (Left). We relaxed the CMS by fitting a smooth surface close to it (e.g., based on spline surface fitting (Lee et al., 1997)). We consider the relaxed CMS as the skeletal sheet, as visualized in Figure 9 (Right).

Fig. 9 Left: The CMS of a caudate. Right: Two views of the relaxed CMS.

Based on our observations, the skeletal sheet of most brain objects has low curvature everywhere, and its flattened version can be seen as 2D GC with two

vertices. We call an SlO with such a skeletal sheet a *regular SlO*; otherwise, an *irregular SlO*.

4.2.1 Regular SlO

For fitting the spine (and consequently slicing planes) of a regular SlO, the idea is to flatten the skeletal sheet based on a suitable manifold dimensionality reduction method to become a 2D GC. Then, we fit the center curve of the 2D GC, map the fitted center curve to the skeletal sheet, and consider it as the SlO's spine. In this sense, the spine is a curve on the skeletal sheet connecting two vertices of the SlO corresponding to the curve connecting the two vertices of the flattened skeletal sheet.
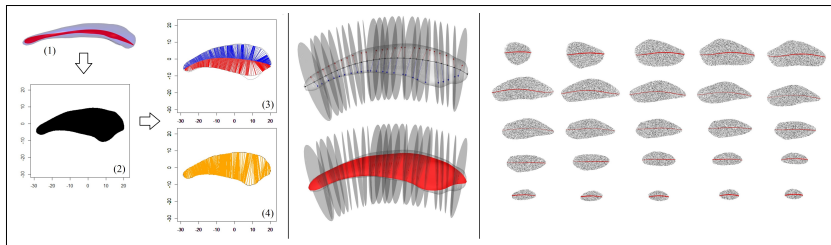
Fig. 10 Left: (1) Skeletal sheet of a caudate in red. (2) The PCA projection of the skeletal sheet as a 2D GC. (3) Relaxed CMS and the implied boundary of the 2D GC. (4) Semi-chordal skeletal of the 2D GC. Middle: Visualization of the slicing planes along the spine of a caudate (top) plus the skeletal sheet of the object (bottom). Right: cross-sections and their center curves as the intersection of the slicing planes with the skeletal sheet.

An appropriate dimensionality reduction method preserves the structure of the high-dimensional data properly in the mapped low-dimensional data (Van der Maaten and Hinton, 2008). For example, *principal component analysis* (PCA) (Hotelling, 1933) is a suitable method when the data has an approximately flat structure relative to the first PCA principal plane (i.e., a plane that is expanded by the first and second eigenvectors originated at the data centroid). In other words, the flattened version of a 3D surface (flattened by PCA) should not be significantly different from its original version. There are various ways to quantify the irregularity or non-flatness of a surface (Bosché and Guenet, 2014; Haitjema, 2017; Mikó, 2021). In this work, we quantify the irregularity based on the maximum local curvature.

For an entirely flat 2D surface, the absolute value of the two principal curvatures (i.e., the eigenvalues of the second fundamental form) are zero everywhere (Pressley, 2013). Assume M as a 2D surface. There is a point on M with absolute average curvature $\kappa_{max} \in [0, \infty)$ such that $\forall \boldsymbol{p} \in M$; $\kappa_{\boldsymbol{p}} \leq \kappa_{max}$, where $\kappa_{\boldsymbol{p}}$ is the average absolute value of the two principal curvatures at $\boldsymbol{p}$. Therefore, κ_{max} can be assumed as the total curvature of the surface. Thus, the irregularity of M can be strictly quantified as $2\arctan(\kappa_{max})/\pi \in [0, 1]$. Obviously, M is entirely flat if it has zero irregularity.

16   *Fitting the Discrete Swept Skeletal Representation to Slabular Objects*

Let $\tilde{M}_{\Omega_3}$ be the skeletal sheet of Ω_3. In this work, we say $\tilde{M}_{\Omega_3}$ is *semi-flat* if its irregularity is less than 0.01. Let $\tilde{M}_{\Omega_3}$ be semi-flat and assume the mapping $\mathscr{F} : \tilde{M}_{\Omega_3} \to \tilde{M}'_{\Omega_3}$ as the orthogonal projection that maps $\tilde{M}_{\Omega_3}$ to the PCA first principal plane along the third principal axis. We say the semi-flat $\tilde{M}_{\Omega_3}$ is *PCA flatable* if $\mathscr{F}$ is a diffeomorphism (i.e., $\mathscr{F}$ is a topological preservative bijective mapping between $\tilde{M}_{\Omega_3}$ and $\tilde{M}'_{\Omega_3}$). We consider Ω_3 as a regular SlO if $\tilde{M}_{\Omega_3}$ is semi-flat, PCA flatable, and $\tilde{M}'_{\Omega_3}$ can be seen as a 2D GC.

Let Ω_3 be a regular SlO, and Γ'_2 be the center curve of the embedded 2D GC $\tilde{M}'_{\Omega_3}$. We consider $\mathscr{F}^{-1}(\Gamma'_2)$ as the spine of Ω_3. Also, if c is a semi-chord of $\tilde{M}'_{\Omega_3}$ we consider $\mathscr{F}^{-1}(c)$ as a non-linear semi-chord of $\tilde{M}_{\Omega_3}$. Note that since we apply orthogonal projection, both c and $\mathscr{F}^{-1}(c)$ are located on a plane. Therefore, we can consider these planes as the slicing planes of Ω_3. Figure 10 shows the cross-sections of a caudate obtained based on the chordal structure of PCA projection of the skeletal sheet.

As depicted in Figure 11, the semi-chordal skeleton (i.e., the union of middle points of the semi-chords) is usually wavier than the CMS, which is not desirable as it violates the *skeleton tidiness* that we discuss in Section 6.3. Therefore, we prefer to consider Γ'_2 as the relaxed CMS of $\tilde{M}'_{\Omega_3}$. Further, if the spine (i.e., $\mathscr{F}^{-1}(\Gamma'_2)$) has low curvature everywhere and is not very wavy, we can consider cross-sections perpendicular to the spine based on the spine moving Frenet frame as discussed by Ma et al. (2018). Figure 11 illustrates the spine based on the semi-chordal skeleton (left column), relaxed CMS (middle column), and relaxed CMS such that cross-sections are normal to the spine (right column).
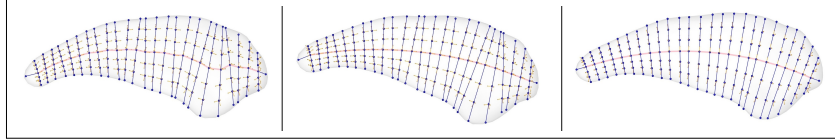
Fig. 11 Fitted tree-like structure of the skeletal sheet of a caudate. Left: Slicing planes and the spine are based on chordal structure. Middle: Slicing planes are based on chordal structure, but the spine is based on the relaxed CMS. Right: The spine is based on the relaxed CMS, and the slicing planes are normal to the spine.

4.2.2 Irregular SlO

But what if the skeletal sheet is not semi-flat? Theoretically, the skeletal sheet of an irregular SlO can be bent and twisted with an extremely curvy structure. However, there are irregular SlOs, such as the mandible, whose skeletal sheet has low local curvature. Thus, the skeletal sheet can be properly flattened. We consider such irregular SlOs as *treatable SlOs* if the flattened skeletal sheet can be seen as a 2D GC. Therefore, analogous to a regular SlO, we consider the inverse map of the center curve of the flatted skeletal sheet, i.e., $\mathscr{F}^{-1}(\Gamma'_2)$

of a treatable SlO as the spine of the object, where $\mathscr{F}$ is a proper embedding. In this case, we define cross-sections normal to the spine.

From initial studies, we found the *t-distributed stochastic neighbor embedding* (t-SNE) method (Van Der Maaten, 2014) suitable for flattening the skeletal sheet of treatable SlOs. The t-SNE maps high-dimensional data to a lower-dimensional space in such a way that preserves the local structure and relationships between data points as much as possible. It is similar to the SNE of Hinton and Roweis (2002), but instead of using a Gaussian distribution to model these relationships, it employs the t-distribution (Bunte et al., 2012). Figure 12 illustrates the skeletal sheet of a mandible (Left), its t-SNE flattened version as a 2D GC plus the center curve in 2D (Middle), and the mandible with the slicing planes along its spine (Right).
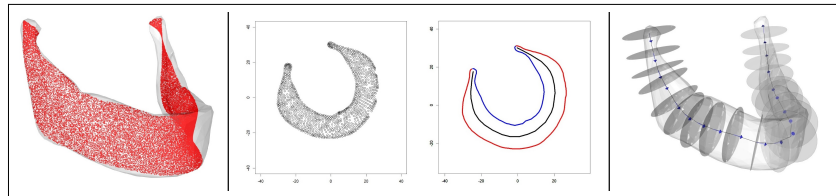
Fig. 12 Left: Skeletal sheet of a mandible (without coronoid processes). Middle: Flattened skeletal sheet by t-SNE (left), and center curve of the flattened skeletal sheet (right). Right: Slicing planes of the mandible along the spine.

Often, the complexity of the model fitting problem can be reduced by partitioning an irregular SlO into several regular SlOs. For example, skeletal analysis of a mandible can be based on skeletal models of two segmented hemimandibles (AlHadidi et al., 2012) as regular SlOs (see Figure 14 (d)). However, since the focus of this article is on regular SlOs, we leave further discussions about the generation of slicing planes along the spine of irregular SlOs to our further studies.

5 Parameterization

As Lele and Richtsmeier (2001) discussed, it is crucial for statistical shape analysis that the shape representation is invariant to rigid transformations as shape analysis based on *noninvariant* shape representation is alignment dependent, while the act of alignment makes the analysis biased and misleading. For example, hypothesis testing to detect local dissimilarity between two groups of objects based on a noninvariant shape representation (e.g., SPHARM-PDM) introduces a large number of false positives and false negatives (Taheri and Schulz, 2022). On the other hand, explaining the type of dissimilarity, such as protrusion, bending, and twisting, is essential for medical researchers. Fortunately, the ds-rep can be parameterized such that the shape representation is invariant and is able to explain the type of dissimilarity. In this regard, Taheri

18   *Fitting the Discrete Swept Skeletal Representation to Slabular Objects*

and Schulz (2022) discussed local frames for ds-reps and introduced the LP-ds-rep as an invariant skeletal shape representation based on a tree-like structure of the skeletal sheet. The tree-like structure of LP-dss-rep is established based on the spine and a set of non-intersecting curves emanating from the spine called *veins*, where the spine and veins are located on the skeletal sheet. The veins connect the spine to the SlO's crest (analogous to Figure 13). In this sense, the spine and veins define paths for a moving frame on the skeletal sheet. By considering veins as the center curves of the non-intersecting cross-sections, we can define a tree-like structure for the skeletal sheet analogous to LP-ds-rep. Therefore, following the idea of Taheri and Schulz (2022), we parameterize the dss-rep to introduce an invariant shape representation called LP-dss-rep.
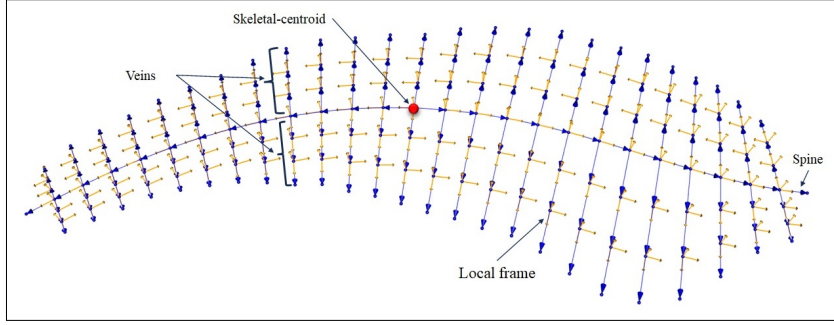
5.1 LP-dss-rep

Fig. 13 Tree-like structure of the skeletal sheet of a caudate, including local frames in yellow and connection vectors in blue.

Let $\tilde{M}_{\Omega_3}$ be the skeletal sheet of the regular SlO Ω_3. For each point $\boldsymbol{p}$ inside $\tilde{M}_{\Omega_3}$, there is a line segment based on the semi-chordal structure of the cross-sections that contains $\boldsymbol{p}$ with endpoints at $\partial\Omega_3^{\pm}$. We consider one up and one down spoke along the line segment with a tail at $\boldsymbol{p}$ and tips on $\partial\Omega_3{}^{+}$ and $\partial\Omega_3{}^{-}$, respectively. Thus, the length of the up and down spokes reflect the local width of Ω_3, and their difference reflects the local symmetry relative to $\tilde{M}_{\Omega_3}$ (i.e., higher differences indicate higher local asymmetry). Assume the middle point of the spine is the *skeletal-centroid*, as depicted in Figure 13. Thus, the spine can be seen as two curves with the starting point at the skeletal-centroid. Also, the center curve of each cross-section consists of two typically non-straight curves called veins emanating from the spine. Thus, we can consider a vein's starting point on the spine and its ending point on the SlO's crest. Since $\boldsymbol{p}$ is on the skeletal sheet, it belongs to a curve $\gamma \subset \tilde{M}_{\Omega_3}$, where γ is the spine or a vein. We define the orthogonal local frame at $\boldsymbol{p}$ as $F_{\boldsymbol{p}}^{\gamma} = (\boldsymbol{n}_{\boldsymbol{p}}^{\gamma}, \boldsymbol{b}_{\boldsymbol{p}}^{\gamma}, \boldsymbol{b}_{\boldsymbol{p}}^{\gamma\perp}) \in SO(3)$, where $\boldsymbol{n}_{\boldsymbol{p}}$ is normal to $\tilde{M}_{\Omega_3}$, $\boldsymbol{b}_{\boldsymbol{p}}^{\gamma}$ is the velocity vector tangent to γ, and $\boldsymbol{b}_{\boldsymbol{p}}^{\gamma\perp} = \boldsymbol{n}_{\boldsymbol{p}}^{\gamma} \times \boldsymbol{b}_{\boldsymbol{p}}^{\gamma}$. For points on the intersections of the spines and cross-sections' center curves (i.e., veins' starting points), we

consider γ as the spine. We do not consider frames at the endpoints of the spine and veins as they are at the edge of the skeletal sheet. Therefore, each frame has only one parent frame but up to three children frames. A vector connecting a frame to its parent is called a *connection vector*, with the tail at the origin of the parent frame and the tip at the origin of the (child) frame. In this sense, the union of the connection vectors has a tree-like structure along the spine from the skeletal-centroid out and along the veins from the spine out. Figure 13 illustrates the tree-like structure of a caudate's skeletal sheet.

We define an LP-dss-rep as a tuple of *geometric object properties* (GOPs) of the object as

$$s = (F_1^*, ..., F_{n_f}^*, \boldsymbol{v}_1^*, ..., \boldsymbol{v}_{n_c}^*, \boldsymbol{u}_1^{\pm*}, ..., \boldsymbol{u}_{n_f}^{\pm*}, v_1, ..., v_{n_c}, r_1^{\pm}, ..., r_{n_f}^{\pm}), \qquad (3)$$

or in the short form $s = (F_i^*, \boldsymbol{v}_j^*, \boldsymbol{u}_i^{\pm*}, v_j, r_i^{\pm})_{i,j}$, where $i = 1, ..., n_f$ and $j = 1, ..., n_c$, n_f is the number of frames, n_c is the number of connection vectors, $F_i^* \in SO(3)$ is the ith frame (orientation) based on its parent coordinate system, $\boldsymbol{v}_j^* \in \mathbb{S}^2$, and $v_j \in \mathbb{R}^+$ are jth connection vector's direction and length, where the direction is based on the local frame (i.e., a frame that tail of the vector is located on), $\boldsymbol{u}_i^{\pm*} \in \mathbb{S}^2$ are the directions of the ith up and down spokes based on their local frames, $r_i^{\pm} \in \mathbb{R}^+$ are the lengths of the up and down spokes at the ith frame. Thus, an LP-dss-rep lives in a Cartesian product of Euclidean symmetric spaces as

$$\mathbf{S} = (SO(3))^{n_f} \times (\mathbb{S}^2)^{n_c+2n_f} \times (\mathbb{R}^+)^{n_c+2n_f}. \qquad (4)$$

Based on our model fitting $\boldsymbol{u}_i^{+*} = -\boldsymbol{u}_i^{-*}$, we can ignore down spokes' directions. Thus, we rewrite $s = (F_i^*, \boldsymbol{v}_j^*, \boldsymbol{u}_i^{+*}, v_j, r_i^{\pm})_{i,j}$. Further, if the skeletal sheet of a regular SlO has low curvature everywhere, we can consider up and down spokes normal to the skeletal sheet. Therefore, the first frame element at each point represents the direction of its up and down spokes, and we have $s = (F_i^*, \boldsymbol{v}_j^*, v_j, r_i^{\pm})_{i,j}$ and consequently $\mathbf{S} = (SO(3))^{n_f} \times (\mathbb{S}^2)^{n_c} \times (\mathbb{R}^+)^{n_c+2n_f}$. However, to avoid ambiguity, we stick to the definition of Equation (3) and Equation (4) as they cover both the LP-ds-rep and the LP-dss-rep. Figure 14 depicts the fitted LP-dss-rep to a caudate (a), a hippocampus (b), a mandible (c), and a hemimandible (d).
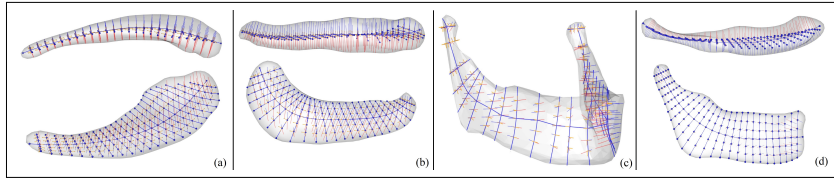

Fig. 14 Fitted LP-dss-rep to a caudate (a), a hippocampus (b), a mandible (c), and a hemimandible (d), including local frames and spokes.

20   *Fitting the Discrete Swept Skeletal Representation to Slabular Objects*

The LP-dss-rep can be used for both shape analysis (i.e., after removing the size) and size-and-shape analysis (i.e., by preserving the size) (Dryden and Mardia, 2016). Since the LP-dss-rep is invariant to rigid transformation, for shape analysis, we remove the scale by dividing the vectors' lengths by the size of the LP-dss-rep, which we call *LP-size* (Taheri and Schulz, 2022). The LP-size is the geometric mean of the vectors' length as

$$\|s\|_{LP} = \exp\big(\frac{1}{2n_f + n_c}(\sum_{j=1}^{n_c}\ln(v_j) + \sum_{i=1}^{n_f}\ln(r_i^+) + \sum_{i=1}^{n_f}\ln(r_i^-))\big).$$

In Section 8, we analyze real data based on LP-dss-rep shape analysis according to features given earlier.

6 Goodness of fit

In Section 4, we discussed the SlO's relaxed skeletal structure by fitting the skeletal sheet close to the CMS and defining the spine by fitting a smooth curve close to the relaxed CMS of the flattened skeletal sheet. Thus, we need to explain the level of relaxation. Also, we explored the possibility of choosing different spines based on the chordal skeleton or the relaxed CMS of the flattened sheet (see Figure 11). In addition, we know by definition the swept skeletal structure of an SlO is not unique. Therefore, we need to discuss which model is superior for establishing correspondence and statistical analysis. Obviously, we prefer a model that represents the object such that the implied boundary of the skeletal model approximates the actual boundary. Also, the model should be locally as symmetric as possible because symmetricity is the key element of any skeletal structure. Further, it should be tidy to avoid false positives in the analysis, as we discuss in Section 8. Thus, it is reasonable to search for a superior model with a more tidy and symmetric structure. This can be done by tuning the model fitting procedure based on the flexibility of the curve or surface fitting methods (e.g., by modifying the number of basis functions in B-spline or Fourier expansion (Kokoszka and Reimherr, 2017) or by changing the degree of the polynomial in *polynomial regression* (Jorgensen, 1993; Montgomery et al., 2015)). In this section, we discuss the goodness of fit of an LP-dss-rep by considering its *volume-coverage*, *skeletal-symmetry*, and *skeletal-tidiness*. Then, in Section 6.4, we discuss our fitting strategy by an example.

6.1 Volume-coverage

Let s be a fitted LP-dss-rep to SlO Ω, where its spokes' tips are located on $\partial\Omega^{\pm}$, and the endpoints of its veins are located on $\partial\Omega^0$. Therefore, we have a point cloud of the spokes' tips and veins endpoints representing the implied boundary of s. We can use this point cloud to generate the implied boundary as a triangular mesh, e.g., by (Pateiro López, 2008), or simply by collapsing

the boundary mesh representing Ω on the point cloud (i.e., by displacing the position of the boundary point $\boldsymbol{p} \in \partial\Omega$ to the nearest point of the point cloud). Alternatively, we can use the quadrilateral patches of the skeletal sheet to interpolate spokes and generate the implied boundary as discussed by Han et al. (2006); Liu et al. (2021).

Let $\hat{\Omega}$ be the object generated by the implied boundary. One important factor for the goodness of fit is to see how well $\hat{\Omega}$ approximates Ω. In other words, we prefer a model in which the implied boundary is as close as possible to the actual boundary. Thus, we consider the volume-coverage as the Jaccard index of the model as $J(\Omega, \hat{\Omega}) \in [0, 1]$, where $J(\Omega, \hat{\Omega}) = 1$ reflects identical volume. Obviously, we prefer models with higher volume-coverage (see Figure 15).

6.2 Skeletal-symmetry

According to the definition of SlOs, the spine is located on the center curve of each cross-section, approximately at its middle point. The union of the cross-sections' center curves forms the object's skeletal sheet. Thus, the skeletal sheet represents the SlO's skeleton, and the spine can be seen as a nonlinear skeleton of the skeletal sheet (Taheri and Schulz, 2022).

In LP-dss-rep, for each up spoke $\boldsymbol{s}_{(\boldsymbol{p},\boldsymbol{u}^+)}$ we have a down spoke $\boldsymbol{s}_{(\boldsymbol{p},\boldsymbol{u}^-)}$ with lengths $r^+ = \|\boldsymbol{s}_{(\boldsymbol{p},\boldsymbol{u}^+)}\|$ and $r^- = \|\boldsymbol{s}_{(\boldsymbol{p},\boldsymbol{u}^-)}\|$, respectively. Also, the spine divides the skeletal sheet into two parts, namely, the *right side* and the *left side*. For each vein $\nu^+_{\boldsymbol{p}_s}$ at the right side, we have a coplanar vein on the left side $\nu^-_{\boldsymbol{p}_s}$ with a common starting point $\boldsymbol{p}_{sp}$ on the spine. Thus, in a symmetric model, we expect $r^+ \sim r^-$, and $\|\nu^+_{\boldsymbol{p}_{sp}}\|_g \sim \|\nu^-_{\boldsymbol{p}_{sp}}\|_g$, where $\|.\|_g$ measures the curve length. Assume we have n_v veins on each side of the spine. Assume vector $\boldsymbol{l}^+ = (r^+_1, ..., r^+_{n_f}, \|\nu^+_1\|_g, ..., \|\nu^+_{n_v}\|_g)^T$, where ν^+_t is the tth vein on the right side and $t \in \{1, ..., n_v\}$. Similarly, assume $\boldsymbol{l}^- = (r^-_1, ..., r^-_{n_f}, \|\nu^-_1\|_g, ..., \|\nu^-_{n_v}\|_g)^T$. For simplicity, we write $\boldsymbol{l}^+ = (l^+_1, ..., l^+_{n_f+n_v})^T$ and $\boldsymbol{l}^- = (l^-_1, ..., l^-_{n_f+n_v})^T$. We define *skeletal length* as $l_s = \sum_{i=1}^{n_f+n_v} l^+_i + \sum_{i=1}^{n_f+n_v} l^-_i$ and define the weight vector $\boldsymbol{w} = (w_1, ..., w_{n_f+n_v})^T$ such that $w_i = \frac{l^+_i + l^-_i}{l_s}$. Then, we define skeletal-symmetry as $\sum_{i=1}^{n_f+n_v} w_i \cdot f_i$, where $f_i = \frac{l^+_i}{l^-_i}$ if $l^-_i \geq l^+_i$ and otherwise $f_i = \frac{l^-_i}{l^+_i}$. Thus, skeletal-symmetry is $\in [0, 1]$. If we have a perfect symmetry (i.e., $\forall i : l^+_i = l^-_i$), then skeletal-symmetry is 1.0.

6.3 Skeletal-tidiness

A model with good volume-coverage and skeletal-symmetry may still be messy. Obviously, we prefer skeletal models that are as tidy as possible for two main reasons. First, untidy models increase the number of false positives and make the analysis misleading because the analysis is a frame-by-frame analysis. Since we consider frames on the skeletal sheet, even a small perturbation on the skeletal sheet violates frame correspondence and hugely affects the results, as we demonstrate by a simple example in Section 8.2.1. Thus, we prefer a model

such that the spine and cross-sections' center curves have the lowest possible curvature. Second, as discussed in Section 1, the center curve at each point must satisfy the RCC.

Let us assume a moving frame F^γ on an open curve γ (representing the spine or a vein) located on the skeletal sheet M. In discrete format we assume a sequence of $N+1$ equidistant points $\boldsymbol{p}_0, ..., \boldsymbol{p}_N$ on γ and define *average perturbation* of γ as $\zeta(\gamma) = \frac{1}{N}\sum_{i=1}^{N} d_g(\boldsymbol{q}_{i-1}, \boldsymbol{q}_i) \in [0, \frac{\pi}{2}]$, where $\boldsymbol{q}_i \in \mathbb{S}^3$ is the unit quaternion representation of the frame $F_{\boldsymbol{p}_i}^\gamma$, and $d_g(\boldsymbol{x}, \boldsymbol{y}) = \arccos(|\boldsymbol{x}^T\boldsymbol{y}|)$ is the first quadrant geodesic distance (Huynh, 2009). Thus, $\zeta(\gamma)$ is the mean integrated rotation of the moving frame along γ when $N \to \infty$.

Assume a discrete skeletal sheet M with a spine γ_s, spinal points $\boldsymbol{p}_0, ..., \boldsymbol{p}_{N+1}$, and N cross-sections' center curves $\{\gamma_i\}_{i=1}^N$ such that $\gamma_s \cap \gamma_i = \boldsymbol{p}_i$. We know $\forall i : \boldsymbol{n}_{\boldsymbol{p}_i}^{\gamma_s} = \boldsymbol{n}_{\boldsymbol{p}_i}^{\gamma_i}$. We define the degree of rotation of the ith cross-section relative to the spine by $d_r(\gamma_s, \gamma_i) = d_g(\boldsymbol{b}_{\boldsymbol{p}_i}^{\perp_{\gamma_s}}, \boldsymbol{b}_{\boldsymbol{p}_i}^{\gamma_i})$. Finally, the average perturbation of the skeletal sheet M is defined as

$$\zeta^\dagger(M) = \frac{2}{(2N+1)\pi}\left(\zeta(\gamma_s) + \sum_{i=1}^N \zeta(\gamma_i) + \sum_{i=1}^N d_r(\gamma_s, \gamma_i)\right) \in [0, 1),$$

and the average tidiness of M as $1 - \zeta^\dagger(M)$. Thus, the average tidiness of the ellipsoid's skeleton is 1.0 if the spine is the ellipsoid's major axis, and the cross-sections (with straight center curves) are normal to the spine, i.e., $\forall i : d_r(\gamma_s, \gamma_i) = 0$.

In practice, we need the skeletal sheet as tidy as possible. Thus, it is reasonable to consider $\zeta(\gamma) = \frac{2}{\pi}\max\{d_g(\boldsymbol{q}_{i-1}, \boldsymbol{q}_i)\}_{i=1}^N$ and consequently define *strict tidiness* as $1 - \zeta^\ddagger(M)$ to judge a model based on its most disordered element, where $\zeta^\ddagger(M) = \frac{2}{\pi}\max\{\zeta(\gamma_s), \max\{\zeta(\gamma_i)\}_{i=1}^N, \max\{d_r(\gamma_s, \gamma_i)\}_{i=1}^N\}$. We define the goodness of fit score as the multiplication of volume-coverage, skeletal-symmetry, and (average or strict) tidiness. In this sense, a model is superior if its score is closer to 1.0.

6.4 Example

The flexibility of our method comes from fitting the skeletal sheet $\tilde{M}_{\Omega_3}$ and the center curve of the flattened skeletal sheet Γ_2'. Although it is possible to define a standard approach to make the fitting procedure straightforward by, for example, fitting $\tilde{M}_{\Omega_3}$ using the B-spline surface fitting of Lee et al. (1997) and fitting Γ_2' using the principal curve fitting of Hastie and Stuetzle (1989), such a standard approach might not be flexible enough to generate distinct LP-dss-reps for an SlO. Therefore, in this work, we prefer to use polynomial regression (PR). Thus, by changing the PR degree from 1 to n (where we consider $n \le 7$), we can fit $n \times n$ different LP-dss-reps to an SlO. Then, we select the best model based on the goodness of fit. We leave a detailed discussion about choosing the best curve or surface fitting method (from various available methods such as

Fitting the Discrete Swept Skeletal Representation to Slabular Objects   23

implicit polynomial (Unsalan and Erçil, 1999), nonlinear regression (Ritz and Streibig, 2008), etc.) for our future studies.

Figure 15 depicts 5 (from 49) fitted LP-dss-reps to a hippocampus at the top row and their corresponding implied boundary at the bottom row in blue. The PR degrees for fitting the $\tilde{M}_{\Omega_3}$ and Γ'_2 are shown in Table 1. Note that the boundary division and, consequently, the CMS for all five samples are the same. For the fit #1 we have a straight line segment as the spine on a perfectly flat skeletal sheet. Although the model is perfectly tidy, its volume-coverage and skeletal-symmetry are weak, resulting in a low model score; see Table 1, where score 1 is based on average tidiness and score 2 is based on strict tidiness.

By adding more flexibility to the spine and the skeletal sheet, we obtained models #2-5. The best skeletal-symmetry and score 1 value belong to model #5. However, as it is obvious from Figure 15 (5), we have a few sudden changes in spinal frames (i.e., cross-sections with high rotation degrees), which reduces the strict tidiness. In contrast, based on score 2, model #3 is the winner as it has good volume-coverage ($\approx 90\%$), skeletal-symmetry ($\approx 87\%$), and strict tidiness ($\approx 90\%$) as we do not observe any extreme changes in frame rotations.
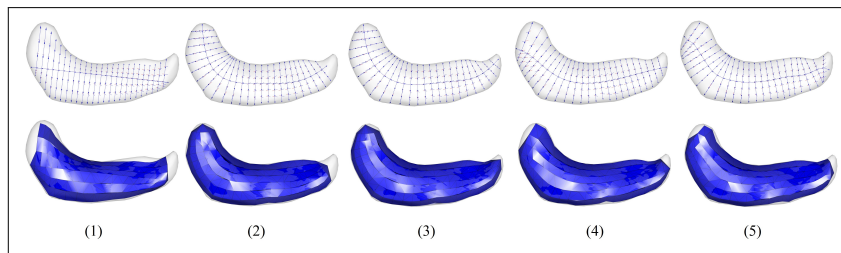
Fig. 15 Top row: Fitted LP-dss-reps with parameters given in Table 1. Bottom: Implied boundary in blue.

Table 1 Goodness of fit.

Fit	PR degrees $\tilde{M}_{\Omega_3}$, Γ'_2	Volume-coverage	skeletal-symmetry	Average tidiness $\zeta^\dagger$	Strict tidiness $\zeta^\ddagger$	Score 1	Score 2
#1	1, 1	0.812	0.724	1	1	0.588	0.588
#2	3, 4	0.877	0.883	0.969	0.861	0.750	0.667
#3	4, 4	0.890	0.873	0.973	0.890	0.756	0.692
#4	4, 5	0.876	0.861	0.972	0.870	0.733	0.656
#5	7, 7	0.878	0.894	0.971	0.735	0.762	0.577

7 Hypothesis testing

One of the main objectives of LP-dss-rep analysis is to detect dissimilarities between two groups of objects. We explain hypothesis testing for LP-ds-reps

24   *Fitting the Discrete Swept Skeletal Representation to Slabular Objects*

similar to LP-dss-reps (Taheri and Schulz, 2022). To do so, in this section, we discuss global and partial LP-dss-rep hypothesis testing based on LP-dss-rep Euclideanization. In addition to the hypothesis testing, LP-dss-rep classification is explained in SUP.

Let $\boldsymbol{q}_i^* \in \mathbb{S}^3$ be the unit quaternion representation of the ith frame (Huynh, 2009). From Equation (3) and Equation (4) we have $s = (\boldsymbol{q}_i^*, \boldsymbol{v}_j^*, \boldsymbol{u}_i^{\pm*}, v_j, r_i^{\pm})_{i,j}$ and $\mathbf{S} = (\mathbb{S}^3)^{n_f} \times (\mathbb{S}^2)^{n_c + 2n_f} \times (\mathbb{R}^+)^{n_c + 2n_f}$, where $\mathbb{S}^3$ is the space of local frames based on their unit quaternion representations. Therefore, for a population of LP-dss-reps, we have $n_c + 3n_f$ sets of spherical data (on $\mathbb{S}^2$ and $\mathbb{S}^3$) and $n_c + 2n_f$ sets of positive real numbers. The spherical data can be Euclideanized by *principal nested spheres* (PNS) (Jung et al., 2012) or for reducing the computational cost by projecting data to the tangent space (that we use in this work) as discussed by (Kim et al., 2020). Given the mapping $\mathscr{F} : \mathbb{S}^d \to \mathbb{R}^d$, $s^e = (\mathscr{F}(\boldsymbol{q}_i^*), \mathscr{F}(\boldsymbol{v}_j^*), \mathscr{F}(\boldsymbol{u}_i^{\pm*}), \log v_j, \log r_i^{\pm})_{i,j}$ is the Euclideanized version of s from Equation (3) that lives on the product space $(\mathbb{R}^3)^{n_f} \times (\mathbb{R}^2)^{n_c + 2n_f} \times (\mathbb{R}^+)^{n_c + 2n_f}$.

Now, assume $A = \{s_{A_m}^e\}_{m=1}^{N_1}$ and $B = \{s_{B_m}^e\}_{m=1}^{N_2}$ are two groups of Euclideanized LP-dss-reps (or LP-ds-rep) of sizes N_1 and N_2. We can consider the vectorized version of LP-dss-reps in the feature space (see classification in SUP) and design a global test to compare A and B as two multivariate distributions. Or we can consider LP-dss-reps as tuples and can compare the two populations of tuples element-wise to detect locational dissimilarities, as discussed by Taheri and Schulz (2022).

7.1   Global test

Let μ_A and μ_B be the means of the sets A and B, respectively. For the global test, we test $H_0 : \mu_A = \mu_B$ versus $H_0 : \mu_A \neq \mu_B$. Since the feature space is a high dimensional space, we apply *direction projection permutation* (DiProPerm) (Wei et al., 2016) with *distance weighted discriminator* (DWD) (Marron et al., 2007).

7.2   Partial test

The main objective of LP-dss-rep is to detect local dissimilarities. Thus, we design partial hypothesis tests on the GOPs (of Equation (3)). Basically, when the result of the global test shows significant dissimilarities, we apply partial tests to detect and explain local dissimilarities.

Let n_t be the total number of GOPs. To test GOPs' mean difference, we design n_t partial tests. Let $\mu_A(k)$ and $\mu_B(k)$ be the observed sample mean of the kth GOP from A and B, respectively. The partial test is $H_{0k} : \mu_A(k) = \mu_B(k)$ versus $H_{1k} : \mu_A(k) \neq \mu_B(k)$, where $k \in \{1, ..., n_t\}$. For the partial test, we can apply Hotelling's T^2 test with normality assumption or permutation test. Finally, we need to control false positives by methods such as the *family wise error rate* of Bonferroni (1936) or the *false discovery rate* (FDR) of Benjamini and Hochberg (1995) (BH).

8 Evaluation

The proposed LP-dss-rep is evaluated in comparison to the available LP-ds-rep that is based on the fitting method of Liu et al. (2021) based on visual inspection and statistical analysis.
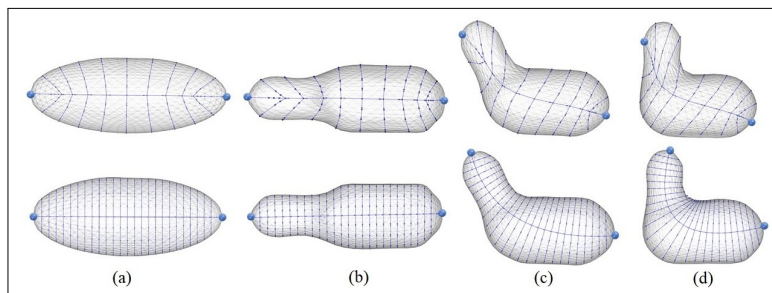
8.1 Visual inspection

Fig. 16 Toy example for comparing the LP-ds-rep (top row) and the LP-dss-rep (bottom row) of SlOs. Bold blue points are the spines' endpoints.

For the visual inspection, first, we start with a few toy examples. To design the toy examples, we slightly deform an ellipsoid to make an SlO as a reference object, as illustrated in column (b) of Figure 16. The reference object can be seen as an arm. By bending the reference object with different degrees of bending at the elbow, we make two other SlOs, as depicted in columns (c) and (d). To obtain LP-ds-reps, we used the SlicerSALT toolkit (Vicory et al., 2018). Apparently, by increasing the degree of bending, the LP-ds-rep (i.e., top row) fails to define a good correspondence as the spine does not show enough flexibility to bend according to the degree of bending we impose on the reference object. Also, the structure of the skeletal sheet becomes more and more chaotic. A possible explanation could be the poor boundary registration or the effect of boundary deformation on the skeletal sheet. In contrast to the LP-ds-rep, we can see the structure of the skeletal sheet in the LP-dss-rep is tidier as depicted in the bottom row of Figure 16. Also, the spine shows more flexibility, such that the endpoints of the spines (depicted by bold blue points) are located at the points corresponding to the vertices of the ellipsoid.
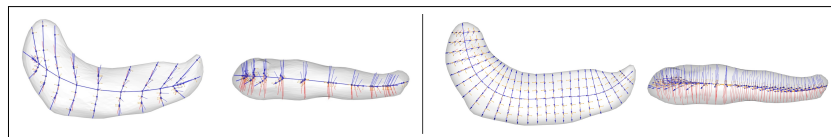

Fig. 17 Fitted LP-ds-rep (Left) and LP-dss-rep (right) in a hippocampus in two angles.

26   *Fitting the Discrete Swept Skeletal Representation to Slabular Objects*

Analogous to the toy examples, we can see the same issues of the LP-ds-rep on real data. Figure 17 illustrates the LP-ds-reps of hippocampus in two angles with the LP-ds-rep (left), and the LP-dss-rep (right). It seems the spine provides a better description of the SlO center curve in LP-dss-rep.

8.2 Statistical analysis

For the statistical analysis, we start with a simulation of a toy example before analyzing real data.

8.2.1 Toy example

We design a very simple example by simulating two groups of fifty ellipsoids based on randomly generated principal radii such that the ellipsoids of the first group are perfectly symmetric. In contrast, in the second group, there is a small protrusion on the boundary, as illustrated in Figure 18 (a). Figure 18 (d) and (e) show the results of the partial tests from Section 7.2 on the fitted LP-ds-reps and LP-dss-reps, respectively. Although both methods point to the area where we expect to see the difference, the LP-dss-rep reflects the dissimilarity more accurately based on the length of the top spokes in the critical region. In fact, the LP-ds-rep introduces more significant GOPs such that we may conclude that the left part of the two groups is totally different. The reason is that there is a perturbation of the skeletal sheet caused by the boundary deformation, as depicted in Figure 18 (b). In comparison, LP-dss-reps show more resistance against the protrusion and thus better correspondence among the skeletal sheets of the two groups (see Figure 18 (c)). The reason is that the relaxed CMS is less sensitive to boundary protrusion.
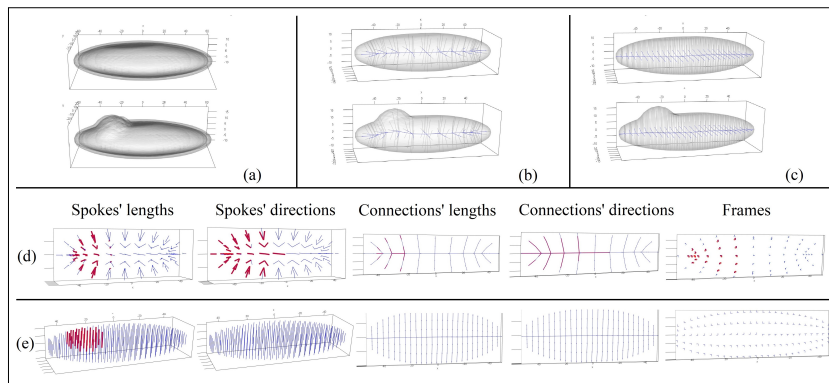

Fig. 18 (a) Two groups of simulated ellipsoids with and without boundary protrusion. (b) and (c) LP-ds-rep and LP-dss-rep of two samples from each group. (d) and (e) results of the partial tests on LP-ds-rep and LP-dss-rep, respectively. Red indicates significant GOPs.

Fitting the Discrete Swept Skeletal Representation to Slabular Objects   27

8.2.2 Real data

For the statistical analysis, we compare the left hippocampus of 182 patients with early Parkinson's disease (PD) with the left hippocampus of 108 healthy people as a control group (CG). The data is provided by the Stavanger University Hospital (https://helse-stavanger.no) and the ParkWest study (http://parkvest.no). For this, LP-dss-reps are fitted to the hippocampi of both populations and compared with global and partial hypothesis tests as described in Section 7.1 and Section 7.2 to evaluate if there are differences between the two populations.

Global test

Figure 19 depicts the result of the global test based on DiProPerm. The p-value is less than 0.001 for LP-dss-reps and 0.103 for LP-ds-reps. Thus, given a significance level of $\alpha = 0.05$, PD and CG are statistically significantly different based on LP-dss-reps. Notably, LP-dss-reps have a better performance compared to LP-ds-reps based on the higher Z-score (6.54 vs. 1.32), which indicates that the data are more separated for LP-dss-reps. This might be the effect of the above-described stiffness of LP-ds-reps. In other words, generated LP-ds-reps are relatively similar to each other, which is also reflected in the classification results as discussed in SUP.
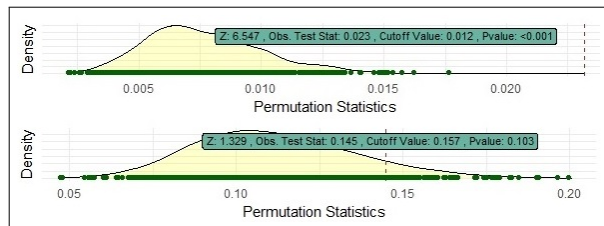
Fig. 19 DiProPerm plots of LP-dss-rep (top) and LP-ds-rep (bottom).

Partial tests

The partial tests are illustrated in Figure 20. Both the LP-ds-rep and the LP-dss-rep show significant differences in the spinal connection vectors. The LP-dss-rep introduces fewer significant connection vectors' directions and frames' orientations. This behavior supports our conclusion about the skeletal sheet from the toy example.

9 Conclusion

In this work, we introduced a novel model of discrete swept skeletal representation for SlOs called the LP-dss-rep. The LP-dss-rep is designed to support good correspondence between a population of objects, which is important for

Fig. 20 Partial tests. Red indicates significant GOPs. Results based on the LP-dss-rep (Top) and the LP-ds-rep (Bottom) before and after BH p-value adjustment in the first and second rows, respectively. Significant level $\alpha = 0.05$ and FDR=0.1.

statistical shape analysis. The fitting is based on dividing the SlO's surface into two parts, obtaining a skeletal sheet based on the relaxed central medial skeleton, and finding a tree-like structure of the skeletal sheet by the act of mapping and inverse mapping between $\mathbb{R}^3$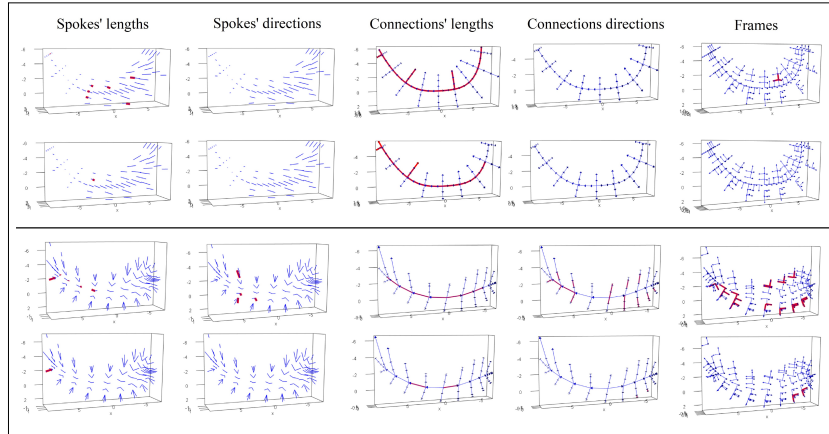 and $\mathbb{R}^2$. The LP-dss-rep is more flexible in comparison with the currently available skeletal model, namely LP-ds-rep. To have a standard measure for choosing the best LP-dss-rep, we introduced goodness of fit criteria based on volume-coverage, skeletal-symmetry, and skeletal-tidiness. The superiority of LP-dss-rep in hypothesis testing over the available LP-ds-rep was demonstrated by visual inspection and statistical analysis on two sets of toy examples and real data. This suggests that by having a proper goodness of fit in a population, the LP-dss-rep provides fewer significant GOPs and a better description of local dissimilarities.

Acknowledgments

Supplementary Material

SPHARM-PDM correspondence

As depicted in Figure 21, SPHARM-PDM fails to define a good correspondence between the boundary of an ellipsoid and the bent versions of it, as the vertices of the ellipsoid do not correspond to the vertices of the objects.
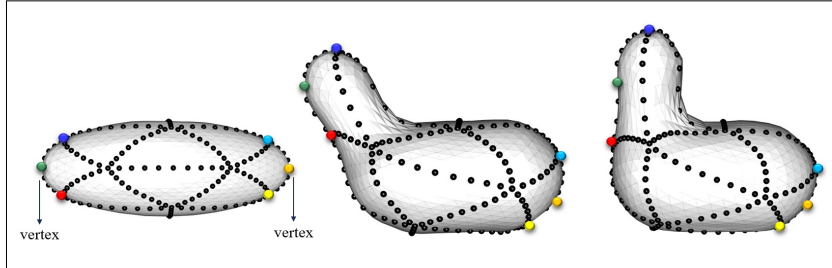
Fig. 21 SPHARM-PDM correspondence. Points with the same color are in correspondence.

Choosing δ for the affinity matrix

Choosing the value of δ that defines the affinity matrix can slightly change the boundary division. However, based on our observation for most of the objects of our study, $\delta = 0.5$ is a reasonable choice. Figure 22 depicts the boundary division of a caudate based on δ as 0.1, 0.2, 0.5, 0.8, and 0.9, from left to right, respectively
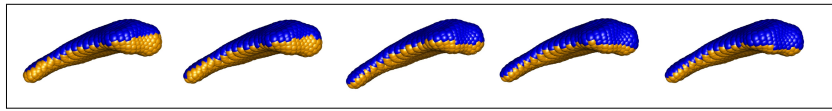
Fig. 22 From left to right, the boundary divisions are based on δ as 0.1, 0.2, 0.5, 0.8, and 0.9, respectively.

Normality versus symmetricity
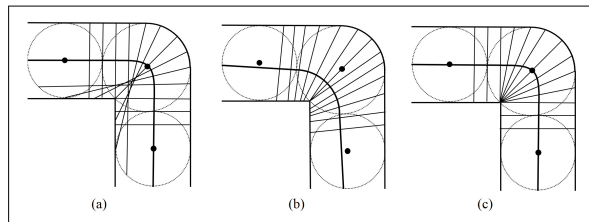
Fig. 23 (a) Cross-sections are normal to the medial skeleton. The RCC is violated. (b) Cross-sections are normal to the center curve, but the center curve is not medial. (c) Cross-sections are not normal to the center curve, but the center curve as the chordal axis traverses the cross-section's middle points.

In this section, we use Figure 23 (which is similar to Figure 3 of (Shani and Ballard, 1984)) to show even if a 2D GC has a non-branching smooth medial skeleton defining a perfectly symmetric model with normality condition is not feasible. In Figure 23 (a), the cross-sections are normal to the medial

skeleton, but the RCC is violated. In Figure 23 (b), cross-sections are normal to the center curve, but the center curve does not meet the middle of the cross-sections. Thus, the model is not symmetric. The model of Figure 23 (c) is perfectly symmetric as the center curve is the chordal skeleton. However, the cross-sections are not normal to the chordal skeleton.

Importance of the RCC

In this section, we provide an illustration to show the importance of the RCC in defining the spine of a swept skeletal structure. Figure 24 depicts two swept skeletal structures of a hippocampus. In Figure 24 (Right), the RCC is satisfied by the spine while in Figure 24 (Left) the RCC is violated. While the spines in both figures exhibit notable similarity, it becomes apparent that defining the spine solely as a curve positioned in the middle of the object is insufficient without considering the RCC.
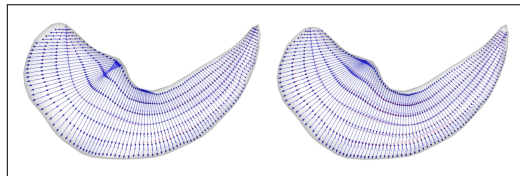
Fig. 24 Left: The RCC is violated. A few cross-sections are intersected within the object. Right: The RCC is satisfied.

Issues with the curve skeleton

There are available methods for calculating the spine of SlOs as a *curve skeleton*. The curve skeleton, as defined by Dey and Sun (2006), is unique but typically has a branching structure. Based on our experiences, most of the recent methods for pruning and smoothing the curve skeleton, such as Laplacian contraction of Au et al. (2008), mean curvature skeleton of Tagliasacchi et al. (2012), L1-medial skeleton of Huang et al. (2013), and skeletonization via local separators of Bærentzen and Rotenberg (2021); Bærentzen et al. (2023)) are more or less suitable for tube-like objects with circular cross-sections. But, they do not provide a suitable spine for slabular objects. The primary issue is that almost all of these methods blindly search for the curve skeleton without considering important boundary properties, such as the crest. We believe a proper spine should be on the skeletal sheet, connecting the SlO's vertices together, and be relatively in the middle of the cross-sections'. Based on our observations, the mentioned methods do not provide such a spine, even for simple SlOs. In addition, they entirely ignore the RCC. The RCC is not a prerequisite for calculating the curve skeleton because the curve skeleton does not necessarily represent the center curve of a swept region. However, the RCC is vital for defining the center curve of a swept region (see Figure 24). Based

on our observations, the curve skeleton exhibits unpredictable behavior inside an SlO. For example, it bends and swings freely inside the object. Therefore, defining corresponding skeletal structures based on the curve skeleton is highly questionable.

For a better intuition, we provide a very simple example to discuss the issue based on skeletonization via local separators of Bærentzen and Rotenberg (2021); Bærentzen et al. (2023). In simple words, the method searches for closed rings called local separators on the boundary. The center points of local separators define the skeleton. Figure 25 shows the spine of two SlOs with smooth boundaries. The obtained spines are based on the PyGEL library (https://www2.compute.dtu.dk/projects/GEL/PyGEL). The spine of each object is not satisfactory as it is non-smooth and perturbed. By considering a smooth version of the spine as depicted by a black curve, the spine still suffers from critical issues. It seems the spine swings and bends freely towards the left parts of the objects. Probably the reason is that the algorithm detects the local separator as the blue curve rather than the yellow curve. On the other hand, the spine violates the RCC.
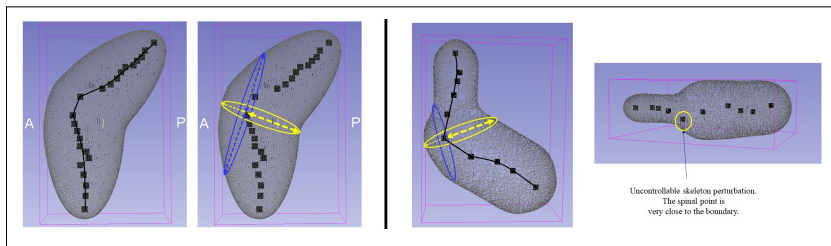
Fig. 25 Visualisation of the spine of two SlOs based on the local separator skeleton. The black curve represents the smooth version of the spine. The spines of both objects are bent and swung toward the left side of the objects.

2D GC straightening

As depicted in Figure 26, we can use the chordal structure of a 2D GC to straighten an object. Let $\{c_i\}_{i=1}^n$ be n consecutive chords (i.e., cross-sections) with points $\{\boldsymbol{p}_i\}_{i=1}^n$, such that $\forall i; \boldsymbol{p}_i$ is the middle of c_i. Let $\|c_i\|$ be the length of the ith chord. To accomplish the object straightening we use a sequence of points $\{\boldsymbol{p}_i'\}_{i=1}^n$ corresponding to $\{\boldsymbol{p}_i\}_{i=1}^n$ on a straight line ℓ such that $\forall i, j$, $\|\boldsymbol{p}_i' - \boldsymbol{p}_j'\| = d_g(\boldsymbol{p}_i, \boldsymbol{p}_j)$, and line segments $\{c_i'\}_{i=1}^n$ corresponding to $\{c_i\}_{i=1}^n$ such that $\forall i$, c_i' is perpendicular to ℓ, the middle of c_i' is on ℓ, and $\|c_i'\| = \|c_i\|$.

Classification

For classification, we follow the idea of *composite PNS* (CPNS) Pizer et al. (2013). We normalize and vectorize the Euclideanized LP-dss-reps (or LP-ds-reps). Thus, the feature space becomes $\mathbb{R}^{2n_c+9n_f}$ (or $\mathbb{R}^{2n_c+9n_f+1}$ in case we
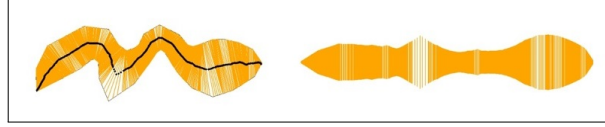
Fig. 26 Illustration of 2D GC straightening based on its chordal structure.

consider scaled LP-dss-reps and include the LP-size). In this sense, the problem becomes a binary classification problem of two groups of vectors that can be solved by, e.g., *support vector machine* (SVM)(Noble, 2006).

For the classification of the real data from Section 7, we applied different standard binary classification methods including *k nearest neighbor* (KNN), SVM with linear and radial kernels, and *naive Bayesian* (NB) classification. Further, we applied 10-fold cross-validation to evaluate the accuracy, specificity, and sensitivity of the outcomes based on Cohen's kappa (Cohen, 1960) as shown in Table 2. As we expected, the classification based on both LP-ds-rep and LP-dss-rep is not promising because, basically, we do not expect to observe separable local distributions at the early stages of PD. However, overall, it seems that the LP-dss-rep has a better performance compared to the LP-ds-rep according to both accuracy and Cohen's kappa.

Table 2 LP-ds-rep classification based on 10-fold cross-validation.

Classes	Model fitting	Assessment	Classification methods			
			KNN	SVM-linear	SVM-radial	NB
PD & CG	LP-ds-rep	Accuracy	0.60	0.55	0.63	0.57
		Kappa	0.10	0.05	0.06	0.14
	LP-dss-rep	Accuracy	0.63	0.63	0.60	0.61
		Kappa	0.18	0.17	0.10	0.11

Declarations

Ethical Approval

Not applicable.

Competing interests

The authors declare no competing interests.

Fitting the Discrete Swept Skeletal Representation to Slabular Objects 33

Authors' contributions

Mohsen Taheri is the first author and writer of the manuscript. Jörn Schulz and Stephen Pizer have supervised the project. All authors read and approved the final manuscript.

Funding

Not applicable

Availability of data and materials

Implementation of the manuscript's methodology is available as R scripts on https://github.com/MohsenTaheriShalmani/LP-dss-rep. Due to limited permission to share the Parkwest data, we only provide R code for producing toy examples and synthetic data in the repository.

References

Abulnaga, S.M., E.A. Turk, M. Bessmeltsev, P.E. Grant, J. Solomon, and P. Golland. 2021. Volumetric parameterization of the placenta to a flattened template. *IEEE Transactions on Medical Imaging 41*(4): 925–936 .

AlHadidi, A., L.H. Cevidanes, B. Paniagua, R. Cook, F. Festy, and D. Tyndall. 2012. 3d quantification of mandibular asymmetry using the spharmpdm tool box. *International journal of computer assisted radiology and surgery 7*(2): 265–271 .

Apostolova, L., G. Alves, K.S. Hwang, S. Babakchanian, K.S. Bronnick, J.P. Larsen, P.M. Thompson, Y.Y. Chou, O.B. Tysnes, H.K. Vefring, et al. 2012. Hippocampal and ventricular changes in parkinson's disease mild cognitive impairment. *Neurobiology of aging 33*(9): 2113–2124 .

Attali, D., J.D. Boissonnat, and H. Edelsbrunner. 2009. Stability and computation of medial axes-a state-of-the-art report. *Mathematical foundations of scientific visualization, computer graphics, and massive data exploration* 1: 109–125 .

Au, O.K.C., C.L. Tai, H.K. Chu, D. Cohen-Or, and T.Y. Lee. 2008. Skeleton extraction by mesh contraction. *ACM transactions on graphics (TOG) 27*(3): 1–10 .

Bærentzen, A. and E. Rotenberg. 2021. Skeletonization via local separators. *ACM Transactions on Graphics (TOG) 40*(5): 1–18 .

Bærentzen, J.A., R.E. Christensen, E.T. Gæde, and E. Rotenberg. 2023. Multilevel skeletonization using local separators. *arXiv preprint arXiv:2303.07210* 1: 1–32 .

34   *Fitting the Discrete Swept Skeletal Representation to Slabular Objects*

Ballard, D. and C. Brown. 1982. Representations of three-dimensional structures. *Computer Vision* 1: 264–311 .

Benjamini, Y. and Y. Hochberg. 1995. Controlling the false discovery rate: a practical and powerful approach to multiple testing. *Journal of the Royal statistical society: series B (Methodological) 57*(1): 289–300 .

Blum, H. et al. 1967. A transformation for extracting new descriptors of shape. *Models for the perception of speech and visual form 19*(5): 362–380 .

Bonferroni, C. 1936. Teoria statistica delle classi e calcolo delle probabilita. *Pubblicazioni del R Istituto Superiore di Scienze Economiche e Commericiali di Firenze* 8: 3–62 .

Bosché, F. and E. Guenet. 2014. Automating surface flatness control using terrestrial laser scanning and building information models. *Automation in construction* 44: 212–226 .

Brady, M. and H. Asada. 1984. Smoothed local symmetries and their implementation. *The International Journal of Robotics Research 3*(3): 36–61 .

Bunte, K., S. Haase, M. Biehl, and T. Villmann. 2012. Stochastic neighbor embedding (sne) for dimension reduction and visualization using arbitrary divergences. *Neurocomputing* 90: 23–45 .

Cohen, J. 1960. A coefficient of agreement for nominal scales. *Educational and psychological measurement 20*(1): 37–46 .

Damon, J. 2003. Smoothness and geometry of boundaries associated to skeletal structures i: Sufficient conditions for smoothness. In *Annales de l'institut Fourier*, Volume 53, pp. 1941–1985.

Damon, J. 2008. Swept regions and surfaces: Modeling and volumetric properties. *Theoretical Computer Science 392*(1-3): 66–91 .

De Berg, M. 2000. *Computational geometry: algorithms and applications.* Springer Science & Business Media.

Dey, T.K. and J. Sun 2006. Defining and computing curve-skeletons with medial geodesic function. In *Symposium on geometry processing*, Volume 6, pp. 143–152.

Dey, T.K. and W. Zhao. 2004. Approximating the medial axis from the voronoi diagram with a convergence guarantee. *Algorithmica* 38: 179–200 .

Dryden, I. and K. Mardia. 1998. *Statistical Shape Analysis.* Wiley Series in Probability & Statistics. Wiley.

Dryden, I. and K. Mardia. 2016. *Statistical Shape Analysis: With Applications in R*. Wiley Series in Probability and Statistics. Wiley.

Fletcher, P.T., C. Lu, S.M. Pizer, and S. Joshi. 2004. Principal geodesic analysis for the study of nonlinear statistics of shape. *IEEE transactions on medical imaging 23*(8): 995–1005 .

Gamble, J. and G. Heo. 2010. Exploring uses of persistent homology for statistical analysis of landmark-based shape data. *Journal of Multivariate Analysis 101*(9): 2184–2199 .

Giblin, P. and B.B. Kimia. 2004. A formal classification of 3d medial axis points and their local geometry. *IEEE Transactions on Pattern Analysis and Machine Intelligence 26*(2): 238–251 .

Giblin, P.J. and S. Brassett. 1985. Local symmetry of plane curves. *The American Mathematical Monthly 92*(10): 689–707 .

Giblin, P.J. and B.B. Kimia. 2003. On the intrinsic reconstruction of shape from its symmetries. *IEEE Transactions on Pattern Analysis and Machine Intelligence 25*(7): 895–911 .

Haitjema, H. 2017. *Flatness*, pp. 1–6. Berlin, Heidelberg: Springer Berlin Heidelberg.

Han, Q., S.M. Pizer, and J.N. Damon 2006. Interpolation in discrete single figure medial objects. In *2006 Conference on Computer Vision and Pattern Recognition Workshop (CVPRW'06)*, pp. 85–85. IEEE.

Hastie, T. and W. Stuetzle. 1989. Principal curves. *Journal of the American Statistical Association 84*(406): 502–516 .

Hinton, G.E. and S. Roweis. 2002. Stochastic neighbor embedding. *Advances in neural information processing systems* 15: 1–5 .

Hotelling, H. 1933. Analysis of a complex of statistical variables into principal components. *Journal of educational psychology 24*(6): 417 .

Huang, H., S. Wu, D. Cohen-Or, M. Gong, H. Zhang, G. Li, and B. Chen. 2013. L1-medial skeleton of point cloud. *ACM Trans. Graph. 32*(4): 65–1 .

Huynh, D.Q. 2009. Metrics for 3d rotations: Comparison and analysis. *Journal of Mathematical Imaging and Vision 35*(2): 155–164 .

Jermyn, I., S. Kurtek, H. Laga, A. Srivastava, G. Medioni, and S. Dickinson. 2017. *Elastic Shape Analysis of Three-Dimensional Objects*. Synthesis Lectures on Computer Vision. Morgan & Claypool Publishers.

36   *Fitting the Discrete Swept Skeletal Representation to Slabular Objects*

Jorgensen, B. 1993. *Theory of Linear Models.* Chapman & Hall/CRC Texts in Statistical Science. Taylor & Francis.

Jung, S., I.L. Dryden, and J. Marron. 2012. Analysis of principal nested spheres. *Biometrika 99*(3): 551–568 .

Kim, B., J. Schulz, and S. Jung. 2020. Kurtosis test of modality for rotationally symmetric distributions on hyperspheres. *Journal of Multivariate Analysis* 178: 104603 .

Kokoszka, P. and M. Reimherr. 2017. *Introduction to Functional Data Analysis.* Chapman & Hall/CRC Texts in Statistical Science. CRC Press.

Laga, H., Y. Guo, H. Tabia, R. Fisher, and M. Bennamoun. 2019. *3D Shape Analysis: Fundamentals, Theory, and Applications.* Wiley.

Lee, S., G. Wolberg, and S.Y. Shin. 1997. Scattered data interpolation with multilevel b-splines. *IEEE transactions on visualization and computer graphics 3*(3): 228–244 .

Lele, S.R. and J.T. Richtsmeier. 2001. *An invariant approach to statistical analysis of shapes.* Chapman and Hall/CRC.

Liu, Z., J. Hong, J. Vicory, J.N. Damon, and S.M. Pizer. 2021. Fitting unbranching skeletal structures to objects. *Medical Image Analysis* 70: 102020 .

Ma, R., Q. Zhao, R. Wang, J.N. Damon, J.G. Rosenman, and S.M. Pizer 2018. Skeleton-based generalized cylinder deformation under the relative curvature condition. In *PG (Short Papers and Posters)*, pp. 37–40.

Marron, J.S., M.J. Todd, and J. Ahn. 2007. Distance-weighted discrimination. *Journal of the American Statistical Association 102*(480): 1267–1271 .

Mendelson, B. 2012. *Introduction to Topology: Third Edition.* Dover Books on Mathematics. Dover Publications.

Mikó, B. 2021. Assessment of flatness error by regression analysis. *Measurement* 171: 108720 .

Montgomery, D., E. Peck, and G. Vining. 2015. *Introduction to Linear Regression Analysis.* Wiley Series in Probability and Statistics. Wiley.

Ng, A., M. Jordan, and Y. Weiss. 2001. On spectral clustering: Analysis and an algorithm. *Advances in neural information processing systems* 14: 849–856 .

Noble, W.S. 2006. What is a support vector machine? *Nature biotechnology 24*(12): 1565–1567 .

Fitting the Discrete Swept Skeletal Representation to Slabular Objects 37

Pateiro López, B. 2008. *Set estimation under convexity type restuctions.* Univ Santiago de Compostela.

Pizer, S.M., D.S. Fritsch, P.A. Yushkevich, V.E. Johnson, and E.L. Chaney. 1999. Segmentation, registration, and measurement of shape variation via image object shape. *IEEE transactions on medical imaging 18*(10): 851–865 .

Pizer, S.M., J. Hong, J. Vicory, Z. Liu, J. Marron, H.y. Choi, J. Damon, S. Jung, B. Paniagua, J. Schulz, et al. 2020. Object shape representation via skeletal models (s-reps) and statistical analysis, *Riemannian Geometric Statistics in Medical Image Analysis*, 233–271. Elsevier.

Pizer, S.M., S. Jung, D. Goswami, J. Vicory, X. Zhao, R. Chaudhuri, J.N. Damon, S. Huckemann, and J. Marron. 2013. Nested sphere statistics of skeletal models, *Innovations for Shape Analysis*, 93–115. Springer.

Pizer, S.M., J. Marron, J.N. Damon, J. Vicory, A. Krishna, Z. Liu, and M. Taheri. 2022. Skeletons, object shape, statistics. *Frontiers in Computer Science* 4: 842637 .

Pressley, A. 2013. *Elementary Differential Geometry.* Springer Undergraduate Mathematics Series. Springer London.

Ritz, C. and J. Streibig. 2008. *Nonlinear Regression with R.* Use R! Springer New York.

Schulz, J. 2013. *Statistical Analysis of Medical Shapes and Directional Data.* Ph. D. thesis, UiT Norges arktiske universitet.

Schulz, J., S.M. Pizer, J. Marron, and F. Godtliebsen. 2016. Non-linear hypothesis testing of geometric object properties of shapes applied to hippocampi. *Journal of Mathematical Imaging and Vision 54*(1): 15–34 .

Shani, U. and D.H. Ballard. 1984. Splines as embeddings for generalized cylinders. *Computer Vision, Graphics, and Image Processing 27*(2): 129–156 .

Siddiqi, K. and S. Pizer. 2008. *Medial Representations: Mathematics, Algorithms and Applications.* Computational Imaging and Vision. Springer Netherlands.

Srivastava, A. and E. Klassen. 2016. *Functional and Shape Data Analysis.* Springer Series in Statistics. Springer New York.

Styner, M., I. Oguz, S. Xu, C. Brechbühler, D. Pantazis, J.J. Levitt, M.E. Shenton, and G. Gerig. 2006. Framework for the statistical shape analysis

38   *Fitting the Discrete Swept Skeletal Representation to Slabular Objects*

of brain structures using spharm-pdm. *The insight journal 1*(1071): 242 .

Tagliasacchi, A., I. Alhashim, M. Olson, and H. Zhang 2012. Mean curvature skeletons. In *Computer Graphics Forum*, Volume 31, pp. 1735–1744. Wiley Online Library.

Taheri, M. and J. Schulz. 2022. Statistical analysis of locally parameterized shapes. *Journal of Computational and Graphical Statistics 0*(ja): 1–28 .

Turner, K., S. Mukherjee, and D.M. Boyer. 2014. Persistent homology transform for modeling shapes and surfaces. *Information and Inference: A Journal of the IMA 3*(4): 310–344 .

Unsalan, C. and A. Erçil 1999. A new robust and fast implicit polynomial fitting technique. In *Proc. Int'l Conf. Mechatronics and Machine Vision in Practice (M2VIP'99)*, pp. 1–8.

Van Der Maaten, L. 2014. Accelerating t-sne using tree-based algorithms. *The Journal of Machine Learning Research 15*(1): 3221–3245 .

Van der Maaten, L. and G. Hinton. 2008. Visualizing data using t-sne. *Journal of machine learning research 9*(11): 2579–2605 .

Van Kaick, O., H. Zhang, G. Hamarneh, and D. Cohen-Or 2011. A survey on shape correspondence. In *Computer graphics forum*, Volume 30, pp. 1681–1707. Wiley Online Library.

Vicory, J., L. Pascal, P. Hernandez, J. Fishbaugh, J. Prieto, M. Mostapha, C. Huang, H. Shah, J. Hong, Z. Liu, et al. 2018. Slicersalt: Shape analysis toolbox. In *Shape in Medical Imaging: International Workshop, ShapeMI 2018, Held in Conjunction with MICCAI 2018, Granada, Spain, September 20, 2018, Proceedings*, pp. 65–72. Springer.

Wei, S., C. Lee, L. Wichers, and J. Marron. 2016. Direction-projection-permutation for high-dimensional hypothesis tests. *Journal of Computational and Graphical Statistics 25*(2): 549–569 .

Paper III

The Mean Shape under the Relative Curvature Condition

The Mean Shape under the Relative Curvature Condition

Mohsen Taheri[*] , Stephen M. Pizer[†] and Jörn Schulz[‡]

May 28, 2024

Abstract

The relative curvature condition (RCC) serves as a crucial constraint, ensuring the avoidance of self-intersection problems in calculating the mean shape over a sample of swept regions. By considering the RCC, this work discusses estimating the mean shape for a class of swept regions called elliptical slabular objects based on a novel shape representation, namely elliptical tube representation (ETRep). The ETRep shape space equipped with extrinsic and intrinsic distances in accordance with object transformation is explained. The intrinsic distance is determined based on the intrinsic skeletal coordinate system of the shape space. Further, calculating the intrinsic mean shape based on the intrinsic distance over a set of ETReps is demonstrated. The proposed intrinsic methodology is applied for the statistical shape analysis to design global and partial hypothesis testing methods to study the hippocampal structure in early Parkinson's disease.

Keywords: Elliptical Tube, Generalized Cylinder, Swept Skeletal Structure, Statistical Shape Analysis, Slabular Objects, Relative Curvature Condition.

---

[*]Mohsen Taheri, Department of Mathematics and Physics, University of Stavanger (UiS), Email: mohsen.taherishalmani@uis.no

[†]Prof. Stephen M. Pizer, Department of Computer Science, University of North Carolina at Chapel Hill (UNC), Email: pizer@cs.unc.edu

[‡]Assoc. Prof. Jörn Schulz, Department of Mathematics and Physics, University of Stavanger (UiS), Email: jorn.schulz@uis.no

1

1 Introduction

Object shapes in 3D or 2D are important for statistical analysis, for example, in the characterization of diseases of the human body. Such analysis is commonly based on moments, especially means and covariances, on abstract metric spaces. For these spaces to support these moments, paths on these spaces are best if they pass through only geometrically valid shapes; distances of these paths then form the basis for calculating means and covariances. Here we create such a shape space from an object representation provided by elliptical tubes, which form a useful approximation of so-called slabular objects, and we focus on the calculation of means.

Considering that a variety of human body parts like the kidney, mandible, and hippocampus are slab-shaped *objects* known as *slabular objects* (SlOs) (Pizer et al., 2022; Taheri and Schulz, 2022), calculating the (sample) *mean shape* of such objects is crucial for hypothesis testing and statistical inferences to reveal underlying patterns and differences within SlO groups (e.g., patients vs. controls) (Fletcher et al., 2004; Styner et al., 2006; Schulz et al., 2016; Taheri et al., 2023). However, calculating the SlO mean shape is not straightforward as the mean shape may violate SlO conditions or might be an inappropriate representative of the sample. In this work, we explore the problem and propose a solution for a class of SlOs called *elliptical SlOs* (E-SlOs) by discussing their shape, shape space, and shape distance.

An SlO is a *swept region* based on a smooth sequence of slicing planes along the SlO's center curve called the *spine* such that the slicing planes do not intersect within the object. Each *cross-section* (i.e., the intersection of a slicing plane with the object) can be seen as a 2-dimensional (2D) *generalized tube*[1] with a (planar) center curve, and the spine of the SlO intersects each cross-section roughly at the midpoint of the cross-section's center curve.

For a 2D generalized tube, the center curve can be considered as the *skeleton*[2], and the cross-sections are line segments divided by the skeleton. Thus, each line segment can be seen as two vectors with opposite directions and a common tail position (see Figure 1

---

[1]A generalized tube or a generalized cylinder is a swept region defined by a center curve where each cross-section is a star-convex set such that the center curve intersects a star center of each cross-section (Ballard and Brown, 1982; Damon, 2008; Ma et al., 2018b).

[2]The skeleton of an object is a curve or a sheet (or a combination of both) that can be understood as a locally centered manifold obtainable by the process of continuous contraction (Siddiqi and Pizer, 2008; Bærentzen and Rotenberg, 2021).

2

(right)). In this sense, a 2D generalized tube has a *skeletal structure* as a set of non-intersecting vectors called *skeletal spokes* emanating from the skeleton with tails on the skeleton and tips on the boundary. The skeletal structure can be seen as a radial vector field that defines an outward flow from the skeleton to the boundary (Damon, 2003).

Since an SlO is the union of its cross-sections that are 2D generalized tubes, we consider a *swept skeletal structure* for the SlO as the union of the cross-sections' skeletal structures (Damon, 2008; Taheri et al., 2023). In this sense, SlO's swept skeletal structure consists of the SlO's skeleton called the *skeletal sheet* as the union of the cross-sections' center curves and the vector field on the skeletal sheet as the union of the skeletal spokes.

Theoretically, SlO analysis could be highly challenging because an SlO as a swept region can be tangled like a knot with an extremely complex structure. However, a fraction of SlOs in a human's body, including most of the brain's subcortical structures (e.g., hippocampus and caudate nucleus), can be seen as E-SlOs. We define an E-SlO as an SlO that can be properly inscribed inside an optimal *elliptical tube* (E-tube), as we discuss in Section 2, where an E-tube is a 3D generalized tube such that all its cross-sections are elliptical discs with non-zero eccentricity centered at the tube's center curve. Figure 1 illustrates a swept skeletal structure of the hippocampus as an E-SlO inscribed inside an optimal E-tube.
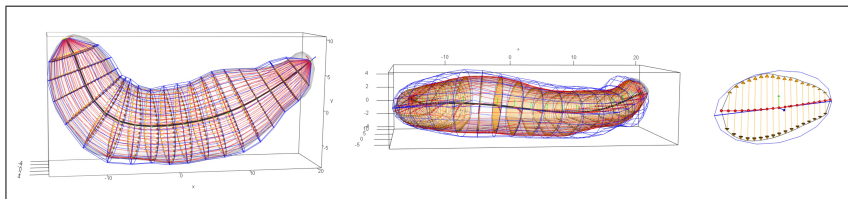
Figure 1: Visualization of a left hippocampus as an E-SlO inscribed inside an optimal E-tube. The right figure illustrates the skeletal structure of a cross-section with its center curve. The skeletal spokes are vectors with tails on the center curve. The cross-section is inscribed inside its corresponding elliptical cross-section of the E-tube.

A suitable shape or *shape representation* should establish locational correspondence among a population of objects based on their common geometric characteristics (Laga et al., 2019). For example, assume a sample of m E-SlOs as $\{P_j\}_{j=1}^m$. In a naive approach, each E-SlO can be represented by a distribution of n points called the *point distribution model* (PDM) on the object's boundary as the n-tuple $P_j = (\boldsymbol{p}_{j1}, ..., \boldsymbol{p}_{jn})$, where $\forall i \in \{1, ..., n\}$; $\boldsymbol{p}_{ji} \in \mathbb{R}^3$ (Styner et al., 2006). That is, the E-SlOs are in a point-wise

3

correspondence. By assuming that the centroids of the PDMs are located at the origin of the global coordinate system (i.e., shapes are aligned such that $\forall j; \frac{1}{n}\sum_{i=1}^{n} \boldsymbol{p}_{ji} = \boldsymbol{0}$), we can scale and represent each PDM as a unit vector as $\boldsymbol{p}_j = \frac{\text{vec}(P_j)}{\|\text{vec}(P_j)\|} \in \mathbb{S}^{3n-1}$, where $\mathbb{S}^{3n-1} = \{\boldsymbol{x} \in \mathbb{R}^{3n} \mid \|\boldsymbol{x}\| = 1\}$ is the $(n-1)$-sphere, vec() is the vectorization operator, and $\|.\|$ is the Euclidean norm. Thus, each PDM becomes a point on the hypersphere (namely Kendall's pre-shape space) (Kendall, 1984; Dryden and Mardia, 2016), which is a manifold equipped with the geodesic distance $d_g(\boldsymbol{x}, \boldsymbol{y}) = \cos^{-1}(\boldsymbol{x} \cdot \boldsymbol{y})$ as the shape distance, where $(\cdot)$ is the dot product (Jung et al., 2012). Therefore, $\{P_j\}_{j=1}^{m}$ can be seen as a distribution of points $\{\boldsymbol{p}_j\}_{j=1}^{m}$ on the manifold, and the mean shape (as the Fréchet mean) is a point on the manifold with the minimum sum of squared geodesic distances to all other points as $\bar{\boldsymbol{p}} = \text{argmin}_{\boldsymbol{p} \in \mathbb{S}^{(n-1)}} \frac{1}{m} \sum_{j=1}^{m} d_g^2(\boldsymbol{p}_j, \boldsymbol{p})$ (Pennec et al., 2019).

However, an E-SlO is a swept region with the *relative curvature condition* (RCC) that assures that the cross-sections do not intersect within the object region (Damon, 2008; Ma et al., 2018b). To the best of our knowledge, PDM analysis (as discussed by an example in Supplementary Materials) and almost all common shape analysis methods such as elastic shape analysis (Jermyn et al., 2017), functional shape analysis (Srivastava and Klassen, 2016), Euclidean distance matrix analysis (Lele and Richtsmeier, 2001), persistence homology (Gamble and Heo, 2010), and even common skeletal-based methods (Fletcher et al., 2004; Pizer et al., 2013; Taheri and Schulz, 2022) do not take into account the important property of RCC for calculating the mean shape.
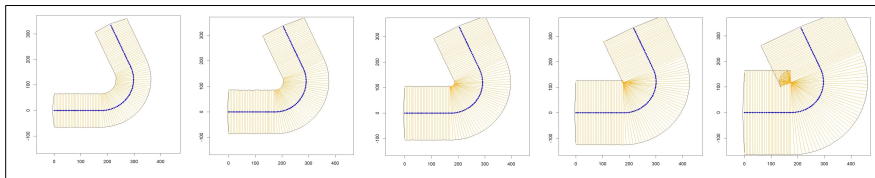
Figure 2: Illustration of the curvature tolerance in 2D. By increasing the object's width from left to right, the cross-sections intersect within the object by violating RCC, as depicted in the right figure.

As depicted in Figure 2, the RCC defines curvature tolerance for a swept region (e.g., in 2D as $\kappa < \frac{1}{r}$) such that the curvature (κ) of the center curve at each point cannot be larger than the inverse of the object's width (r) in the direction of the curve's normal.

Analogously, in E-SlO, the slicing planes intersect within the object if the center curve

4

violates the RCC (see Figures 3 and 5). The ultimate objective of this work is to define the shape and shape space for E-SlOs by considering the RCC such that the shape is an element of the shape space, and each element of the space is associated with a valid unique E-SlO that satisfies the RCC. In this sense, by moving from one element to another element of the space along a path, the object corresponding to the first element transforms into the object corresponding to the second element.
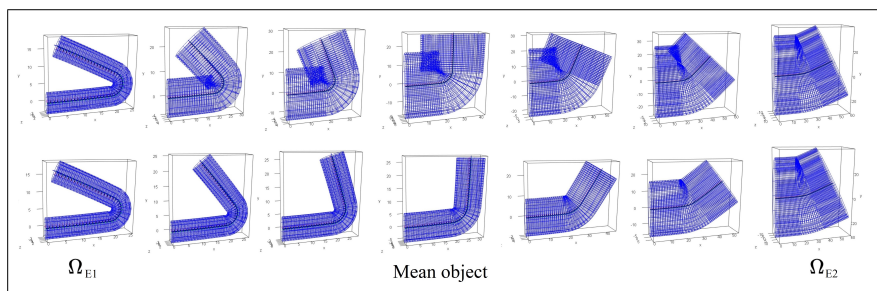
Figure 3: Top row: Extrinsic transformation between the 3D E-tubes Ω_{E1} and Ω_{E2}. Bottom row: Intrinsic transformation between E-tubes Ω_{E1} and Ω_{E2}. The middle column depicts the mean object.

Without considering the RCC, the path can be defined extrinsically. However, we are interested in determining the path intrinsically such that transformation associated with the path does not violate the RCC and the path complies with the structure of the shape space. For a better intuition, imagine two (valid) 3D E-tubes Ω_{E1} and Ω_{E2} (represented by a sequence of elliptical disks), as depicted in Figure 3. The top row shows the extrinsic transformation between Ω_{E1} and Ω_{E2} without considering the RCC based on an extrinsic path between their shapes. The path is invalid because the transformation violates the RCC with an obvious self-intersection. In other words, a part of the extrinsic path is located outside the underlying shape space. The bottom row depicts an intrinsic transformation based on an intrinsic path following the RCC that avoids self-intersection. We discuss the underlying shape space, corresponding paths, and transformations in Section 4. Based on the definition of the path, we can define the (extrinsic or intrinsic shape) distance and the mean shape as a shape with the minimum sum of squared distances to the shapes of Ω_{E1} and Ω_{E2}. We call the object corresponding to the mean shape the *mean object*. The middle column of Figure 3 depicts the E-tube associated with the mean object of Ω_{E1} and Ω_{E2}.

5

Note that the extrinsic mean object might be a valid object, but it might be an inappropriate representative of the population as its shape does not comply with the boundary condition of the underlying shape space (as discussed by a simple example in Supplementary Materials). Also, we do not consider arbitrary object modifications to remove self-intersections from the mean object, for example, by elongating or narrowing the objects or by smoothing the boundary (Ma et al., 2018a). Such modifications can be considered as arbitrary projections of the invalid shape into the underlying shape space.

To define the shape space and intrinsic path, we need a robust shape representation. Since, for an E-SlO, there is a moving plane along the spine that sweeps the object's skeletal structure, Taheri et al. (2023) introduced *locally parameterized discrete swept skeletal representations* (LPDSSRep) based on a sequence of orthonormal *material frames* (Yang et al., 2022; Giomi and Mahadevan, 2010) (representing a moving frame) on the E-SlO's spine with one element tangent to the spine and one element normal to the skeletal sheet (see Figure 4). The LPDSSRep is a powerful shape representation as it is invariant to the act of rigid transformation and alignment-independent (i.e., translation and rotation do not affect the shape representation). Besides, the E-SlO's boundary can be reconstructed precisely based on the LPDSSRep's *implied boundary* (i.e., the envelope of the skeletal spokes' tips). However, considering the RCC, defining the LPDSSRep shape space and intrinsic transformation is not straightforward because of the complex structure of the cross-sections that are 2D generalized tubes. Since each cross-section of an E-SlO can be inscribed and approximated by an ellipse, it seems reasonable to use a simplified version of the LPDSSRep called *elliptical tube representation* (ETRep), where the 2D generalized tube cross-sections are replaced with elliptical disks (see Figures 1 and 4). Thus, the ETRep is an E-SlO representation as a discrete E-tube compatible with the object's swept skeletal structure, which enables us to explain the shape space and intrinsic transformation explicitly.

The structure of this work is as follows. Section 2 discusses basic terms and definitions regarding the swept skeletal structure. Section 3 explains the discrete material frame that we use to define the ETRep space based on the RCC. Section 4 shows how to calculate the mean shape by demonstrating ETRep model fitting, RCC for ETReps, the ETRep space, skeletal coordinate system, and extrinsic and intrinsic transformations. Section 5 discusses statistical shape analysis of ETRep by applying global and partial hypothesis testings on a

6

real data set to compare hippocampal differences between patients with Parkinson's disease versus a control group. Finally, Section 6 summarizes and concludes the work.

2 Basic terms and definitions

In this section, we review some basic terms and definitions regarding E-SlO and the swept skeletal structure essential for defining the ETReps.

The (Cartesian) product space over sets $O_1, ..., O_d$ is $\{(o_1, ..., o_d) | \forall i \in \{1, ..., d\}; o_i \in O_i\}$ denoted by $O_1 \times ... \times O_d$ or if the sets are identical by $(O_1)^d$. The d-dimensional Euclidean space is the product space $(\mathbb{R})^d$ denoted by $\mathbb{R}^d$, where $\mathbb{R}$ is the set of real numbers. A point or a vector is an element of $\mathbb{R}^{d>1}$ denoted by small and bold letters. The set $B_r^d(\boldsymbol{p}) = \{\boldsymbol{x} \in \mathbb{R}^d \, | \, \|\boldsymbol{x} - \boldsymbol{p}\| \leq r\}$ defines a d-dimensional closed ball in $\mathbb{R}^d$ with center $\boldsymbol{p} \in \mathbb{R}^d$ and radius $r \in \mathbb{R}^+$, where $\mathbb{R}^+ = (0, \infty)$. Similarly, a d-dimensional open ball is defined by $B_{<r}^d(\boldsymbol{p}) = \{\boldsymbol{x} \in \mathbb{R}^d \, | \, \|\boldsymbol{x} - \boldsymbol{p}\| < r\}$.

Let the unit closed ball $B_1^d(\boldsymbol{0})$ be denoted by $\mathbb{B}^d$. We consider the set $\Omega \subset \mathbb{R}^d$ as a d-dimensional object if it is homeomorphic to $\mathbb{B}^d$ (i.e., there is a continuous invertible mapping between Ω and $\mathbb{B}^d$ (Gamelin and Greene, 1999)). A point $\boldsymbol{p} \in \Omega$ is an interior point of Ω if $\exists r \in \mathbb{R}^+$ such that $B_r^d(\boldsymbol{p}) \subset \Omega$. Let Ω_{in} be the set of all interior points of Ω. Then, the boundary of Ω is $\partial\Omega = \Omega/\Omega_{in}$ (Siddiqi and Pizer, 2008).

Assume an interior point $\boldsymbol{p} \in \Omega_{in}$ and a unit direction $\boldsymbol{u} \in \mathbb{S}^{d-1}$. If we start at $\boldsymbol{p}$ and move straight forward in the direction of $\boldsymbol{u}$, we ultimately reach the boundary at a point $\boldsymbol{q} \in \partial\Omega$. Such an interior path is a line segment called *spoke*, which can be seen as the vector $\overrightarrow{\boldsymbol{p}\boldsymbol{q}}$. The set of skeletal spokes of Ω is a set of (non-crossing) spokes emanating from the object's skeleton denoted by M_Ω. Thus, the *skeletal structure* of Ω is a field of skeletal spokes S on M_Ω denoted by (M_Ω, S). The envelope of the skeletal spokes' tips forms the object's (implied) boundary as $\partial\Omega = \{\boldsymbol{p} + S(\boldsymbol{p}) | \boldsymbol{p} \in M_\Omega\}$, where $S(\boldsymbol{p})$ is the set of all skeletal spokes with tail on $\boldsymbol{p}$ (Damon, 2003; Pizer et al., 2013).

Now, assume $\Gamma(\lambda)$ as a parameterization of a curve Γ in $\mathbb{R}^d$ such that $\lambda \in [0, 1]$, where $\Gamma(0)$ and $\Gamma(1)$ denote the curves' endpoints. Let $\Pi(\lambda)$ denote a $(d-1)$-dimensional plane crossing $\Gamma(\lambda)$ normal to Γ at $\Gamma(\lambda)$. In this work, a d-dimensional object Ω is a swept region with the center curve Γ if Ω is a disjoint union of cross-sections $\Omega(\lambda) = \Omega \cap \Pi(\lambda)$

7

such that $\forall \lambda$; $\Omega(\lambda)$ is a $(d-1)$-dimensional object and $\Gamma(\lambda)$ is a central point (e.g., the barycentroid (Rustamov et al., 2009)) of $\Omega(\lambda)$. The skeletal structure (M_Ω, S) is a *swept skeletal structure* if for each $\boldsymbol{p} \in \Omega(\lambda) \cap M_\Omega$ we have $S(\boldsymbol{p}) \subset \Omega(\lambda)$ (Damon, 2008).

A *slab* is a 3D object whose skeleton is a smooth 2D topological disk called the skeletal sheet. An SlO is a slab with a swept skeletal structure such that each cross-section is a 2D generalized tube (Pizer et al., 2022; Taheri et al., 2023). Thus, any E-tube is also an SlO with a *developable*[3] skeletal sheet where the center curve of each elliptical cross-section is its major axis (based on the chordal locus of Brady and Asada (1984)). A semi-flat SlO is an SlO whose entire skeletal sheet has relatively low curvature everywhere (i.e., the total curvature of the sheet is close to zero, like an entirely flat surface). For example, a mandible (without considering the coronoid process) is an SlO but not semi-flat, while a hemimandible is a semi-flat SlO (Taheri et al., 2023).

An SlO Ω is an E-SlO if it can be inscribed inside an (optimal) E-tube Ω_E such that $\forall \lambda \in [0,1]$; $\Omega(\lambda) \subset \Omega_E(\lambda)$ and the SlO's spine be the E-tube's spine Γ. Additionally, at each spinal point $\Gamma(\lambda)$, the material frame of both objects coincides (i.e., $\forall \lambda \in [0,1]$ the skeletal sheets of both objects are tangent at $\Gamma(\lambda)$), and the area of $\Omega_E(\lambda)$ approximates the area of $\Omega_E(\lambda)$, i.e., the Jaccard index $J(\Omega(\lambda), \Omega_E(\lambda)) = \frac{|\Omega(\lambda) \cap \Omega_E(\lambda)|_A}{|\Omega(\lambda) \cup \Omega_E(\lambda)|_A} \approx 1$, where $|.|_A$ measures the area.

Based on the definition, the swept skeletal structure of an SlO provides insight into whether the object qualifies as an E-SlO. However, calculating the swept skeletal structure of SOs (like the mandible) that are not semi-flat is an open question. Therefore, in this work, we provide examples and study E-SlOs regarding semi-flat SOs. Nevertheless, the theoretical discussions are valid for E-SlOs in general.

3 Discrete moving frame

For statistical shape analysis, we usually consider the swept skeletal structure in the discrete format to establish a meaningful correspondence (Van Kaick et al., 2011) among a population of E-SlOs. The correspondence between different objects can be established by using the curve registration (Srivastava and Klassen, 2016) of the spine and a discrete moving

---

[3]A developable surface is a ruled surface that can be swept out by moving a line (Abbena et al., 2017).

frame along the spine. Essentially, this method represents the spine as a finite set of points that correspond with those of other objects. At each spinal point, there is an orthonormal frame that defines the orientation of the cross-section at that point. Consequently, we have a set of corresponding cross-sections. The size, skeletal structure, and orientation of the corresponding cross-sections can be used for comparisons and statistical inferences. Note that without considering the local frames, cross-sectional analysis analogous to the approach of Apostolova et al. (2012) is not desirable as it is alignment-dependent (Taheri and Schulz, 2022). In this work, we define and use *discrete Frenet frames*[4] and *discrete material frames* to deal with the RCC in E-SlO analysis.

Assume λ_i as $n+1$ equally spaced points on $[0,1]$ as $\lambda_i = \frac{i}{n}$, where $i = 0, ..., n$. Thus, the spine of an E-SlO can be registered by a sequence of $n+1$ points $\boldsymbol{p}_i = \Gamma(\lambda_i)$. We consider the discrete Frenet frame associated with the point $\boldsymbol{p}_i$ as $T_i = (\boldsymbol{t}_i, \boldsymbol{n}_i, \boldsymbol{n}_i^\perp) \in SO(3)$, where $\boldsymbol{t}_i = \frac{\boldsymbol{p}_{i+1}-\boldsymbol{p}_i}{\|\boldsymbol{p}_{i+1}-\boldsymbol{p}_i\|}$, $\boldsymbol{n}_i^\perp = \frac{\boldsymbol{t}_{i-1}\times\boldsymbol{t}_i}{\|\boldsymbol{t}_{i-1}\times\boldsymbol{t}_i\|}$, $\boldsymbol{n}_i = \boldsymbol{n}_i^\perp \times \boldsymbol{t}_i$, and $i = 1, ..., n-1$ (Lu, 2013). Thus, $\boldsymbol{n}_i$ is the normal of the spine at $\boldsymbol{p}_i$, which is coplanar with the triangle $\triangle\boldsymbol{p}_{i-1}\boldsymbol{p}_i\boldsymbol{p}_{i+1}$. For the spine's endpoints (i.e., $\boldsymbol{p}_0$ and $\boldsymbol{p}_n$) we assume $T_0 = T_1$, and $T_n = T_{n-1}$. Since the Frenet frame is sensitive to flipping (specifically when the spine has zero curvature), as noted by Carroll et al. (2013), we use the material frame for establishing correspondence.

Let γ_i be the center curve of the ith cross-section $\Omega(\lambda_i)$. Based on the definition of E-SlO, we have a smooth sequence of cross-sections. Thus, the union $\cup_{i=0}^n \gamma_i$ defines a discrete surface representing the orientable smooth skeletal sheet M_Ω with two sides, namely the *positive* and *negative* sides. We consider a discrete material frame on $\Gamma(\lambda_i)$ consistent with the orientation of M_Ω as $F_i = (\boldsymbol{t}_i, \boldsymbol{a}_i, \boldsymbol{b}_i) \in SO(3)$, where $\boldsymbol{t}_i$ is the first element of the ith discrete Frenet frame, $\boldsymbol{a}_i$ is the unit vector tangent to γ_i at $\boldsymbol{p}_i$, and $\boldsymbol{a}_i \times \boldsymbol{b}_i = \boldsymbol{t}_i$. Therefore, in an E-tube, $\boldsymbol{a}_i$ and $\boldsymbol{b}_i$ are along the semi-major and semi-minor axes of the ith elliptical cross-section, respectively (see Figure 4). There are two possible options to choose $\boldsymbol{a}_i$ and $\boldsymbol{b}_i$ (as an ellipse has two semi-major and two semi-minor axes). We choose F_i such that $\forall i; \boldsymbol{b}_i$ lies on the positive side of the M_Ω. In other words, (based on the right-hand rule) the orientation induced by the material frame is consistent with the orientation of M_Ω (Guillemin and Pollack, 2010). We consider F_{i-1} as the parent frame of F_i, where

---

[4]The Frenet frame, alternatively referred to as the TNB frame, is formed by the combination of the tangent vector, normal vector, and binormal vector of a curve (do Carmo, 2016).

9

$i = 1, ..., n$, and we assume F_0 as the parent of itself.

To calculate the frame orientation based on its parent frame, we use the *spherical rotation matrix* $R(\boldsymbol{x}, \boldsymbol{y}) = I_3 + (\sin \psi)(\boldsymbol{y} \otimes \boldsymbol{z} - \boldsymbol{z} \otimes \boldsymbol{y}) + (\cos \psi - 1)(\boldsymbol{y} \otimes \boldsymbol{y} + \boldsymbol{z} \otimes \boldsymbol{z})$, where $\boldsymbol{x}, \boldsymbol{y} \in \mathbb{S}^2$, $\boldsymbol{z} = \frac{\boldsymbol{x} - \boldsymbol{y}(\boldsymbol{x} \cdot \boldsymbol{y})}{\|\boldsymbol{x} - \boldsymbol{y}(\boldsymbol{x} \cdot \boldsymbol{y})\|}$, $\psi = d_g(\boldsymbol{x}, \boldsymbol{y})$, $I_3 = (\boldsymbol{e}_1, \boldsymbol{e}_2, \boldsymbol{e}_3)$ is the identity matrix based on the unit vectors $\boldsymbol{e}_1 = (1, 0, 0)$, $\boldsymbol{e}_2 = (0, 1, 0)$, and $\boldsymbol{e}_3 = (0, 0, 1)$, and $\otimes$ denotes the outer product. Therefore, the rotation $R(\boldsymbol{x}, \boldsymbol{y})$ transfers $\boldsymbol{x}$ to $\boldsymbol{y}$ along the shortest geodesic path on $\mathbb{S}^2$ such that $R(\boldsymbol{x}, \boldsymbol{y})\boldsymbol{x} = \boldsymbol{y}$ (Amaral et al., 2007). Assume frame $F^\dagger = (\boldsymbol{t}, \boldsymbol{a}, \boldsymbol{b})$ be the parent of $\tilde{F}$. We align $F^\dagger$ to I_3 by $R_2 R_1 F^\dagger = I_3$, where $R_1 = R(\boldsymbol{t}, \boldsymbol{e}_1)$, and $R_2 = R(R_1 \boldsymbol{a}, \boldsymbol{e}_2)$. Thus, $\tilde{F}^* = R_2 R_1 \tilde{F}$ represents $\tilde{F}$ in its parent coordinate system. Let frame F^* be the orientation of F based on its parent. To find F based on the global coordinate system I_3, we align $F^\dagger$ to I_3 by $R_2 R_1 F^\dagger = I_3$. Thus, $F = [R_2 R_1]^{-1} F^*$ (Taheri and Schulz, 2022).

The vector $\overrightarrow{\boldsymbol{p}_{i-1}\boldsymbol{p}_i}$ called the ith *spinal connection* with length $x_i = \|\overrightarrow{\boldsymbol{p}_{i-1}\boldsymbol{p}_i}\|$, connects frame F_i to its parent F_{i-1}. Thus, the spine can be locally parameterized by a sequence of tuples as $((F_i^*, x_i)_i)_{i=0}^n$, where F_i^* is the ith material frame's orientation based on its parent frame. Note that by having a locally parameterized spine, we can reconstruct the spine in 3D. Thus, the parameterization also provides Frenet frames. Based on the locally parameterized spine, we define ETRep.

4 ETRep

In Sections 2 and 3, we discussed E-tubes. In this section, we define ETRep as an alignment-independent shape representation for an E-tube. We explain ETRep model fitting based on an optimal E-tube. Then, we discuss the ETRep shape space by explaining the extrinsic and intrinsic paths. To define the intrinsic path, we discuss the RCC for ETReps. Further, we explain the intrinsic sample mean shape based on the intrinsic skeletal coordinate system of the shape space.

4.1 ETRep model fitting

An ETRep is a shape representation. Therefore, we need to discuss the ETRep model fitting procedure to explain how an ETRep represents the actual object.

Let $\Omega_E(\lambda_i)$ be the ith cross-section of the E-tube Ω_E with principal radii a_i and b_i.

10

Since in the discrete format $\Omega_E = \cup_{i=0}^n \Omega_E(\lambda_i)$, we consider the ETRep of Ω_E as the sequence $s = (\omega_i)_{i=0}^n$, where $\omega_i = (F_i^*, x_i, a_i, b_i)$ is the representation of $\Omega_E(\lambda_i)$. Based on the definition, an E-SlO Ω can be inscribed inside an optimal E-tube, as we defined in Section 2. Let Ω_E be the optimal E-tube of Ω. Thus, we consider the shape representation for the Ω as $s = (\omega_i)_{i=0}^n$. In this sense, there is an optimal E-tube for Ω that its shape approximates the shape of Ω.

To find the optimal E-tube of an E-SlO Ω, we calculate the swept skeletal structure of Ω, as discussed by Taheri et al. (2023). Then, we inscribe Ω inside an E-tube $\tilde{\Omega}_E$ such that the spine and material frames of Ω and $\tilde{\Omega}_E$ are the same and $\forall \lambda_i; \; \Omega(\lambda_i) \subset \tilde{\Omega}_E(\lambda_i)$. Let a_i and b_i be the principal radii of $\tilde{\Omega}_E(\lambda_i)$. The area of each cross-section $\tilde{\Omega}_E(\lambda_i)$ is $\pi a_i b_i$. Since shrinkage of $\tilde{\Omega}_E(\lambda_i)$ does not violate the RCC in $\tilde{\Omega}_E$, we optimize the size of $\tilde{\Omega}_E(\lambda_i)$ by maximizing the Jaccard index $J(\tilde{\Omega}_E(\lambda_i), \Omega_E(\lambda_i))$ (or alternatively by maximizing the multiplication of the Jaccard index and the eccentricity of $\tilde{\Omega}_E(\lambda_i)$). This can be done by (iteratively) reducing the value of a_i and b_i to minimize $a_i b_i$ as much as possible such that (in each iteration) $b_i < a_i$ and $\tilde{\Omega}_E(\lambda_i)$ contains $\Omega(\lambda_i)$ (see Figure 1 (right)). By optimizing all the cross-sections $\forall \lambda_i$, the $\tilde{\Omega}_E$ becomes an optimal E-tube Ω_E for Ω. Note that if Ω cannot be inscribed inside an E-tube or after the optimization $\exists i$ such that $J(\tilde{\Omega}_E(\lambda_i), \Omega_E(\lambda_i))$ is relatively small (e.g., less than 0.8), then we do not consider Ω as an E-SlO. Figure 4 illustrates the ETRep of a hippocampus and a caudate nucleus.
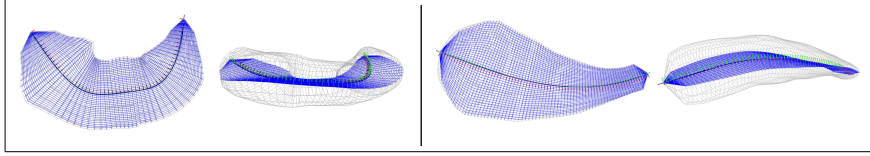
Figure 4: ETRep of a hippocampus (left) and a caudate nucleus (right) in two angles. The spine is depicted by a dark curve equipped with material frames. The cross-sections are non-intersecting elliptical disks. The skeletal sheet is the union of the cross-section's center curves (i.e., thier major axes).

4.2 Extrinsic approach

Based on the defined shape representation, we are in the position to discuss shape space and shape distance. In this section, we ignore the RCC and explain the shape space equipped with an extrinsic distance. Afterward, the intrinsic approach will be discussed.

11

Without considering the RCC, ETRep $s = (\omega_i)_{i=0}^n = ((F_i^*, x_i, a_i, b_i)_i)_{i=0}^n$ is living on the product space $(SO(3) \times (\mathbb{R}^+)^3)^{n+1}$. Assume two ETReps $s_1 = (\omega_{1i})_{i=0}^n$ and $s_2 = (\omega_{2i})_{i=0}^n$ associated with two E-tubes Ω_{E1} and Ω_{E2}, where $\omega_{ji} = (F_{ji}^*, x_{ji}, a_{ji}, b_{ji})_i$, and $j = 1, 2$. Let $\boldsymbol{f}_{ji}^* \in \mathbb{S}^3$ be the unit quaternion representation of the frame F_{ji}^* (Huynh, 2009). Thus, $s = (\omega_i)_{i=0}^n = (\boldsymbol{f}_{ji}^*, x_{ji}, a_{ji}, b_{ji})_i$ is living on $\mathbf{S}^{n+1} = (\mathbb{S}^3 \times (\mathbb{R}^+)^3)^{n+1}$, which is a differentiable manifold because it is the product space of finite sets of differentiable manifolds (Lee, 2013; do Carmo, 2016). The extrinsic distance between s_1 and s_2 can be defined as $d_s(s_1, s_2) = \left(\sum_{i=0}^n d_\omega^2(\omega_{1i}, \omega_{2i}) \right)^{\frac{1}{2}}$, where $d_\omega = \left(\sum_{i=0}^n d_g^2(\boldsymbol{f}_{1i}^*, \boldsymbol{f}_{2i}^*) + \|x_{1i} - x_{2i}\|^2 + \|a_{1i} - a_{2i}\|^2 + \|b_{1i} - b_{2i}\|^2 \right)^{\frac{1}{2}}$. Thus,

$$d_s(s_1, s_2) = \left(\sum_{i=0}^n d_g^2(\boldsymbol{f}_{1i}^*, \boldsymbol{f}_{2i}^*) + \|x_{1i} - x_{2i}\|^2 + \|a_{1i} - a_{2i}\|^2 + \|b_{1i} - b_{2i}\|^2 \right)^{\frac{1}{2}}. \tag{1}$$

We know the geodesic path between $\boldsymbol{f}_{1i}^*$ and $\boldsymbol{f}_{2i}^*$ on the unit sphere is

$$\zeta_F(\lambda; \boldsymbol{f}_{1i}^*, \boldsymbol{f}_{2i}^*) = \frac{1}{\sin(\psi)} [\sin(\psi(1 - \lambda)) \boldsymbol{f}_{1i}^* + \sin(\lambda\psi) \boldsymbol{f}_{2i}^*], \tag{2}$$

where $\psi = d_g(\boldsymbol{f}_{1i}^*, \boldsymbol{f}_{2i}^*)$, and $\lambda \in [0, 1]$ (Srivastava and Klassen, 2016). We define the extrinsic path from s_1 to s_2 as $\zeta_s(\lambda; s_1, s_2) = (\omega_{\lambda i})_{i=0}^n$ such that

$$\omega_{\lambda i} = (\zeta_F(\lambda; \boldsymbol{f}_{1i}^*, \boldsymbol{f}_{2i}^*), \zeta(\lambda; x_{1i}, x_{2i}), \zeta(\lambda; a_{1i}, a_{2i}), \zeta(\lambda; b_{1i}, b_{2i}))_i, \tag{3}$$

where $\forall \boldsymbol{x}, \boldsymbol{y} \in \mathbb{R}^d$; $\zeta(\lambda; \boldsymbol{x}, \boldsymbol{y}) = (1 - \lambda)\boldsymbol{x} + \lambda\boldsymbol{y}$ is a straight path in the Euclidean space $\mathbb{R}^d$. Thus, the extrinsic transformation is based on an extrinsic path that converts each cross-section of Ω_{E1} to its corresponding cross-section of Ω_{E2}.

In the discrete format, we assume $k + 1$ steps for the transformation. The λ can be considered as the arithmetic sequence $\lambda_j = \frac{j}{k} \in [0, 1]$ (i.e., $0, \frac{1}{k}, ..., \frac{k-1}{k}, 1$), where $j = 0, ..., k$. Let $s_{\lambda_j} = \zeta_s(\lambda_j; s_1, s_2)$. Therefore, the distance between s_1 and s_2 can be expressed as $d_s(s_1, s_2) = \lim_{k \to \infty} \sum_{j=1}^k d_s(s_{\lambda_{j-1}}, s_{\lambda_j})$ (which is identical to Equation (1)).

Given a set of m observations $s_1, ..., s_m \in \mathbf{S}^{n+1}$. The extrinsic mean shape is

$$\bar{s}_{ext} = \underset{s \in \mathbf{S}^{n+1}}{\mathrm{argmin}} \sum_{j=1}^{m} d_s^2(s, s_j). \tag{4}$$

Following the approach of Taheri and Schulz (2022), the extrinsic sample mean can be calculated as $\bar{s}_{ext} = (\bar{\omega}_i)_{i=0}^n$ such that $\bar{\omega}_i = (\bar{\boldsymbol{f}}_i^*, \bar{x}_i, \bar{a}_i, \bar{b}_i)_i$, where $\bar{\boldsymbol{f}}_i^*$ is the mean frame of $\{\bar{\boldsymbol{f}}_{ji}^*\}_{j=1}^m$ that is obtainable based on *principal nested sphere analysis* (PNS) of Jung et al. (2012) (or alternatively based the approach of Moakher (2002)), and $\bar{x}_i$, $\bar{a}_i$, and $\bar{b}_i$ are the arithmetic (or geometric) means of $\{x_{ji}\}_{j=1}^m$, $\{a_{ji}\}_{j=1}^m$, and $\{b_{ji}\}_{j=1}^m$, respectively. Thus, the mean ETRep represents an E-tuple based on the mean of the corresponding cross-sections.

As we mentioned in Section 1, if the extrinsic mean object is invalid, it is almost always possible to make it valid based on object modifications (e.g., by narrowing or elongation). Such arbitrary modifications result in an arbitrary mean shape and unreliable statistics. In other words, any shape in the shape space can be considered the mean shape. On the other hand, even if the mean shape is valid, it does not necessarily comply with the structure of the space, as the extrinsic path ignores the RCC. In fact, based on the extrinsic path, the actual ETRep space is not convex. That is to say, $\exists s_1, s_2 \in \mathcal{A}^{n+1}$, and $\exists \lambda \in (0, 1)$ such that $\zeta_s(\lambda; s_1, s_2) \notin \mathcal{A}^{n+1}$ (O'Searcoid, 2006), where $\mathcal{A}^{n+1}$ denotes the actual space of ETReps (that we discuss later) by considering RCC.
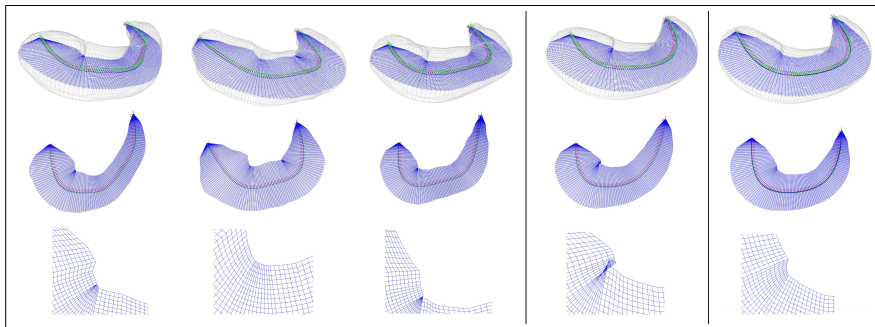

Figure 5: Self-intersecting issue in the mean shape. Left column: Three E-tubes representing three hippocampi. The skeletal sheets are flattened for better visualization. Middle column: The extrinsic mean exhibiting a self-intersection problem. Right column: The intrinsic mean without self-intersection.

Figure 5 (middle column) illustrates the extrinsic mean of three ETRep of three hip-

13

pocampi with an obvious self-intersection. Although such self-intersections are rare and often considered as artifacts, they reflect that $\mathcal{A}^{n+1}$ is more complicated than $\mathbf{S}^{n+1}$. By providing an explicit definition for $\mathcal{A}^{n+1}$, we can follow the idea of Rustamov et al. (2009) to map $\mathcal{A}^{n+1}$ to a convex space, calculate the mean and paths, and transfer them back to $\mathcal{A}^{n+1}$. Figure 5 (right column) and Figure 3 (bottom row) illustrates such an intrinsic mean and path. To define $\mathcal{A}^{n+1}$ and to explain the intrinsic approach, we discuss the RCC.

4.3 The RCC for discrete E-tubes

In this section, we discuss the RCC for discrete E-tubes based on the fact that each cross-section of an E-tube is an elliptical disk. For simplicity in writing, we denote $\Pi(\lambda_i)$, $\Omega(\lambda_i)$, and $\Gamma(\lambda_i)$ by $\Pi_{(i)}$, $\Omega_{(i)}$, and $\Gamma_{(i)}$, respectively.

For a discrete E-tube Ω_E, we have a sequence of slicing planes $\Pi_{(i)}$, $i = 0, ..., n$. We consider a local self-intersection at spinal point $\Gamma_{(i)}$ if $\Pi_{(i)}$ intersects with $\Pi_{(i-1)}$ or $\Pi_{(i+1)}$ within Ω_E. Since any two slicing planes of a swept region are adjacent or not adjacent, it is sufficient to discuss the RCC for each slicing plane relative to its previous one. Note that by considering non-local self-intersections, the E-tube space becomes highly complex as we need to define the shape space and an intrinsic path on the shape space of tangled knot-like objects such that object transformation (that can be seen as transforming a tangled knot to another tangled knot) associated with the path does not produce non-local self-intersections. In Supplementary Materials, we provide an iterative algorithm to calculate the Fréchet mean for a class of E-tubes called *simply straightenable* by considering the problem of non-local self-intersection. In this work, we focus on the problem of local self-intersections that can be explored via the RCC, and we leave a detailed study of non-local self-intersections to our future research.

To define shape space based on the RCC, we need to consider the spine curvature. Since there are various ways to define the curvature of a discrete curve (Vouga, 2014), we take a closer look at the structure of the slicing planes to provide a clear definition of the RCC in the discrete format.

Assume two consecutive cross-sections $\Omega_{(i-1)}$ and $\Omega_{(i)}$ associated with the spinal points $\boldsymbol{p}_{i-1} = \Gamma_{(i-1)}$ and $\boldsymbol{p}_i = \Gamma_{(i)}$ of an E-tube with their corresponding material frames F_{i-1}

14

118

and F_i, where $F_i = (\boldsymbol{t}_i, \boldsymbol{a}_i, \boldsymbol{b}_i)$ as described in Section 3. Assume $\varphi_i = d_g(\boldsymbol{t}_{i-1}, \boldsymbol{t}_i) \in [0, \frac{\pi}{2}]$ as the curvature angle of $\Omega_{(i)}$ based on $R_{\boldsymbol{n}_i^\perp}(\varphi_i)\boldsymbol{t}_{i-1} = \boldsymbol{t}_i$, where $\boldsymbol{n}_i^\perp = \frac{\boldsymbol{t}_{i-1} \times \boldsymbol{t}_i}{\|\boldsymbol{t}_{i-1} \times \boldsymbol{t}_i\|}$ and $R_{\boldsymbol{u}}(\varphi) = I_3 + \sin\varphi[\boldsymbol{u}]_\times + (1 - \cos\varphi)(\boldsymbol{u} \otimes \boldsymbol{u} - I_3)$ is the rotation around axis $\boldsymbol{u}$ by φ degrees (Lu, 2013). Further, let $\theta_i \in [-\pi, \pi]$ be the twisting angle between $\boldsymbol{a}_i$ and $\boldsymbol{n}_i$ relative to $\boldsymbol{t}_i$ according to the right-hand rule as $R_{\boldsymbol{t}_i}(\theta_i)\boldsymbol{a}_i = \boldsymbol{n}_i$, as depicted in Figure 6.

Assume $\varphi_i \in (0, \frac{\pi}{2}]$, i.e., $\Pi_{(i-1)} \nparallel \Pi_{(i)}$ (as $\varphi_i \neq 0$). Thus, $\Pi_{(i-1)}$ and $\Pi_{(i)}$ intersect where the intersection is a line orthogonal to $\boldsymbol{t}_{i-1}$ and $\boldsymbol{t}_i$ and parallel to $\boldsymbol{t}_i \times \boldsymbol{t}_{i-1}$ (Georgiades, 1992). Let point $\boldsymbol{q}$ be a point on the intersection line with minimum Euclidean distance to $\boldsymbol{p}_i$ (i.e., $\left\|\overrightarrow{\boldsymbol{p}_i\boldsymbol{q}}\right\|$ is the radius of a circle on $\Pi_{(i)}$ centered at $\boldsymbol{p}_i$ tangent to $\Pi_{(i-1)}$). Since the slicing planes cannot intersect within the object, $\boldsymbol{q}$ must be on the boundary or outside the E-tube Ω_E. Let $\boldsymbol{q}'$ be an arbitrary point on the intersection line and let $\theta_i = \angle\boldsymbol{q}\boldsymbol{p}_i\boldsymbol{q}'$. Obviously, $\theta_i \in [-\frac{\pi}{2}, \frac{\pi}{2}]$ and the width of $\Omega_{(i)}$ in the direction of $\overrightarrow{\boldsymbol{p}_i\boldsymbol{q}'}$ cannot exceed $\left\|\overrightarrow{\boldsymbol{p}_i\boldsymbol{q}'}\right\|$. In other words, if $\boldsymbol{q}''$ is the boundary point of ω_i along $\overrightarrow{\boldsymbol{p}_i\boldsymbol{q}'}$, then $\left\|\overrightarrow{\boldsymbol{p}_i\boldsymbol{q}''}\right\|\cos\theta_i \leq \left\|\overrightarrow{\boldsymbol{p}_i\boldsymbol{q}}\right\|$. Let $\kappa_i = \frac{1}{\left\|\overrightarrow{\boldsymbol{p}_i\boldsymbol{q}}\right\|}$. Then, condition $\left\|\overrightarrow{\boldsymbol{p}_i\boldsymbol{q}''}\right\|\cos\theta_i \leq \frac{1}{\kappa_i}$ is compatible with RCC in a continuous format (i.e., $r\cos\theta < \frac{1}{\kappa}$) (Damon, 2008). Therefore, the RCC at $\boldsymbol{p}_i$ can be strictly defined as the maximum possible size of the $\Omega_{(i)}$ such that $\Omega_{(i)}$ does not intersect with $\Pi_{(i-1)}$. Also, we overlook the size of the $\Omega_{(i-1)}$ because if $\Omega_{(i)}$ intersects with $\Pi_{(i-1)}$ without intersecting $\Omega_{(i-1)}$, then the area bounded by the envelope of $\Omega_{(i-1)}$ and $\Omega_{(i)}$ may not be a convex region, which is problematic for defining a smooth implied boundary as the issue produces thorn shape bumps on the implied boundary.
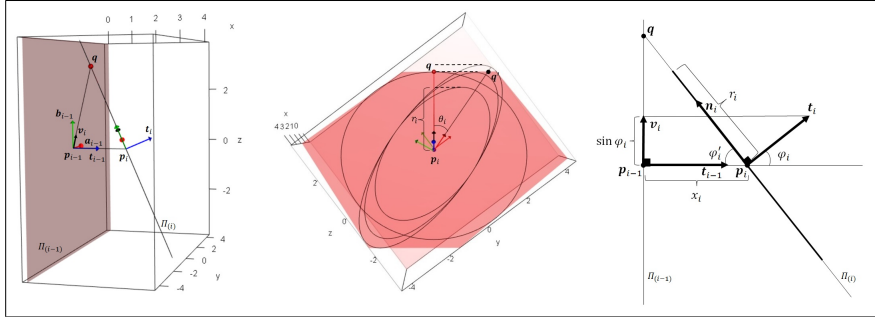
Figure 6: Visualization of two consecutive slicing planes $\Pi_{(i-1)}$ and $\Pi_{(i)}$. Left: Planes crossing $\boldsymbol{p}_{i-1}$ and $\boldsymbol{p}_i$ with normals $\boldsymbol{t}_{i-1}$ and $\boldsymbol{t}_i$. Middle: Elliptical cross-sections of different sizes. The largest cross-section violates the RCC. Right: Illustration of a slice of the left and middle figures crossing $\boldsymbol{p}_{i-1}$, $\boldsymbol{p}_i$, and $\boldsymbol{q}$.

15

The ith cross-section $\Omega_{(i)}$ is an elliptical disk in $\Pi_{(i)}$ centered at $\boldsymbol{p}_i$. We apply orthogonal projection to map $\Omega_{(i)}$ on the line $\overleftrightarrow{\boldsymbol{p}_i\boldsymbol{q}_i}$. Obviously, the projection is a line segment centered at $\boldsymbol{p}_i$ with a maximum length of $2\lVert\overrightarrow{\boldsymbol{p}_i\boldsymbol{q}}\rVert$. Let r_i be half the length of the line segment divided by $\boldsymbol{p}_i$. Therefore, we have $r_i \leq \lVert\overrightarrow{\boldsymbol{p}_i\boldsymbol{q}}\rVert$. Let $\varphi'_i = \angle\boldsymbol{p}_i\boldsymbol{p}_{i-1}\boldsymbol{q}$, and $\varphi_i = \frac{\pi}{2} - \varphi'_i$ be the complement of φ'_i. Thus, $\lVert\overrightarrow{\boldsymbol{p}_i\boldsymbol{q}}\rVert = \frac{x_i}{\cos\varphi'_i}$, and we have $r_i \leq \frac{x_i}{\cos\varphi'_i}$, where $x_i = \lVert\overrightarrow{\boldsymbol{p}_{i-1}\boldsymbol{p}_i}\rVert$. The RCC of $\Omega_{(i)}$ can be expressed as $r_i \leq \frac{x_i}{\sin\varphi_i}$ (because $\sin\varphi_i = \cos\varphi'_i$). Therefore, given φ_i and x_i, to check whether ω_i complies with the RCC, it is sufficient to calculate r_i. Hence, analogous to the approach of Vouga (2014), the curvature of the discrete curve at $\boldsymbol{p}_i$ representing the rate of frame rotation can be considered as $\kappa_i = \frac{\sin\varphi_i}{x_i}$.

The boundary of $\Omega_{(i)}$ is an ellipse that can be parameterized as $\partial\Omega_{(i)} = (a_i\cos t, b_i\sin t)$, where $t \in [0, 2\pi]$. By rotating $\partial\Omega_{(i)}$ with θ_i degree clockwise relative to F_i we have

$$\begin{bmatrix} \cos\theta_i & -\sin\theta_i \\ \sin\theta_i & \cos\theta_i \end{bmatrix} \begin{bmatrix} a_i\cos t \\ b_i\sin t \end{bmatrix} = \begin{bmatrix} a_i\cos t\cos\theta_i - b_i\sin t\sin\theta_i \\ a_i\cos t\sin\theta_i + b_i\sin t\cos\theta_i \end{bmatrix}.$$

Thus, $a_i\cos t\cos\theta_i - b_i\sin t\sin\theta_i$ is the parameterized projection of $\partial\omega_i$ onto the line $\overleftrightarrow{\boldsymbol{p}_i\boldsymbol{q}_i}$. Assume we have the function $h(t; a, b, \theta) = a\cos t\cos\theta - b\sin t\sin\theta$. For given a_i, b_i, and θ_i, the maximum value of $h(t; a_i, b_i, \theta_i)$ defines r_i. Thus, based on $\frac{\partial h(t; a_i, b_i, \theta_i)}{\partial t} = 0$ we have

$$-a_i\sin t\cos\theta_i - b_i\cos t\sin\theta_i = 0 \Rightarrow \frac{\sin t}{\cos t} = -\frac{b_i}{a_i}\frac{\sin\theta_i}{\cos\theta_i} \Rightarrow t = \tan^{-1}(\frac{-b_i}{a_i}\tan\theta_i).$$

Hence,

$$r_i = |a_i\cos\left(\tan^{-1}(\frac{-b_i}{a_i}\tan\theta_i)\right)\cos\theta_i - b_i\sin\left(\tan^{-1}(\frac{-b_i}{a_i}\tan\theta_i)\right)\sin\theta_i|. \tag{5}$$

Let $s = (\omega_i)_{i=0}^n = ((\boldsymbol{f}_i^*, x_i, a_i, b_i)_i)_{i=0}^n$, where ω_i represents $\Omega_{(i)}$. Based on $\boldsymbol{f}_i^*$, we can calculate F_i^* of ω_i and consequently the curvature and twisting angles φ_i and θ_i. Thus, by considering the RCC, $\mathcal{A}^{n+1}$ can be seen as a subspace of $\mathbf{S}^{n+1}$ such that if $s \in \mathcal{A}^{n+1}$, then $\forall i; r_i \leq \frac{x_i}{\sin\varphi_i}$, where r_i comes from Equation (5). For a *circular tube* (C-tube) $\forall i$, $\Omega_{(i)}$ is a circle, and we have $r_i = a_i = b_i$. Figure 6 illustrates two slicing planes $\Pi_{(i-1)}$ and $\Pi_{(i)}$ with an elliptical cross-section $\Omega_{(i)}$ of different sizes.

16

4.4 Semi-intrinsic approach

In this section, we discuss a simple and straightforward approach called the semi-intrinsic approach for defining the ETRep shape space and mean shape. This approach is a modified version of the extrinsic approach discussed in Section 4.2, incorporates the RCC.

Let $s = (\omega_i)_{i=0}^n = ((\boldsymbol{f}_i^*, x_i, a_i, b_i)_i)_{i=0}^n \in \mathcal{A}^{n+1}$ and let $\tau_i = \frac{b_i}{a_i} \in (0, 1]$. Equation (5) becomes

$$r_i = |a_i \cos(\tan^{-1}(-\tau_i \tan(\theta_i))) \cos(\theta_i) - \tau_i a_i \sin(\tan^{-1}(-\tau_i \tan(\theta_i))) \sin(\theta_i)|. \qquad (6)$$

Since $r_i \leq \frac{x_i}{\sin \varphi_i}$, the ratio $\rho_i = \frac{\tan^{-1}(r_i)}{\tan^{-1}(\frac{x_i}{\sin \varphi_i})}$ is in $(0, 1]$, where $\tan^{-1}(x)$ is a *control function* that maps $\mathbb{R}^+$ to the finite interval $[0, \frac{\pi}{2}]$. Thus, τ_i reflects the eccentricity of $\Omega_{(i)}$, and ρ_i reflects the ratio of its size relative to its maximum possible size.

Obviously, $r_i = \tan(\rho_i \tan^{-1}(\frac{x_i}{\sin \varphi_i}))$. By replacing r_i in Equation (6) we have

$$a_i = \frac{\tan(\rho_i \tan^{-1}(\frac{x_i}{\sin \varphi_i}))}{|\cos(\tan^{-1}(-\tau_i \tan \theta_i)) \cos \theta_i - \tau_i \sin(\tan^{-1}(-\tau_i \tan \theta_i)) \sin \theta_i|}, \qquad (7)$$

and $b_i = \tau_i a_i$.

In fact, we map the non-convex space $\mathcal{A}^{n+1}$ to a convex space, namely $\mathcal{A}^{\dagger n+1}$, by the invertible mapping $\mathscr{F}^\dagger(\boldsymbol{f}_i^*, x_i, a_i, b_i)_i = (\boldsymbol{f}_i^*, x_i, \tau_i, \rho_i)_i$, where $\mathcal{A}^\dagger = \mathbb{S}^3 \times \mathbb{R}^+ \times (0, 1]^2$. Thus, ω_i can be represented as $\omega_i^\dagger = (\boldsymbol{f}_i^*, x_i, \tau_i, \rho_i)_i$ in $\mathcal{A}^{\dagger n+1}$. Assume $s_1^\dagger = ((\boldsymbol{f}_{1i}^*, x_{1i}, \tau_{1i}, \rho_{1i})_i)_{i=0}^n$ and $s_2^\dagger = ((\boldsymbol{f}_{2i}^*, x_{2i}, \tau_{2i}, \rho_{2i})_i)_{i=0}^n$. The convexity of $\mathcal{A}^{\dagger n+1}$ can be explained based on a straight path between $s_1^\dagger$ and $s_2^\dagger$. It is sufficient to replace τ_{ji} and ρ_{ji} with a_{ji} and b_{ji}, in Equation (3), where $j = 1, 2$. Thus, the straight path between $s_1^\dagger$ and $s_2^\dagger$ is

$$\zeta_{s^\dagger}(\lambda; s_1^\dagger, s_2^\dagger) = ((\zeta_F(\lambda; \boldsymbol{f}_{1i}^*, \boldsymbol{f}_{2i}^*), \zeta(\lambda; x_{1i}, x_{2i}), \zeta(\lambda; \tau_{1i}, \tau_{2i}), \zeta(\lambda; \rho_{1i}, \rho_{2i}))_i)_{i=0}^n.$$

Thus, $\mathscr{F}^{-1}(\zeta_{s^\dagger}(\lambda; s_1^\dagger, s_2^\dagger))$ is a valid path in $\mathcal{A}^{n+1}$ corresponding to $\zeta_{s^\dagger}(\lambda; s_1^\dagger, s_2^\dagger)$ in $\mathcal{A}^{\dagger n+1}$. The rest of the discussion regarding distance and sample mean is the same as the extrinsic distance and sample mean from Equation (1) and Equation (4). Thus, we have

$$d_{s^\dagger}(s_1^\dagger, s_2^\dagger) = \left(\sum_{i=0}^n d_g^2(\boldsymbol{f}_{1i}^*, \boldsymbol{f}_{2i}^*) + \|x_{1i} - x_{2i}\|^2 + \|\tau_{1i} - \tau_{2i}\|^2 + \|\rho_{1i} - \rho_{2i}\|^2 \right)^{\frac{1}{2}},$$

17

121

and

$$\bar{s}^\dagger = \operatorname*{argmin}_{s^\dagger \in \mathbf{S}_{n+1}^\dagger} \sum_{j=1}^{m} d_{s^\dagger}^2(s^\dagger, s_j^\dagger).$$

Finally, the sample mean shape is $\mathscr{F}^{-1}(\bar{s}^\dagger)$.

The main concern about the semi-intrinsic approach is defining the control function. There is a variety of functions that can be considered as control functions. For instance, the numerator of Equation (7) changes to the term $(\tan(\rho_i \tan^{-1}(\frac{x_i}{\sin \varphi_i})^\eta))^{\frac{1}{\eta}}$ by considering the control function as $\tan^{-1}(x^\eta)$, where $\eta \in (0, \infty)$. Therefore, as depicted in Figure 7, the semi-intrinsic transformation and the mean object are very sensitive to the selection of the control function. On the other hand, in the semi-intrinsic approach, the rotation of the cross-section is not commensurate with its size during the transformation. Besides, the structure of the shape space is not explicit.
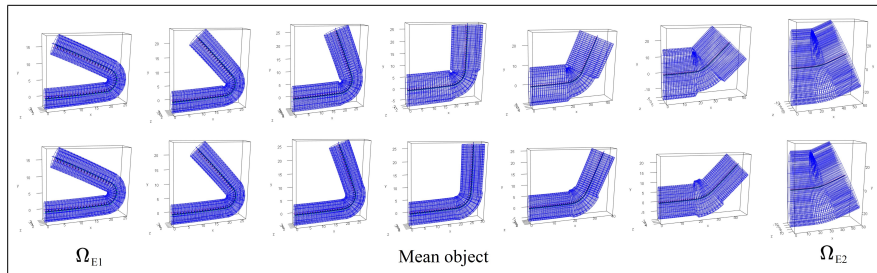

Figure 7: Top row: The semi-intrinsic transformation between E-tubes Ω_{E1} and Ω_{E2} based on the control function $\tan^{-1}(x^\eta)$, wherein the top row η is 0.8, and in the bottom row η is 2.

To explain the ETRep space in the semi-intrinsic approach, we considered the RCC as the maximum size of the cross-section $\Omega_{(i)}$ based on its curvature angle φ_i. That is to say, what the maximum size of $\Omega_{(i)}$ could be based on a given φ_i. To commensurate the rotation of $\Omega_{(i)}$ (i.e., rotation of the material frame) with the size of $\Omega_{(i)}$, we propose a shape space and intrinsic path by considering the RCC as the maximum value of φ_i based on the given $\Omega_{(i)}$. To provide an explicit intuition about the structure of the space, first, we discuss the shape space for C-tubes.

18

4.5 C-tube shape space

This section discusses the shape space of C-tubes (with circular cross-sections) based on the fact that a C-tube can be seen as an E-tube with infinitesimal cross-sectional eccentricity. Afterward, Section 4.6 generalizes the discussion of this section to propose an intrinsic approach for calculating the mean shape of a sample of ETReps.

As discussed in Section 4.3, in an ETRep $s = ((F_i^*, x_i, a_i, b_i)_i)_{i=0}^n$, $\forall i \in \{1, ..., n\}$ vectors $\boldsymbol{t}_i$, $\boldsymbol{t}_{i-1}$, $\boldsymbol{n}_i$ are coplanar. Thus we have, $\sin \varphi_i = \|\boldsymbol{v}_i\|$, where $\boldsymbol{v}_i$ is the projection of $\boldsymbol{t}_i$ on $\Pi_{(i-1)}$, as depicted in Figure 6 (Left and Right). The RCC of $\Omega_{(i)}$ can be expressed as $\|\boldsymbol{v}_i\| \leq \min\{1, \frac{x_i}{r_i}\}$, where r_i comes from Equation (5). If $x_i \geq r_i$ then $\|\boldsymbol{v}_i\|$ can take any value in $[0, 1]$; also, if $\theta_i = 0$ then $\|\boldsymbol{v}_i\| \leq \min\{1, \frac{x_i}{a_i}\}$, and if $\theta_i = \pm\frac{\pi}{2}$ then $\|\boldsymbol{v}_i\| \leq \min\{1, \frac{x_i}{b_i}\}$, as discussed in Section 4.3. In this sense, based on the size of r_i we impose bending restriction on c_i such that $\|\boldsymbol{v}_i\|$ cannot exceed $\frac{x_i}{r_i}$.

By considering very small but not zero eccentricity for all the cross-sections of a discrete E-tube, we have $\forall i; a_i \simeq b_i \simeq r_i$ (but not equal). In fact, a C-tube can be seen as an E-tube with a skeletal sheet equipped with material frames. Thus, the ETRep becomes the representation of a C-tube that we call CTRep, denoted by $s_c = ((F_i^*, x_i, r_i)_i)_{i=0}^n$, where r_i is the radius of the ith cross-section. Thus, the RCC is $\|\boldsymbol{v}_i\| \leq \min\{1, \frac{x_i}{r_i}\}$.
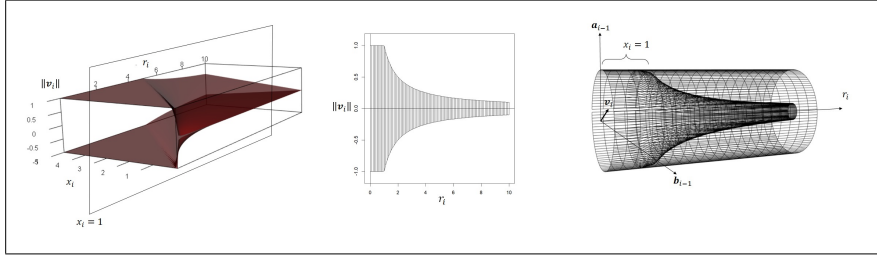

Figure 8: Left: Illustration of $\mathcal{A}_{c_2}$. Middle: The swept skeletal structure of a slice of $\mathcal{A}_{c_2}$ based on $x_i = 1$. Right: A slice of $\mathcal{A}_c$ based on $x_i = 1$ located inside a convex cylinder with radius 1.0.

In 2D we have $F_i^* = (\boldsymbol{t}_i, \boldsymbol{a}_i) \in SO(2)$. Thus, $\boldsymbol{v}_i$ has one scalar element $v_i \in [-1, 1] = \mathbb{B}$. The ith cross-section $\Omega_{(i)}$ can be represented by the vector $\boldsymbol{\omega}_i = (v_i, x_i, r_i) \in \mathcal{A}_{c_2}$, where $\mathcal{A}_{c_2} \subset \mathbb{R}^3$ is a 3D space with hyperbolic boundary such that if $(v, x, r) \in \mathcal{A}_{c_2}$, then $v \in [-1, 1]$, $r, x \in \mathbb{R}^+$, and $|v| \leq \min\{1, \frac{x}{r}\}$. In 3D, $\Omega_{(i)}$ can be represented as $\boldsymbol{\omega}_i = (v_{i1}, v_{i2}, x_i, r_i) \in \mathcal{A}_c$, where $\mathcal{A}_c \subset \mathbb{R}^4$ is a 4D space with hyperbolic boundary such that if

19

$(v_1, v_2, x, r) \in \mathcal{A}_c$, then $(v_1, v_2) \in \mathbb{B}^2$, $r, x \in \mathbb{R}^+$, and $\left\| (v_1, v_2) \right\| \leq \min\{1, \frac{x}{r}\}$. Thus, the CTRep with $n+1$ cross-sections lives on the product space $(\mathcal{A}_c)^{n+1}$, which we denote by $\mathcal{A}_c^{n+1}$. Figure 8 (left) illustrates $\mathcal{A}_{c_2}$. Figure 8 (middle) depicts a slice of $\mathcal{A}_{c_2}$ by considering $x_i = 1$ (with its swept skeletal structure). The visualization of $\mathcal{A}_c$ is challenging as it is a 4D space. Analogous to the middle figure, by considering $x_i = 1$, Figure 8 (right) depicts a slice of $\mathcal{A}_c$, which is a non-convex 3D hyperbolic area located inside a convex region as a cylinder with radius 1.0.

Each slice of $\mathcal{A}_c$ is symmetric relative to the r_i axis. Therefore, each slice is a C-tube with a swept skeletal structure. In this sense, the product space $\mathcal{A}_c^{n+1}$ is a combination of swept regions with swept skeletal structures. Since any point inside a swept region with a swept skeletal structure has an intrinsic *skeletal coordinate*, analogous to the approach of Pizer et al. (2022), we can consider an intrinsic skeletal coordinate system for $\mathcal{A}_c^{n+1}$. To elaborate further, we discuss *the skeletal coordinate system*.

4.5.1 Skeletal coordinate system

The skeletal coordinate system is an intrinsic coordinate system that can be established based on the skeletal structure of the space (Pizer et al., 2022). This section explains the skeletal coordinate system for spaces with swept skeletal structures.

Let Ω_E be a 3D E-tube with the parameterized spine $\Gamma(\lambda)$ based on the curve length parameterization. Thus, λ can be seen as the proportion of the curve length at $\Gamma(\lambda)$ from the starting point $\Gamma(0)$ relative to the total length of the curve. Assume $\boldsymbol{p}_\lambda = \Gamma(\lambda)$, and let $F_\lambda = (\boldsymbol{t}_\lambda, \boldsymbol{a}_\lambda, \boldsymbol{b}_\lambda)$ be the material frame at $\boldsymbol{p}_\lambda$. For any interior point of a swept region with a swept skeletal structure, there is a unique skeletal spoke crossing the point and connecting the Γ to the boundary (Damon, 2008). Let $\boldsymbol{p}$ be an interior point of Ω_E. Without loss of generality, let $\overrightarrow{\boldsymbol{p}_\lambda \boldsymbol{q}}$ be the direction of the skeletal spoke crossing $\boldsymbol{p}$ such that $\boldsymbol{q} \in \partial\Omega_E$. Thus, $\boldsymbol{p} = \boldsymbol{p}_\lambda + \varsigma_1 \overrightarrow{\boldsymbol{p}_\lambda \boldsymbol{q}}$, where $\varsigma_1 = \frac{\left\| \overrightarrow{\boldsymbol{p}_\lambda \boldsymbol{p}} \right\|}{\left\| \overrightarrow{\boldsymbol{p}_\lambda \boldsymbol{q}} \right\|} \in [0, 1]$. Therefore, $\boldsymbol{p}$ can be represented by the tuple $(\lambda, \varsigma_1 \overrightarrow{\boldsymbol{p}_\lambda \boldsymbol{q}})$. Since vector $\varsigma_1 \overrightarrow{\boldsymbol{p}_\lambda \boldsymbol{q}}$ is coplanar with $\boldsymbol{a}_\lambda$ and $\boldsymbol{b}_\lambda$, by assuming ς_2 as the clockwise angle between $\boldsymbol{a}_\lambda$ and $\varsigma_1 \overrightarrow{\boldsymbol{p}_\lambda \boldsymbol{q}}$ relative to $\boldsymbol{t}_\lambda$ based on the right-hand rule, the direction of $\boldsymbol{v}$ relative to F_λ can be represented by $\varsigma_2 \in [-\pi, \pi]$ such that $\varsigma_1 \overrightarrow{\boldsymbol{p}_\lambda \boldsymbol{q}} = R_{\boldsymbol{t}_\lambda}(\varsigma_2) \boldsymbol{a}_\lambda$. Thus, given the spine Γ, any interior point $\boldsymbol{p}$ can be represented as a unique vector $(\lambda, \varsigma_1, \varsigma_2)$ in $[0,1] \times [0,1] \times [-\pi, \pi]$. Besides, for the given $(\lambda, \varsigma_1, \varsigma_2)$,

20

there is a unique skeletal spoke with the tail at $\Gamma(\lambda) = \boldsymbol{p}_\lambda$ and the direction $R_{\boldsymbol{t}_\lambda}(\varsigma_2)\boldsymbol{a}_\lambda$, which is identical to the direction of $\varsigma_1\overrightarrow{\boldsymbol{p}_\lambda\boldsymbol{q}}$. Thus, the tip of the skeletal spoke is at $\boldsymbol{q}$. Therefore, $(\lambda, \varsigma_1, \varsigma_2)$ corresponds to the point $\boldsymbol{p} = \boldsymbol{p}_\lambda + \varsigma_1\overrightarrow{\boldsymbol{p}_\lambda\boldsymbol{q}} \in \Omega$. Hence, there is a bijective mapping $\mathscr{F}_s : \Omega_E \to [0, 1] \times [0, 1] \times [-\pi, \pi]$. Note that in 2D, we do not have ς_2 as the local frame associated with λ belongs to $SO(2)$. Thus, $\boldsymbol{p}$ can simply be represented as the vector $(\lambda, \pm\varsigma_1)$ in the product space $[0, 1] \times [-1, 1]$. The same discussion is valid for the generalized tubes by considering the local frames as the Frenet frames.
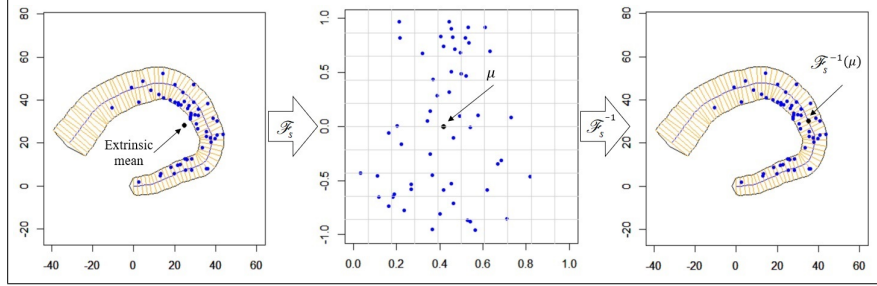

Figure 9: Left: A distribution of points inside a 2D C-tube with a swept skeletal structure. The bold dot is the extrinsic mean, which is outside the region. Middle: The mapped distribution to the product space and the Euclidean mean μ inside the product space. Right: Intrinsic mean as $\mathscr{F}_s^{-1}(\mu)$ depicted as a bold dot which is inside the C-tube.

Since the product space is convex, given a distribution of points $\boldsymbol{p}_1, ..., \boldsymbol{p}_m$ in Ω_E, the intrinsic mean can be considered as $\mathscr{F}_s^{-1}(\mu)$, where μ is the Euclidean mean of $\mathscr{F}_s(\boldsymbol{p}_1), ..., \mathscr{F}_s(\boldsymbol{p}_m)$. Figure 9 (left) depicts a distribution of points inside a 2D C-tube with the Euclidean mean (as the extrinsic mean) that is located outside the region. Figure 9 (middle) illustrates the mapped distribution to the product space and the Euclidean mean μ inside the product space. Figure 9 (right) shows the intrinsic mean as $\mathscr{F}_s^{-1}(\mu)$ inside the C-tube.

A C-tube can be seen as an E-tube with infinitesimal eccentricity in all the cross-sections, i.e., $\forall\lambda; a_\lambda \simeq b_\lambda$. Let $\mathcal{A}_c(x_i)$ be a slice of $\mathcal{A}_c$ at x_i, as depicted in Figure 8 (middle and right). $\mathcal{A}_c(x_i)$ is a C-tube with a straight spine, namely the axis r_i. Thus, the material frames similar to the Frenet frames can be considered as $I_3 = (\boldsymbol{e}_1, \boldsymbol{e}_2, \boldsymbol{e}_3)$ along the spine (i.e., the material frames coincide with the Frenet frames). By considering a large number $R >> 1$ such that $\forall i; r_i < R$, $\mathcal{A}_c(x_i)$ has a finite spine with an intrinsic skeletal coordinate

21

system. However, $\mathcal{A}_c(x_i)$ is not finite. Nevertheless, it can be seen as an infinite swept region with a straight infinite spine such that each cross-section is a circular disk.

Therefore, each point $\boldsymbol{p} = (v_1, v_2, r) \in \mathcal{A}_c(x_i) \subset \mathbb{R}^3$ is located on a skeletal spoke $\overrightarrow{\boldsymbol{p}_r \boldsymbol{q}}$ with tail at $\boldsymbol{p}_r = (0, 0, r)$ and tip at $\boldsymbol{q} = (\min\{1, \frac{x}{r}\}u_1, \min\{1, \frac{x}{r}\}u_2, r)$ with direction $\boldsymbol{u} = \frac{\boldsymbol{v}}{\|\boldsymbol{v}\|}$, where $\boldsymbol{v} = (v_1, v_2, 0)$. Thus, $\boldsymbol{p} = \boldsymbol{p}_r + \varsigma_1 \overrightarrow{\boldsymbol{p}_r \boldsymbol{q}}$, where $\varsigma_1 = \frac{\|\boldsymbol{v}\|}{\|\overrightarrow{\boldsymbol{p}_r \boldsymbol{q}}\|} = \frac{\sqrt{v_1^2 + v_2^2}}{\min\{1, \frac{x}{r}\}} \in [0, 1]$. Hence, $\boldsymbol{p}$ can be represented based on a cylindrical coordinate as $\mathscr{F}_s(\boldsymbol{p}) = (\varsigma_1 \cos \varsigma_2, \varsigma_1 \sin \varsigma_2, r)$, where $\varsigma_2 \in [-\pi, \pi]$ is the clockwise angle between $\boldsymbol{e}_2$ and $\boldsymbol{v}$. Since $\boldsymbol{u}$ and $\boldsymbol{v}$ have the same direction, we have $\mathscr{F}_s(\boldsymbol{p}) = (\varsigma_1 u_1, \varsigma_1 u_2, r)$ or more explicitly as $\mathscr{F}_s(\boldsymbol{p}) = (\varsigma_1 \boldsymbol{u}, r)$ in the convex cylinder $\mathbb{B}^2 \times \mathbb{R}^+$, as illustrated in Figure 8 (right). In other words, $\mathscr{F}_s$ can be seen as the bijective mapping $\mathscr{F}_s : \mathcal{A}_c(x_i) \to \mathbb{B}^2 \times \mathbb{R}^+$.

Based on the fact that $\mathcal{A}_c$ is a combination of its slices and by considering that the mapping $\mathscr{F}_s(\boldsymbol{p})$ acts on the first two elements of $\boldsymbol{p}$, any arbitrary point $\boldsymbol{\omega} = (v_1, v_2, x, r)$ (representing a cross-section) inside $\mathcal{A}_c$ can be represented as an element of the convex 4D product space $\widehat{\mathcal{A}_c} = \mathbb{B}^2 \times (\mathbb{R}^+)^2$ as $\mathscr{F}_s(\boldsymbol{\omega}) = (\varsigma_1 \boldsymbol{u}, x, r)$ (based on the skeletal coordinate system of the slice that $\boldsymbol{\omega}$ belongs to), i.e., $\mathscr{F}_s : \mathcal{A}_c \to \widehat{\mathcal{A}_c}$ is a bijective mapping. The same discussion is valid if we consider the slices based on the r-axis. In this sense, the plane expanded by the x and r axes can be seen as the skeletal sheet of $\mathcal{A}_c$ (see Figure 8 (left)).

4.6 Intrinsic approach

Let $\mathcal{A}_e \subset \mathbb{R}^6$ be the space of elliptical cross-sections $\boldsymbol{\omega} = (v_1, v_2, \theta, x, a, b) \in \mathcal{A}_e$, where $\boldsymbol{v} = (v_1, v_2) \in \mathbb{B}^2$, $a, b, x \in \mathbb{R}^+, \theta \in [-\pi, \pi]$, $a \geq b$, and the condition $\|\boldsymbol{v}\| \leq \min\{1, \frac{x}{r}\}$ associated with RCC is satisfied, where r comes from Equation (5) (by considering (a_i, b_i, θ_i) as (a, b, θ)). Thus, $\boldsymbol{\omega}$ can be considered as a representation of an elliptical cross-section. Obviously, the concavity of $\mathcal{A}_e$ comes from the condition $\|\boldsymbol{v}\| \leq \min\{1, \frac{x}{r}\}$ as by ignoring this condition $\boldsymbol{\omega}$ can be represented by $\boldsymbol{\omega} = (\boldsymbol{v}, \theta, x, a, b)$ belongs to the convex product space $\widehat{\mathcal{A}_e} = \mathbb{B}^2 \times [-\pi, \pi] \times (\mathbb{R}^+)^3$. Therefore, analogous to $\mathcal{A}_c$, we consider an intrinsic skeletal coordinate for $\boldsymbol{\omega}$ (based on the mapping $\mathscr{F}_s$) as $\mathscr{F}_s(\boldsymbol{\omega}) = (\varsigma_1 \boldsymbol{u}, \theta, x, a, b) \in \widehat{\mathcal{A}_e}$, where $\varsigma_1 = \frac{\|\boldsymbol{v}\|}{\min\{1, \frac{x}{r}\}}$ and $\boldsymbol{u} = \frac{\boldsymbol{v}}{\|\boldsymbol{v}\|}$ (intuitively, there is a skeletal spoke with tail and tip at $(0, 0, \theta, x, a, b)$ and $(\min\{1, \frac{x}{r}\}u_1, \min\{1, \frac{x}{r}\}u_2, \theta, x, a, b)$). Thus, $\mathscr{F}_s(\boldsymbol{\omega}) : \mathcal{A}_e \to \widehat{\mathcal{A}_e}$, and we consider intrinsic coordinate systems for $\mathcal{A}_e$ and for the product space $(\mathcal{A}_e)^{n+1}$. We denote

22

$(\mathcal{A}_e)^{n+1}$ by $\mathcal{A}_e^{n+1}$ and its corresponding convex space $(\mathscr{F}_s(\mathcal{A}_e))^{n+1}$ by $\widehat{\mathcal{A}_e}^{n+1}$.

By representing ETRep as $\mathscr{F}_s(s) = ((\varsigma_{1i}\boldsymbol{u}_i, \theta_i, x_i, a_i, b_i)_i)_{i=0}^n$ in $\widehat{\mathcal{A}_e}^{n+1}$, we can reconstruct the E-tube associated with s in 3D. Since $\forall i$; $(v_{i1}, v_{i2}) = \min\{1, \frac{x_i}{r_i}\}\varsigma_{1i}\boldsymbol{u}_i$, we calculate the ith tangent vector based on its parent frame (which is the $(i-1)$th material frame) as $\boldsymbol{t}_i = (\sqrt{1 - v_{i1}^2 - v_{i2}^2}, v_{i1}, v_{i2})$. Thus, by considering the geodesic path on the unit sphere from Equation (2), we obtain the ith Frenet frame based on its parent frame as $T_i^* = (\boldsymbol{t}_i, \boldsymbol{n}_i, \boldsymbol{n}_i^\perp)$, where $\boldsymbol{n}_i^\perp = \frac{1}{\sin\psi}(-\boldsymbol{e}_1 + \sin(\psi - \frac{\pi}{2})\boldsymbol{t}_i)$, $\psi = d_g(-\boldsymbol{e}_1, \boldsymbol{t}_i)$, and $\boldsymbol{n}_i = \boldsymbol{n}_i^\perp \times \boldsymbol{t}_i$. Consequently, the ith material frame based on its parent is $F_i^* = (\boldsymbol{t}_i, \boldsymbol{a}_i, \boldsymbol{b}_i)$, where $\boldsymbol{a}_i = R_{\boldsymbol{t}_i}(-\theta_i)\boldsymbol{n}_i$, and $\boldsymbol{b}_i = \boldsymbol{t}_i \times \boldsymbol{a}_i$. Since x_i provides the distance between the frames, by assuming $T_0 = F_0 = I_3$, we can obtain the spine by calculating the material frames in the global coordinate system as discussed in Section 3. Finally, a_i and b_i define the size of the ith cross-section.

Assume ETReps $s_1 = (\boldsymbol{\omega}_{1i})_{i=0}^n$ and $s_2 = (\boldsymbol{\omega}_{2i})_{i=0}^n$ in $\mathcal{A}_e^{n+1}$. We define the intrinsic path between s_1 and s_2 as $\zeta_I(\lambda, s_1, s_2) = (\mathscr{F}_s^{-1}(\zeta(\lambda, \mathscr{F}_s(\boldsymbol{\omega}_{1i}), \mathscr{F}_s(\boldsymbol{\omega}_{2i}))))_{i=0}^n$. Let $s_1, ..., s_m$ as a set of ETReps. By assuming the intrinsic distance as the Euclidean distance in the convex space $\widehat{\mathcal{A}_e}^{n+1}$, the intrinsic mean is the inverse map of the Euclidean mean of the mapped shapes as $\bar{s} = \mathscr{F}_s^{-1}(\frac{1}{m}\sum_{j=1}^m \mathscr{F}_s(s_j))$. Figure 10 illustrates the intrinsic mean object of a set of arbitrary 3D E-Tubes. For better visualization, the E-Tubes are aligned based on their initial material frames.
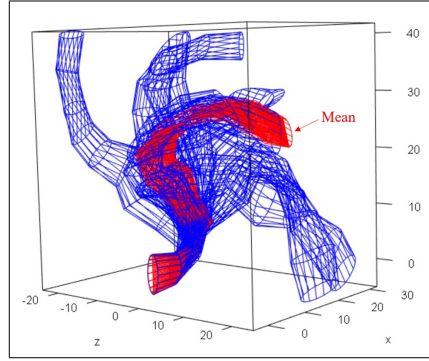

Figure 10: The intrinsic mean object of ten 3D E-tubes, which need not be aligned.

23

5 Application

One significant application of sample mean shape is in studying shape differences based on hypothesis testing. In this section, we discuss ETRep hypothesis testing based on the intrinsic approach of Section 4.6 using a hippocampal data set provided by the Stavanger University Hospital from the ParkWest study (Alves et al., 2009). In the Supplementary Materials, the same data set is used to examine hypothesis testing through the semi-intrinsic approach of Section 4.4.

The ETRep intrinsic representation is invariant to the act of rigid transformation. For the statistical shape analysis, we need to remove the scale. Assume an ETRep $s = ((\varsigma_1 u_{1i}, \varsigma_1 u_{2i}, \theta_i, x_i, a_i, b_i)_i)_{i=0}^n \in \widehat{\mathcal{A}}_e^{n+1}$. Following Taheri and Schulz (2022), we have $\ell = \exp\left(\frac{1}{3n+2}(\sum_{i=1}^n \ln x_i + \sum_{i=0}^n \ln a_i + \sum_{i=0}^n \ln b_i)\right)$ as the *LP-size* of s. Thus, the scaled and vectorized form of s is a vector $\boldsymbol{s} = (\varsigma_1 u_{1i}|_{i=0}^n, \varsigma_1 u_{2i}|_{i=0}^n, \theta_i|_{i=0}^n, \frac{x_i}{\ell}|_{i=0}^n, \frac{a_i}{\ell}|_{i=0}^n, \frac{b_i}{\ell}|_{i=0}^n)$ living on the convex feature space $(\mathbb{B})^{2(n+1)} \times ([-\pi, \pi])^{n+1} \times (\mathbb{R}^+)^{3(n+1)} \subset \mathbb{R}^{6(n+1)}$.

Let $A = \{\boldsymbol{s}_{Aj}\}_{j=1}^{m_1}$ and $B = \{\boldsymbol{s}_{Bj}\}_{j=1}^{m_2}$ be two groups of scaled ETReps of sizes m_1 and m_2. Since each ETRep is represented as a vector. The global test can be considered as $H_0 : \mu_A = \mu_B$ versus $H_{1k} : \mu_A \neq \mu_B$ where μ_A and μ_B are the observed Euclidean sample means in the convex feature space. For the hypothesis testing, we consider the permutation test with minimal assumption. Given the pooled group of two data sets (here $A \cup B$), the permutation method randomly partitions the pooled group into two groups of sizes m_1 and m_2 without replacement many times and measures the test statistic between the paired groups. The empirical p-value is $\eta = \frac{1 + \sum_{h=1}^L \chi_I(|t_h| \geq |t_o|)}{L+1}$ (Rizzo, 2007), where t_o is the observed test statistics (e.g., Hotelling's T^2 metric $T^2 = (\bar{\boldsymbol{x}} - \bar{\boldsymbol{y}})^T \hat{\Sigma}^{-1} (\bar{\boldsymbol{x}} - \bar{\boldsymbol{y}})$, where $\hat{\Sigma}$ is the common covariance matrix (Mardia et al., 1982)), t_h is the hth permutation test statistic, L is the number of permutation (usually greater than 10^4), and χ_I is the indicator function (i.e., $\chi_I(\varphi) = 1$ if φ is true, otherwise $\chi_I(\varphi) = 0$) (Taheri and Schulz, 2022). Since in ETRep analysis, the feature space is a high dimensional space, for the global test, we considered the *direction projection permutation* (DiProPerm) method of Wei et al. (2016).

Further, to detect local dissimilarities, we compare ETReps element-wise based on partial permutation tests $H_{0k} : \mu_A(k) = \mu_B(k)$ versus $H_{1k} : \mu_A(k) \neq \mu_B(k)$ based on the test statistic as t-statistic (i.e., $t = \frac{\bar{x} - \bar{y}}{\hat{\sigma}_p \sqrt{\frac{1}{m_1} + \frac{1}{m_2}}}$), where $\mu_A(k)$ and $\mu_B(k)$ are the observed

24

sample mean of the kth feature, and $k = 1, ..., 6(n+1)$. Since the partial tests are multiple comparisons, to control false positives, we adjust p-values using the *false discovery rate* (FDR) of Benjamini and Hochberg (1995). Figures 11 and 12 illustrate the result of the

Figure 11: Global test based on DiProPerm. Left: DiProPerm projection score of the observed distributions. Class labels -1 and 1 are associated with CG and PD. Right: The permutation statistics.
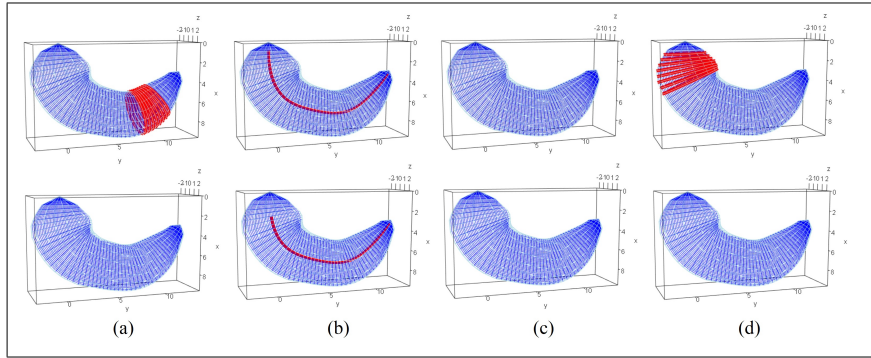

Figure 12: Hypothesis testing based on the significant level $\alpha = 0.1$. The top row depicts significant features based on raw p-values. The bottom row shows significant features after p-value adjustment with $FDR = 0.1$. Significant features are highlighted in bold where columns (a-d) depict significant sizes associated with principal radii a_i and b_i, significant spinal connections' lengths associated with x_i, significant twisting degrees associated with θ_i, and significant rotation of the material frame according to the tangent vectors associated with v_{1i} and v_{2i}, respectively.

global and partial hypothesis tests on ParkWest data comparing hippocampi of patients with Parkinson's disease (PD) versus a healthy control(CG), where in PD and CG we have 182 and 108 samples, respectively. As depicted in Figure 11, there is a statistically significant difference between PD and CG based on the obtained p-value, which is 0.048, and the significant level of $\alpha = 0.05$. Further, Figure 12 visualizes significant features that reflect the size, spinal elongation, degree of twist, and cross-sectional rotation with (bottom row) and without (top row) p-value adjustment.

25

6   Conclusion

In this work, we proposed a novel framework aimed at analyzing swept regions, particularly addressing the issue of self-intersection. We focused on a specific class of swept regions called elliptical slabular objects (E-SlOs). We introduced elliptical tube representation (ETRep) as a robust method for representing E-SlOs. The ETRep is invariant to rigid transformation and can be seen as a sequence of elliptical cross-sections along the object's center curve. To deal with the self-intersection problem in the ETRep analysis, we discussed the relative curvature condition (RCC). By considering the RCC, we defined ETRep space with an intrinsic skeletal coordinate system. We explained ETRep intrinsic distance and mean shape based on the introduced space. We introduced an intrinsic distance measure for the underlying shape space to avoid self-intersection and ensure valid statistics. We briefly outlined the issue of non-local intersections and proposed a solution for a specific class of ETReps that are simply straightenable. The advancement of the proposed solution, detailed in the Supplementary Materials, could serve as a focal point for future research. Finally, we demonstrated the application of ETRep analysis by comparing the hippocampi of patients with Parkinson's disease to those of a healthy control group.

Acknowledgments

SUPPLEMENTARY MATERIALS

Supplementary: Supplementary Materials referenced in this work are available as a pdf.
R-code: In Supplementary.zip, R codes and files are placed. (zip)

References

Abbena E, Salamon S, Gray A (2017) Modern differential geometry of curves and surfaces with Mathematica. CRC press

26

Alves G, Müller B, Herlofson K, HogenEsch I, Telstad W, Aarsland D, Tysnes OB, Larsen JP (2009) Incidence of parkinson's disease in norway. the norwegian parkwest study. Journal of Neurology, Neurosurgery & Psychiatry

Amaral GA, Dryden I, Wood ATA (2007) Pivotal bootstrap methods for k-sample problems in directional statistics and shape analysis. Journal of the American Statistical Association 102(478):695–707

Apostolova L, Alves G, Hwang KS, Babakchanian S, Bronnick KS, Larsen JP, Thompson PM, Chou YY, Tysnes OB, Vefring HK, et al. (2012) Hippocampal and ventricular changes in parkinson's disease mild cognitive impairment. Neurobiology of aging 33(9):2113–2124

Bærentzen A, Rotenberg E (2021) Skeletonization via local separators. ACM Transactions on Graphics (TOG) 40(5):1–18

Ballard D, Brown C (1982) Representations of three-dimensional structures. Computer Vision pp 264–311

Benjamini Y, Hochberg Y (1995) Controlling the false discovery rate: a practical and powerful approach to multiple testing. Royal Statistical Society 57:289–300

Brady M, Asada H (1984) Smoothed local symmetries and their implementation. The International Journal of Robotics Research 3(3):36–61

do Carmo M (2016) Differential Geometry of Curves and Surfaces: Revised and Updated Second Edition. Dover Books on Mathematics, Dover Publications

Carroll D, Köse E, Sterling I (2013) Improving frenet's frame using bishop's frame. arXiv preprint arXiv:13115857

Damon J (2003) Smoothness and geometry of boundaries associated to skeletal structures i: Sufficient conditions for smoothness. In: Annales de l'institut Fourier, vol 53, pp 1941–1985

Damon J (2008) Swept regions and surfaces: Modeling and volumetric properties. Theoretical Computer Science 392(1-3):66–91

27

Dryden I, Mardia K (2016) Statistical Shape Analysis: With Applications in R. Wiley Series in Probability and Statistics, Wiley

Fletcher PT, Lu C, Pizer SM, Joshi S (2004) Principal geodesic analysis for the study of nonlinear statistics of shape. IEEE transactions on medical imaging 23(8):995–1005

Gamble J, Heo G (2010) Exploring uses of persistent homology for statistical analysis of landmark-based shape data. Journal of Multivariate Analysis 101(9):2184–2199

Gamelin T, Greene R (1999) Introduction to Topology. Dover books on mathematics, Dover Publications, URL https://books.google.no/books?id=thAHAGyV2MQC

Georgiades P (1992) Plane-to-plane intersection. In: Graphics Gems III (IBM Version), Elsevier, pp 233–235

Giomi L, Mahadevan L (2010) Statistical mechanics of developable ribbons. Physical review letters 104(23):238104

Guillemin V, Pollack A (2010) Differential Topology. AMS Chelsea Publishing, AMS Chelsea Pub., URL https://books.google.no/books?id=FdRhAQAAQBAJ

Huynh DQ (2009) Metrics for 3d rotations: Comparison and analysis. Journal of Mathematical Imaging and Vision 35(2):155–164

Jermyn I, Kurtek S, Laga H, Srivastava A, Medioni G, Dickinson S (2017) Elastic Shape Analysis of Three-Dimensional Objects. Synthesis Lectures on Computer Vision, Morgan & Claypool Publishers, URL https://books.google.no/books?id=oq42DwAAQBAJ

Jung S, Dryden IL, Marron J (2012) Analysis of principal nested spheres. Biometrika 99(3):551–568

Kendall DG (1984) Shape manifolds, procrustean metrics, and complex projective spaces. Bulletin of the London Mathematical Society 16(2):81–121

Laga H, Guo Y, Tabia H, Fisher R, Bennamoun M (2019) 3D Shape Analysis: Fundamentals, Theory, and Applications. Wiley

28

Lee J (2013) Introduction to Smooth Manifolds. Graduate Texts in Mathematics, Springer New York, URL https://books.google.no/books?id=w4bhBwAAQBAJ

Lele SR, Richtsmeier JT (2001) An invariant approach to statistical analysis of shapes. Chapman and Hall/CRC

Lu Y (2013) Discrete frenet frame with application to structural biology and kinematics. PhD thesis, The Florida State University

Ma R, Zhao Q, Wang R, Damon J, Rosenman J, Pizer S (2018a) Deforming generalized cylinders without self-intersection by means of a parametric center curve. Computational Visual Media 4:305–321

Ma R, Zhao Q, Wang R, Damon JN, Rosenman JG, Pizer SM (2018b) Skeleton-based generalized cylinder deformation under the relative curvature condition. In: PG (Short Papers and Posters), pp 37–40

Mardia K, Bibby J, Kent J (1982) Multivariate analysis. Probability and mathematical statistics, Acad. Press

Moakher M (2002) Means and averaging in the group of rotations. SIAM journal on matrix analysis and applications 24(1):1–16

O'Searcoid M (2006) Metric Spaces. Springer Undergraduate Mathematics Series, Springer London, URL https://books.google.no/books?id=aP37I4QWFRcC

Pennec X, Sommer S, Fletcher T (2019) Riemannian Geometric Statistics in Medical Image Analysis. Elsevier Science

Pizer SM, Jung S, Goswami D, Vicory J, Zhao X, Chaudhuri R, Damon JN, Huckemann S, Marron J (2013) Nested sphere statistics of skeletal models. In: Innovations for Shape Analysis, Springer, pp 93–115

Pizer SM, Marron J, Damon JN, Vicory J, Krishna A, Liu Z, Taheri M (2022) Skeletons, object shape, statistics. Frontiers in Computer Science 4:842637

Rizzo M (2007) Statistical Computing with R. Chapman & Hall/CRC The R Series, Taylor & Francis, URL https://books.google.no/books?id=BaHhdqOugjsC

29

133

Rustamov RM, Lipman Y, Funkhouser T (2009) Interior distance using barycentric coordinates. In: Computer Graphics Forum, Wiley Online Library, vol 28, pp 1279–1288

Schulz J, Pizer SM, Marron J, Godtliebsen F (2016) Non-linear hypothesis testing of geometric object properties of shapes applied to hippocampi. Journal of Mathematical Imaging and Vision 54(1):15–34

Siddiqi K, Pizer S (2008) Medial Representations: Mathematics, Algorithms and Applications. Computational Imaging and Vision, Springer Netherlands

Srivastava A, Klassen E (2016) Functional and Shape Data Analysis. Springer Series in Statistics, Springer New York

Styner M, Oguz I, Xu S, Brechbühler C, Pantazis D, Levitt JJ, Shenton ME, Gerig G (2006) Framework for the statistical shape analysis of brain structures using spharm-pdm. The insight journal 1(1071):242

Taheri M, Schulz J (2022) Statistical analysis of locally parameterized shapes. Journal of Computational and Graphical Statistics 0(ja):1–28

Taheri M, Pizer SM, Schulz J (2023) Fitting the discrete swept skeletal representation to slabular objects, URL https://doi.org/10.21203/rs.3.rs-2927062/v1, submitted

Van Kaick O, Zhang H, Hamarneh G, Cohen-Or D (2011) A survey on shape correspondence. In: Computer graphics forum, Wiley Online Library, vol 30, pp 1681–1707

Vouga E (2014) Lectures in discrete differential geometry 1–plane curves

Wei S, Lee C, Wichers L, Marron J (2016) Direction-projection-permutation for high-dimensional hypothesis tests. Journal of Computational and Graphical Statistics 25(2):549–569

Yang K, Ke C, Tian J, Liu J, Guo Z, Liu D (2022) Three-dimensional curve reconstruction based on material frame and twisted multicore fiber. IEEE Photonics Journal 14(6):1–8

30

Supplementary Materials of "The Mean Shape under the Relative Curvature Condition"

Mohsen Taheri[*] , Stephen M. Pizer[†] and Jörn Schulz[‡]

March 31, 2024

GPA mean

In this section, we provide a simple example to show the problem of PDM analysis without considering the RCC in swept regions. As depicted in Figure 1, the boundaries of two 2D C-tubes (as two swept regions) are represented by two PDMs based on an equal number of corresponding boundary points (as the tip of the skeletal spokes). The mean shape obtained by *generalized Procrustes analysis* (GPA) is not a swept region, as it violates the RCC with an obvious self-intersection.
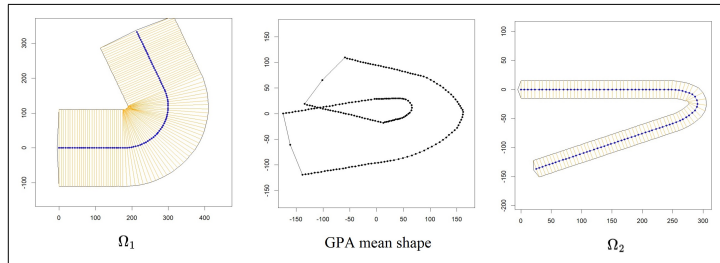

Figure 1: Illustration of the GPA mean shape of two C-tubes Ω_1 and Ω_2.

[*]Mohsen Taheri, Department of Mathematics and Physics, University of Stavanger (UiS), Email: mohsen.taherishalmani@uis.no

[†]Prof. Stephen M. Pizer, Department of Computer Science, University of North Carolina at Chapel Hill (UNC), Email: pizer@cs.unc.edu

[‡]Assoc. Prof. Jörn Schulz, Department of Mathematics and Physics, University of Stavanger (UiS), Email: jorn.schulz@uis.no

1

Extrinsic mean versus intrinsic mean

In this section, we compare extrinsic and intrinsic means based on a simple example to provide an intuition about the compatibility of the means with the structure of the space.

Imagine two distributions of points inside a non-convex space, as depicted in Figure 2 (left). The extrinsic mean based on the extrinsic Euclidean distance of the blue distribution is not acceptable as it is outside the region, and the extrinsic mean of the red distribution is very close to the boundary, while most of the red points are not. In contrast, by considering an intrinsic distance based on the skeletal coordinate system, as discussed in the main manuscript, the intrinsic means of both distributions are inside and relatively far away from the boundary. In other words, despite the extrinsic distance and mean, the intrinsic distance and mean comply with the structure of the space. Figure 2 (right) shows a closed path as a circle in $[0, 1] \times [-1, 1]$ and its corresponding closed path inside the non-convex region based on the bijective mapping $\mathscr{F}_s$.
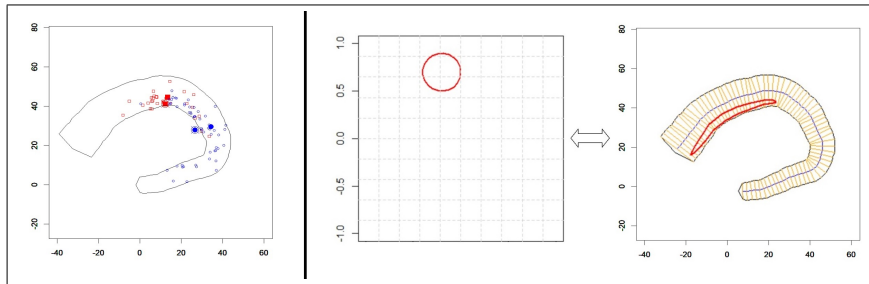

Figure 2: Left: Illustration of the intrinsic and extrinsic means of two distributions in a non-convex region in red and blue. The intrinsic mean of each distribution is bold with the same color. The extrinsic means are bold with the cross. Right: Visualization of a closed path as a circle in $[0, 1] \times [-1, 1]$ and its corresponding closed path inside the non-convex region.

Non-local self-intersection

In the main manuscript, we discussed the problem of local self-intersections in calculating the mean ETRep based on the RCC. However, in addition to the local self-intersections, we need to consider the problem of non-local self-intersection as the mean object with a non-local self-intersection is also an invalid object. In this section, we discuss the issue and

2

propose a possible solution for a class of ETReps called *simply straightenable*. We leave the generalization of the solution to future research.

The definition of a suitable space by considering the condition of non-local self-intersections for ETRep is a complex problem because the corresponding object can be twisted and intertwined like a tangled knot such that it is exceedingly difficult or even impractical to unravel it. Consequently, even by considering the RCC, the mean shape of a population of valid ETReps could be a shape with no local self-intersections but with a non-local self-intersection issue. Figure 3 provides an intuition about the problem as the mean object associated with the mean shape of two ETReps s_1 and s_2 (that are relatively symmetric) has no local self-intersection, but it is self-intersected non-locally.
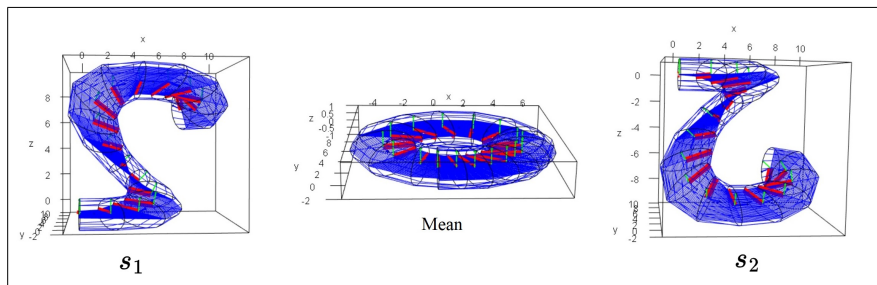

Figure 3: Illustration of non-local self-intersection in the mean object obtained based on the intrinsic mean shape of two ETReps s_1 and s_2.

A valid transformation between two tangles E-tubes is like transforming a tangled knot into another tangled knot without producing non-local self-intersections, which is not straightforward. In fact, the actual ETRep space is a subspace of $\mathcal{A}_e^{n+1}$. However, for simply straightenable ETReps, we can define a valid transformation that avoids non-local self-intersections, in addition to a suitable distance and, consequently, the mean shape.

Let $s_1 \rightarrow s_2$ denote the path $\zeta_I(\lambda, s_1, s_2)$. We call $s_1 \rightarrow s_2$ a linear path (or transformation) between s_1 and s_2. A linear path is valid if there are no occurrences of local or non-local self-intersections. Note that the non-local self-intersections are intersecting ellipses that are detectable based on the discussion of Eberly (2000). We recognize s as simply straightenable if $s \rightarrow s^\star$ is valid where $s = ((\boldsymbol{v}_i, \theta_i, x_i, a_i, b_i)_i)_{i=1}^n$ and $s^\star$ is its straightened version $s^\star = (((1,0), 0, x_i, a_i, b_i)_i)_{i=1}^n$, i.e., $s^\star$ is not twisted or bent. Thus, the space of simply straightable ETReps is a subspace of the ETReps' space that we denote by $\mathcal{A}_e^{\star(n+1)}$.

3

We consider any non-linear path $s_1 \rightsquigarrow s_2$ between $s_1, s_2 \in \mathcal{A}_e^{\star(n+1)}$ as valid if it is a combination of a finite number of valid linear paths. Let $s_{\lambda_0},...,s_{\lambda_m}$ be sequence of ETReps, where $s_1 = \lambda_0$ and $s_m = \lambda_m$ such that $\forall j \in 1,...,m$; $s_{\lambda_{j-1}} \rightarrow s_{\lambda_j}$ is valid. Thus, there is a non-linear valid path $s_1 \rightsquigarrow s_2$ as $s_{\lambda_0} \rightarrow s_{\lambda_1} \rightarrow ... \rightarrow s_{\lambda_m}$, with the length $d_s^{\rightsquigarrow}(s_1, s_2) = \sum_{j=1}^m d_s(s_{\lambda_{j-1}}, s_{\lambda_j})$. Assume $\hat{d}_s^{\rightsquigarrow}(s_1, s_2)$ is the path length of the shortest non-linear valid path between s_1 and s_2. The sample mean of $s_1, ..., s_m \in \mathcal{A}_e^{\star(n+1)}$ can be defined as $\bar{s} = \text{argmin}_{s \in \mathcal{A}_e^{\star(n+1)}} \sum_{j=1}^m (\hat{d}_s^{\rightsquigarrow}(s, s_j))^2$. Calculating the shortest path analytically is not trivial. However, since $s_1^\star \rightarrow s_2^\star$ is valid (because the curvature angles in both ETReps are zero), we know there is at least one evident valid non-linear path as $s_1 \rightarrow s_1^\star \rightarrow s_2^\star \rightarrow s_2$. Analogous to the approach of Srivastava and Klassen (2016, ch.6) in geodesic computation, it is possible to generate the evident path and then optimize it to become as short as possible. For this purpose, we propose Algorithm 1.

Algorithm 1 Valid path

Require: $s_1, s_2 \in \mathcal{A}_e^{\star(n+1)}$, and number of steps $n, m \in \mathbb{N}$
Ensure: $\mathrm{S}_{s_1 \rightsquigarrow s_2}$ as the optimized non-linear path between s_1 and s_2 with length $\hat{d}_s^{\rightsquigarrow}(s_1, s_2)$.
    Generate $n+1$ shapes s_{λ_j} such that $s_{\lambda_j} = \zeta_I(\lambda_j, s_1, s_1^\star)$, $j = 0, ..., n$
    $\mathrm{S}_{s_1 \rightsquigarrow s_2} \leftarrow \{\}$, $\hat{d}_s^{\rightsquigarrow}(s_1, s_2) \leftarrow \infty$, and $j \leftarrow 0$
    while $j < n$ **do**
        Generate $m+1$ shapes $s_{\lambda'_k}$ such that $s_{\lambda'_k} = \zeta_I(\lambda'_k, s_j, s_2)$, where $k = 0, ..., m$.
        Calculate $d = \sum_{i=0}^j d_s(s_{\lambda_i}, s_{\lambda_{i+1}}) + \sum_{i=0}^{m-1} d_s(s_{\lambda'_i}, s_{\lambda'_{i+1}})$
        if $\forall k; s_{\lambda'_k}$ is valid (with no self-intersection) and $d < \hat{d}_s^{\rightsquigarrow}(s_1, s_2)$ **then**
            $\mathrm{S}_{s_1 \rightsquigarrow s_2} \leftarrow \{s_{\lambda_1}, ..., s_{\lambda_j}, s_{\lambda'_1}, ..., s_{\lambda'_m}\}$
            $\hat{d}_s^{\rightsquigarrow}(s_1, s_2) \leftarrow d$
        end if
        $j \leftarrow j + 1$
    end while
($\leftarrow$ indicates the assigning operator.)

Note that Algorithm 1 checks the validity of $\mathrm{S}_{s_1 \rightsquigarrow s_2}$ based on its elements, which depends on n and m. Thus, theoretically, they must be large enough so that $\mathrm{S}_{s_1 \rightsquigarrow s_2}$ represents a smooth transformation between s_1 and s_2. However, selecting extremely large n and m is unreasonable because of the computational expenses. Figure 4 depicts six distinct paths between objects A and B that involve different amounts of straightening. Paths #1 and #2 are not valid, and #3 is valid with the minimum path length as mentioned in Table 1. Sample #5 on path #3 (depicted inside an ellipse) can be considered as the sample mean

4

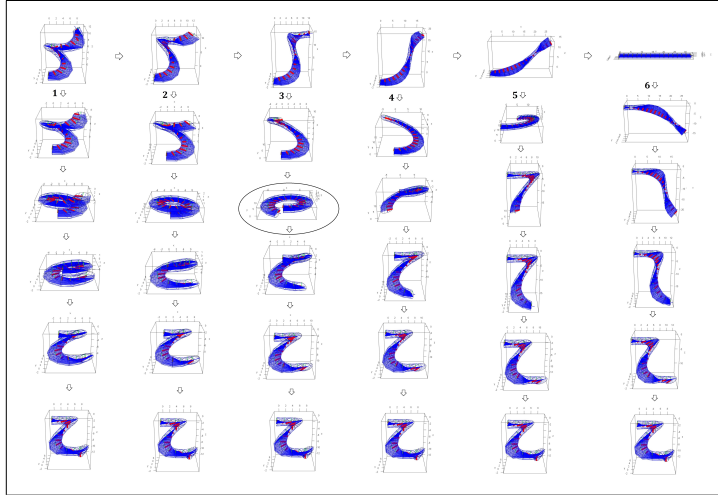with the minimum sum of squared distances to s_1 and s_2.

Figure 4: Illustration of six paths from s_1 to s_2. The first and the second paths are not valid. All shapes in the bottom row (are similar and) represent s_2.

Steps	Path 1	Path 2	Path 3	Path 4	Path 5	Path 6
1	4.89	4.89	4.89	4.89	4.89	4.89
2	3.39	5.28	5.28	5.28	5.28	5.28
3	2.57	3.49	6.39	6.39	6.39	6.39
4	2.57	2.70	4.00	8.15	8.15	8.15
5	3.39	2.82	3.16	4.89	10.52	10.52
6	4.89	3.63	3.27	4.00	6.33	11.10
7		4.89	3.93	3.97	5.46	10.52
8			4.89	4.30	4.97	8.15
9				4.89	4.75	6.39
10					4.89	5.28
11						4.89

Table 1: The sum of squared distances between shapes associated to Figure 4. Path #3 is the shortest valid non-linear path as depicted in Figure 4. Sample #5 on path #3 can be considered as the sample mean as it has the minimum sum of squared distances to s_1 and s_2.

To calculate the sample mean shape, we can consider the gradient descent Algorithm 2. We leave the detailed discussion regarding the algorithm's convergence to our future research. Figure 5 illustrates the convergence of the algorithm in $\mathbb{R}^2$.

5

Algorithm 2 Sample mean

Require: Observations $s_1, ..., s_n \in \mathcal{A}_e^{\star(n+1)}$, and the threshold δ
Ensure: Mean shape $\bar{s}$
1: $\bar{s} \leftarrow s_1$; $D_{new} \leftarrow \infty$; $D_{old} \leftarrow 0$
2: **while** $|D_{new} - D_{old}| \geq \delta$ **do**
3:     $D_{old} \leftarrow \sum_{i=0}^n (\hat{d}_s^{\leadsto}(\bar{s}, s_i))^2$
4:     $S \leftarrow \{S_{\bar{s} \leadsto s_i}\}_{i=0}^n$ (NB: S is the union of all paths from $\bar{s}$ to the observations.)
5:     $s^* \leftarrow \mathrm{argmin}_{s \in S} \sum_{i=0}^n (\hat{d}_s^{\leadsto}(s, s_i))^2$
6:     $D_{new} \leftarrow \sum_{i=0}^n (\hat{d}_s^{\leadsto}(s^*, s_i))^2$
7:     **if** $D_{new} < D_{old}$ **then**
8:         $\bar{s} \leftarrow s^*$
9:     **end if**
10: **end while**
($\leftarrow$ indicates the assign operator.)

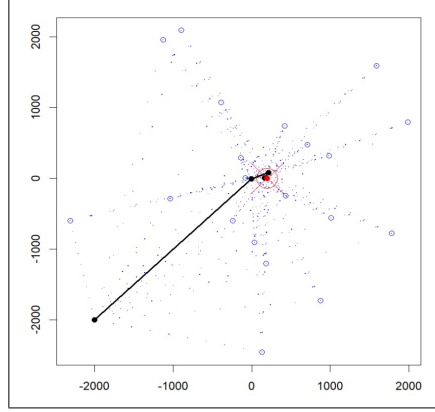Figure 5: Convergence of Algorithm 2 in the Euclidean space $\mathbb{R}^2$. The red dot is the arithmetic mean. The small dots are the generated samples (regarding set S) based on the paths between observations. The black line is the non-linear path as a combination of several linear paths toward the mean.

Hypothesis testing regarding the semi-intrinsic approach

Section 5 of the main manuscript discussed the ETRep hypothesis testing based on the intrinsic approach. This section discusses global and partial hypothesis testing regarding the semi-intrinsic approach.

Let $\{s_j^\dagger\}_{j=1}^m$ be a set of scaled (but not vectorized) ETReps with $n+1$ cross-sections. Based on the semi-intrinsic approach, we have $s_j^\dagger = (\omega_{ji}^\dagger)_{i=0}^n$ where $\omega_{ji}^\dagger = (\boldsymbol{f}_{ji}^*, x_{ji}, \tau_{ji}, \rho_{ji})_i \in$

6

$\mathbb{S}^3 \times (\mathbb{R}^+)^3$, where $x_{ji}, \tau_{ji}, \rho_{ji}$ are obtained after the act of scaling. Since we have non-euclidean data regarding the frames on the unit sphere $\mathbb{S}^3$, we use PNS Euclideanization as discussed by Jung et al. (2012); Taheri and Schulz (2022) to Euclideanize the spherical data. The PNS defines a mapping from the unit sphere to a cube as $\mathscr{F}_{\mathbb{S}^d} : \mathbb{S}^d \to ([-\pi, \pi])^d$ based on a given spherical distribution on $\mathbb{S}^d$ such that the sample mean of the spherical data is mapped to the center of the cube (i.e., the origin of the Euclidean space $\mathbf{0}$). Thus, we can map $\{\boldsymbol{f}_{ji}^*\}_{i=1}^m$ by PNS into $([-\pi, \pi])^3$. Let $\mathscr{F}_{\mathbb{S}^3}(\boldsymbol{f}_{ji}^*) = \boldsymbol{f}_{ji} = (f_{1ji}, f_{2ji}, f_{3ji})$. Therefore, the jth ETRep can be represented as $s_j^\dagger = ((f_{1ji}, f_{2ji}, f_{3ji}, x_{ji}, \tau_{ji}, \rho_{ji})_i)_{i=0}^n$ (such that $\forall j$; $\frac{1}{m} \sum_{i=1}^m (f_{1ji}, f_{2ji}, f_{3ji}) = (0, 0, 0)$). Thus, $s_j^\dagger$ can be represented as the vector

$$\boldsymbol{s}_j^\dagger = \text{vec}(s_j^\dagger) = (f_{1ji}|_{i=0}^n, f_{2ji}|_{i=0}^n, f_{3ji}|_{i=0}^n, x_{ji}|_{i=0}^n, \tau_{ji}|_{i=0}^n, \rho_{ji}|_{i=0}^n),$$

living in the convex product space $([-\pi, \pi])^{3(n+1)} \times (\mathbb{R}^+)^{n+1} \times ([-1, 1])^{2(n+1)} \subset \mathbb{R}^{6(n+1)}$.

Let $A = \{s_{Aj}^\dagger\}_{j=1}^{m_1}$ and $B = \{s_{Bj}^\dagger\}_{j=1}^{m_2}$ be two groups of scaled ETReps of sizes m_1 and m_2. Assume the pooled group $A \cup B$ as $\{s_j^\dagger\}_{j=1}^m$, where $m = m_1 + m_2$. By applying PNS on $\{s_j^\dagger\}_{j=1}^m$ and vectoring its elements, we obtain two groups of vectorized ETReps as $\{\boldsymbol{s}_{Aj}^\dagger\}_{j=1}^{m_1}$ and $\{\boldsymbol{s}_{Bj}^\dagger\}_{j=1}^{m_2}$. The rest of the discussion regarding the global test and the partial tests is the same way as we discussed in the main article.

Figure 6 shows the result of the global test on PD and CG based on the DiProPerm test. Despite the intrinsic approach, PD and CG are not significantly different as the p-value is greater than 0.1. Further, Figure 7 depicts the result of the partial tests before and after p-value adjustment. Analogous to the intrinsic approach, it seems the main difference comes from the length of the spine, as depicted in column (c).
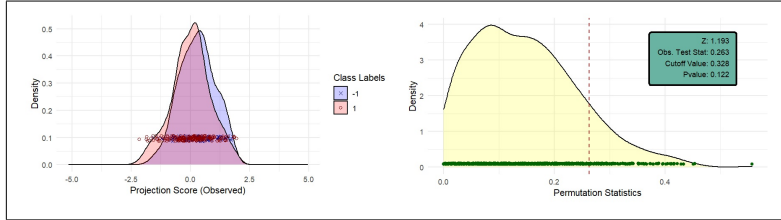

Figure 6: Global DiProPerm test based on the semi-intrinsic approach. Left: DiProPerm projection score of the observed distributions. Class labels -1 and 1 are associated with CG and PD, respectively. Right: Plot of the permutation statistics.
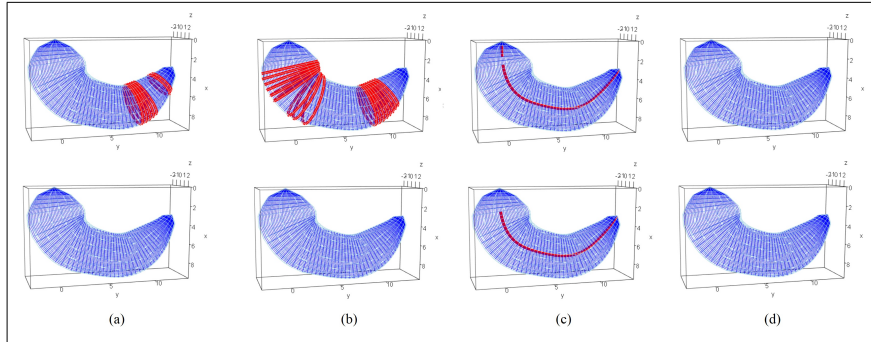
7

Figure 7: Shape analysis. Significant level $\alpha = 0.1$. The top row depicts significant features based on raw p-values. The bottom row shows significant features after p-value adjustment with $FDR = 0.1$. Significant features are depicted in red. Columns (a-d) illustrate significant eccentricities associated with ρ_i, significant relative sizes associated with τ_i, significant spinal connections' lengths associated with x_i, and significant frames' orientations associated with F_i, respectively.

References

Eberly D (2000) Intersection of ellipses. Geom Tools 200:1998–2008

Jung S, Dryden IL, Marron J (2012) Analysis of principal nested spheres. Biometrika 99(3):551–568

Srivastava A, Klassen E (2016) Functional and Shape Data Analysis. Springer Series in Statistics, Springer New York, URL https://books.google.no/books?id=0cMwDQAAQBAJ

Taheri M, Schulz J (2022) Statistical analysis of locally parameterized shapes. Journal of Computational and Graphical Statistics 0(ja):1–28, URL https://doi.org/10.1080/10618600.2022.2116445

8